UNIVERSITÀ DEGLI STUDI DI NAPOLI

‘‘FEDERICO II’’

SCUOLA POLITECNICA E DELLE SCIENZE DI BASE

Department of Chemical, Materials and Production Engineering

Ph.D. program in

INDUSTRIAL PRODUCT AND PROCESS ENGINEERING

XXXIV CYCLE

TURBULENT FLAME PROPAGATION OF DUSTS AND DUST MIXTURES

Tutors

Prof. Almerinda Di Benedetto

Eng. Roberto Sanchirico

Doctoral Candidate

Eng. Maria Portarapillo

Ph.D. Program Coordinator

Prof. Andrea D’Anna

ABSTRACT

The present work aims at studying the explosive phenomena of dust and dust mixtures to get insights into the driving mechanisms and the explosion features affecting the flame propagation and then the course of explosion. This will be achieved by means of an extensive experimental and simulative study. The major activities that will be carried out during my PhD period are:

1. Modelling of the flame propagation of combustible dust/air and hybrids;
2. Understanding of all the issues of the standard equipment;
3. Investigation of flame propagation features and key parameters (physical, operating, chemical) controlling the flame velocity

The activities are strictly related to each other. The formulation and application of a Mallard-Le Chatelier-inspired theoretical flame propagation unveils that the flame laminar burning velocity depends on several parameters that take into account the thermal behavior of the dust subjected to heating starting from the flame front to the colder layers. As a consequence, a thermal analysis of any combustible dust seems to be of crucial importance in order to fully understand the explosive behavior both in terms of intrinsic (laminar) burning velocity but also in terms of flammability/explosibility parameters. Moreover, the analysis of the thermal behavior of combustible dusts can be useful to explain a series of synergistic effects that arise in dust mixtures that can sometimes be more dangerous than pure dusts, as found by Sanchirico et al. (2018). Moreover, starting from a deep study of the fundamentals of the flame propagation of dusts and dust mixtures, the main issues related to standard test vessels will be investigated and evaluated. In particular, *CFD* simulations of the 20 L vessel with dust mixtures and 1 m^3 sphere for the measurements of $P_{max}/(dP/dt)_{max}/K_{St}$ will be developed to understand their ability dispersing a uniform dust cloud and generating a uniform turbulence field. In both the vessel, the effect of the pre-ignition turbulence level on the turbulent combustion regime and on the deflagration index was also investigated. Moreover, the overdriving phenomenon as well as the thermal effects due to the pyrotechnic ignitors explosion were assessed in both the vessel and relative to combustible dusts characterized by homogeneous or heterogeneous flame propagation. Finally, we tried to formulate a procedure to fully understand the flame propagation mechanism of the investigated dust, which standard test vessel is better to use to have conservative and reliable evaluations of explosion parameters and which issues have to be considered during testing.

Keywords:

Dust flame propagation; Thermal behaviour investigation; Non-traditional dusts; Standard devices issues; Pre-ignition turbulence level effects; Pyrotechnic ignitors effects

Summary

List of Symbols

$(dP/dt)_{max}$	*Maximum rate of pressure rise, bar s^{-1}*
A	*Cross-sectional area, m^2*
A	*Ash from proximate analysis, %*
a_1, a_2 and a_3	*Constants given by Morsi and Alexander (1972), -*
A_f	*Flame front area, m^2*
A_i	*Area under the XRD curve for the sample i, -*
A_p	*Projected flame area on a plane perpendicular to the direction of flame propagation, m^2*
Bi	*Biot number, -*
C	*Dust concentration, g m^{-3}*
C_D	*Drag coefficient, -*
C_{nom}	*Nominal dust concentration fed to the standard test vessels, g m^{-3}*
Cp_{dust}	*Specific heat, J mol^{-1} K^{-1}*
$Cp_{gas,II}$	*Weight average value of heat capacity in the II zone, J kg^{-1} °C^{-1}*
Cp_{gas_hyb}	*Specific heat of the flammable gas or vapour within hybrid, J kg^{-1} °C^{-1}*
C_{stoich}	*Stoichiometric concentration, g m^{-3}*
C_u	*Maximum explosible concentration, g m^{-3}*
$C_{worstcase}$	*Most critical concentration, g m^{-3}*
D	*Thermal diffusivity, m^2 s^{-1}*
$D(0.1)$	*Percentile (10%) value of the diameters, µm*
$D(0.5)$	*Percentile (50%) value of the diameters, µm*
$D(0.9)$	*Percentile (90%) value of the diameters, µm*
$D(4,3)$	*Volume-weighted mean diameters, µm*
Da	*Damköhler number, -*
d_{dust} or d_p	*Dust diameter, m*
D_{eq}	*Equivalent diameter, µm*
d_f	*Fibre diameter, µm*
D_{max}	*Dispersibility parameter, J^{-1}*
D_{O2}	*Effective oxygen diffusivity in the bulk material, m^2 s^{-1}*
E_1	*The highest energy at which ignition fails to occur in ten successive attempts to ignite the dust-air mixture, mJ*
E_2	*The lowest energy at which ignition occurs once at least within ten successive attempts, mJ*
E_a	*Activation energy, J mol^{-1}*
E_a^{COMB}	*Activation energy of the combustion reaction, J mol^{-1}*
f	*Additional forces per unit particle mass, N kg^{-1}*
$f(\alpha)$	*Expression of the reaction mechanism, -*
FC	*Fixed carbon from proximate analysis, %*
f_D	*Drag force per unit particle mass, N kg^{-1}*
FP	*Flash point, °C*
$f_{XRD,i}$	*XRD curve reported for each sample, -*
h_c	*Heat transfer coefficient, W m^{-2} K^{-1}*
K	*Reaction rate constant at a specific temperature, s^{-1}*
k	*Turbulent kinetic energy, m^2 s^{-2}*
Ka	*Karlovitz number, -*
Ka_δ	*Second turbulent Karlovitz number, -*
Kc	*Convective mass transfer film coefficient, m s^{-1}*

K_{disp}	*Dispersibility efficiency factor, -*
k_{in}	*Intrinsic kinetic constant for the first exothermic peak found in oxidative atmosphere, s^{-1}*
K_{MIT}	*Constant of Cassel (1964) model*
K_{St}	*Deflagration index, bar m s^{-1}*
$K_{St,max}$	*Maximum value of deflagration index, bar m s^{-1}*
l	*Integral length scale, m*
L	*Fibre length, µm*
l_F	*Flame thickness, m*
LFL	*Lower flammable limit, $\%_{vol}$*
LIT	*Minimum ignition temperature of a dust layer, °C*
LOC	*Limiting oxygen concentration, $\%_{vol}$*
$\dot{m}_{dev}$	*Mass rate of the unburnt gas mixture, kg s^{-1}*
$\dot{m}_{gas\_hyb}$	*Mass rate of the flammable gas or vapour within hybrid, kg s^{-1}*
m_{disp}	*Dispersed dust mass within the 20 L sphere, kg*
m_{dep}	*Deposited dust mass within the 20 L sphere, kg*
M	*Moisture from proximate analysis, %*
MEC (or LEL or C_1)	*Minimum explosible concentration, g m^{-3}*
MIE or Es	*Minimum ignition energy, mJ*
MIE_A	*Minimum ignition energy of component A, mJ*
MIE_B	*Minimum ignition energy of component B, mJ*
MIT	*Minimum ignition temperature, °C*
$\vec{n}$	*Unit vector normal to the flame front, -*
P	*Absolute pressure, bar*
P_0	*Ambient pressure, bar*
P_{acc}	*Maximum pressure generated by pyrotechnic ignitors, bar*
Pc	*Ratio of pyrolysis and combustion reaction time, -*
P_{max}	*Maximum pressure developed in unvented standard explosion testing, bar*
P_{red}	*Reduced pressure, bar*
P_{stat}	*Static venting activation pressure, bar*
R	*Gas constant, J mol^{-1} K^{-1}*
r_f	*Flame radius in thin-flame model by Dahoe et al. (1996), m*
r_{dust}	*Particle radius, m*
Re_t	*Turbulent Reynold number, -*
RMS	*Root mean square velocity, m s^{-1}*
r_p	*Pyrolysis reaction rate, kg m^{-3} s^{-1}*
R_{vessel}	*Standard explosion vessel radius, m*
Sc	*Schmidt number, -*
S_{dust}	*Laminar burning velocity of the combustible dust, m s^{-1}*
S_f	*Flame speed, m s^{-1}*
Sh	*Sherwood number, -*
S_l	*Laminar burning velocity, m s^{-1}*
$S_{l,\ gas\_hyb}$	*Laminar burning velocity of the flammable gas or vapour, m s^{-1}*
SSA	*Specific surface area, m^2/g*
S_t	*Turbulent burning velocity, m s^{-1}*
$St\text{-}0$	*Dust explosion hazard class, -*
$St\text{-}1$	*Dust explosion hazard class, -*
$St\text{-}2$	*Dust explosion hazard class, -*

St-3	*Dust explosion hazard class, -*
Stk	*Stokes number, -*
S_u	*Fundamental burning velocity, m* s^{-1}
t	*Time, s*
T	*Absolute temperature, K*
T_0	*Unburned temperature of mixture, K or °C*
T_1	*Temperature at which the second weight loss (before inflection temperature) occurs in TG curve, K or °C*
T_2	*Temperature at which the third weight loss (before inflection temperature) occurs in TG curve, K or °C*
T_{ad}	*Adiabatic temperature, K or °C*
t_c	*Characteristic time of internal heat transfer, s*
t_{comb}	*Characteristic time of combustion reaction, s*
t_d or t_v	*Ignition delay time, s*
t_e	*Characteristic time of external heat transfer, s*
T_{flex}	*Inflection temperature in TG curve, K or °C*
Th	*Thermal Thiele number, -*
$T_{Iexopeak}$	*1st exothermic peak temperature in TG curve, K or °C*
T_{ign}	*Autoignition temperature, K or °C*
$T_{ign,\ gas\_hyb}$	*Ignition temperature of the flammable gas or vapour within hybrid, °C*
T_{offset}	*Temperature at which weight loss ends in TG curve, K or °C*
T_{onset}	*Temperature at which weight loss starts in TG curve, K or °C*
t_{pyro}	*Characteristic time of pyrolysis reaction, s*
u	*Velocity of the unburned mixture just ahead of the flame, m* s^{-1}
u'	*Velocity fluctuations, m* s^{-1}
$\vec{U}$	*Flow velocity vector, m* s^{-1}
UFL	*Upper flammable limit,* $\%_{vol}$
u_p	*Particle velocity, m* s^{-1}
V	*Vessel volume,* m^3
VM	*Volatile matter from proximate analysis, %*
VP	*Volatile point, °C*
W_{min}	*Minimum work to break all the inter-particles bonds, J*
x	*Distance, m*
x_A	*Mass fraction of component (A), -*
y_{disp}	*Mass fraction of dispersed dust present in the 20 L sphere, -*
y_{dep}	*Mass fraction of deposited dust present in the 20 L sphere, -*
Z	*Pre-exponential factor,* s^{-1}

Greek symbols

α	*Fraction reacted of the mass of solid particle (S), -*
β	*Heating rate, °C* min^{-1}
γ	*Ratio between the actual dust concentration and the nominal dust concentration fed to the vessel, -*
δ	*Reaction zone thickness, m*
δ_{III}	*Weight average value of the thickness of the reaction zone, m*
ΔH_{dev}	*Devolatilization heat, J* kg^{-1}
$\Delta H_{Iexopeak}$	*1st exothermic peak enthalpy in TG curve, K or °C*
ΔT_i	*Temperature difference between particle and surrounding gases, K*

ε_λ	*Emissivity, -*
ε	*Dissipation rate of turbulent kinetic energy, $m^2\ s^{-3}$*
η	*Kolmogorov dissipation scale, m*
κ	*Heat capacity ratio, -*
λ_{dust}	*Thermal conductivity of the solid, $W\ m^{-1}\ K^{-1}$*
λ_{III}	*Weight average value of the burned gas thermal conductivity, $W\ m^{-1}\ °C^{-1}$*
μ	*Continuum (air) viscosity, Pa s*
μ_u	*Unburned mixture viscosity, Pa s*
ν	*Kinematic viscosity, $m^2\ s^{-1}$*
ρ	*Continuum (air) density, $kg\ m^{-3}$*
ρ_b	*Combustion products density, $kg\ m^{-3}$*
ρ_{dev}	*Weight average value of gas density in the II zone, $kg\ m^{-3}$*
ρ_{gas_hyb}	*Density of the flammable gas or vapour within hybrid, $kg\ m^{-3}$*
ρ_p *or* ρ_{dust}	*Particle density, $kg\ m^{-3}$*
ρ_u	*Initial unburned mixture density, $kg\ m^{-3}$*
σ	*Stefan–Boltzmann constant, $W\ m^{-2}\ K^{-4}$*
τ	*Relaxation time, s*
τ^+	*Dimensionless relaxation time, -*
τ_t	*Integral turbulent time, s*
σ_D	*Polydispersity, -*
Φ	*Weisz–Prater module, -*
Φ_{Th}	*Thiele modulus, -*

Acronyms

ATR-FTIR	*Attenuated total reflection-Fourier-transform infrared spectroscopy*
BET	*Brunauer–Emmett–Teller analysis*
CFD	*Computational fluid dynamics*
DDT	*Deflagration-to-detonation transition*
DPM	*Discrete Phase Model*
DSC	*Differential scanning calorimetry*
DTG	*Derivative thermogravimetry*
HPLC	*High-performance liquid chromatography*
MDF	*Medium density fibreboard*
MSC	*Mixtures safety classes*
RANS	*Reynolds averaged Navier Stokes*
S	*Solid phase*
SEM	*Scanning electron microscopy*
SSA	*Specific surface area*
TGA	*Thermogravimetric analysis*
XRD	*X-ray diffraction*

List of Figures

Figure IV.117 Explanation of each section of the suggested procedure

List of Tables

I. INTRODUCTION

Each year, in the process industry, many accidents are ascribable to dust explosions with devastating impacts on lives, properties, and the environment. The high number of casualties and the severe material damage have motivated all branches of industry and interested authorities to finance and perform scientific experimental investigations of explosion processes. The goal is to develop safety measures which will prevent explosions and protect from their effects, thus enabling industrial enterprises to achieve a high level of safety in their operations [1].

International standards were established and they are always and continuously updated in order to prescribe technical requirements necessary to manage safety to life and property from fire, flash fire, and explosion hazards involving particulate solids and to minimize the resulting damage from a fire or an explosion [2]. Until 2006, dusts have been defined as materials having a particle size of 420 μm or smaller (which means they are fine enough to pass through a U.S. No. 40 standard sieve). With the new normative, combustible dusts are defined as "a combustible particulate solid that presents a fire or deflagration hazard when suspended in air or some other oxidizing medium over a range of concentrations, regardless of particle size or shape" [3]. Despite the advancement of recent years on the comprehension of the behaviour of dust explosions, further knowledge is required as several aspects of this complex combustion phenomenon are still unclear.

The first explosion that was recognized as a dust explosion occurred in Italy on December 14 in 1785. It was reported by the Turin Academy of Science as a flour dust explosion in a warehouse in Turin. In **Table I.1**, five additional explosions creating considerable damages occurred over the next 100 years.

With increasing industrialization and the change from smaller facilities to large industrial complexes, the frequency of dust explosions has increased. Most early, dust explosions occurred in places where production and dust generation were high due to size and productivity. Up to 1922, the USA and Canada experienced 217 dust explosions. These involved organic dusts from mills, elevators, and silos, starch plants and refineries, as well as plants processing aluminium, chocolate, paper, rubber, seasoning, etc. The multitude of installations affected by dust explosions is striking [1].

Table I.1 *Dust explosions from 1785 to 1900* [1]

Year	Location	Installation	Dust type	Damage
1785	Turin (Italy)	Warehouse	Flour	Warehouse destroyed
1858	Stettin (Poland)	Roller mill	Grain	Mill building destroyed
1860	Milwaukee (USA)	Mill	Flour	Mill building destroyed
1864	Mascoutah (USA)	Mill	Flour	Mill building destroyed
1869	Unknown (Germany)	Mill	Pea flour	Local damage to mill
1887	Hameln (Germany)	Silo	Grain	Silo and building destroyed

Since the beginning of the 20th century were recorded 1404 explosions in North America (1900-2005), 269 explosions in Japan (1952-1995), 357 explosions in Germany (1965-1980), 984 fires and explosions in the United Kingdom (1958-1988) and 72 explosions in China (1981-2011) [4].
No Occupational Safety and Health Administration (OSHA) standard comprehensively addresses combustible dust explosion hazards in general industry. The OSHA Hazard Communication Standard (HCS) inadequately addresses dust explosion hazards, or safe work practices and guidance documents, in Material Safety Data Sheets (MSDSs). The 41 % of the 140-combustible dust MSDSs the CSB surveyed did not warn users about explosion hazards, and only 7 referenced appropriate NFPA dust standards to prevent dust explosions [5].
Since 2016 [1], Dust Safety Science has published semi-annual reports, in **Table I.2**, analysing the materials, industries and equipment involved in combustible dust fires and explosions around the world.

Table I.2 *Incident data overview (2016-2020)* [4]

	USA					Canada					International			
	2016	**2017**	**2018**	**2019**	**2020**	**2016**	**2017**	**2018**	**2019**	**2020**	**2017**	**2018**	**2019**	**2020**
Fire	-	117	158	175	116	-	15	17	22	14	37	38	53	35
Explosions	31	28	37	37	26	2	4	4	1	7	36	27	37	27
Injuries	22	52	40	42	35	0	9	1	4	2	102	73	72	51
Fatalities	3	6	2	1	1	0	0	0	0	0	7	21	7	9

In 2020, 70% of the recorded fatalities happened due to dust explosions. Of the injuries, 73%

occurred due to explosions and 27% occurred due to fires. From the global incident data (**Figure I.1 a)**), food and wood products made up over 75% of the fires and explosions recorded. These materials also resulted in 57% of the injuries and 40% of the fatalities. As shown in **Figure I.1 b)**, wood processing, wood products, agricultural activity and food production make up a large portion of the overall fire and explosion incidents. Since 2017, wood and wood products have ranged from 21% to 28% of the incidents, while agricultural activity and food production has ranged from 33% to 44%.

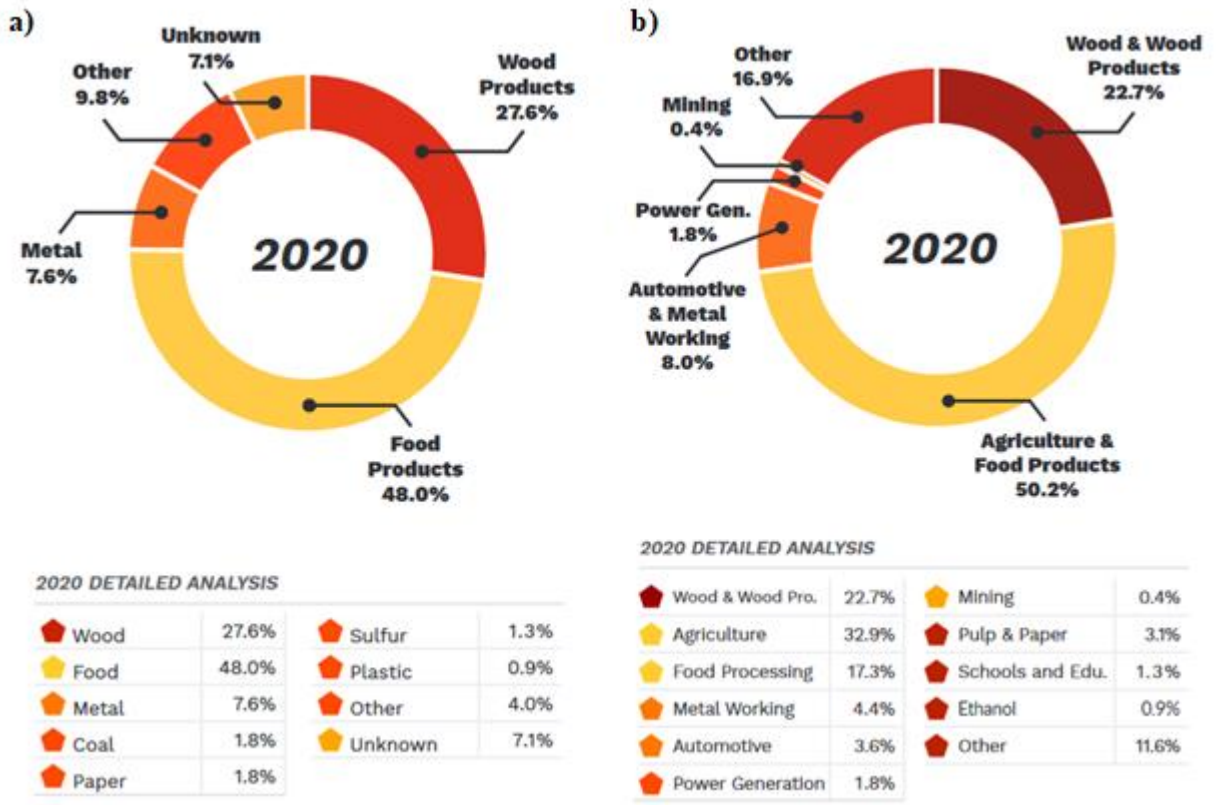

Figure I.1 *Materials (a) and industries (b) involved in dust explosions and fires in 2020* [4]

Inherently safer design is a proactive approach which aims to eliminate or lessen hazards, and consequently the risk, with decreased reliance on engineered devices and procedural measures. The four basic principles of inherent safer design (Minimization, Substitution, Moderation, and Simplification) have gained widespread acceptance in the process industry (**Figure I.2**). Minimization consists in the use of smaller quantities of hazardous materials when the use of such materials cannot be avoided or eliminated. With Substitution, the substance is replaced with a less hazardous material or processing route with one that does not involve hazardous material. Moderation involves the use of hazardous materials in their least hazardous forms or identify

processing options that involve less severe processing conditions. Simplification consists in designing processes, processing equipment, and procedures to eliminate opportunities for errors by eliminating excessive use of add-on safety features and protective devices.

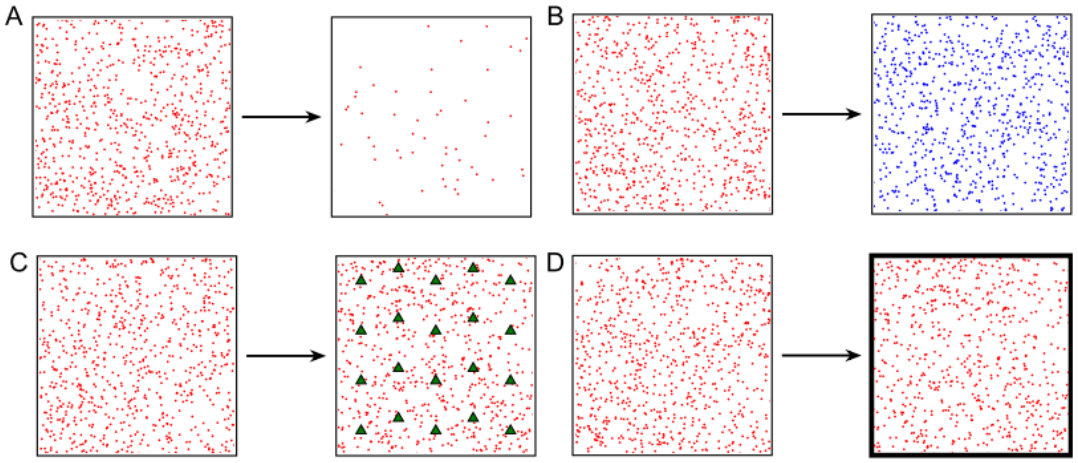

Figure I.2 *Basic principles of inherent safety: Minimization (A), Substitution (B), Moderation (C) and Simplification (D)* [6]

Inherent safety is the most effective approach to risk reduction, and it is followed in the hierarchy of risk controls by *ad-hoc* designed safety measures. The safety measures about the handling of explosive dusts can be grouped into two distinct categories: prevention and protection measures. Prevention measures have the purpose of reducing and/or eliminating all the conditions that allow the formation of an explosive mixture and all the possible causes of ignition. They include:

- Reduction/elimination of the dust by cleaning of working environment;
- Reduction/elimination of oxidant by means of suitable inerting procedures;
- Reduction/elimination of ignition source by avoiding free flames, hot surfaces, sparks and installing appropriate electrical system for hazardous areas.

The protection/mitigation measures aim to reduce the effects of the explosion that are strongly correlated to the phenomenon severity. Hazardous area classification (HAC) specific to dust applications is also an important dust hazard mitigation strategy as improperly classified or unclassified electrical components installed in areas having the potential to form combustible dust clouds can act as an ignition source resulting in a deflagration or explosion. Other mitigation measures to be adopted are mainly:

- the containment of explosion, that is the employment of equipment appropriately dimensioned to withstand the maximum explosion overpressure;

- the separation of equipment with the installation of different apparatus in different places, or physical division of the operations with higher explosion risk;
- the explosion suppression by using appropriate extinguishing substances;
- the venting that consists in a surface that can be broken against an unacceptable pressure increase.

Deflagration venting is the method more extensively used to mitigate dust explosion process [7]. Relief venting aims to prevent the generation of an unacceptably high explosion pressure within a vessel by the prompt opening of a defined aperture. Pressure relief devices may be designed for a single use (e.g., rupture discs) or for repeated use (e.g., explosion doors). A large number of analytical and highly empirical correlations including nomograms reflecting changing standards have been or are being proposed for gas and dust explosion relief venting [8]. In principle modelling developed for gas explosions venting should also apply to dust explosion venting. The difference in approach arises mainly because the models or correlations for gas explosions involve the use of the laminar or fundamental burn velocity and a turbulence correlation factor which are more difficult to specify separately for dust explosions. The deflagration venting calculations for dust and hybrid mixtures are based on the methodology outlined in NFPA 68 [8]. These calculations depend on a number of factors (**Figure I.3**) such as the deflagration explosibility index of the dust (K_{St}); the reduced pressure (P_{red}), which is the maximum pressure developed in the enclosure during a vented deflagration; the static activation pressure (P_{stat}), which is the pressure at which the vent panel opens; the maximum pressure developed in unvented standard testing (P_{max}); the inertia of the vent panel; and the geometry of the enclosure.

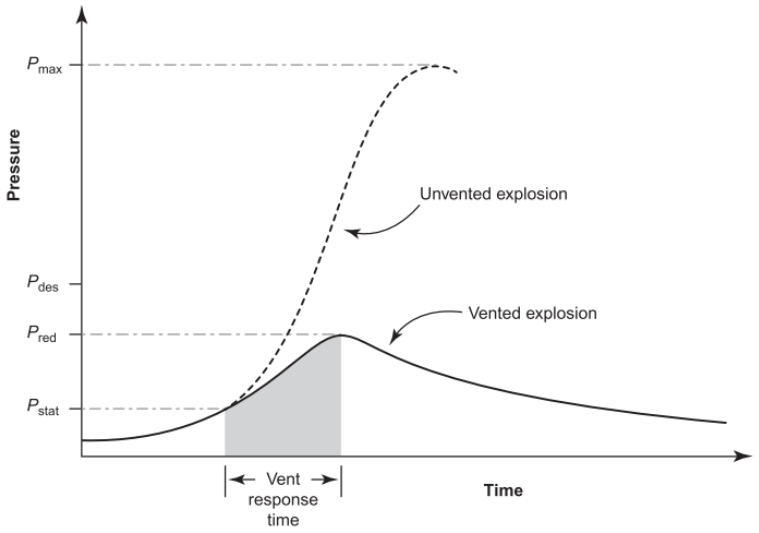

Figure I.3 *Illustration of pressure rise in vented and unvented equipment during explosion* [6]

Both P_{max} and K_{St} are determined by means of standard test procedures [9]. In order to design an adequate and effective venting against the vessel catastrophic rupture due to an internal explosion, the reliability and repeatability of the measurements of these explosion parameters is of crucial importance.

II. THEORETICAL FRAMEWORK

Dust explosions are exothermic chemical reactions (combustion) which produce a fast and significant increase of temperature and, in a confined vessel, of pressure. Like all fires, a dust fire occurs when a combustible dust is exposed to heat (an ignition source) in the presence of an oxidant (oxygen or air). Removing any one of these elements of the fire triangle (**Figure II.1 a)**) eliminates the possibility of a fire. A dust explosion requires the simultaneous presence of two additional elements: the dust dispersion and the confinement of the dust cloud. Suspended dust burns more rapidly due to the larger contact area between fuel and oxidizer, while the confinement leads to pressure build-up. These five elements are summarised in the fire pentagon (**Figure II.1 b)**). Removing either the dispersion or the confinement elements prevent an explosion, although a fire may still occur [10].

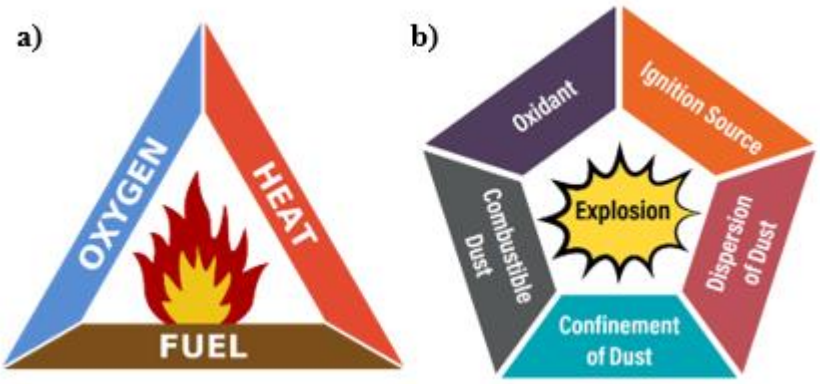

Figure II.1 *Fire triangle (a) and explosion pentagon (b)*

II.1. Types of dust explosions

There are two different kinds of dust explosion and they differ, principally, by the source of ignition and the way in which the explosion conditions are generated:

- Primary explosion
- Secondary explosion

A primary explosion occurs when the dust cloud is ignited by an external source such as heat,

sparks, or open flame. This often occurs inside or near running machinery in processing operations (a mill, a filter unit, a cyclone, a storage silo, etc.) [11].

Secondary dust explosions are the most severe ones and occur when the blast wave from a primary explosion entrains dust layers already present in the plant, creating a large dust-air flammable mixture ignited by the first explosion. As the blast wave propagates through the plant, dust fuels the emerging flame, leading to extensive damages owing to the large quantity of dusts involved and the consequent strong pressure wave (**Figure II.2**) [11].

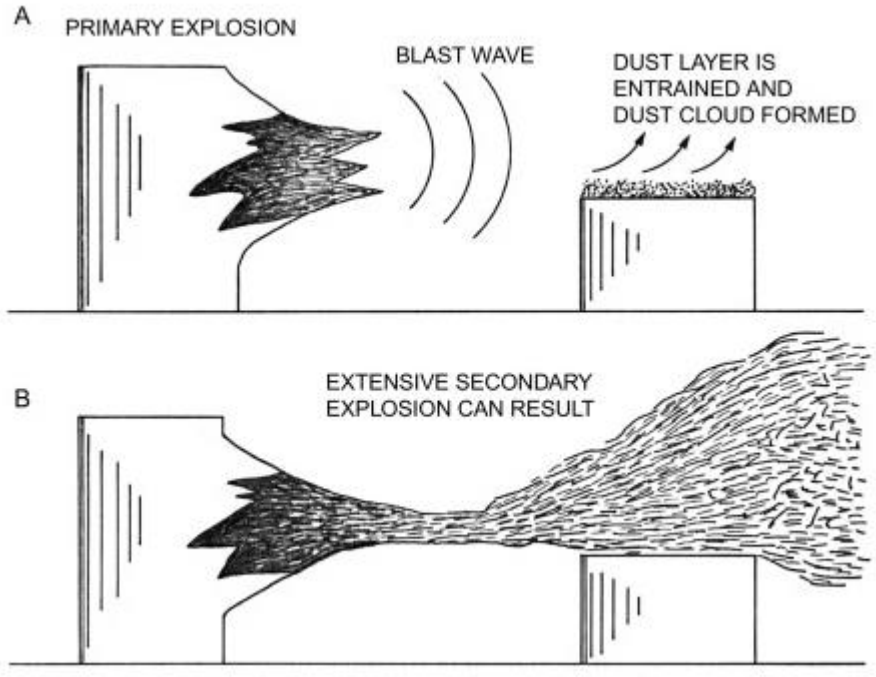

Figure II.2 Illustration of the chain effect primary to secondary explosion [11]

Another combustible dust hazard is smoldering. Smoldering is a combustion wave that travels through a fixed bed of combustible particulate solids. This fixed bed of dust may take the form of a thin layer deposited on horizontal surfaces or it may be a pile of material. However, if disturbed to create a dust suspension, a smoldering wave can act as an ignition source resulting in a dust explosion. Thus, combustible dusts are a hazard in both the dispersed state and the undisturbed state. Smoldering requires fuel, oxidizer, an ignition source and a critical thickness for the deposit. The fuel must satisfy two criteria: it must be porous and form a solid char. The ignition source may be external (independent of the fuel) or internal (self-heating caused by oxidation). A flash fire is a dust deflagration that does not result in a rise in pressure. This requires that the confinement volume must be much larger than the volume of the unburnt dust cloud. The hazards of a

combustible dust flash fire are radiant heat and direct contact with burning particles. Flame acceleration effects arise when the mass burning rate of the deflagration increases due to the influence of turbulence. The combustion process releases heat causing a localized expansion of the burnt gas. The burnt gas expansion results in an acceleration of the flame speed and increases the turbulent characteristics of the flame resulting in an increase in the mass burning rate. This results in an increasing heat release rate which accelerates the flame motion. Flame acceleration results in the magnification of dust explosion hazards. Flame acceleration is significantly more hazardous when it occurs in confinement. Sometimes, confined flame accelerations are characterized by a transition from deflagration to a detonation (*DDT*) [12].

II.2. Source of ignition

Dust explosion will occur only if the pentagon requirements are simultaneously satisfied. Preventive measures are aimed at avoiding the presence of all these factors in the system. Generally, latent hazards always exist when explosive mixtures in dangerous quantities are generated during regular operations. In such situations, protective measures must be taken. If operational ignition sources cannot be avoided, listed in **Figure II.3**, the selection and the extent of protective measures must be based on systematic risk analysis [13].

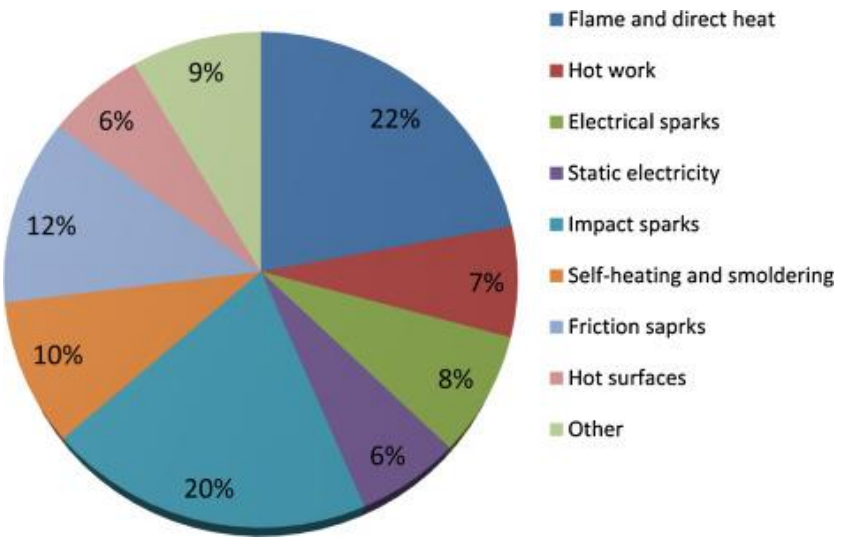

Figure II.3 *Type of ignition sources involved in dust explosions* [13]

II.2.1. Flames and hot surfaces

Open flames or hot surfaces are by far the most common sources of ignition in factory processes. The flame or hot surface may be produced inadvertently. For example, a welding or cutting

operation could be carried out on or close to a vessel or device containing flammable dust. In this case, no work should be carried out until all the dust has been removed from the area. No dust should be readmitted to the area until all sources of ignition have been removed and eventually the surfaces cooled. Indirect methods of heating processes are always to prefer to those involving open flames in order to prevent accidentally ignitions [14].

II.2.2. Spontaneous ignition

The storage itself of many dusts is able to promote spontaneous heating. If the heat is not dissipated, the ignition temperature of the dust may be reached. The immediate result of spontaneous ignition is fire, but explosions may follow if the dust is subsequently dispersed in a cloud and the resulting mixture is confined. Organic substances, such as sewage sludge, corn meal and fertilizers, are particularly prone to spontaneous heating. More recently, the global transition to renewable energy sources and the use of biomass in large quantities, especially wood pellets, has given rise to a significant number of self-heating fires. Metal dusts are also susceptible to spontaneous heating [14].

II.2.3. Friction sparks

Many explosions have been caused as the result of foreign objects entering a grinding mill or disintegrator with the feedstock. The machinery itself may cause ignition. Friction in bearings, for example, may generate sufficient heat to ignite dust, and it is important that bearings should be properly lubricated and maintained. Ideally, bearings should be external to the dust cloud as part of the machinery design [14].

II.2.4. Electrical plant

Flammable dusts may be ignited by sparks generated by electrical equipment, for example, during the operation of switchgear, when fuses blow, cables or equipment are damaged. Ignition may also occur if the surface temperatures of the equipment are excessive, particularly if accumulations of dust are allowed to form on such surfaces [14].

II.2.5. Static electricity

Precautions should be taken to minimize the possibility of the formation of static charges on plant. All conducting materials should be efficiently earthed using bonding strips, and routine tests for electrical resistance should be made at frequent intervals. Where static charges are likely to be

developed on plant made of non-conducting materials such as belts and rubber sleeves, these components can often be replaced by anti-static rubber or similar non-conducting materials. Dust in bulk may retain charges for a very long time if its electrical resistivity is high [14].

II.3. Assessment of ignitability and explosibility of dusts

Committee E27 of ASTM International, which deals with the Hazard Potential of Chemicals, has been in existence since 1967. During that time, its members have developed and approved over 20 consensus standards relating to ignitability, flammability, and chemical reactivity. These ASTM E27 ignitability, flammability, and explosibility standards are used to assess the gas, vapor, and dust explosion hazard properties of materials; to establish safe operating conditions; and to perform consequence analysis for hypothesized accidents [15].

Ignitability test methods determine the ease of ignition of the most sensitive mixture of fuel-air (oxidant). The parameters that characterize the ease of ignition are the Minimum Ignition Temperature of a dust cloud (*MIT*), the Minimum Ignition Energy of a dust cloud (*MIE*) and the Hot-Surface Ignition Temperature of Dust Layers (*LIT*) ([16]–[18]). Flammability limit test methods determine the concentration limits of fuel, air (oxidant), or suppressant that can propagate a flame in the presence of a sufficiently strong ignition source. This concept can also be extended to temperature limits of flammability, as related to commonly used flash-point values for liquids. The parameters that characterize the flammability limit are the Volatile Point (*VP*), the Minimum Explosion Concentration (*MEC*, for dusts), the Lower and Upper Flammability Limits (*LFL* and *UFL*, for gases), the Limiting Oxygen Concentration (*LOC*) ([19]–[22]). The explosibility testing methods assume the presence of both a sufficiently strong ignition source and the worst case or most energetic mixture of fuel and oxidizer. They aim to characterize the severity of the dust explosion through the measurement of the maximum explosion pressure P_{max}, the maximum rate of pressure rise $(dP/dt)_{max}$ and the deflagration index K_{St} [9].

II.3.1. Minimum ignition temperature (MIT)

The minimum ignition temperature (*MIT*) is the minimum temperature at which a given dust cloud will ignite when exposed to air heated in a furnace at local atmospheric pressure. The equipment used to assess *MIT* is generally the Godbert-Greenwald furnace, an apparatus in which a dust/air mixture flammability is observed [18]. Hot surfaces capable of igniting dust clouds are very common in industries, such as in furnaces, burners, and dryers of various kinds. In addition, hot surfaces can be generated accidentally by overheating of mechanical parts. If a flammable dust

cloud is generated in the proximity of a hot surface of temperature equal or above the actual minimum ignition temperature, the result can be a dust explosion. It is important, therefore, to know the actual *MIT* of a material and to adopt adequate precautions to ensure that temperatures of hot surfaces in areas where explosive dust clouds can occur, do not rise to this value. However, the minimum ignition temperature is not a constant for a given material but depends on the physical properties of the dust itself, such as particle dimension and moisture content, and on constructive parameters of equipment used for the tests, for example the geometry of the hot surface and the dynamics of the cloud during the tests.

During the years, some models have been proposed to predict *MIT* of dusts, knowing the particle size. The two models that return results closest to the experimental data are those of Cassel (1964) and Mitsui & Tanaka (1973) ([23], [24]). The two models are based on different assumptions and make different simplifications. Cassel developed a model of a single dust particle ignition by performing a heat balance around a single dust particle in an oxidizing atmosphere. The minimum ignition temperature predicted by this model is given by Equation (1) :

$$MIT = \frac{K_{MIT} \cdot \left(\frac{\frac{E_a^{COMB}}{R \cdot MIT} - 1}{\frac{E_a^{COMB}}{R \cdot MIT}} \right)}{r_{dust}^{\left(\frac{1}{\frac{E_a^{COMB}}{R \cdot MIT} - 2} \right)}} \quad (1)$$

Where K_{MIT} (K) is a constant, r_{dust} (m) is the particle radius, E_a^{COMB} (J mol^{-1}) is the activation energy of the combustion reaction, R (J mol^{-1} K^{-1}) is the gas constant. In this model, Cassel ignored the effect of radiations produced by burning particle and its surrounding unburning particles and the vessel wall [23].

Mitsui and Tanaka (1973) developed their model considering both heat exchange between burning and unburning particle, and the heat loss to the vessel wall. The resulting model is composed by a system of two coupled equations, more complex than the Cassel one, where at the same time are calculated the temperature of the particle and the gas surrounding the particles. Results were validated against experimental data available for metal dusts showing good agreement. This model shows discrepancies in its application to most of the organic dusts. The discrepancies in results for organic dusts are since the Mitsui and Tanaka model is based on the assumption that the oxidation of the dust particle is a surface phenomenon and the reaction on the particle surface is responsible for autoignition of the dust cloud. This is acceptable for some metals and non-volatile solids. For organic dusts, the devolatilization/decomposition of the particles followed by homogeneous oxidation of volatile/decomposed products can be visualized as the main mechanism

of ignition of the dust cloud [24]. Mitta and Guha (1998) proposed a model for determining the minimum ignition temperature for an organic dust cloud, polyethylene, simulating the conditions in the Godbert–Greenwald furnace. It is based on the two-stage oxidation mechanism involving devolatilization/decomposition of the solid particle and homogeneous combustion of volatile combustible products. The predicted values by the model developed were in close agreement with the experimental data which confirm the proposed ignition mechanism. The model can be used for the prediction of minimum ignition temperature of organic dusts having an autoignition mechanism similar to polyethylene dust [25].

II.3.2. Minimum ignition energy (MIE)

MIE is determined as the electrical energy stored in a capacitor which, when released as a high voltage spark, is just sufficient to ignite the dust cloud at its most easily ignitable concentration in air. The experimental determination of the minimum ignition energy is done using different types of electric sparks in a clear plastic or glass Hartmann tube apparatus, typically 0.5 or 1.2 L [16]. *MIE* values depend on the composition of the mixtures, the nature of the spark, the properties of the electric circuit and varies also with particle size, shape and moisture content. For example, *MIE* value decrease with the particle size while increases with the moisture content that reduce the dispersibility of the dust cloud.

Kalkert and Schecker (1979) presented a model for the theoretical calculation of *MIE* of a dust cloud proportional to the particle volume. Comparing their theoretical predictions with experimental data from other researchers, Kalkert and Schecker (1979) were able to confirm a close agreement between their predictions and experimental *MIE* values for polyethylene dust of various median particle sizes [26].

Copelli et al. (2021) developed a simple mathematical model able to theoretically estimate *MIE* of organic powders using very few easily accessible experimental information, such as granulometric analysis and thermogravimetric analysis (*TGA*). Particularly, *TGA* was used to determine the pyrolysis kinetics of the dust, which is then used within the model to compute the rate of combustible volatiles released by the dust particles. The model first required the definition of *LFL* of the volatile gases produced during the dust pyrolysis. This was not a simple task, since different flammable gases can be emitted during the dust pyrolysis, possibly also changing the composition with temperature. To simplify this problem, they assumed that when polymer dusts are involved, their monomers are representative of the flammability properties of the volatile gases produced, whereas, for all the other organic dusts, methane is the species that can effectively represent the

flammable properties of the volatile gases. The proposed procedure has been validated by comparison with literature experimental data of minimum ignition energy of several organic dusts, showing a good agreement [27].

*II.3.3. Hot-Surface Ignition Temperature of Dust Layers (*LIT*)*

The layer ignition (*LIT*) test determines the lowest temperature at which a layer of dust of specific thickness, usually 5 mm, ignites on a heated surface. It is an important test for industrial applications where heat-generating equipment are present, for examples electric motors, as it evaluates the maximum allowable surface temperature to prevent fires and smoldering material. The test material is placed within a metal ring on top of a hot plate, that is set at a constant temperature. The sample temperature is monitored to determine temperature rise due to oxidative reactions or decomposition reactions, or both [17]. *LIT*, together with *MIT*, give clear information about the maximum temperature allowable in a determined plant, handling a specified dust.

II.3.4. Volatile point (VP)

The flash point is the lowest temperature at which a liquid generates enough vapours to form a mixture with air (or another oxidative agent, such as pure oxygen) at lower flammable limit (*LFL*). For dusts that are characterized by a homogeneous combustion, a specular parameter has been proposed [22]. The Volatile Point (*VP*) represents the temperature at which pure dusts, dust mixtures and hybrid mixtures are able to produce volatiles which form, in contact with an oxidizing medium, a flammable vapor mixture at *LFL*. Volatile Point is measured by using the same apparatus used for Flash Point (*FP*). The device is a closed cup instrument that allows the measurement of *FP*/*VP* for liquid/solid samples following different international standards over the range ambient to 300 °C [21]. According to the model by Di Benedetto and Russo (2007), explosion of a dust occurs through several steps summarized in **Figure II.4** [28]. In the step of dust devolatilization, flammable gases are produced and when their amount is enough, an explosion occurs. Depending on the temperature at which devolatilization occurs, the amount of gases produced changes. At *VP*, the volatiles formed have a composition equal to the lower flammability limit, thus a flammable cloud is formed. The principal difference between *FP* and *VP* is that, in case of liquids, vapours are produced by evaporation while, in case of dusts, they are formed through physical and/or chemical processes (e.g., pyrolysis). As a consequence, this temperature is very important since it allows protecting from the formation of flammable vapor

cloud. Notably, *VP* of dusts and dust mixtures results much lower than *MIT* and *LIT*, suggesting it is worth using to use this temperature to assess the maximum temperature to avoid ignition [22].

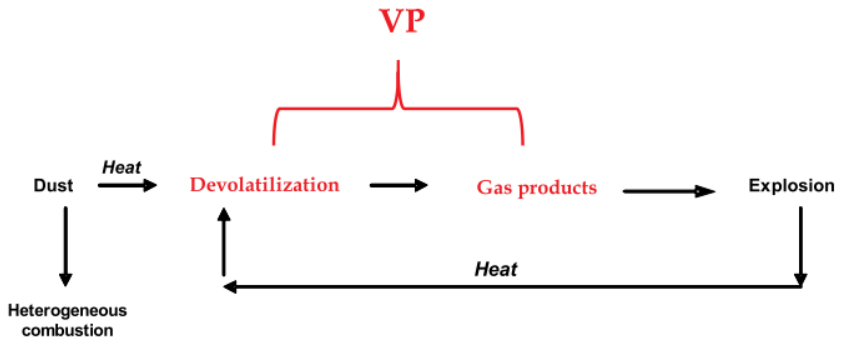

Figure II.4 *Explosion path of a dust* [28]

Moreover, results showed that *VP* of the mixtures may be lower than *VP*s of the pure compounds, probably for the occurrence of a strong interaction leading to the reduction of the pyrolysis temperature and then of *VP* (**Figure II.5**). This synergistic behaviour should be carefully considered when storing and handling dust mixtures and hybrid mixtures [22].

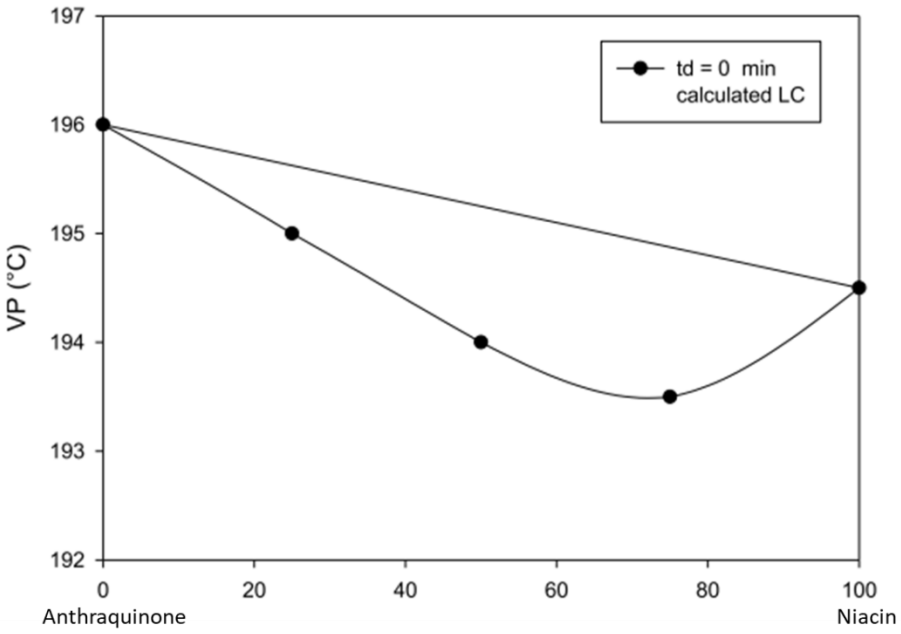

Figure II.5 *Values of VP as a function of the anthraquinone content in the anthraquinone/niacin mixture* [22]

II.3.5. Minimum Explosion Concentration (MEC)

Minimum explosible concentration of dust clouds is an important factor requiring special attention for hazard evaluation if any technological equipment is to be protected by inertisation. Often called Lower Explosive Limit (*LEL*), *MEC* is the minimum concentration of combustible dust suspended in air, measured in mass per unit of volume, capable of propagating a deflagration. Conversely, the upper explosive limit for dusts is not well defined and have poor repeatability under laboratory test conditions. Since the upper explosive limit is of little practical importance, data for this parameter is rarely available. *MEC* is dependent on the size of the particles, the temperature of the ignition source, and the amount of oxygen in the air. If the amount of dust in the air per cubic meter is greater than *MEC*, explosive conditions are present. The tests are made in laboratory chambers that have volumes of 20 L or larger [20]. The determination of *MEC* is really difficult, especially for the realization of a homogeneous dispersion of the dust. Therefore, several models have been proposed in order to calculate *MEC* of a metal and organic dusts. The models which are considered to be important and have been able to explain the dust explosion successfully are that by Jaeckel (1924) [29], Zehr (1957) [30], Schonewald (1971) [31], Ishihama (1961) [32], Mitsui and Tanaka (1973) [24], Hertzberg et al. (1981) [33], Buksovicz and Wolanski (1983) [34] and Bradley et al. (1989) [35]. Most of these are based on the assumption of oxidation reaction taking place on the solid surface of the dust and, consequently, they work well for metal dusts but not for organic ones. The Hertzberg model explains the reaction mechanism during organic dust explosions correctly. However, it requires experimental values of flame propagation velocity which will depend on the method of its determination. The effect of particle size on minimum explosible dust concentration is described by the empirical correlation [33].

II.3.6. Limiting oxygen concentration

The Limiting Oxygen Concentration (*LOC*) is the oxygen (oxidant) concentration at the limit of flammability for the worst case (most flammable) fuel concentration [19]. Below this limit, adding any amount of combustible substances to the dust cloud, an explosive mixture will not form. In order to prevent hazards associated with explosions, the oxygen content in the system is decreased by mixing the fuel–air mixture with an inert substance in order to prevent the flame propagation. *LOC* strictly depends on the type of inert gas used, temperature and pressure of the system. An increase in the initial pressure may lead to a decrease in the maximum oxygen concentration, due to a higher oxygen diffusion. Furthermore, both the maximum pressure and maximum rate of pressure rise decrease by decreasing oxygen content. An inverse behavior is shown with the

variation of initial temperature; an increase in initial temperature coincides with a decrease in *LOC*.

II.3.7. Maximum explosion pressure and deflagration index

If a flammable dust is suspended in air, at a concentration at least equal to *MEC* in presence of an appropriate source of ignition, an accidental explosion can occur. The violence of an explosion is dependent on the rate of energy release from the chemical reactions involved. In order to assess the severity of a dust explosion, two parameters should be analysed: the maximum explosion pressure P_{max} and the maximum rate of pressure rise $(dP/dt)_{max}$. P_{max} indicates the highest pressure an explosion, at the optimum concentration, that can be reached in a closed vessel while $(dP/dt)_{max}$ represents the maximum slope of a tangent line at the pressure-time curve at the optimum concentration. Their knowledge is essential wherever a combustible material is handled, particularly to design *ad-hoc* mitigation systems. From the extensive tests in large vessels (1–60 m^3), Bartknecht (1989) deduced that provided conditions such as concentration, pressure, and ignition characteristics remain the same, as the volume of the vessel changes the maximum explosion pressure remains largely constant, but the maximum rate of pressure rise varies according to the cubic law (Equation (2)) [36]:

$$\left(\frac{dP}{dt}\right)_{max} \cdot V^{\frac{1}{3}} = K_{St} \tag{2}$$

Where V (m^3) is the vessel volume. The cubic law for dust explosion basically states that for the same dust of identical concentration, the same deflagration index will be obtained regardless of the volume of the confined area. The stronger the explosion, the higher is the deflagration index, and, depending on the value of the deflagration index, dusts are classified into four classes (**Table II.1**).

Table II.1 *Classes for Dusts Based on K_{St} Value ([9], [36])*

Deflagration Index, K_{St} (bar m/s)	**Explosion Features**	**Class**
0	No explosion	*St-0*
1-200	Weak	*St-1*
200-300	Strong	*St-2*
>300	Very strong	*St-3*

At lab scale, these parameters, like *MEC* and *LOC*, are measured in the 20 L sphere that came out

of a systematic investigation of several combustible dusts in spherical shaped equipment to find the minimum volume for dust testing ([36]–[38]). Indeed, the test method described in ASTM E1226-19 for 20 L sphere provides a procedure for performing laboratory tests to evaluate deflagration parameters of dusts that can be correlated to those from the 1 m^3 vessel ([9], [39]).

II.4. Key combustible dusts properties

These safety parameters are not intrinsic dust properties. The most important physical properties that affect the safety parameters are:

- Dust chemistry and flame propagation mechanism
- Particle size and specific surface area
- Particle shape
- Moisture content
- Agglomeration degree of dust particles
- Dust dispersion in the dust cloud
- Initial turbulence degree of the dust cloud

II.4.1. Dust chemistry and flame propagation mechanism

The materials that can cause dust explosions are:

- Natural organic materials (grain, linen, sugar, etc.)
- Synthetic organic materials (plastics, organic pigments, pesticides, etc.)
- Coal and peat
- Metals (aluminium, magnesium, zinc, iron, etc.)

Dust chemistry strongly influences both thermodynamics and kinetics: thermodynamics characterizes the amount of heat generated by combustion while kinetics the rate at which the heat is liberated. However, when comparing the various materials in terms of heat generated by combustion related to their potential hazard, it is useful to contextually consider the amount of oxygen consumed. This is because the gas in a confined volume of dust cloud contains a limited amount of oxygen, which determines how much heat can be released in an explosion per unit volume of dust cloud [12]. **Table II.2** lists the heat of combustion of various dusts per mole of oxygen consumed. **Table II.2** is in accordance with the experience: the heat of combustion of metallic dusts are very high compared with those of flames of organic dust and coal [12].

Table II.2 *Heats of combustion (oxidation) of various substances per mole O_2 consumed* [12]

Substance	**Oxidation product(s)**	**kJ/mol O_2**
Ca	CaO	1270
Mg	MgO	1240
Al	Al_2O_3	1100
Si	SiO_2	830
Cr	Cr_2O_3	750
Zn	ZnO	700
Fe	Fe_2O_3	530
Cu	CuO	300
Sucrose	CO_2 and H_2O	470
Starch	CO_2 and H_2O	470
Polyethylene	CO_2 and H_2O	390
Carbon	CO_2	400
Coal	CO_2 and H_2O	400
Sulphur	SO_2	300

The severity of a dust explosion strongly depends on the mode of flame propagation. Moreover, key temperatures as *MIT*, *LIT* and *VP* are very important in affecting the flame propagation. During the flame propagation, dusts have to be heated up to reach the temperature at which volatile are produced, VP. In this heating phase, several volatiles production processes may occur, such as physical transformations (sublimation and/or melting-boiling) or chemical ones (i.e., pyrolysis) [28]. When volatiles are produced then combustion of the gas products starts.

Dust clouds with different thermal characteristics and particle size distributions would form entirely different flame structures. Two types of flames can be distinguished. The first, the Nusselt type, is controlled by the diffusion of oxygen to the surface of individual solid particles, where the heterogeneous chemical reaction takes place (Path A in **Figure II.6**). In the second type, the volatile flame, the rate of gasification, pyrolysis, or devolatilization is the controlling process and the chemical reaction takes place mainly in the homogeneous gas phase (Path B in **Figure II.6**) [12].

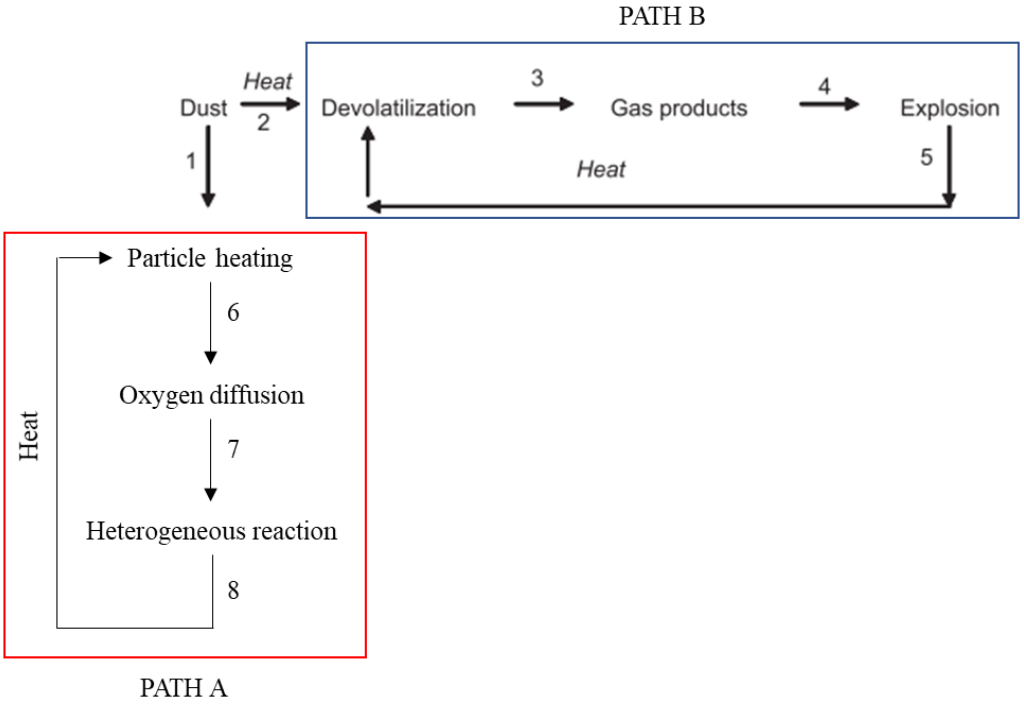

Figure II.6 *Schematic representation of the paths occurring during dust explosion*

When kinetics controls the flame propagation, flame front formed is smooth in shape similar to the premixed gas explosions. The flame zone consists of premixed blue flame at the leading zone and luminous flames behind it.

When the devolatilization controls the flame propagation, flame front has a complicated structure. The flame zone consists of blue spot flames at the leading zone and luminous flames behind them. The yellow luminous zone formed in the two different flame propagation regimes was explained as follows: around the particles, local high concentration regions of fuel existed; when those particles burned without sufficient oxygen, soot particles were formed, and these particles emitted yellow flame. Because the particles were scattered, the pyrolysis fuel concentration was not uniform. This is the reason for the irregular shape of the luminous zone (**Figure II.7**) [40].

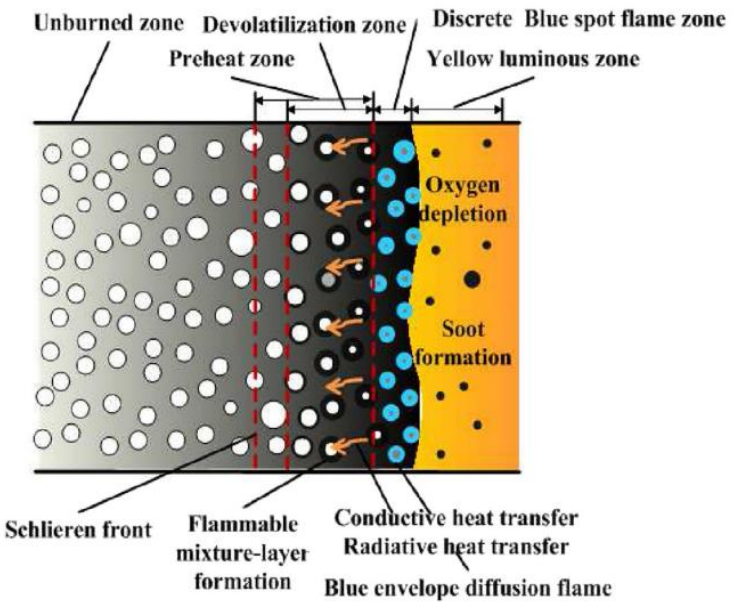

Figure II.7 *Schematics of flame propagation mechanisms in dust explosions (Devolatilization-controlled regime)* [40]

To the aim at elucidating the mechanisms governing the explosion process of these systems, a brief preliminary study on the dust explosion is mandatory. For organic materials, it was observed that the dust explosion occurs through different steps [41]:

- internal and external heating
- pyrolysis/sublimation/melting/boiling (devolatilization)
- heating of volatiles
- gas phase combustion

All of these steps are mutually dependent and are strongly affected by the particle size. Di Benedetto et al. (2010) studied this effect on the dust reactivity developing a model that takes into account all of the steps above mentioned [41]. Varying the dust size, they identified different regimes depending on the values of the characteristic time of each step and several dimensionless numbers (Biot number, *Bi*; Damköhler number, *Da*; Thiele number, *Th*; *Pc* number). According to Menon et al. (2002) the production of volatiles from nicotinic acid can be assumed to occur in one step, the sublimation (with melting/evaporation at higher pressure) [42]. The used model is based on the approach that involves the kinetic mechanism of the sublimation process, inferred from thermo-gravimetric analyses, which allows the solid to decompose over a characteristic temperature range. Starting from the solid, *S*, the only sublimation step (k) leads to the formation of volatiles, *VM*:

$$S \rightarrow VM$$

The mass balance equation considered in a dimensionless form is (Equation (3)):

$$\frac{d\alpha}{dt} = K \cdot f(\alpha) \tag{3}$$

where α (-) is the fraction reacted of the mass of solid particle (*S*), $f(\alpha)$ (-) is the expression of the reaction mechanism and K (s^{-1}) is the reaction rate constant at a specific temperature. Using the Arrhenius equation, K can be written as (Equation (4)):

$$K = Z \cdot \exp\left(\frac{-E_a}{RT}\right) \tag{4}$$

where Z (s^{-1}) is the pre-exponential factor, E_a (J mol^{-1}) is the energy of activation, R (J mol^{-1} K^{-1}) is the universal gas constant and T (K) is the absolute temperature. Starting from the thermo-gravimetric analysis, A and E_a were calculated assuming a kinetic of zero order ($f(\alpha)=1$) as found by Menon et al. (2002) [42]. On the basis of the work of Di Benedetto et al. (2010) [41], it is necessary identifying the process controlling step by the use of dimensionless numbers defined as follows:

$$Bi = \frac{t_c}{t_e} = \frac{d_{dust} \cdot (h_c \cdot \Delta T_i + \varepsilon_\lambda \cdot \sigma \cdot \Delta T_i^4)}{\lambda_{dust} \cdot \Delta T_i} \tag{5}$$

$$Da = \frac{t_e}{t_{pyro}} = \frac{r_p \cdot \Delta T_i \cdot Cp_{dust} \cdot d_{dust}}{h_c \cdot \Delta T_i + \varepsilon_\lambda \cdot \sigma \cdot \Delta T_i^4} \tag{6}$$

$$Th = \frac{t_c}{t_{pyro}} = \frac{r_p \cdot Cp_{dust} \cdot {d_{dust}}^2}{\lambda_{dust}} \tag{7}$$

$$Pc = \frac{t_{pyro}}{t_{comb}} = \frac{\rho_{\mathrm{dust}} \cdot S_l}{r_p \cdot l_F} \tag{8}$$

where t_c (s) is the characteristic time of internal heat transfer, t_e (s) is the characteristic time of external heat transfer, t_{pyro} (s) is the characteristic time of pyrolysis reaction, t_{comb} (s) is the characteristic time of combustion reaction, d_{dust} (m) is the dust diameter, ΔT_i (K) is the temperature difference between particle and surrounding gases, h_c (W m^{-2} K^{-1}) is the heat transfer coefficient, ε_λ (-) is the emissivity, σ (W m^{-2} K^{-4}) is the Stefan–Boltzmann constant, λ_{dust} (W m^{-1} K^{-1}) is the thermal conductivity of the solid, r_p (kg/m^3 s) is the pyrolysis reaction rate, Cp_{dust} (J kg^{-1} K^{-1}) is the specific heat, l_F is the flame thickness (typically, 1 mm) and S_l (m/s) is the laminar burning velocity assumed equal to 2 m/s, which corresponds to a fully developed turbulent regime typical of the standard 1 m^3 and 20 L spheres. On the basis of the values assumed by these number the controlled step can be established [41].

Two limit conditions can be observed, depending on the value of the Biot number:

- $Bi \ll 1$: the internal heat transfer rate is much faster than the external heat transfer rate. The characteristic times of external heat transfer (the slowest process) should be compared

with the characteristic reaction time. This is usually done through the Damköhler number. If $Da \gg 1$, the conversion occurs under the external heat transfer control; if $Da \ll 1$, it occurs under the control of the pyrolysis chemical reaction.

- $Bi \gg 1$: the internal heat transfer is the controlling mechanism. The characteristic time associated with internal heat transfer (the slowest process) should be again com- pared with the characteristic time of pyrolysis chemical reaction. This is usually done by means of the thermal Thiele number. If $Th \gg 1$, the conversion occurs under the internal heat transfer control; if $Th \ll 1$, it occurs under the control of the pyrolysis chemical reaction.

Once the regime of the devolatilization process is identified, the step controlling the overall dust explosion phenomenon can be determined by comparing the characteristic time of the devolatilization controlling step with that relevant to the gas combustion (Pc) [41].

Several studies on the flame propagation for the dusts have been carried out mainly by using tube method, but however the knowledge on the fundamental mechanism of flame propagation in dust-air mixtures is still lacking ([40], [43]–[53]). Among several great obstacles to dust combustion research, the most fundamental one may be the understanding and dealing with the influence of turbulence on flame propagation. In the experiments, dust particles must be suspended in the air to form a combustible dust cloud. This prerequisite is accomplished by the process of dust dispersion. Various types of dispersion process used for dust combustion research will generate turbulence in the test vessel, which, on the other hand, is proven necessary to maintain dust in suspension. Therefore, some degree of turbulence is always present in the dust cloud before ignition. The turbulence structures may vary from one apparatus to the next, depending on factors such as the dispersion method and vessel geometry. By choosing the ignition delay time, the flame propagates different initial state in terms of turbulence level and dust concentration. Wang et al. (2006) measured the root-mean-square (*RMS*) of the turbulent velocity fluctuations in the horizontal and vertical directions, generated in the tube after dust injection, as a function of the ignition delay time elapsing between the time of injection and the time of ignition. They were able to measure the dust concentration at different heights along the tube showing that the dust concentration is not uniform along the tube height (**Figure II.8**) [54].

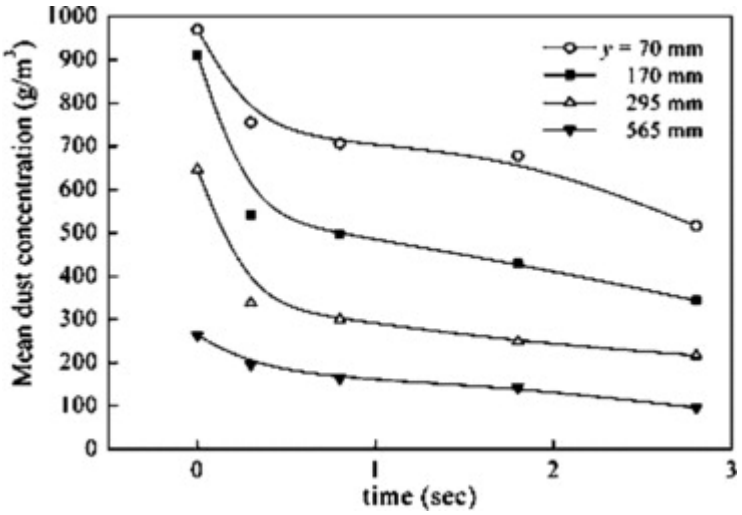

Figure II.8 *Mean dust concentration as a function of time at four heights of the duct* [54]

With the increase of ignition delay time, two different kinds of flame were observed: turbulent and laminar flames. To characterize these different flame propagation regimes in the duct, an important parameter used is the flame speed, S_f. Experimentally, this value is obtained considering the measured flame displacement as function of time [48]. Indeed, it is defined as the speed of a flame front relative to a fixed reference point. Flame speed is dependent on turbulence, the equipment geometry, and the fundamental burning velocity S_u. It is the maximum rate of flame propagation relative to unburned gas ahead of the flame front for the fastest burning composition at 25 °C and 760 mmHg [55].

In the case of laminar flames, if considering a tube with both ends open and assuming a flame front as a geometrical surface of zero thickness and a coordinate system co-moving with the flame front, the unburned fuel mixture moves into the flame front with velocity S_l (the laminar burning velocity) and the combustion products flow out of the flame front with velocity S_f. The laminar burning velocity (S_l) is the speed at which a laminar (planar) combustion wave propagates relative to the unburned gas mixture ahead of it. The fundamental burning velocity (S_u) is similar, but generally not identical to, the observed laminar burning velocity. This is because S_u is a characteristic parameter referring to standardized unburned gas conditions (normally 760 mmHg and 25 °C), and which has been corrected for nonidealities in the measurement [55].

A relation exists between S_l and S_f for a plane flame front obtained by the condition of conservation of the total mass flux: the total mass of gas entering the flame per unit area of the front must be equal to the mass of combustion products leaving this surface downstream:

$$\rho_b S_f = \rho_u S_l \tag{9}$$

where ρ_u and ρ_b are the densities of the initial unburned mixture and combustion products [56].

In the case of turbulent flames, the unburned fuel mixture moves into the flame front with velocity S_t (turbulent burning velocity) that exceeds the burning velocity measured under laminar conditions to a degree depending on the scale and intensity of turbulence in the unburned gas. As a measure of the turbulence, the root mean square *RMS* of flow fluctuations, *u'*, can be used. The grade of turbulence can be express also in term of turbulent Reynold number, Re_t, by means of *RMS* velocity, *u'*:

$$Re_t = \frac{\rho_u u' r_{dust}}{\mu_u} \tag{10}$$

where μ_u (Pa·s) is the viscosity of the unburned fuel. The evaluation of the turbulent burning velocity S_t as function of the turbulent fluctuations (*u'*) was performed by using the formula available in the literature.

In **Table II.3** formulas available from literature for the turbulent burning velocity as function of the turbulence level are reported: formulas 1-3 were obtained for gas, formulas 4-6 for dust while only formula 7 correlates both gas and dust data. Such formulas depend on the turbulent combustion regimes in which the explosion is occurring.

Table II.3 *Formulas of turbulent burning velocity*

N°	S_t (m/s)	Dust/Gas	Reference
1	$S_l \cdot \left(1 + \left(\frac{u'}{S_l}\right)^2\right)^{0.5}$	Gas	Pocheau [57]
2	$S_l \cdot (1 + 2 \cdot \frac{u'}{S_l})$	Gas	Phylakotu et al. [58]
3	$S_l \cdot (1 + \left(\frac{u'}{S_l}\right)^2)$	Gas	Clavin and Williams [59]
4	$S_l + 0.45u'$	Dust	Kauffman et al. [60]
5	$S_l + Ku'$	Dust	Gieras et al. [61]
6	$S_l \cdot (1 + 1.65 \cdot \frac{u'^{0.5}}{S_l})$	Dust	Zhen and Leuckel [62]
7	$6.8 \cdot S_l^{0.6} l_t^{0.15} u'^{0.15}$	Dust/Gas	Van Wingerden et al. [63]

In all the formulas of S_t, the laminar burning velocity is required [64]. Its measurement can be done by means of the burner or tube system. The burner system consists of a tube in which the fuel passes and reaches the top part in which the annular space separating the flame from the burner edge provides a continuous ignition source and anchors the flame to burner. In this way is

guaranteed the stability of the flame. The tube system consists of a transparent, semi-open tube in which the ignition system is installed at the open end of the tube. With this last apparatus, two different methods can be used: the "tube" method and the "direct" method [50]. With the tube method, S_l can be derived from the flame speed and shape according to the following expression:

$$S_l = S_f \cdot \frac{A_p}{A_f} \tag{11}$$

where A_f (m^2) is the flame front area and A_p (m^2) is the projected flame area on a plane perpendicular to the direction of flame propagation. Provided the flame geometry is simple enough the determination of S_l by this method is simple and only requires a video equipment. For the "tube" method to give reliable results some requirements have to be fulfilled. For instance, the laminar burning velocity has to be constant over the flame front. The "direct" method allows the determination of the local burning velocity. In this latter method S_l is directly derived from its definition:

$$S_l = \overrightarrow{S_f} \cdot \vec{n} - \vec{U} \cdot \vec{n} \tag{12}$$

where $\vec{n}$ is the unit vector normal to the flame front at the point under consideration and $\vec{U}$ (m/s) is the flow velocity vector. The experimental determination of S_l with this method is difficult since S_f and $\overrightarrow{U}$ have to be sufficiently accurate and $\vec{U}$ has to be determined very close to the flame front. The evaluation of S_l is strongly dependent on the turbulence control, the equipment geometry and the operating conditions. For this reason, even with the same concentration, the experimental results are often different. By way of example, measurements relating to cornstarch are reported (**Figure II.9**). Proust and Veyssière (1988) observed and evaluated the flame propagation of cornstarch-air mixtures (mean diameter 20 μm, concentration 100-220 g/m^3) within a 3 m long tube where the dust dispersion was realized though the elutriation above a fluidized bed [65]. Proust (1993) assessed S_l within a 1.5 m long tube where the dust dispersion was realized though the elutriation above a fluidized bed for starch dust-air mixtures, lycopodium-air mixtures and sulphur flower-air mixtures (mean particle diameter 25-45 μm, concentration 100-300 g/m^3) through the tube and direct methods [66]. Nagy and Verakis (1983) derived laminar burning velocities and the deflagration index for clouds at 500 g/m^3 in concentration in air of various dusts through experimental dust explosion data from the elongated 1.2 litre Hartmann bomb [67]. Mazurkiewicz et al. (1993) measured the laminar burning velocity of cornstarch-air flames (mean particle diameter 15 μm, concentration 500 g/m^3) in a vertical 50x50 mm square tube, 1 m long, where the suspension was generated through elutriation of dust particles above a fluidized bed [68].

van Wingerden and Stavseng (1996) measured the laminar burning velocity of cornstarch-air and maize starch-air flames (mean particle diameter <100 μm, concentration 80-200 g/m^3 and 45-300 g/m^3, respectively) in an 1.6 m long vertical tube made of transparent polycarbonate where the dust was supplied continuously into the top of the tube from a horizontally vibrating sieve and a vibratory dust feeder [51]. The burning velocity in laminar flows was studied in a vertical cylindrical tube of 2 m in length and 300 mm in diameter where dust was layered on a porous filter plate and elutriated in a fluidized bed at the beginning of each experiment by Krause and Kasch (1994) [69]. In **Figure II.9,** it is possible to note the large variable of the measurement especially at low dust concentration. The development of a theoretical flame propagation model for combustible dusts and hybrids could be useful to support experimental evaluations and/or to make preliminary considerations.

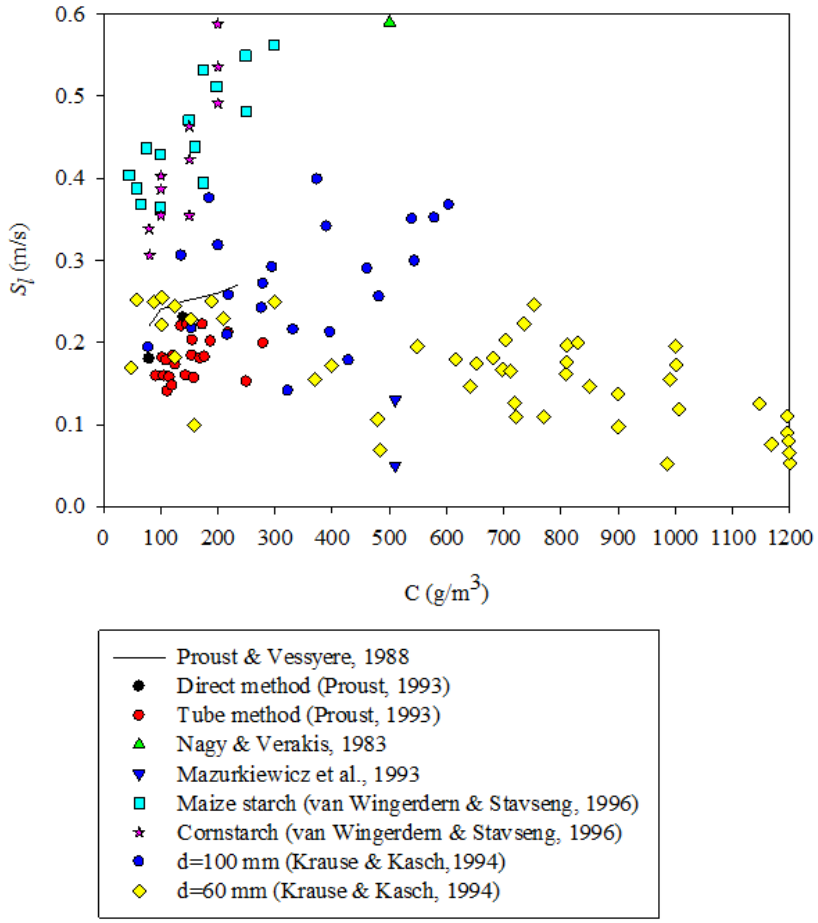

Figure II.9 *Literature data about laminar burning velocity of cornstarch as a function of dust concentration* ([51], [65]–[69])

II.4.2. Particle size and specific surface area

Generally, the ignitability and the explosion severity of a combustible dust/air cloud increases with decreasing dust particle size. This phenomenon occurs due to the rise of the specific surface area of dust particles and, consequently, the increase of the oxidant-fuel contact surface. A higher specific surface area means a higher reactivity and consequently a higher tendency to ignite and explode. **Figure II.10** shows the trend of the maximum rate of pressure rise of clouds of aluminium dust in air as a function of the specific surface area. The curve is monotonous increasing [36]. **Figure II.11** shows how a reduction in particle size strongly affects the minimum ignition energy (*MIE*) of dusts of different nature [36]. **Figure II.12** shows how *MIT* changes with particle size of graded flour. The minimum ignition temperature drops with a reduction in particle sizes. A surface area enhancement leads to a more uniform heated process that accelerate the particle oxidation, so a lower temperature it is necessary [70].

However, a continuous decrease of particle size does not increase inevitably the reactivity of the system. If the particles are so small that devolatilization no longer controls the explosion rate, further particle size reduction will not increase the overall combustion rate [11]. This critical particle size strictly depends on the type of analysed substance. For example, for many metals, the critical particle size is sensibly smaller than that of most of the organic materials. This is because metal particles do not produce a homogeneous combustible gas phase by devolatilization/pyrolysis as organic compounds but tend to burn as different entities.

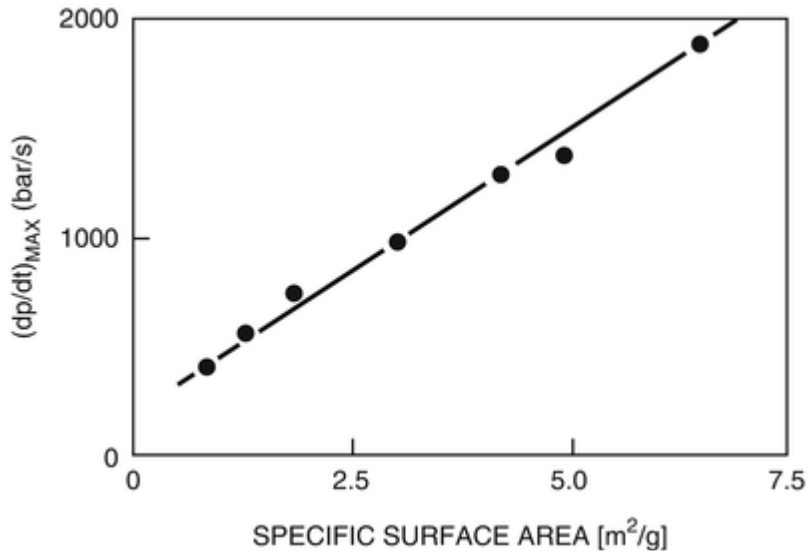

Figure II.10 *Influence of specific surface area of aluminium powder on maximum rate of rise of pressure during dust explosion in air* [36]

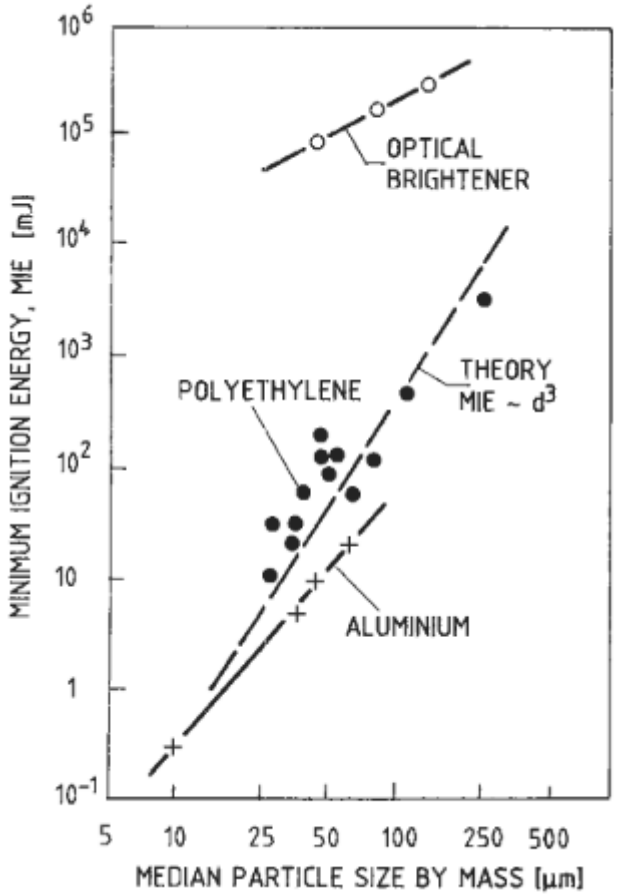

Figure II.11 *Minimum ignition energy (MIE) of clouds in air of three different powders, as function of particle size* [36]

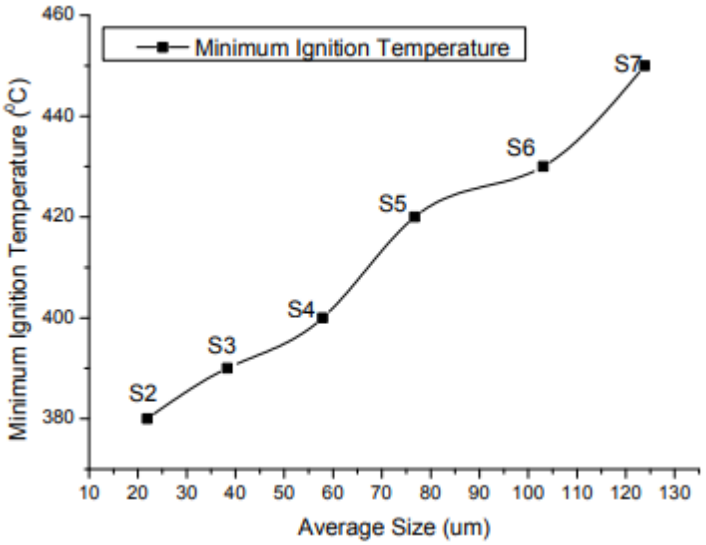

Figure II.12 *Variation trend of minimum ignition temperatures with average sizes of graded flour* [70]

II.4.3. Particle shape: non-traditional dusts

The majority of all studies dealing with dusts explosibility and flammability were performed assuming the particles sphericity. Indeed, according to the U.S. National Fire Protection Association (NFPA), a dust is defined as a finely divided solid with the diameter as the only characteristics dimension of less than 420 μm (0.017 in.). A dust will pass through a US No. 40 standard sieve [8]. Combustible dusts do not necessarily follow this definition and may therefore be considered "non-traditional" dusts. Generally, non-traditional dusts come from the textile sector but also from agriculture and food processing. Their explosibility has been investigated occasionally over the years and, consequently, there is a very low level of awareness of the risk of explosions due to these non-traditional dusts. In the last 50 years, several explosions episodes can be attributed to non-traditional dusts. In **Table II.4**, some of them are listed. One of the major accidents occurred in 1987 in Harbin in a linen textile plant and resulted in fatalities and financial losses due to extensive structural damage. The incident was described by Eckhoff (2003) [11]. A more recent powerful explosion, which occurred in a wool manufacturing facility in northern Italy in 2001, was described by Piccinini (2008) [71] and Salatino et al. (2012) [72]. This accident caused 3 fatalities, 3 serious injuries and led to large monetary losses. In most cases, the source of ignition was probably an electrical discharge or spark.

Table II.4 *Explosions episodes due to non-traditional dusts*

Episode (year)	Death	Injured	Material	Process
China (1986)	5	11	Unknown	Textile mill
Harbin (1987)	58	177	Linen	Dust collector system
California (1990)	-	1	Textile products	-
Okaharu (1994)	-	-	Cotton waste	-
California (1994)	-	1	Textile products	-
Maiden Mills (1995)	-	27	Nylon	Flocking unit
Connecticut (1997)	-	3	Plastic textile products	-
Biella (2001)	-	3	Nylon	Dryer
Biella (2001)	3	6	Wool	Collection system
Mississippi (2002)	1	-	Plastic textile products	-

Non-spherical dusts may have the shape of fibres, flakes, chips or flocks. The size of this kind of dusts cannot be identified by a unique parameter like the particle diameter but often are better

described in terms of a length-to-diameter ratio. Depending on the particle shape, at least two parameters are required for an accurate modelling ([73], [74]). As seen for spherical particles, Bartknecht (1989) showed that the flammability and explosion parameters of flocks are significantly affected by the dust fineness and, in particular, as the fineness is increased, ignition and explosion behaviours become more severe [1]. Marmo and Cavallero (2008) explored the effect of both diameter and length on the explosibility parameters. They measured the *MIE* of nylon flocks demonstrating that its values are affected by the diameter much more than by the length of the fibre [75]. These results have been confirmed by tests on textile fibres [76]. There are two possible causes for the effect of length on the *MIE*. The first is the melting process. Indeed, the melting temperatures of some flocculent materials are lower than their ignition temperature, so the materials would likely begin to melt and assume spherical shape before ignition. The second possible explanation could reside in the high tendency of fibrous materials to coagulate forming a sort of spherical agglomerates which would reduce dispersion and increase *MIE* [73].

A sensible difference between traditional and non-traditional combustible, can be found in the propensity to remain in suspension. In order to characterize the tendency to form dust cloud, Klippel et al. (2013) defined a parameter called Dustiness, demonstrating its strong correlation with the deflagration index [77]. Dustiness is deeply affected by particles shape, but also by particles size, moisture content, agglomeration forces and particles density. Moreover, these properties strongly influenced the sedimentation process. During sedimentation, particles trajectories are vertical for spherical particles. Non-spherical particles have a different behaviour. They can rotate, vibrate, or follow spiral trajectories due to the different drag coefficient. Drag coefficient, function of Reynolds number, shows higher values for non-spherical particles than for spherical ones. For this reason, non-spherical particles (fibrous dusts, flocculent dusts, flakes) may remain suspended in air, forming dusts clouds, for a longer time than traditional spherical particles until they generate agglomerates [74].

Another source of non-traditional dust production is biomass industry. Wood is the largest biomass energy source: examples include forest residues, yard clippings, wood chips and even municipal solid waste. Wood may be used directly as a fuel or to be processed into pellet fuel or other forms. However, the concern with this is that during the processing of wood biomass, wood dust was produced, which results in fire and explosion hazards. Moreover, stored biomass may deteriorate over time. This deterioration often conducts to the generation of flammable gases (such as carbon monoxide) [78]. The safe storage time depends on the level of humidity within the biomass store. Generally, higher humidity leads to more self-heating issues as does a lack of air circulation through the storage [79]. Also transport may lead to the generation of fine dust. Indeed, wood

pellets are typically 12x6 mm but during transport they can deteriorate reaching different dimensions and generating up to 10% of dust (**Figure II.13**) [80]. The particularity of wood dust is its shape heterogeneity. The typical shapes are fibres or flakes of any sizes. Other forms of biomass also contain proportions of dust, which can typically occur in pockets within the bulk material. There is a large number of biomass incidents which have resulted in not only the loss of large quantities of materials and damage to plant, but also environmental pollution, injury to personnel and, in a number of cases, loss of life. The list of incidents includes pellet production plants, power stations, storage facilities and medium density fibreboard (*MDF*) production plants and some of them are reported in **Table II.5** ([79], [80]).

Table II.5 *Biomass dust incidents ([79], [80])*

Date	Company - Location	Description
2002	Sonae - Merseyside	Dust explosions of MDF production plant
2012	Dong energy - Netherlands	Dust explosions of wood pellets
2013	Port of Tyne	Wood pellet fire in conveying system
2013	Koda Energy - Minnesota	Explosions and fire in biomass storage
2015	Boseley Wood Mill - UK	Dust explosions with 4 fatalities

Figure II.13 *Wood pellet particle size distribution samples during processing* [80]

The applicability of the standard procedures and apparatus to non-spherical particles is a further issue. Incomplete feeding is a crucial issue for non-spherical particles ([81], [82]). It has been

observed during explosion tests of dust particles with non-spherical shape in both 20 L and 1 m^3 standard vessels [83]. To overcome this issue, alternative dispersion systems have been proposed specifically for flocks and fibrous dusts ([1], [39], [84]). In particular, in the standard procedure for the 1 m^3 dust explosion vessel the rebound nozzle is suggested as an alternative in the case of fibrous dusts testing ([9], [39], [84]). However, Amyotte et al. (2012) investigated the explosion features of fibrous wood and polyethylene dusts of different particle sizes inside the 20 L equipped with the rebound nozzle [81]. Results showed that at high concentration and larger particle size, only a part of the dust sample was placed inside the dust container, whereas the remaining part was placed directly around the rebound nozzle to avoid the obstruction of the pneumatic valve. Iarossi et al. (2013) also used this approach with polyamide and polyester fi0bers and found that the maximum explosion pressure for wood samples is variable due to the variability of dust dispersion patterns [82]. Moreover, Marmo (2010) and Marmo et al. (2018) studied the explosibility of textile fibres in the 20 L sphere equipped with a rebound nozzle, showing that problems of dispersion and turbulence generation arise due to their non-spherical flocculent nature ([76], [85]). Di Sarli et al. (2019) carried out *CFD* simulations of turbulent flow field, feeding and dispersion of non-spherical dust particles in the standard 20 L sphere, fully neglecting the interaction between non-spherical particles and rebound nozzle. Results showed that the turbulence level and the dust dispersion established inside the sphere are strongly dependent on the shape factor. Interestingly, moving from spherical shape to fibrous shape, the model predicts that the fraction of dust actually fed into the vessel increases. Since experimental results indicate the opposite, this suggests that the experimentally observed partial feeding can be attributed only to the geometrical interaction between the non-spherical dust particles and the holes of the rebound nozzle. As a consequence, in order to improve the feeding efficiency for non-spherical dust particles into the 20 L explosion vessel, a proper design of the nozzle is required [86].

II.4.4. Moisture content

Moisture in the dust reduces both the ignition sensitivity and explosion violence of dust clouds. The moisture content strongly affects the flammability and explosibility of a dust. Firstly, the water concentration changes the agglomeration behaviours of dusts. The moisture gradually agglomerates the fine dust particles by reducing inter-particle distance and forming liquid bridges between particles. This behavior causes an increase of the effective particle size and the reduction of the dust dispersibility. Moreover, higher the moisture in dust, lower is the possibility to generate flammable clouds (Dustability). **Figure II.14** shows *MIE* and *MIT* trends as a function of the

equilibrium relative humidity for magnesium stearate. Both the curves show a rise with the degree of moisture [87].

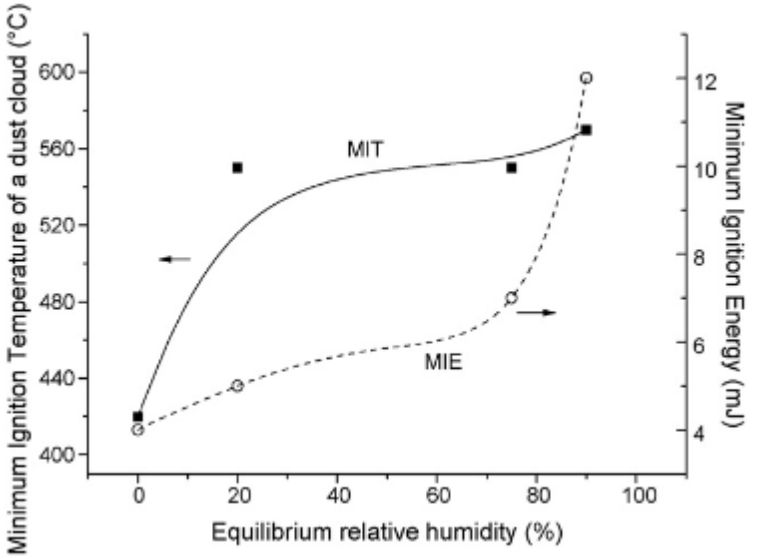

Figure II.14 *Evolution of the minimum ignition temperature and minimum ignition energy of magnesium stearate as a function of the equilibrium relative humidity* [87]

The explosion parameters, such as K_{St} or P_{max}, have not a well-defined behaviour. **Figure II.15 a)** shows the maximum rate of pressure rise trend (linked to deflagration index) as a function of magnesium stearate concentration while **Figure II.15 b)** illustrates P_{max} trend as a function of aluminium concentration, parametric in the relative humidity [87].

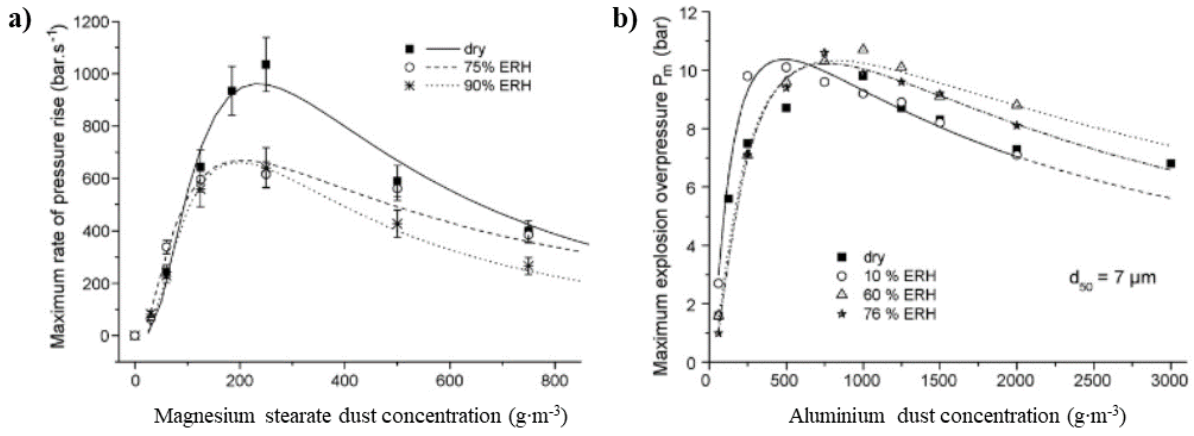

Figure II.15 *Evolutions of the maximum rate of pressure rise as a function of the magnesium stearate concentration parametric in the equilibrium relative humidity (a) and trends P_{max} as function of the aluminum dust concentration parametric in the equilibrium relative humidity (b)* [87]

In the case of the magnesium stearate, a moisture increment leads to a sensible drop of the maximum rate of pressure rise. As regards the aluminium dust, P_{max} increases with the relative humidity, reaching critical values for 60% RH. At the highest value of analysed moisture (76% RH), P_{max} decreases compared to data at 60% RH [87]. The explanation behind this phenomenon dwells in the violent reaction between aluminium and water. If the protective layer of alumina, which is formed on the metallic surface, is broken during the explosion, a rapid chemical reaction occurs between the metal and the water generating a large heat release and hydrogen production [88]. Thus, the promotion of explosion violence is probably due to the following reaction between water and aluminium [89]:

$$2Al_{(s)} + 3H_2O_{(g)} \rightarrow Al_2O_{3_{(s)}} + 3H_{2_{(g)}} \tag{13}$$

Consequently, accurate analysis on the influence of water in dust explosion is recommended, because materials reacts differently, and no generalizations are possible.

II.4.5. Agglomeration degree of dust particles

The formation of explosive dust clouds from deposits is strictly connected to the propensity of the powder itself to be separated and suspended in the air to form a cloud. Eckhoff (1976) defined a Dispersibility parameter, D_{max}, for a powder deposit, based on a simple consideration: a unit mass of a given powder contains a finite number of inter-particle bonds and each of them needs a definite work to be broken. The minimum work to break all these bonds, defined as W_{min}, is calculated as integral of each single work. The Dispersibility is defined as the mass that ideally could be dispersed into primary particles per unit of work [12].

$$D_{max} = \frac{1}{W_{min}} \tag{14}$$

Obviously, not all particles can be dispersed perfectly in an air stream, for this reason considering an efficiency factor K_{disp} is mandatory:

$$D_{max} = \frac{K_{disp}}{W_{min}} \tag{15}$$

Inter-particle forces comprehend:

- Van der Waals' forces
- Electrostatic forces (Coulomb-forces)
- Forces due to liquid (liquid bridges, capillary under pressure).

When considering electrostatic forces, electrically conducting and nonconducting particles must

be distinguished. In the case of conducting particles, electrostatic inter-particle attraction may occur even if the particles do not carry any net excess charge. For electrically nonconducting particles, such as plastics, the electrostatic contact force is negligible. In this case, electrostatic attraction is caused by excess charges on the particle surfaces, acquired during the production and handling. Particles of different size implicate a different intensity of the velocity flow fields to guarantee a correct dispersion of dust deposit. Lower the particles dimension, higher the shear forces necessary to form primary particles clouds (**Figure II.16**) [12].

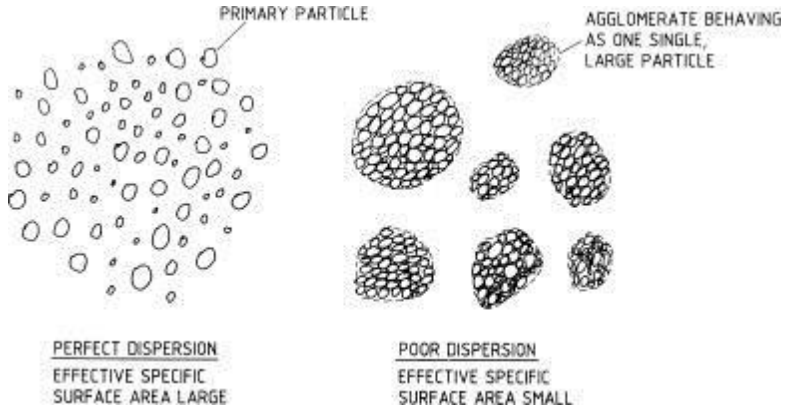

Figure II.16 *Illustration of a perfectly dispersed dust cloud consisting of primary particles only, and a cloud consisting of agglomerates* [12]

II.4.6. Dust dispersion in the dust cloud

The explosion rate as well as the flammability tendency strongly depend on the dust concentration analysed. Illustration of typical variation of explosion rate and *MIE* with dust concentration within the explosible range is reported in **Figure II.17**, where C_1 is *MEC*, C_{stoich} is the stoichiometric concentration, $C_{worstcase}$ is the most critical concentration that corresponds to the maximum value of the explosion rate as well as to the minimum one of *MIE* and C_u is the maximum explosible concentration.

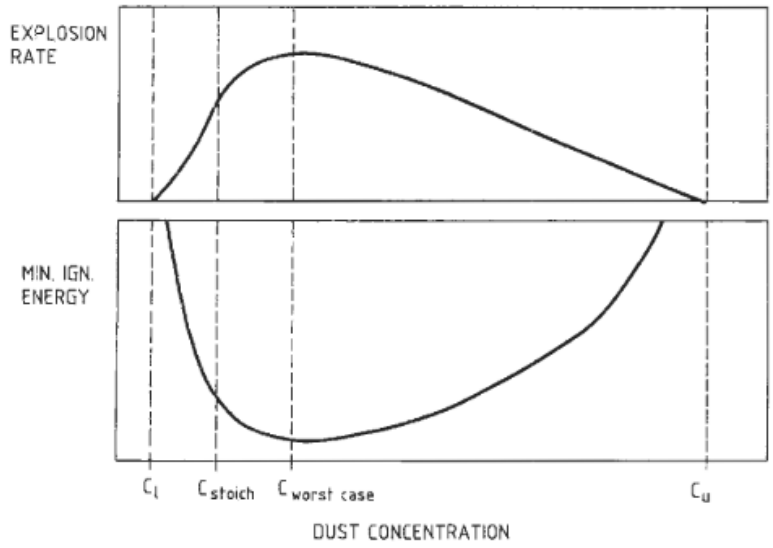

Figure II.17 *Typical trends of explosion rate (top) and minimum ignition energy (bottom) as a function of the dust concentration* [12]

A dust cloud can ignite if the concentration of solid material, suspended in the oxidizing gas, is at least equal to *MEC* and not higher than the maximum explosion concentration. To determine *MEC* of a heterogeneous mixture correctly, respecting some requisites is mandatory:

- careful control of the particle size distribution of the dust
- uniform dispersion of the dust throughout the test apparatus
- uniform degree of turbulence within the test device

II.4.7. Initial turbulence degree of the dust cloud

The turbulence of a dust cloud deeply affects its ignitability and explosibility. Practically, turbulence is a state of rapid internal, more or less random movement of elements of the dust cloud relative to each other in three dimensions [12]. A burning cloud is generally a complex system formed by three different zones: burning, burnt and unburning zone. The presence of turbulence during a combustion will allow the dust cloud to burn faster than a quiescent one; at the same time in a turbulent system the energy or the temperature necessary to ignite the dust is higher than the energy required to burn the same dust in a quiescent cloud due to the strong convective heat exchange between gas and source of ignition. Talking about turbulence is possible to consider two different types of contributes, based on their origin:

- Pre-ignition turbulence
- Post-ignition turbulence

Pre-ignition turbulence is the turbulence generated by the industrial process in the various process units. If a blast of air invests a dust deposit in a process unit, it is likely that a flammable cloud could be formed. Considering that an ignition source is present and has enough energy, it could produce an explosion [12]. Before ignition, the dust/air system will evolve between two extremes: at time $t = t_0$, immediately after the air blast, the system will be characterized by a high degree of turbulence, while at $t = t_1$, at the instant of the ignition, the dust cloud could be more or less turbulent, at most quiescent, depending on the ignition delay time. High level of turbulence implies high ignition energy, that fortunately, in the context of ignition by electrostatic discharge, means a higher level of security. Consequently, the evaluation of explosibility parameters deeply depends on the degree of turbulence within the dust/air mixture, as can be seen in **Figure II.18**. **Figure II.18** shows *MIE*s of different dusts (such as coal, pea flour, cellulose, lycopodium and a light protection agent) as a function of the ignition delay time. The trends are always decrescent with the ignition delay time due to the heat dissipation caused by turbulence [12].

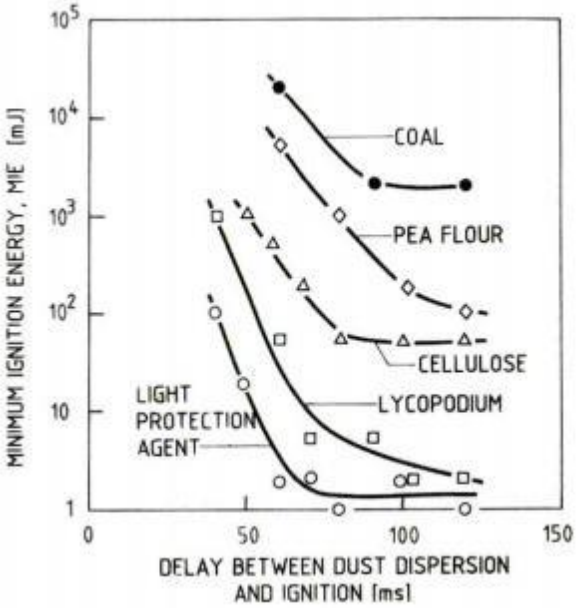

Figure II.18 *Influence of initial turbulence of explosive dust clouds on the minimum electric spark energies required for ignition* [12]

Differently from *MIE* behaviour, the explosion severity increases with the initial turbulence, as shown in **Figure II.19**. For a given mixture, P_{max} is dependent on the initial conditions of temperature and pressure and on the temperature reached during the explosion. The final temperature is linked to the thermodynamic value and is affected by both, the adiabaticity of the explosion vessel and the nature of the reactive mixture. In vessels with different shapes and/or

sizes, the same mixture will give exactly the same maximum pressure, provided that explosion occurs under adiabatic conditions. Conversely, $(dP/dt)_{max}$ is a kinetic parameter and, as such, is strongly dependent on the flame propagation velocity. This latter is dependent not only on the mixture reactivity, but also on the turbulence level present in the vessel that accelerate the flame front.

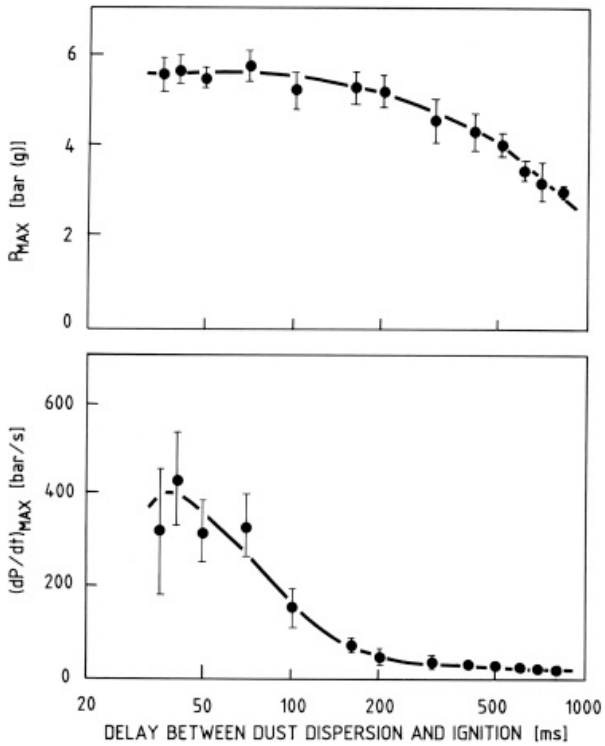

Figure II.19 *Influence of initial turbulence on P_{max} and $(dP/dt)_{max}$ as a function of the ignition delay time* [12]

The second kind of turbulence is generated by the explosion itself due to the increase of the unburnt dust cloud specific volume that precedes the flame front. In the absence of flow in the burned gases behind the flame, the velocity u of the unburned mixture just ahead of the flame is given by the product of the specific volume expansion and the fundamental burning velocity S_u:

$$u = \left(\frac{\rho_u}{\rho_b} - 1\right) \cdot S_u \tag{16}$$

The burning velocity, however, is strongly affected by disturbances in the flow of unburned gases, and laminar flame propagation is rarely observed in practice. Therefore, the flame accelerates as it enters the turbulent flow created by the expansion of the burned gases; the flow velocity and turbulence level of the unburned mixture increase, leading to further flame acceleration that may result in a deflagration-detonation transition (*DDT*) [90]. Depending on the flame burning rate and

the turbulence level, the interaction between the flame front and the eddies generated by turbulence significantly changes, thus leading to different turbulent combustion regimes. Depending on the laminar burning velocity S_l, the flame thickness (l_F), the turbulent fluctuations (u') and the vessel scale (R_{vessel}), different combustion regimes have been identified in the Borghi diagram (**Figure II.20**) ([91]–[94]).

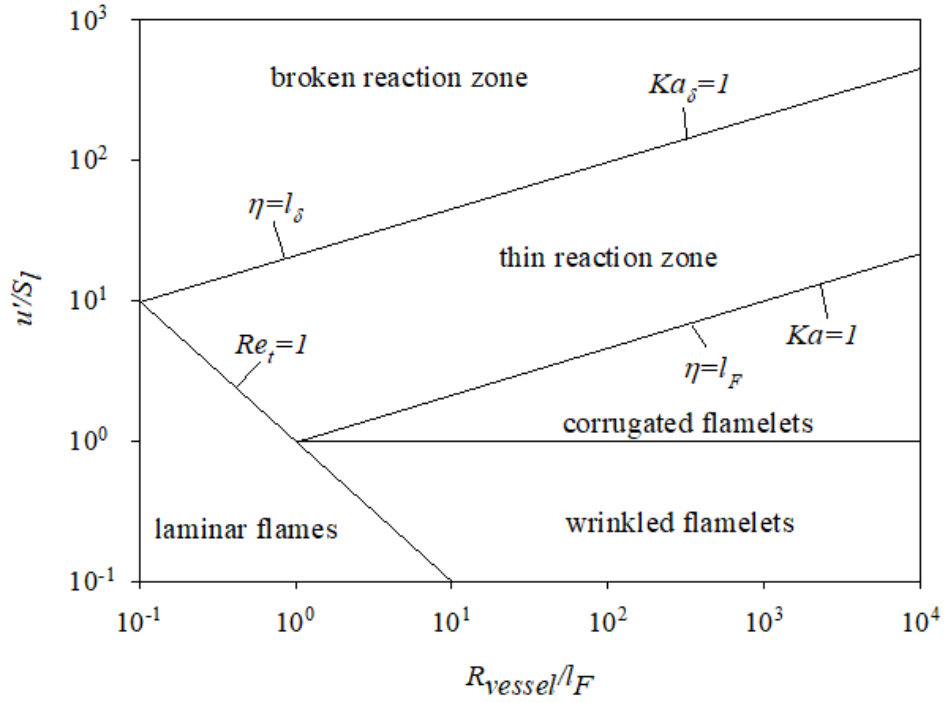

Figure II.20 *Regime diagram for premixed turbulent combustion* ([91]–[94])

In the study of turbulent combustion, for scaling purposes (i.e., to go from small to large scale turbulence), it is useful to assume a Schmidt number *Sc* (Equation (17)) of unity and to define the flame thickness as in Equation (18) [95].

$$\mathrm{Sc} = \nu/D = 1 \tag{17}$$

$$l_F = D/S_l \tag{18}$$

Where ν (m^2/s) is the kinematic viscosity (defined as the ratio of dynamic viscosity and density) and D (m^2/s) is the thermal diffusivity. From Equations (17)-(18), the kinematic viscosity can be expressed as [95]:

$$\nu = S_l l_F \tag{19}$$

According to Kolmogorov's 1941 theory on the universal range of turbulence, there is a transfer from the energy containing eddies of characteristic size of the integral length scale *l* to smaller and smaller eddies. The energy transfer per unit turnover time of the large eddies is equal to the

dissipation of energy at the Kolmogorov dissipation scale η [96]. Therefore:

$$\epsilon = \frac{u'^3}{l} \tag{20}$$

Where l (m) is the integral length scale (i.e., the radius of the vessel r_{vessel}).

In terms of the kinematic viscosity v and dissipation rate of turbulent kinetic energy ε, the Kolmogorov dissipation scale η is:

$$\eta = \left(\frac{\nu^3}{\varepsilon}\right)^{1/4} \tag{21}$$

According to Equations (20)-(21), the Kolmogorov dissipation scale η can be expressed as:

$$\eta = \left(\frac{S_l^3 {l_F}^3 l}{u'^3}\right)^{1/4} \tag{22}$$

The lines turbulent Reynolds number Re_t =1 and turbulent Karlovitz number $Ka=1$ represent boundaries between different regimes of premixed turbulent combustion with Re and Ka defined as follows:

$$Re_t = \frac{u' l}{S_l l_F} \tag{23}$$

$$Ka = \left(\frac{l_F}{\eta}\right)^2 \tag{24}$$

In particular, the line $Re_t=1$ separates all turbulent flame regimes characterized by $Re_t > 1$ from the regime of laminar flames ($Re_t < 1$), which is situated in the lower-left corner of the diagram. Moreover, a second turbulent Karlovitz number Ka_δ may be introduces as:

$$Ka_\delta = \delta^2 Ka \tag{25}$$

Where δ (m) is the reaction zone thickness. To characterize the flame nature in terms of flame thickness and reaction zone thickness, the adiabatic temperature T_{ad}, unburned temperature of mixture T_0 and autoignition temperature T_{ign} are used. Flame thickness and reaction zone thickness can be expressed as reported in Equations (26)-(27) and as shown in the flame thermal profile in **Figure II.21**.

$$l_F = \frac{T_{ad} - T_0}{\left(\frac{dT}{dx}\right)_{max}} \tag{26}$$

$$\delta = \frac{T_{ad} - T_{ign}}{\left(\frac{dT}{dx}\right)_{max}} \tag{27}$$

The value of flame thickness must be larger than that of the corresponding thickness of reaction zone, as another flame parameter, the flame preheat zone is involved within it.

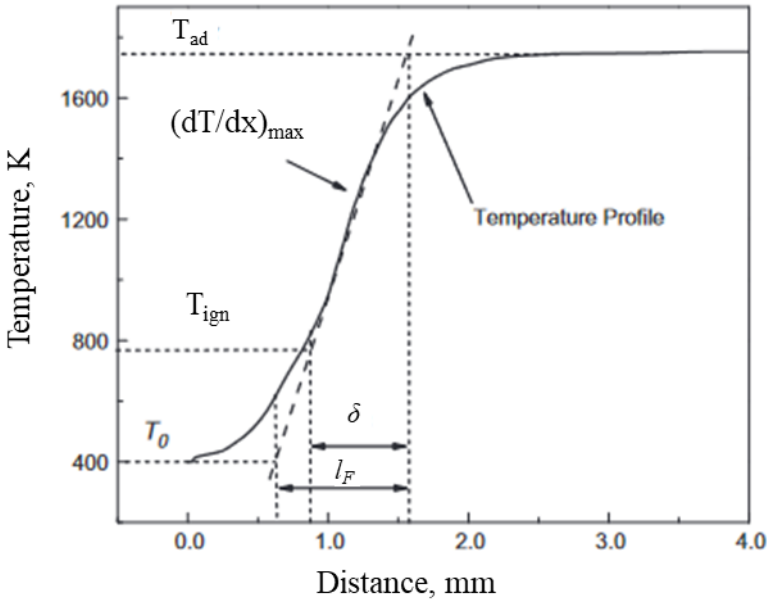

Figure II.21 *Flame thermal profile as a function of distance. The characteristic temperature (T_0, T_{ign} and T_{ad}) as well as the flame characteristics dimensions (l_F and δ) are also showed* [97]

Other boundaries of interest are the line $u'/S_l=1$ which separates the wrinkled flamelets from the corrugated flamelets, and the line denoted by $Ka_\delta=1$, which separates thin reaction zones from broken reaction zones. In the wrinkled flamelet regime, u' of the large eddies is not big enough to compete with the advancement of the flame front with the laminar burning velocity S_l ($u'< S_l$). Laminar flame propagation therefore is dominating over flame front corrugations by turbulence. In the corrugated flamelet regime, the laminar flame thickness is smaller than the Kolmogorov scale η, and hence $Ka<1$. Turbulence will therefore wrinkle the flame but will not enters in the laminar flame structure (the flow is quasi laminar). In the thin reaction zones regime, the Kolmorogov scale becomes smaller than the flame thickness, which implies $Ka>1$. Turbulence then increases the transport within the preheating region. Moreover, mixing is enhanced at higher Ka numbers, which leads to higher volumetric heat release and shorter combustion times. Beyond the line $Ka_\delta=1$ there is the regime called the broken reaction zones regime where Kolmogorov eddies are smaller than the reaction zone thickness. Eddies may enter into the reaction layer and perturb it with the consequence that chemistry breaks down locally due to enhanced heat loss to the preheat zone followed by temperature decrease and the loss of radicals. Consequently, the flame will extinguish, and fuel and oxidizer will interdiffuse and mix at lower temperatures where combustion reactions have ceased. Because the reaction zone thickness can be estimated to be an order of magnitude smaller than the flame thickness, the transition to the broken reaction zones

regime occurs at approximately *Ka* =100 [97].

II.5. Critical issues of standard explosion tests vessels

As discussed in Section II.4.7, the pre-ignition turbulence level control during the explosion standard tests is a crucial issue. The evaluation of the explosion parameters of dusts was initially performed in a 1 m^3 vessel, which was the only internationally accepted dust explosion testing device ([39], [84]). However, it requires large amounts of powder and is hard to manage. As a consequence, the 20 L sphere came out of a systematic investigation of several combustible dusts in spherical shaped equipment to find the minimum volume for dust testing ([1], [37], [38]). The acceptance of the 20 L sphere as a standardized dust explosion testing device was dependent on whether it was capable to give the same K_{St} values as the 1 m^3 vessel. Therefore, the major issue afforded was the control of the turbulence of the dust clouds ignited in the test vessels. Indeed, flame propagation velocity is significantly increased by turbulence. Consequently, it has been assumed that tests in vessels with different scales may be comparable only if the initial level of turbulence is the same. During the tests, turbulence is generated by the dust injection into the vessel. Immediately after dispersion, turbulence builds up and starts decreasing. Consequently, the turbulence level at moment of ignition significantly depends on the ignition delay time t_d which is the delay between the onset of dust dispersion and the activation of the ignition source.

Therefore, for dust testing in 20 L sphere, the ignition delay time has been standardized to (60±5) ms, at which the degree of turbulence should be comparable to that achieved in the 1 m^3 vessel at (600±100) ms ([9], [39]).

Over a few years, several dusts have been tested with both equipment and significant discrepancies have been found between the results obtained with the 20 L sphere and the 1 m^3 vessel as concerning the minimum explosive concentration (*MEC*), the deflagration index (K_{St}), and the maximum pressure (P_{max}) ([98]–[104]). In a recent work, Clouthier et al. (2019) provided a comprehensive dust explosibility dataset for niacin, Lycopodium clavatum, and two metallic powders (iron and aluminum) at three different particle size distributions. They demonstrated that, with thorough equipment calibration and adherence to standard test protocols, while it is possible to obtain good agreement of explosion severity (P_{max} and K_{St}) and *MEC* among data measured at different testing scales for some materials, this cannot be said for all materials. The exceptions are for highly reactive fine aluminium or samples approaching their corresponding reactivity limits. The following **Figure II.22** shows the obtained results [102].

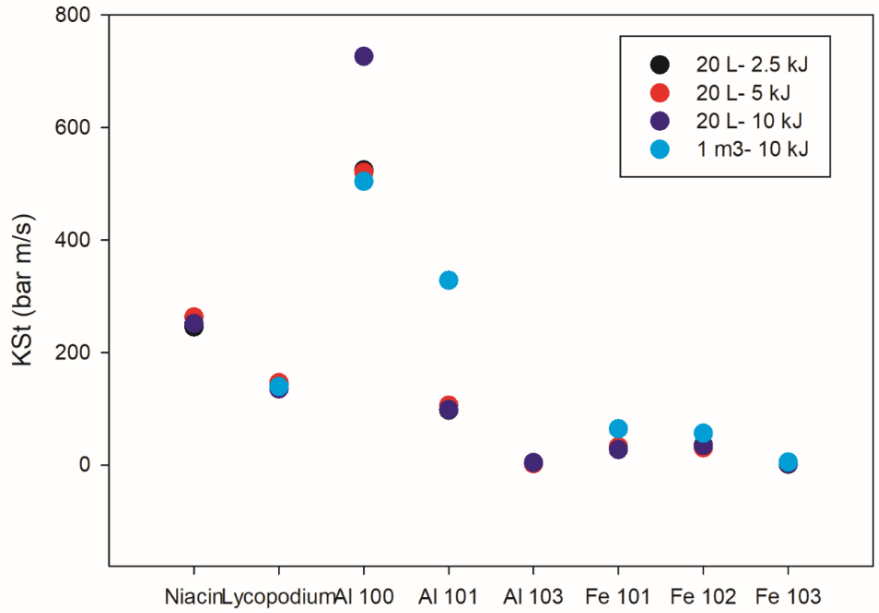

Figure II.22 *K_{St} values measured in the 20 L sphere at different ignition energies (2.5, 5 and 10 kJ) and in the 1 m^3 vessel at 10 kJ for different materials* [102]

Proust et al. (2007) carried out a systematic comparison and analysis of the discrepancies between the measurements of the violence of dust explosions with the 20 L sphere and with the standard ISO 1 m^3 vessel. **Figure II.23** shows the measured values of the deflagration index in the 20 L vessel versus the values measured in the 1 m^3 vessel [105]. It is worth noting that the values measured in the 20 L vessel are always different from those measured in the 1 m^3 vessel and, more specifically, dusts can be grouped into three classes. Class A contains dusts that are explosive in the 20 L but not explosive in the 1 m^3 vessel. Indeed, Proust et al. (2007) found that a significant proportion of dusts (5 over 21) explode, although weakly, in the 20 L sphere and not at all in the 1 m^3 vessel. As a general rule, dusts with a KSt under 50 bar m/s are candidates for clarification testing in the 1 m^3 chamber ([9], [105], [106]). Class B contains the cases in which the deflagration index measured in the 20 L vessel is higher than that measured in the 1 m^3 vessel (●). Generally, organic dusts belong to this class. Most studies have ascribed this effect to the overdriving phenomenon ([9], [98]–[101]). In Class C are present the cases in which the deflagration index measured in the 20 L vessel is lower than that measured in the 1 m^3 vessel (■). Unlike organic dusts, metal ones (e.g., iron, zinc, and aluminium) can be prone to exhibit significantly lower K_{St} values in the 20 L chamber than in a 1 m^3 chamber ([102]–[104]). This increase of explosion severity of metal dusts in the larger vessel has been addressed to the effect of thermal radiation, which can be an order of magnitude greater for metal dusts compared to common organic dusts [104]. For this reason, NFPA 68 recommends measuring the explosion severity of the most

reactive metal dusts in the 1 m^3 chamber [107].

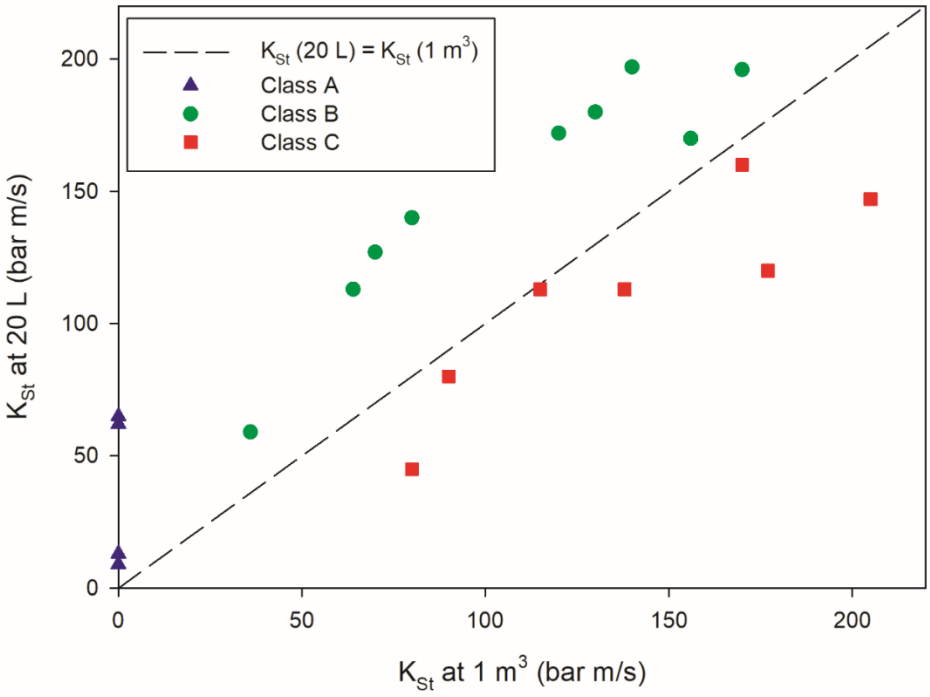

Figure II.23 *K_{St} (bar m/s) obtained with the 20 L sphere versus those measured in the 1 m^3 vessel* [105]

Going et al. (2000) measured *MEC* for Pittsburgh coal, gilsonite, RoRo93, lycopodium and iron powder and demonstrated that overdriving can occur when using strong chemical ignitors in the 20 L chamber. The result was that apparent *MEC* values are found which are lower than the "true" values. For most dusts tested, the best agreement with literature data was found between 20 L chamber data with 2.5 kJ ignitors and 1 m^3 data with 10 kJ ignitors. The following **Figure II.24** shows the obtained results [99].

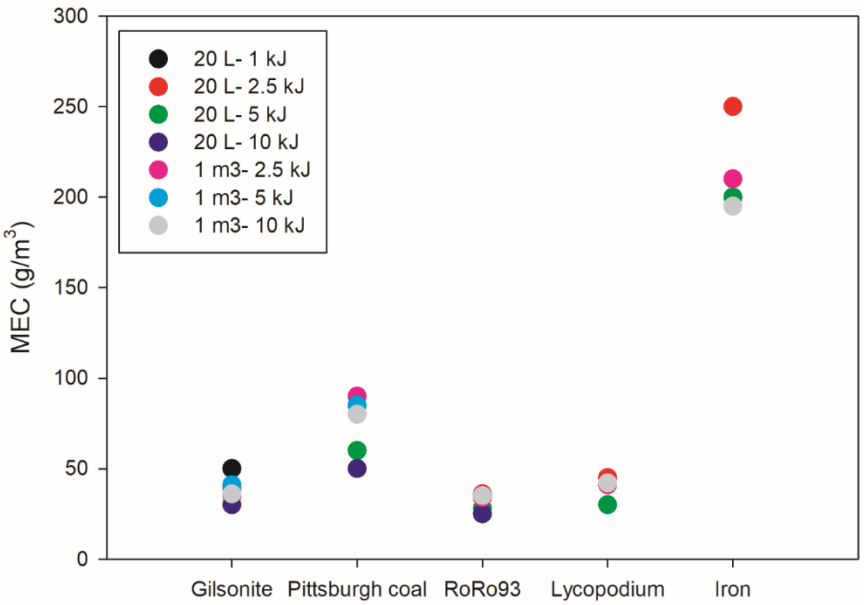

Figure II.24 *MEC values measured in the 20 L sphere at different ignition energies (1, 2.5, 5 and 10 kJ) and in the 1 m³ vessel at different ignition energies (2.5, 5 and 10 kJ) for different materials* [99]

To explain these discrepancies, some phenomena have been invoked like overdriving, underdriving phenomena, in addition the pre-ignition turbulence level effect.

Overdriving is caused by high-energy pyrotechnic ignitors (10000 J) which can trigger the dust and hybrid mixtures explosion ([9], [98]–[101], [108]–[113]). Underdriving is related to the heat losses toward the environment: the external walls of the standard test vessels subtract heat from the dust cloud explosion, eventually quenching the flame propagation. This phenomenon is more relevant for the 20 L vessel rather than for the 1 m³ vessel due to the higher surface-to-volume ratio (S/V). Both these phenomena degrade the test data and thus impede the establishment of adequate explosion hazard mitigation [114]. As regards the maximum explosion pressure, P_{max} values obtained with the 20 L sphere are significantly and systematically below the ones determined in the 1 m³ vessel [105]. Actually, because of the cooling effect from the walls of the 20 L sphere and the pressure effect caused by the pyrotechnic ignitors, in ASTM E1226-19 standard some correction correlation are present [9]. The reasons why this difference occurs are not known but may suggest different combustion regimes in both equipment [105].

II.5.1. Turbulence and dust dispersion in standard tests vessels

Moreover, it is well known that pre-ignition turbulence may play a major role in affecting the explosion behaviour. As a result, the control of the turbulence level in both vessels is of primary

importance ([100], [115]). Over the years, some doubts arise about the generally accepted ignition delay time of 60 ms in the 20 L sphere which could be too short to create turbulent conditions equal to the larger standard vessel. For this reason, the small vessel was used to determine the role of turbulence in the propagation of a dust explosion.

Di Benedetto et al. (2012) performed measurements of the pressure history of methane/nicotinic acid/air mixtures in the 20 L Siwek sphere, by changing the ignition delay time (t_d). From the obtained results, the violence of the explosion of an hybrid mixture decreases as t_d increases independent of the ignition energy level [100]. Moreover, different authors measured the turbulence level inside the 20 L sphere ([64], [116]–[118]) and the 1 m^3 spherical/cylindrical vessel ([62], [119]). Turbulence measurements were performed through hot wire or laser doppler anemometry in few points of the vessel, mainly positioned at the centre or close to the dispersion system. Collected data allowed the evaluation of the temporal values of the instantaneous velocity and of the root mean square velocity fluctuations only in the selected points. Pu et al. (1990) measured the *RMS* turbulent velocity at the centre of the 20 L vessel and showed that the dispersion induced turbulence may play a crucial role in the formation of dust-air mixtures than in the direct effect on the combustion process, and the reduction of dust particle size will increase the turbulent burning velocity in dust-air mixtures very significantly. The kind of dust seemed to have no significant influence on explosion data if their particle sizes are the same. Moreover, results clearly showed that the turbulent conditions in the 20 L sphere at 60 ms were considerably more intense than the conditions in the large vessel at the standard time (**Figure II.25**) [116]. Notably, a delay time of 250 ms in the 20 L sphere resulted in much more comparable conditions. **Figure II.26** shows the *RMS* profiles in the standard test vessel centre as a function of the normalized time as measured by Dahoe et al. (2002) [64] and Hauert and Vogl (1995) [119]. Notably, at each time, the pre-ignition turbulence level generated by the dust dispersion system is always lower in the 1 m^3 vessel than in the 20 L sphere in the vessels centre where the ignition occurs.

As mentioned in the Section I, Bartknecht and Siwek measured equal K_{St} values in the 20 L sphere and the 1 m^3 vessel ([1], [37], [38]). Apart from giving rise to the notion that equal turbulence levels exist in both test vessels at the prescribed ignition delay times of 60 ms and 600 ms, their research also inspired the widespread belief that a formal cube-root-law agreement exists between dust explosion severities measured in the two test vessels. In addition to that, their research encouraged the use of the cube-root-law as a predictive tool to assess the severity of an industrial dust explosion on the basis of dust explosion severities measured in laboratory test vessels. **Figure II.26** shows that significantly different turbulence levels exist in the two test vessels at the prescribed ignition delay times. Hence, the results of Bartknecht and Siwek, which form the

experimental basis of the cube-root-law, were obtained by igniting dust clouds under significantly different conditions of turbulence in the two test vessels. As a result, the cube-root-law may not be considered as a generally valid. In fact, its use in the practice of scaling laboratory test results into what might happen during accidental industrial dust explosions must be regarded as fundamentally wrong. This conclusion supports the idea of abandoning the cube-root-law and replacing it with a more fundamental approach.

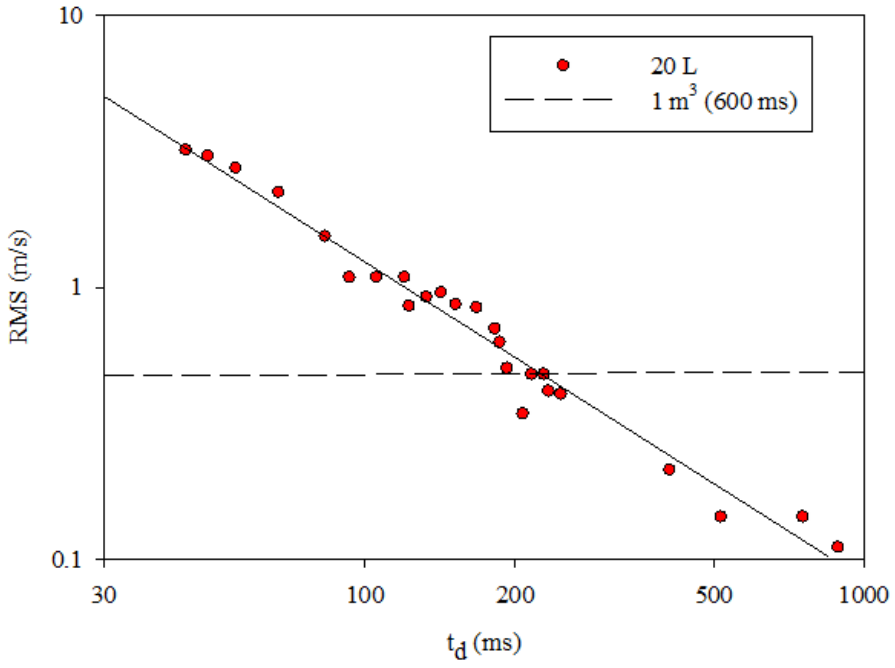

Figure II.25 *RMS value of the velocity fluctuations in the 20 L versus ignition delay time. The dashed line represents the RMS value in the 1 m^3 vessel at 600 ms delay* [116]

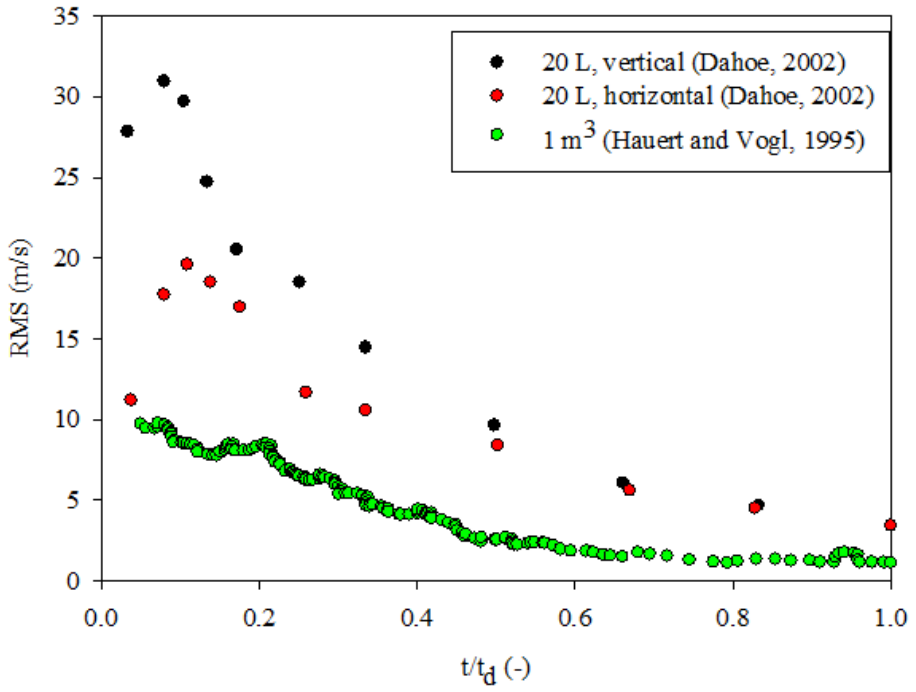

Figure II.26 *RMS profiles in the standard test vessel centre (black and red circles for 20 L sphere, green one for 1 m³ vessel) as a function of normalized time (defined as the ratio time to ignition delay time)* ([64], [119])

In addition to the turbulence level issue, both standard vessels must be capable of dispersing a fairly uniform dust cloud of solid particles for a reliable and repeatable estimation of safety parameters ([9], [19], [20], [39], [106]). Some researchers investigated the effectiveness of dust dispersion in various test vessels using optical dust probes in the 20 L sphere ([120], [121]) and in the 1 m^3 ISO vessel ([98], [119]). The measuring principle is based on the attenuation by absorption and dispersion of the intensity of a light beam penetrating a cloud with solid particles. Kalejaiye et al. used optical dust probes to measure optical transmittance through the dust cloud at six locations within the 20 L sphere, with the two standard dispersion nozzles (rebound and perforated annular nozzles). They tested the dispersion of three different dusts, showing that the transmission data of the three dusts were significantly lower than those corresponding to the nominal value. They attributed this difference to the reduction in particle size that occurred during dispersion [120], [121]. Cashdollar and Chatrathi (1992) carried out comparisons between the uniformity of the dust cloud formed in the 20 L chamber and Fike 1 m^3 test vessel, using optical dust probes. They observed that the 1 m^3 transmission data were somewhat lower than in the 20 L chamber at low dust concentrations. A possible explanation for this behaviour is an increased agglomeration in the 20 L chamber [98]. Hauert and Vogl (1995) measured the dust concentration of maize starch

(diameter 15 μm, density 1000 kg/m^3, nominal concentration 120 g/m^3) in the 1 m^3 vessel in 9 different locations. Results showed differences in the transmission data at the different points, indicating that the dust cloud is non-uniform. In particular, the highest values of dust concentration were found on the bottom of the vessel due to the sedimentation phenomenon [119].

Due to the possibility of measurement of turbulence level and dust concentration only in few points of the vessels, maps of velocity vectors, turbulence degree, and dust concentration cannot be derived from experimental analyses. Di Benedetto et al. (2013) developed a 3D *CFD* model developed to describe the turbulent flow field induced by dust feeding and dispersion within the 20 L sphere, and the associated effects on the distribution of dust concentration. The developed *CFD* model was validated against measurements of time histories of pressure and root mean square velocity available in the literature. The time sequences of velocity vector and kinetic energy *k* maps showed that multiple turbulent vortex structures are established within the sphere. The presence of these vortices generates dead volumes for the dust which is pushed toward the walls of the sphere, as shown in **Figure II.27**. **Figure II.27** shows the velocity vectors (a) and the particles track (b) coloured by γ, defined as the ratio between the actual dust concentration and the nominal dust concentration C_{nom} fed to the vessel (C=250 g/m^3), at 60 ms [122].

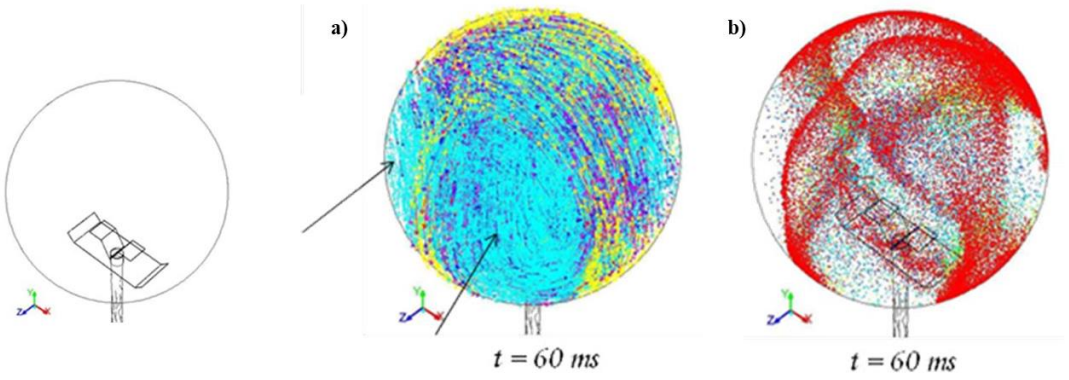

Figure II.27 *Velocity vectors (a) and particles track (b) colored by γ at 60 ms, isometric view* [122]

The dust concentration is not uniform in the sphere, being higher close to the vessel walls and much lower than the nominal value inside the sphere. However, the turbulent kinetic energy *k* is higher at the center of the sphere and, thus, close to the igniters. Moreover, comparison between the results obtained in the cases of dust free air and dust-air mixture shows that, in the presence of dust, the fluid flow becomes asymmetric because of the entrainment effect of particle sedimentation [122]. Further studies were carried out to evaluate the effect of dust size and size

distribution ([41], [123], [124]), dust concentration [125], dust shape (as reported and discussed in Section II.4.3) [126] and dust dispersion systems ([127], [128]). Di Sarli et al. (2013) found that at low values of the dust diameter (d = 10 μm), the dust is partially entrained by the fluid filling the outer region of the vortex and partially the internal zones. Conversely, on increasing the dust diameter (d = 100 μm and d = 250 μm), the dust and the fluid flows are independent and the dust follows flow paths completely different being concentrated mainly at the vessel walls [124]. Di Sarli et al. (2014) investigated the effect of dust concentration on the turbulence level and the dust dispersion within the 20 L sphere. They found that at low nominal concentration (100 g/m^3), the dust mainly accumulates at the boundary of the vortices, while at higher nominal concentration (500 g/m^3), the dust sedimentation prevails giving rise to highly concentrated regions close to the vessel walls [125]. Di Sarli et al. (2015) performed *CFD* simulations of turbulent fluid flow and dust dispersion in the 20 L vessel equipped with the perforated annular nozzle. **Figure II.28** shows the turbulent kinetic energy maps at 60 ms for the 20 L sphere equipped with rebound nozzle (a) and perforated annular nozzle (b) and the particles tracks at 60 ms for the 20 L sphere equipped with rebound nozzle (c) and perforated annular nozzle (d) [128]. Simulation results showed that the turbulent kinetic energy *k* and dust/air cloud are more uniform than those attained with the rebound nozzle (**Figure II.28**). However, a consistent fraction of the dust remains trapped inside the perforated annular nozzle and, thus, it does not contribute to the explosion process [128]. In order to overcome the critical issues linked to the actual standard equipment and procedure, a 3D *CFD* model was developed by Di Benedetto et al. (2015) to test a novel fan-equipped vessel for flammability and explosion tests [127]. Simulations were performed in the presence of two counterrotating fans positioned at the top and at the bottom of the vessel and also after having switched-off the fans. Numerical results have shown the rotation of two fans guarantees a controlled turbulence level, but it does not allow a uniform dust concentration. Only after the switch-off of the fans, the dust starts filling the empty volumes inside the sphere, reaching a quite uniform distribution (with concentration equal to the nominal value) and simultaneously ensuring a controlled low value of turbulent kinetic energy. The results obtained suggest that it is possible to achieve a uniform cloud of dust/air inside the vessel if two fans are used and the novel procedure is implemented [127].

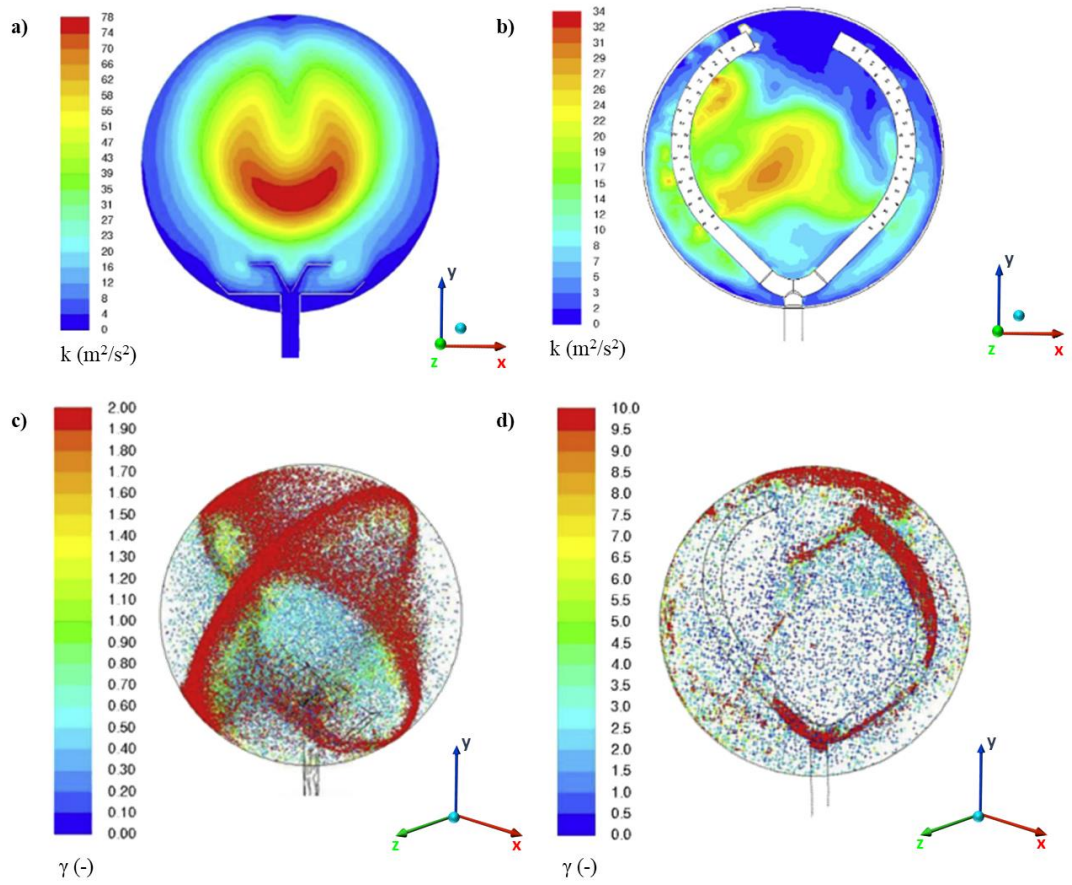

Figure II.28 *Turbulent kinetic energy k (m^2/s^2) maps for the 20 L sphere equipped with rebound nozzle (a) and perforated annular nozzle (b) and the particles tracks (in terms of γ) for the 20 L sphere equipped with rebound nozzle (c) and perforated annular nozzle (d), 60 ms* [128]

The results obtained and here discussed suggest that a different dust dispersion method has to be developed mainly for the measurement of the minimum explosive concentration, MEC.

Surprisingly, no simulation is available for 1 m^3 vessel which allows the quantification of the turbulent kinetic energy and dust distribution maps.

II.6. Open issues

The flammability and the explosibility of combustible dusts are complex phenomena and the most critical mechanisms are still not completely understood.

More specifically:

1. A procedure for fully characterising the dust explosion likelihood and severity has not yet been developed
2. All the issues affecting the standard testing device have already been identified but are

scarcely discussed in literature. Moreover, the effects of these critical phenomena on dusts characterized by different flame propagation path have not been investigated yet

3. A fundamental investigation of flame propagation features and key parameters (physical, operating, chemical) controlling the flame velocity has never been proposed

II.7. Aim of the work

The main motivation of this thesis work is to try to give an answer to all these open issues. This will be achieved by means of an extensive experimental and simulative study. The major activities that will be carried out during my PhD period are:

1. Modelling of the flame propagation of combustible dust/air and hybrids;
2. Understanding of all the issues of the standard equipment;
3. Investigation of flame propagation features and key parameters (physical, operating, chemical) controlling the flame velocity

The first part of the activities consists of the discussion and the applications of a Mallard-Le Chatelier inspired theoretical flame propagation model for combustible dusts and hybrids. In this section, it was evidenced the need for a thermal characterization for all the combustible dusts in order to assess key parameters influencing the flame propagation.

Consequently, a complete characterization procedure for dusts and dust mixtures was developed and applied. Several examples of coupled thermal investigations and flammability/explosibility analysis on different kind of combustible dusts and dust mixtures are reported. The importance of conducting coupled flammability analyses, chemico-physical and thermal characterization is highlighted to fully understand the reason for the occurrence of synergistic effects in dust mixtures. Moreover this kind of complete characterization was carried out on two non-traditional dusts (nylon and grape pomace) in order to understand the different flammable behavior of the same powders as the size or the chemical composition varies.

Once understood the key parameters that influence the flame propagation and therefore the dust explosion, the second part of the thesis aims to understand all the critical phenomena that influence the measurements of the parameters within the standard devices. Particularly, the dust dispersion inside the 20 L sphere was simulated for nicotinic acid/anthraquinone mixtures (with different pure dust ratios, while keeping the total dust concentration constant) with a validated three-dimensional *CFD* model. Since the fields of dust concentration, flow velocity and turbulence are strongly affected by both diameter and density of the pure dusts, a simulative campaign was carried out by varying these parameters in order to build a graph in which focusing diameter/density

independence zones.

Since no simulation is available for 1 m^3 vessel which allows the quantification of maps of velocity vectors, turbulence degree, and dust concentration, a *CFD* model was formulated and validated to simulate the flow field and the dust concentration distribution in the 1 m^3 spherical vessel equipped with both the perforated annular and the rebound nozzles. The effect of the dust size was also investigated. Thanks to the use of CFD models developed for both standard vessels, the effect of pre-ignition turbulence level as well as of the pyrotechnic ignitors action was investigated in order to focus all the phenomena affecting the deflagration index evaluation within the 20 L sphere and the 1 m^3 vessel. Finally, all the issues affecting the standard test vessels were discussed together with a simple procedure proposed to choose the standard vessel able to give the most conservative parameters values and to take into account the possible issues.

III. MATERIALS AND METHODS

In the following sections, the investigated materials and the involved techniques will be presented in general. It is worth underlining that to ease the reading of this thesis, all the results will be divided in sub-sections within the Results section anticipated by a specific section of Materials and Methods.

III.1. Materials

In this work, several organic dusts were investigated. All the materials are listed in **Table III.1**.

Table III.1 *List of all the investigated materials*

Dust	Description
Cornstarch	Starch derived from corn grain. It is a common food ingredient, often used to thicken sauces or soups, and to make corn syrup and other sugars.
Niacin	Organic compound classified as a B-vitamin. It is mainly used in pharmaceutical industries and it is also a reference dust for testing dust explosion.
Anthraquinone	Aromatic compound. It is used in the production of dyes and natural pigments, as catalyst in the production of wood pulp and paper industry, and as laxative in pharmaceutical industry.
Lycopodium	Lycopodium is composed of the dry spores of clubmoss plants. It is used in standard explosion and flammability tests, and also in fireworks and explosives.
Glucose	The most abundant monosaccharide, a subcategory of carbohydrates. It may be added to foods as a sweetening agent.
L-ascorbic acid	Water-soluble vitamin, known as vitamin C, acting as a coenzyme, a flour treatment agent, a food antioxidant as well as a plant metabolite.
Irganox 1222	Polymer additive with antioxidant properties. It is also a reference dust for testing dust explosion.
Nylon fibres	Nylon is a generic designation for a family of synthetic polymers composed of polyamides. Nylon is a silk-like thermoplastic, generally made from petroleum, that can be melt-processed into fibers, films, or shapes.
Grape pomace	Solid remains of grapes, olives, or other fruit after pressing for juice or oil. It contains the skins, pulp, seeds, and stems of the fruit.

Niacin, Anthraquinone, Lycopodium, Glucose and L-ascorbic acid were purchased from Sigma-Aldrich (except Irganox 1222, provided by Kuhner AG) and characterized as received. Cornstarch (1500 kg/m^3 and 15 μm) was bought in a common grocery store. Nylon fibres characterized by different colours and surface activations were provided by a flocking manufacturing plant located

in the north of Italy. Grape pomace came from the waste stream of a wine distillery in Northern Italy.

III.2. Apparatus and techniques

III.2.1. Apparatus for flammability and explosibility testing

MIT of dust/air mixtures is measured in the "Godbert-Greenwald" furnace. The "Godbert-Greenwald" furnace test apparatus includes a heated quartz furnace tube with a volume of 0.27 L, two thermocouples, a sample container, an electromagnetic valve, a heater and a stop stock. The tube with bottom exposure is insulated and equipped with thermostatically controlled electric resistance wires. After setting the temperature of the furnace at the desired value, a weighed amount of dust is placed in the sample container, and then the sample is dispersed into the test chamber forming dust clouds by compressed air of 0.08 MPa after opening the electromagnetic valve. During the experiment, the flame can be observed underneath the furnace tube [18].

The minimum ignition energy (*MIE*) was determined by means of a MIKE 3 device (Kuhner, CH), according to the ASTM E2019-03 standard [16]. Samples (size 300–2400 mg) were dispersed through a mushroom shaped nozzle in a modified Hartman tube. Using 120 ms as ignition delay time, from the air blast used for the dispersion of the dust, an electrostatic spark was triggered between the tips of a couple of tungsten rods (spark gap: 6 mm) by releasing the energy stored in a condenser bench. In all the cases, an inductance of 1mH (prolonged sparks) was coupled to the capacitive electric circuit.

The maximum pressure (P_{max}) and deflagration index (K_{St}) were measured in the 20 L Siwek sphere, according to the standard [9]. The ignition source is placed at the center of the sphere through a couple of Teflon electrodes fixed to a flange located on the top of the combustion chamber. Chemical igniters of 200 J (2x100J) were used. The chemical igniters are activated electrically by a low-voltage source and provide a dense cloud of hot dispersed particles with very little gas by-product. The delay time (60 ms) was set constant for all tests performed. 10 g sample (close to the stoichiometric value for all the samples) was placed into the dust container. The explosion chamber, which was initially filled with air at atmospheric pressure, was then evacuated to 0.6 bar absolute. An automatic test sequence was initiated to pressurize the dust container to 20 bar gauge, and then the fast-acting valve on the dust container outlet was opened to inject dust into the explosion chamber through a rebound nozzle. The rebound nozzle should ensure an uniform distribution of dust within the explosion chamber [9].

III.2.2. Apparatus for thermal screening

Differential scanning calorimetry (*DSC*) thermograms were recorded with a heat power compensation DSC (PerkinElmer DSC 8000 instrument), calibrated for the enthalpies measurements and equipped with an Intracooler II apparatus. Approximately 3 mg sample was weighed into stainless-steel high-pressured pans (Volume 50 μL, Perkin Elmer Part n. B016–9321). Dry nitrogen was used as purge gas at a flow rate of 20 mL/min. Data were collected at a heating rate of 20°C/min over a temperature range of 25–400°C.

The thermal behavior of dusts was also assessed by using a *TG/DSC* TA Instrument Q600SDT. TG and DSC profiles have been recorded simultaneously. Tests were performed both in open platinum crucible and in closed aluminum pan, the latter to investigate the overall process and preventing/reducing the sublimation process. Briefly, for open cup tests, a certain amount sample was placed in the crucible and was heated up with heating rate β = 2.0, 5.0, and 10.0 °C/min, to investigate the effect of the heating rate on the position of the peaks. Measurements were performed in both N_2 and airflow (100 mL/min) to assess the influence of different atmospheres. For closed cup tests, a thin layer of sample was put on the bottom of an aluminum pan in order to leave a free space for volatiles. The cup was fitted with a coverlid with a hole in the top to allow pressure to escape. Then, the material was heated up to 400 °C with heating rate of 5.0 °C/min in nitrogen flow (100 mL /min). From TG analysis, the proximate analysis determined the moisture content (*M*), volatile matter (*VM*), ash (*A*) and the calculation of fixed carbon (*FC*) in the analysis of samples tested in N_2 atmosphere [129]. To analyse gases product from samples degradation, an *FTIR* gas was carried out through *TGA*/*FTIR* interface linked by transfer line to TGA furnace. The cell and transfer line of the *TGA*/*FTIR* interface were heated and kept at 220 °C. In this way, product gases from samples degradation could not condense. The output of this analysis is a Gram-Schmidt diagram.

III.2.3. Apparatus for chemico/physical analysis

To analyse the solids and residues, the *HPLC* analyses were performed with an Agilent 1100 series, correlated with UV lamp and analyzer. The column, used for the separation, was a Zorbax Agilent XDB-C18, 4.6 x 150 mm, with porous silica as base. Pure acetonitrile was used as eluent agent, and the flow rate is fixed to 1 mL/min. The samples were prepared by recovering the mixture at the end of a *DSC* run (almost 3 mg of dust) into 10 mL of acetonitrile. Spectra were collected in the UV-Vis light range.

Moreover, *FTIR* spectroscopy analysis was carried out using a Nicolet 5700 FTIR Thermo Fisher

Scientific apparatus. *FTIR* analysis on solid samples was carried out in transmission mode in the range 400–4000 cm^{-1} using KBr disks prepared by mixing 2 mg of powdered sample and 200 mg of KBr. *FTIR* spectra were recorded on pure dusts and on the mixtures before, during and after the TG/DSC test to evaluate the chemical/physical transformations. *FTIR-ATR* spectra were collected using a NICOLET 5700 spectrometer (Thermo Scientific, USA) equipped with *ATR* Accessory with a Zn-Se crystal. For characterization of size and shape, *SEM* analysis was carried out through Philips mod. XL30 at magnifications from 100x to 6000x. From these images, the shape of the dust was identified. In addition, ImageJ was used to estimate particle sizes by means of a statistical analysis. To determine both the crystallographic structure and the degree of crystallinity, *XRD* analysis was carried out through *XRD* diffractometer PANalytical X'Pert Pro using Cu Kα radiation (1.5406 Å). The range of variability of 2θ is [5°; 79.99°] with a step size of 0.013° and a scan step time of 8.67 s. To measure of the specific surface area and the density of materials, BET analysis was carried out by N_2 adsorption at 77 K with a CHEMBET 300 Quantachrom instrument. A laser diffraction granulometer (Malvern Instruments Mastersizer, 2000) was used to measure the granulometric distribution of dusts.

III.3. CFD simulation and modelling

In this work, the *CFD* model of dust dispersion within the 1 m^3 vessel was developed and validated. The model consists of the continuity and momentum conservation equations (Eulerian approach) (Eqs.(28)-(29)).

$$\frac{\partial \rho}{\partial t} + \nabla \cdot \left(\rho \vec{U}\right) = 0 \tag{28}$$

$$\frac{\partial (\rho \vec{U})}{\partial t} + \nabla \cdot \left(\rho \vec{U} \vec{U}\right) = -\nabla \mathrm{p} + \nabla \cdot (\bar{\bar{\tau}}) + \rho \vec{g} + \vec{F} \tag{29}$$

where p (bar) is the static pressure, $\bar{\bar{\tau}}$ is the stress tensor, and $\rho \vec{g}$ and $\vec{F}$ are the gravitational body force and external body forces. The Equations (28)-(29) were solved by using the standard k-ε model as turbulent sub-model with standard wall function and considering compressibility effects [130]. The fluid flow equations were discretized using a finite-volume formulation on the three-dimensional non-uniform unstructured grid (478449 elements) shown previously. The semi-implicit method for pressure-linked equations (SIMPLE) was used to solve the pressure-velocity coupled equations. The spatial discretization of the model equations used first order schemes for convective terms and second order schemes for diffusion terms. First-order time integration was used to discretize temporal derivatives with a time step of $4 \cdot 10^{-5}$ s. The flow of the solid phase was solved with the Lagrangian formulation using the Discrete Phase Model (*DPM*).

The momentum balance equation of the *DPM* reads as follows [131]:

$$\frac{du_p}{dt} = f_D + \frac{g(\rho_p - \rho)}{\rho_p} + f \tag{30}$$

Where ρ_p (kg/m^3) is the particle density, ρ (kg/m^3) is the continuum (air) density and f_D (N/kg) is the drag force per unit particle mass, function of the Reynolds number according to the following Equation (31):

$$f_D = \frac{18\mu}{\rho_p d_p^2}\frac{C_D Re}{24}(u - u_p) \tag{31}$$

The Reynolds number in Equation (32) is defined in the following

$$Re = \frac{\rho d_p |u_p - u|}{\mu} \tag{32}$$

Where u_p (m/s) is the particle velocity, μ (Pa·s) is the molecular viscosity of the fluid, ρ (kg/m^3) is the fluid density, ρ_p (kg/m^3) is the density of the particle, C_D (-) is the drag coefficient and d_p (m) is the particle diameter. The Equation (30) incorporates additional forces (f) per unit particle mass. The first of these is the "virtual mass" force, the force required to accelerate the fluid surrounding the particle. This force can be written as:

$$f = \frac{1}{2}\frac{\rho}{\rho_p}\frac{d}{dt}(u - u_p) \tag{33}$$

An additional force arises due to the pressure gradient in the fluid:

$$f = \left(\frac{\rho}{\rho_p}\right) u_p \frac{\partial u}{\partial x} \tag{34}$$

Several laws for drag coefficients, C_D, are available for the Euler-Lagrange Model. The spherical drag law for smooth particles is defined in the following

$$C_D = a_1 + \frac{a_2}{Re} + \frac{a_3}{Re^2} \tag{35}$$

where a_1, a_2 and a_3 (-) are constants given by Morsi and Alexander (1972) [132].

The discrete phase formulation used by Ansys Fluent contains the assumption that the second phase is sufficiently dilute that particle-particle interactions and the effects of the particle volume fraction on the gas phase are negligible. In practice, these requirements imply that the discrete phase must be present at a fairly low volume fraction, usually less than 10-12% [131]. In this work, the dust concentration investigated was equal to 100 g/m^3 (close to the MEC value for several combustible dusts) with a dust density of 2046 kg/m^3, corresponding to a solid fraction equal to $\alpha = 4.9 \cdot 10^{-5}$. In these conditions, the momentum transfer from the particles is large enough to alter the turbulence structure while the particle/particle collision may be neglected. This interaction is called two-way coupling according to the classification of Elghobashi [133].

Fluent predicts the trajectory of a discrete phase particle by integrating the force balance on the

particle. Therefore, the *DPM* uses its own numerical mechanisms and discretization schemes. The unsteady particle tracking integration time step was taken equal to the fluid flow time step. Parallel calculations were performed by means of the segregated pressure-based solver of the code ANSYS Fluent (release 19). In order to achieve convergence, all residuals were set equal to $1 \cdot 10^{-6}$. For 1 m^3 simulation, the fluid phase was air at constant atmospheric temperature. As initial conditions, we adopted the same conditions used in the standard tests: the container vessel was initially at pressure equal to 21 bar; the connecting tube and the sphere were set to 1 bar.

IV. RESULTS AND DISCUSSION

The Results Section was organized in separated sub-sections to ease the reading.

The first section consists of the discussion and the applications of a Mallard-Le Chatelier inspired theoretical flame propagation model for combustible dusts and hybrids. In this section, it is evidenced the need for a thermal characterization for all the combustible dusts in order to assess key parameters influencing the flame propagation.

Consequently, in the second section, a complete characterization procedure for dusts and dust mixtures was developed and applied. In this second section, the importance of conducting coupled flammability analyses, chemico-physical and thermal characterization is highlighted to fully understand the reason for the occurrence of synergistic effects in dust mixtures.

In the third section, the coupled flammability analyses, chemico-physical and thermal characterization was carried out on two non-traditional dusts (nylon and grape pomace) in order to understand the different flammable behavior of the same powders as the size or the chemical composition varies.

Once understood the key parameters that influence the flame propagation and therefore the dust explosion, the second part of the thesis aims to understand all the critical phenomena that influence the measurements of the parameters within the standard devices.

In the fourth section, the dust dispersion inside the 20 L sphere was simulated for nicotinic acid/anthraquinone mixtures (with different pure dust ratios, while keeping the total dust concentration constant) with a validated three-dimensional *CFD* model. Since the fields of dust concentration, flow velocity and turbulence are strongly affected by both diameter and density of the pure dusts, a simulative campaign was carried out by varying these parameters in order to build a graph in which focusing diameter/density independence zones.

In the fifth section, a *CFD* model was formulated and validated to simulate the flow field and the dust concentration distribution in the 1 m^3 spherical vessel equipped with both the perforated annular and the rebound nozzles. The effect of the dust size was also investigated.

In the sixth and seventh sections, the effect of pre-ignition turbulence level as well as of the pyrotechnic ignitors action was investigated in order to focus all the phenomena affecting the deflagration index evaluation within the 20 L sphere and the 1 m^3 vessel.

Finally, in the eighth section all the issues affecting the standard test vessels were discussed together with a simple procedure proposed to choose the standard vessel able to give the most conservative parameters values and to take into account the possible issues.

The Results section titles are reported below:

1. Modelling of the flame propagation of dust/air and dust mixture/air mixtures
2. Synergistic behavior of flammable dust mixtures: A novel classification
3. Chemico-physical and thermal analysis of non-traditional dusts
4. CFD simulation of the dispersion of binary dust mixtures in the 20 L vessel: effect of dust diameter and density
5. CFD simulations of dust dispersion in the 1 m^3 explosion vessel
6. Effect of turbulence spatial distribution on the deflagration index: Comparison between 20 L and 1 m^3 vessels
7. Role of pyrotechnic ignitors in dust explosion testing: comparison between 20 L and 1 m^3 explosion vessels
8. Which standard vessel should I use and which issues I have to consider?

IV.1. Modelling of the flame propagation of dust/air and dust mixture/air mixtures

IV.1.1. Methodology

To get insight into the chemical/physical transformations that take place during dust flame propagation, a detailed study of each phase is required. The knowledge of the dust flame propagation mechanism would drive the evaluation of the flame velocity thus eventually allowing the theoretical evaluation of the most important explosion parameters. The model is inspired by the thermal theory by Mallard and Le Chatelier (1883) [97] developed for gas flames. According to the model of Mallard and Le Chatelier, the flame propagation is controlled by heat back diffusion from the reaction zone to the unburnt gas pre-heating zone and by the combustion reaction. In the model for dust flames, we distinguished additional and different phases.

IV.1.2. Dust flame propagation model development

In **Figure IV.1** the scheme of the dust flame thickness is show. Three zones are identified: zone I, zone II and zone III.

I. The dust is pre-heated up to the volatile point (*VP*) at which devolatilization occurs (red dotted line). This is the only layer relative to the solid phase.
II. The gases are pre-heated up to the ignition temperature (T_{ign})
III. Reaction zone.

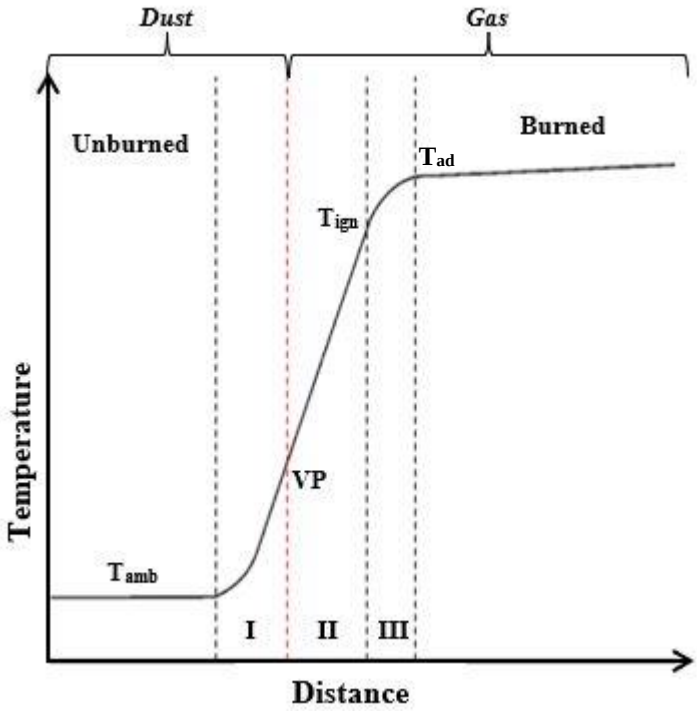

Figure IV.1 *Proposed thermal profile of dusts and dust mixtures flames*

As stated by Mallard and Le Chatelier (1883) [97], the heat diffusing from zone III to zone II and zone I in **Figure IV.1** is equal to that necessary to raise the dust to the volatile point (the boundary between zones I and II), sustain the devolatilization and to heat up the unburned gases to the ignition temperature (the boundary between zones II and III). If it is assumed that the slope of the temperature curve is linear, the heat back diffusing can be evaluated by the following expression:

$$\frac{(T_{ad} - T_{ign})}{\delta_{III}} \tag{36}$$

Where δ_{III} (m) is the thickness of the reaction zone.

Equation (37) represents the energy balance:

$$\lambda_{III} \frac{(T_{ad} - T_{ign})}{\delta_{III}} A = \dot{m}_{dust} (Cp_{dust}(VP - 25) + \Delta H_{dev}) + \dot{m}_{dev} Cp_{gas,II}(T_{ign} - VP) \tag{37}$$

Where λ_{III} ($W/m\ °C$) is the thermal conductivity of gases in the zone III, $Cp_{gas,II}$ (J/kg °C) is the specific heat of the unburnt gases, $\dot{m}_{dev}$ (kg/s) is the mass rate of the unburnt gas mixture produced by devolatilization into the combustion wave, $\dot{m}_{dust}$ (kg/s) is the mass rate of the combustible dust, Cp_{dust} (J/kg °C) is the specific heat of the combustible dust, ΔH_{dev} (J/kg) is the devolatilization heat and A (m^2) is the cross-sectional area.

Mass balance equations are the following:

$$\dot{m}_{dev} = \rho_{dev} u A = \rho_{dev} S_l A \quad (38)$$

$$\dot{m}_{dust} = \rho_{dust} S_{dust} A \quad (39)$$

where ρ_{dev} (kg/m^3) is the density of unburnt gases, S_l (m/s) is the laminar burning velocity of the gaseous mixture with air and S_{dust} (m/s) is the laminar burning velocity of the combustible dust. By rearranging all the equations, Equation (37) becomes:

$$\lambda_{III} \frac{(T_{ad} - T_{ign})}{\delta_{III}} = \rho_{dust} S_{dust} (Cp_{dust}(VP - 25) + \Delta H_{dev}) + \rho_{dev} S_l Cp_{gas,II}(T_{ign} - VP) \quad (40)$$

$$S_{dust} = \frac{-\rho_{dev} S_l Cp_{gas,II}(T_{ign} - VP) + \lambda_{III} \frac{(T_{ad} - T_{ign})}{\delta_{III}}}{\rho_{dust}(Cp_{dust}(VP - 25) + \Delta H_{dev})} \quad (41)$$

In **Figure IV.2** and **Figure IV.3**, the trends of S_{dust} as a function of *VP* parametric in S_l and ΔH_{dev} are reported. By increasing S_l, S_{dust} decreases because the heat necessary to dust to reach VP and devolatilize is subtracted by the gases. In this condition, the phenomena involved in the I phase control the flame propagation. By decreasing ΔH_{dev}, S_{dust} increases because the dust devolatilization subtracts a lower amount of energy from the flame and the remaining energy can be used for the dust and gases pre-heating. In this condition, the devolatilization is a fast step and does not control the flame propagation.

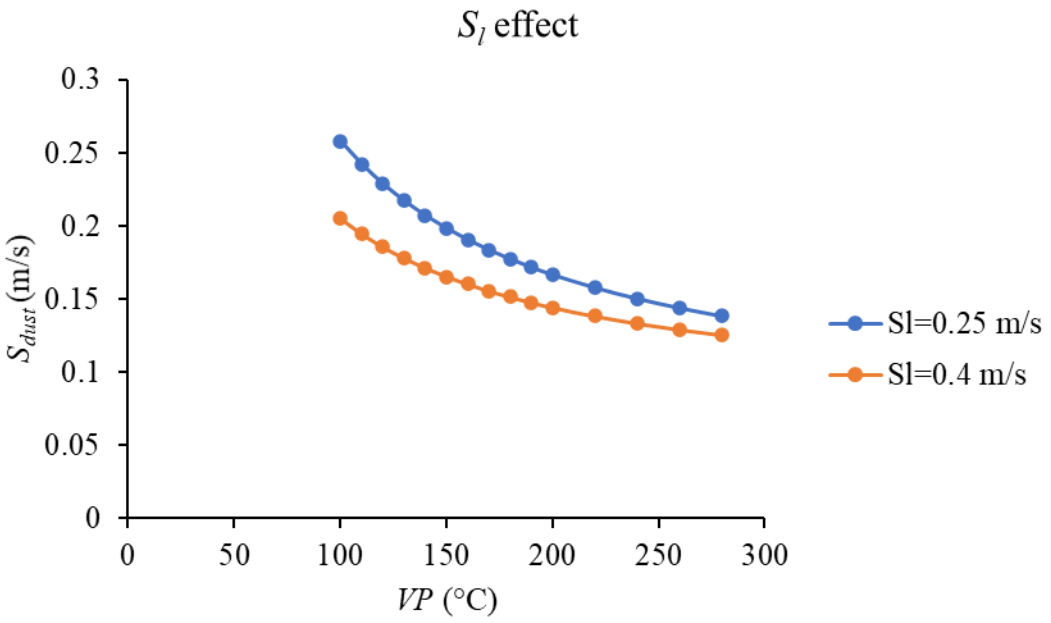

Figure IV.2 *S_{dust} profiles as functions of VP and parametric in S_l*

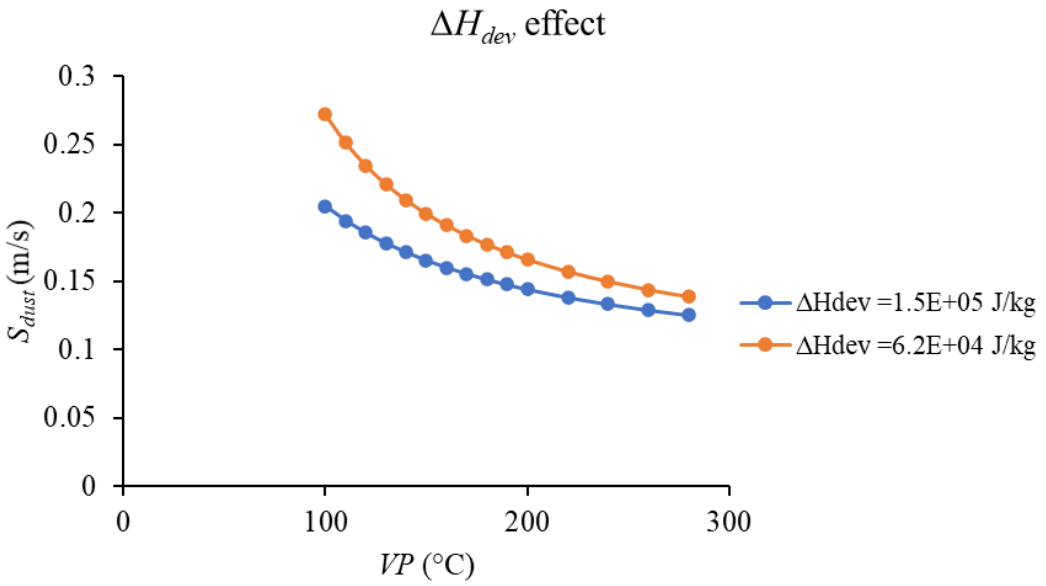

Figure IV.3 *S_{dust} profiles as functions of VP and parametric in ΔH_{dev}*

The theoretical model here reported may be expressed for hybrid mixtures. Bartknecht (1989) defines a dust/air mixture containing flammable gases or vapour in the combustible atmosphere as "hybrid mixture" or even "mixture of two-fold origin" [1].

In this case, the enthalpy balance becomes:

$$\lambda_{III}\frac{(T_{ad}-T_{ign})}{\delta_{III}} = \dot{m}(Cp_{dust}(VP-25)+\Delta H_{dev}) + \dot{m}_{dev}\,Cp_{gas,II}(T_{ign}-VP) + \dot{m}_{gas\_hyb}\,Cp_{gas\_hyb}(T_{ign,gas\_hyb}-25) \quad (42)$$

Where $\dot{m}_{gas\_hyb}$ (kg/s) is the mass rate of the flammable gas or vapour, Cp_{gas_hyb} (J/kg °C) is the specific heat of the flammable gas or vapour and $T_{ign,\,gas\_hyb}$ (°C) is the ignition temperature of the flammable gas or vapour.

Since the problem as described is fundamentally one-dimensional,

$$\dot{m}_{gas\_hyb} = \rho_{gas\_hyb} S_{l,gas\_hyb} A \quad (43)$$

Where ρ_{gas_hyb} (kg/m^3) is the density of the flammable gas or vapour and $S_{l,\,gas\_hyb}$ (m/s) is the laminar burning velocity of the flammable gas or vapour.

In this case S_{dust} can be expressed as

$$S_{dust} = \frac{-\rho_{gas\_hyb}S_{l,gas\_hyb}Cp_{gas\_hyb}(T_{ign,gas\,ibr}-25)-\rho_{dev}S_lCp_{gas,II}(T_{ign}-VP)+\lambda_{III}\frac{(T_{ad}-T_{ign})}{\delta_{III}}}{\rho_{dust}((Cp_{dust}(VP-25)+\Delta H_{dev}))} \quad (44)$$

Parameter values

To calculate the dust flame speed (S_{dust}), all the chemical/physical parameters of equation have to be estimated. These parameters as well as the measurement/calculation procedures are listed in **Table IV.1**.

Table IV.1 *Theoretical model parameters and procedures for their measurement and/or calculation*

Parameter	Procedure
ρ_{dust} and Cp_{dust}	Dust properties
VP	Measured according the procedure proposed by Sanchirico et al. (2018) [22]
ΔH_{dev}	DSC analysis (N_2 flow, 20 °C/min)
S_l	CHEMKIN calculation [134], once determined the composition of gases produced by devolatilization through TG/FTIR analysis and/or by literature data
T_{ad}	GASEQ calculation [135], once determined the composition of gases produced by devolatilization through TG/FTIR analysis and/or by literature data
T_{ign}	Weight average value computed according to the Le Chatelier rule, once determined the composition of gases produced by devolatilization through TG/FTIR analysis and/or by literature data
ρ_{dev} and $Cp_{gas,II}$	Weight average values of gas density and heat capacity in the II zone computed once determined the composition of gases produced by devolatilization through TG/FTIR analysis and/or by literature data
λ_{III} and δ_{III}	Weight average values of the burned gas thermal conductivity and the thickness of the reaction zone computed once determined the composition of gases produced by devolatilization through TG/FTIR analysis and/or by literature data

The theoretical model was applied by way of example on cornstarch and lycopodium. To determine the composition of gases produced by devolatilization for each dust, literature data were used for cornstarch. For lycopodium, literature data were not available and *TG/FTIR* analysis was carried out. All the details are reported in the following paragraphs.

Cornstarch

Mazurkiewicz et al. (1993) reported results of tests carried out by heating to different temperatures (300, 450, 550 °C) cornstarch dust, at stoichiometric concentration (233 g/m^3), in a cylindrical steel container located in an oven [68]. The composition of the product gases was analysed by means of a gas chromatograph after thermal decomposition of the dust. The cornstarch used consists of particles nearly spherical in shape with a mass mean diameter of 15 μm. The results of measurement of the gas composition showed that, at a temperature of 300 °C the reactions of decomposition of dust produces mainly CO_2 and a small amount of CO. At higher temperatures, the relation between CO and CO_2 becomes inverse, some methane and hydrogen occurring in addition. However, the authors highlight that, being the products of thermal decomposition dependent on the rate of temperature rise, the results of the measurements reported, which were

obtained under conditions of very slow heating of a sample, cannot be conclusive for processes going on under real conditions, in an atmosphere of chemically active flame. In our calculations, we tested the pyrolysis composition obtained by Mazurkiewicz et al. (1993) at 450 and 550 °C [68].

Lycopodium

In the case of lycopodium, the experiment for *VP* evaluation, typically carried out in the flash point apparatus, was replicated in the *TG/DSC* equipment in open cup conditions. 10 mg sample were heated up to *VP* (210 °C) (heating rate 20 °C/min) in airflow atmosphere and the produced gases were continuously analysed by means of an *FTIR* gas through *TGA/FTIR* interface linked by transfer line to TGA furnace. The cell and transfer line of the *TGA/FTIR* interface were heated and kept at 220 °C. In this way, product gases from samples degradation could not condense. Analysing the *FTIR* spectra at the maximum of the Gram-Schmidt diagram, butane can be considered as the main gaseous product at *VP*.

Dust flame speed calculation: cornstarch

Calculations were performed for both cornstarch dust and lycopodium dust.

All the properties values used for cornstarch are given in

Table IV.2 as well as the procedure involved for their calculations/measurements. As regards the parameters which values are variable (i.e., functions of dust concentration), their calculations were performed once set the composition of gases produced by literature data [68]. In particular, Mazurkiewicz et al. (1993) determined the thermal decomposition products of the cornstarch at two temperatures, 450 °C and 550 °C. Volatile matter was determined equal to 80%wt of the dried sample initial weight by measuring the weight loss when heated up to 1000 °C at 10 °C/min (N_2 flow) during a TG analysis. In **Table IV.3** and **Table IV.4** the composition of volatiles at varying the dust concentration in a closed vessel are reported for the composition at 450 °C and 550 °C, respectively. Moreover, all the calculated parameters as well as S_{dust} are listed in the above mentioned **Table IV.3** and **Table IV.4.** In **Figure IV.4**, the dust laminar burning velocity obtained by the theoretical model calculations are shown starting from the volatile compositions at 450 °C and 550 °C. Literature data ([51], [65]–[69]) obtained with different experimental rigs, granulometries and concentration are also reported (literature data were shown and discussed in **Figure II.9**). From the data shown in **Figure IV.4**, it appears that a very good agreement is obtained with the data provided by Krause and Kasch (1994) [47].

Table IV.2 *Theoretical model parameters, procedures and values for cornstarch*

Parameter	Value	Procedure
ρ_{dust} and Cp_{dust}	1500 kg/m^3 and 1970 J/kg °C	Dust properties [136]
VP	260 °C	Measured according the procedure proposed by Sanchirico et al. (2018) [22]
ΔH_{dev}	1.54E+05 J/kg	DSC analysis (N_2 flow, 20 °C/min)
S_l	Variable	CHEMKIN calculation [134], once determined the composition of gases produced by literature data [68]
T_{ad}	Variable	GASEQ calculation [135], once determined the composition of gases produced by literature data [68]
T_{ign}	Variable	Weight average value computed according to the Le Chatelier rule, once determined the composition of gases produced by literature data [68]
ρ_{dev} and $Cp_{gas,II}$	Variable	Weight average values of gas density and heat capacity in the II zone computed once determined the composition of gases produced by literature data [68]
λ_{III} and δ_{III}	Variable	Weight average values of the burned gas thermal conductivity and the thickness of the reaction zone computed once determined the composition of gases produced by literature data [68]

Table IV.3 *Volatiles produced by the pyrolysis of cornstarch, oxygen and nitrogen at varying the dust concentration at 450 °C. The stoichiometric oxygen amount as well as all the calculated parameters are also shown*

C (g/m^3)	H_2 (%)	O_2 (%)	N_2 (%)	CO (%)	CH_4 (%)	CO_2 (%)	$O_{2,stoich}$ (%)	ρ_{dev} (kg/m^3)	S_l (m/s)	$Cp_{gas,II}$ (J/kg °C)	T_{ign} (°C)	λ_{II} (W/m °C)	T_{ad} (°C)	S_{dust} (m/s)
400	0.17	16.84	63.36	8.46	3.62	7.55	11.55	1.30	0.17	0.256	586.5	0.0257	1844.4	0.15
500	0.20	16.05	60.37	10.08	4.31	8.99	13.76	1.31	0.25	0.259	586.5	0.0256	2050.5	0.17
550	0.23	15.33	57.66	11.55	4.94	10.30	15.76	1.31	0.29	0.260	586.5	0.0256	2112.6	0.176
600	0.26	14.67	55.17	12.89	5.51	11.50	17.60	1.31	0.32	0.261	586.5	0.0256	2142.2	0.179
650	0.29	14.06	52.89	14.12	6.04	12.60	19.28	1.31	0.327	0.262	586.5	0.0256	2135.3	0.178
700	0.31	13.50	50.79	15.26	6.52	13.61	20.83	1.31	0.323	0.263	586.5	0.0256	2094.5	0.174

Table IV.4 *Volatiles produced by the pyrolysis of cornstarch, oxygen and nitrogen at varying the dust concentration at 550 °C. The stoichiometric oxygen amount as well as all the calculated parameters are also shown*

C (g/m^3)	H_2 (%)	O_2 (%)	N_2 (%)	CO (%)	CH_4 (%)	CO_2 (%)	$O_{2,stoich}$ (%)	ρ_{dev} (kg/m^3)	S_l (m/s)	$Cp_{gas,II}$ (J/kg °C)	T_{ign} (°C)	λ_{II} (W/m °C)	T_{ad} (°C)	S_{dust} (m/s)
233	0.66	18.12	68.18	5.35	3.43	4.25	9.87	1.280	0.074	0.272	580	0.027	1630	0.127
250	0.70	17.95	67.51	5.68	3.65	4.52	10.48	1.279	0.106	0.274	580	0.027	1705	0.136
270	0.75	17.74	66.73	6.07	3.89	4.82	11.19	1.279	0.140	0.276	580	0.027	1789	0.147
300	0.82	17.44	65.60	6.63	4.25	5.27	12.22	1.278	0.190	0.279	580	0.027	1904	0.161
400	1.03	16.50	62.09	8.36	5.36	6.65	15.43	1.275	0.350	0.289	580	0.027	2162	0.194
428	1.09	16.26	61.17	8.81	5.66	7.01	16.26	1.275	0.367	0.291	580	0.027	2193	0.199
500	1.23	15.67	58.93	9.92	6.36	7.89	18.30	1.273	0.380	0.298	580	0.027	2179	0.198
550	1.31	15.28	57.47	10.64	6.83	8.46	19.63	1.272	0.340	0.302	580	0.028	2106	0.190
600	1.40	14.91	56.09	11.33	7.27	9.01	20.90	1.271	0.260	0.305	580	0.028	2015	0.179

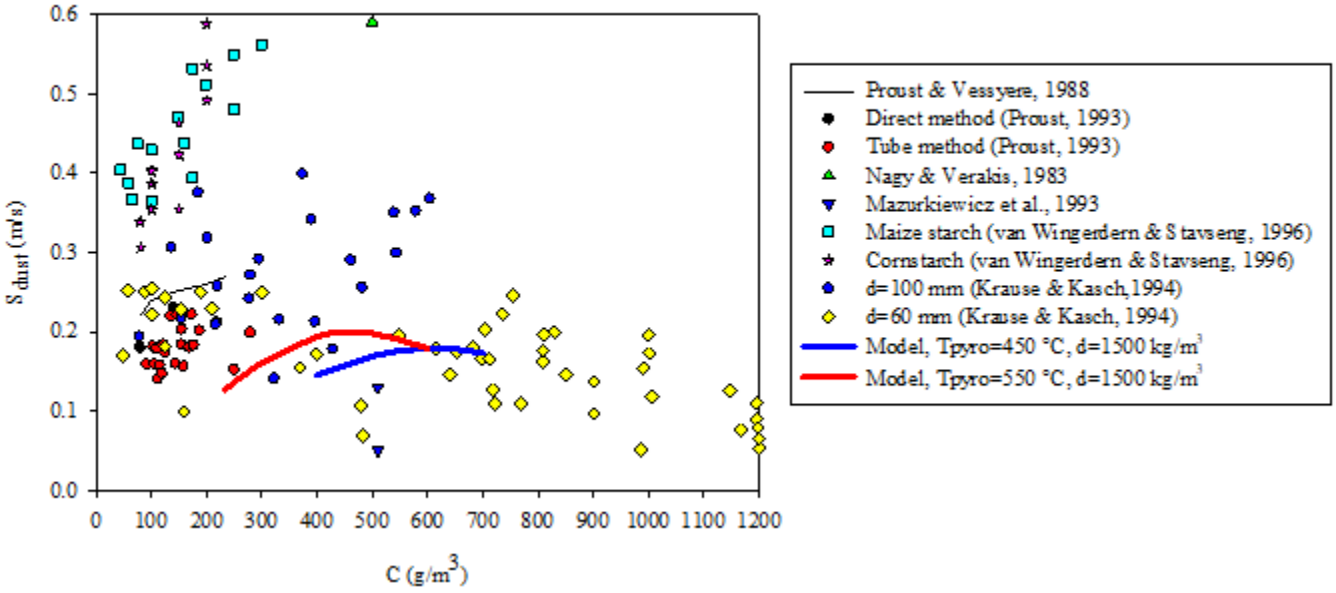

Figure IV.4 *S_{dust} as function of cornstarch concentration as computed at pyrolysis temperature: 450 °C and 550 °C. Literature data are also shown* ([51], [65]–[69])

Dust flame speed calculation: Lycopodium

All the properties values used are reported in **Table IV.5** as well as the procedure involved for their calculations/measurements.

As regards the parameters which values are variable (i.e., functions of dust concentration), their calculations were performed once determined the composition of gases produced by TG/FTIR analysis. [68]. Particularly, the thermal analysis shows that the main component of lycopodium decomposition is butane. Volatile matter was determined equal to 80%wt of the dried sample initial weight by measuring the weight loss when heated up to 1000 °C at 10 °C/min (N_2 flow) during a TG analysis.

In **Table IV.6** the compositions of volatiles at varying the dust concentration in a closed vessel are reported. Moreover, all the calculated parameters as well as S_{dust} are listed in **Table IV.6.** In **Figure IV.5**, the dust laminar burning velocity obtained by the theoretical model calculations are shown starting from the volatile compositions reported in **Table IV.6**. Literature data obtained with different experimental rigs, granulometries and concentration are also reported ([51], [65], [66], [69], [137]). Han et al. (2001) studied the flame propagation mechanisms in lycopodium dust clouds within a vertical duct of 1800 mm height with 150 mm × 150 mm square cross-section where the dust dispersion was realized though the elutriation above a fluidized bed for lycopodium-air (mean particle diameter 31 μm, concentration 30-100 g/m^3) [137]. Proust (2006)

assessed the lycopodium S_l (i.e., S_{dust}) within a 1.5 m long tube where the dust dispersion was realized though the elutriation above a fluidized bed for lycopodium-air (mean particle diameter 31 μm, concentration 30-100 g/m^3) through the tube and direct methods [50]. van Wingerden and Stavseng (1996) measured the laminar burning velocity of the lycopodium-air flame (mean particle diameter 30 μm, concentration 50-175 g/m^3) in an 1.6 m long vertical tube made of transparent polycarbonate where the dust was supplied continuously into the top of the tube from a horizontally vibrating sieve and a vibratory dust feeder [51]. The burning velocity in laminar flows was studied in a vertical cylindrical tube of 2 m in length and 300 mm in diameter where dust was layered on a porous filter plate and elutriated in a fluidized bed at the beginning of each experiment by Krause and Kasch (1994) (mean particle diameter 30 μm, concentration 100-600 g/m^3) [69]. From the experimental and model data shown in **Figure IV.5**, it appears that the model is quite in agreement for low concentrations, even if as in the case of cornstarch, there is a large scattering of the experimental data due to the different experimental conditions.

Table IV.5 *Theoretical model parameters, procedures and values for lycopodium*

Parameter	Value	Procedure
ρ_{dust} and Cp_{dust}	1000 kg/m^3 and 1004.8 J/kg °C	Dust properties [22]
VP	210 °C	Measured according the procedure proposed by Sanchirico et al. (2018) [22]
ΔH_{dev}	3.07E+05 J/kg	DSC analysis (N_2 flow, 20 °C/min)
S_l	Variable	CHEMKIN calculation [134], once determined the composition of gases produced by TG/FTIR analysis
T_{ad}	Variable	GASEQ calculation [135], once determined the composition of gases produced by TG/FTIR analysis
T_{ign}	Variable	Weight average value computed according to the Le Chatelier rule, once determined the composition of gases produced by TG/FTIR analysis
ρ_{dev} and $Cp_{gas,II}$	Variable	Weight average values of gas density and heat capacity in the II zone computed once determined the composition of gases produced by TG/FTIR analysis
λ_{III} and δ_{III}	Variable	Weight average values of the burned gas thermal conductivity and the thickness of the reaction zone computed once determined the composition of gases produced by TG/FTIR analysis

Table IV.6 *Volatiles produced by the pyrolysis of lycopodium, oxygen and nitrogen at varying the dust concentration. The stoichiometric oxygen amount as well as all the calculated parameters are also shown*

C (g/m^3)	C_4H_{10} (%)	O_2 (%)	N_2 (%)	$O_{2,stoich}$ (%)	ρ_{dev} (kg/m^3)	S_l (m/s)	$Cp_{gas,II}$ (J/kg °C)	T_{ign} (°C)	λ_{II} (W/m °C)	T_{ad} (°C)	S_{dust} (m/s)
40	1.65	20.65	77.69	10.75	1.30	0.10	0.246	405	0.026	1327	0.20
50	2.06	20.57	77.37	13.38	1.31	0.17	0.246	405	0.026	1427	0.22
90	3.65	20.23	76.12	23.70	1.32	0.36	0.249	405	0.025	1827	0.31
100	4.03	20.15	75.81	26.23	1.32	0.31	0.250	405	0.025	1727	0.28
150	5.93	19.75	74.31	38.56	1.34	0.07	0.253	405	0.025	1427	0.22
200	7.76	19.37	72.87	50.42	1.36	0.05	0.256	405	0.025	1127	0.15
250	9.51	19.00	71.49	61.82	1.37	0.04	0.259	405	0.024	927	0.11

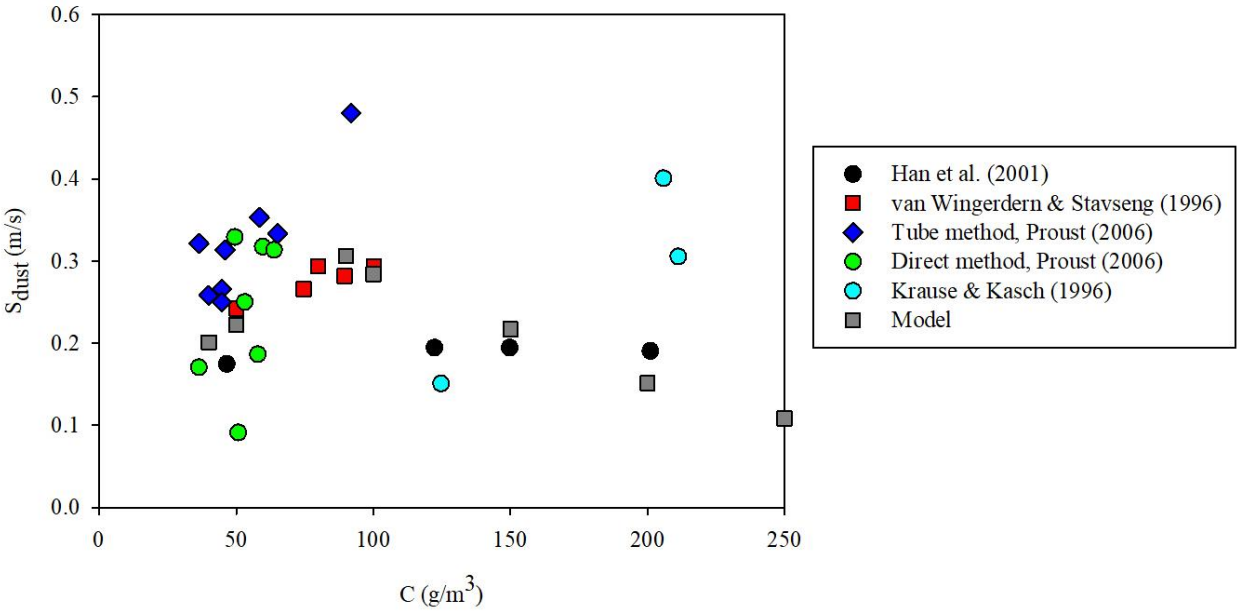

Figure IV.5 *S_{dust} as function of lycopodium concentration as computed at pyrolysis temperature: 450 °C and 550 °C. Literature data are also shown* ([51], [65]–[69])

IV.1.3. Final remarks

In this section, the preliminary results of the application of a Mallard-Le Chatelier-inspired theoretical flame propagation model were shown. It is worth noting that the way the flame propagates (represented by the laminar burning velocity S_{dust}) depends on several parameters that

take into account the thermal behavior of the dust subjected to heating starting from the flame front to the colder layers. As a consequence, a thermal screening of any combustible dust seems to be of crucial importance in order to fully understand the explosive behavior both in terms of intrinsic (laminar) burning velocity but also in terms of flammability/explosibility parameters. Moreover, the analysis of the thermal behavior of combustible dusts can be useful to explain a series of synergistic effects that arise in dust mixtures that can sometimes be more dangerous than pure dusts, as found by Sanchirico et al. (2018) [22].

IV.2. Synergistic behavior of flammable dust mixtures: A novel classification

In this section, the flammable/explosive behaviour coupled to the thermal analysis of dust mixtures is investigated to evaluate the behaviour of the mixture with respect to the behaviour of the single dust. Minimum ignition temperature, minimum ignition energy, maximum pressure and deflagration index were measured at varying the relative content of dusts in the mixtures. For the same mixtures, the thermal analysis was carried out by means of *DSC* analysis coupled to chemical analysis performed by *HPLC* and *ATR-FTIR*. In each analysed mixture, a synergistic behaviour was found: at some concentrations, the mixture flammability/explosion features may be much more severe than that of the pure dusts. The analyses unveil that, depending on the mixture, the synergistic behaviours can occur due to physical and/or chemical reactions. Based on the obtained results, a new classification of dusts mixtures in three mixtures safety classes (*MSC*) was proposed.

IV.2.1. Methodologies

In this work, the flammable and explosive behavior of dust mixtures was investigated by measuring *MIT*, *MIE*, P_{max} and K_{St} of binary mixtures, at changing relative amount of the dusts. Notably, due to the amount of tested samples was set at 10 g that is close to the stoichiometric value for the dusts, the explosion pressure and the deflagration index were considered as the maximum explosion pressure and the maximum deflagration index. All the mixtures were also analyzed by *DSC* and subsequent chemical analysis by *HPLC* and *ATR-FTIR* in order to unveil the physical and chemical transformations, as well as formation of intermediate chemical compounds underlying the flammable/explosive behavior of each dust mixture. We characterized the behavior of glucose, niacin, L-ascorbic acid, anthraquinone, irganox 1222 and their mixtures.
For characterization, scanning electron microscopy (*SEM*) (Philips mod. XL30) was used and the images were acquired using different magnifications. A laser diffraction granulometer (Malvern Instruments Mastersizer, 2000) was used to measure the granulometric distribution of dusts. The approach used to conduct the experimental campaign is divided into three parts.
Flammable and explosive behaviours of pure dusts and mixtures were characterized first. Minimum ignition temperature (*MIT*) and minimum ignition energy (*MIE*) were determined using standard testing procedures ([9], [16], [18]). As regards maximum pressure (P_{max}) and deflagration index (K_{st}), all the tests were performed at fixed dust concentration (500 g/m^3) with two 100 J igniters. A thermal screening by means of differential scanning calorimetric analysis (*DSC*) of pure dusts and mixtures was then performed. The analyzed mixtures were

25%comp(A)/75%comp(B), 50%comp(A)/50%comp(B), 75%comp(A)/25%comp(B) by weight. Finally, in order to assess the occurrence of any chemical interaction between the dusts, *HPLC* and *ATR-FTIR* analyses were performed.

IV.2.2. Results

In **Figure IV.6**, the *SEM* images are shown for all the dusts investigated at different magnifications. From *SEM* images of niacin and anthraquinone show that the samples are composed of smooth-faced prismatic particles. *SEM* images of L-ascorbic acid show that particles have a quietly spherical shape and high tendency to agglomeration. *SEM* images of irganox 1222 show non-spherical particles that tends to a soft agglomeration. *SEM* images of glucose show quite spherical particles surrounded with others finest particles, maybe of rice starch.

As it is well known [12], the granulometric distributions strongly affects the explosion behaviour. Details of the percentile diameters (*D(0.1)*, *D(0.5)* and *D(0.9)*) of dusts are given in **Table IV.7**. Polydispersity (σ_D), an important parameter to influence explosion characteristics, is defined as shown in Equation (45) and given in **Table IV.7**.

$$\sigma_D = \frac{D(0.9) - D(0.1)}{D(0.5)} \tag{45}$$

Ascorbic acid is the most heterogeneous in particle size while niacin presents the highest homogeneity.

Table IV.7 *Percentile diameters and MIE, MIT, P_{max} and K_{St} of pure dusts* [138]

Dusts	**Percentile diameters (μm)**			**σ_D**	**MIE (mJ)**	**MIT (°C)**	**K_{St} (bar m/s)**	**P_{max} (bar)**	**St class**
	D(0.1)	D(0.5)	D(0.9)						
Niacin	33.9	55.3	87.0	0.96	1.4	600	262	7.5	2
Anthraquinone	7.4	19.2	47.2	2.1	1.4	670	364	10.6	3
Ascorbic Acid	6.2	19.2	47.5	2.2	14	460	74	6.2	1
Irganox 1222	10.2	34.0	69.4	1.7	130	460	212	7.2	2
Glucose	6.6	12.2	23.9	1.4	82	400	4	2.8	1

In **Table IV.7** the values of *MIE*, *MIT*, P_{max} and K_{St} measured for each dust are shown. Niacin and anthraquinone have low values of the minimum ignition energy (1.4 mJ), almost comparable to that of some gases (i.e., the minimum ignition energy of methane is equal to 1.3 mJ). Glucose and

irganox 1222 have very high values, 82 and 130 mJ, respectively. As shown in **Table IV.7**, irganox has a high particles diameter which significantly affects the surface area available for the ignition. Compared to niacin, that shows the highest particles size, irganox appears to have a greater tendency to generate agglomerates, that strongly affect the dispersibility in a dust cloud and consequently the minimum ignition energy. It can be seen glucose owns the lowest *MIT* among all the analyzed powders, with a value of 400°C. Contrarily, anthraquinone presents the highest *MIT* value, equal to 670°C. Both the flammability and explosion parameters are strongly dependent on the physical/chemical transformations the dust undergoes to during heating. The flame propagation can be divided in three phases: dust heating up to the volatile point (*VP*), melting/boiling/sublimation and/or pyrolysis and volatiles combustion. In order to identify these steps, we performed *DSC* measurements for each dust.

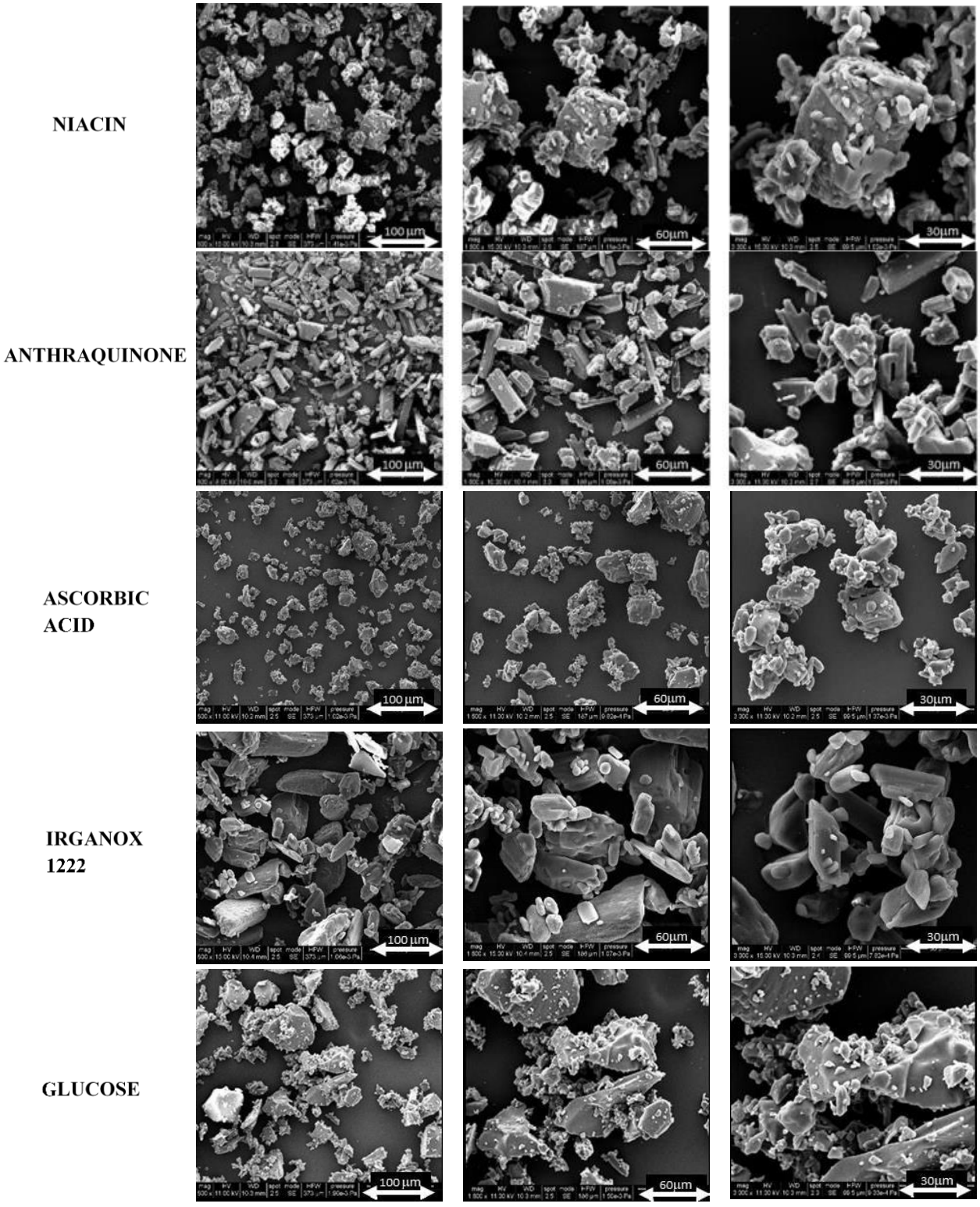

Figure IV.6 *SEM images of all dusts investigated at 800× (left), 1600x (centre) and 3000× (right) magnification* [138]

In **Figure IV.7**, the *DSC* profiles are shown for all investigated dusts. The curve a in **Figure IV.7** represents the *DSC* trend of niacin. Two peaks are found. The former represents the niacin melting (onset temperature ~233 °C, fusion heat ~200 J/g). The latter (onset temperature ~ 303 °C, reaction heat ~-160 J/g) can be addressed to the partial thermal decomposition of niacin. In **Figure IV.7 (b)**, the *DSC* profile of anthraquinone is shown. One endothermic peak is found at 290 °C which is well known as the melting temperature [139]. On increasing temperature, up to 400 °C, the sample does not show any transformation. Devolatilization phenomena occurs at higher temperature [140]. **Figure IV.7 (c)** shows the *DSC* curve for ascorbic acid. Two main peaks are found: one endothermic peak at 190 °C, related to the melting process, in agreement with literature data [141], and an exothermic peak at higher temperature (~ 250 °C) related to an oxidative decomposition process, as found in the literature. The main decomposition process occurs in three stages. In the first stage, decarboxylation and dehydration are the main decomposition reactions, in the second, further decarboxylation and decarbonylation occur. At the third stage (only a slow carbonization process takes place. The decomposition of ascorbic acid produces a series of furan derivatives, in which the main product is furfural [142]. In **Figure IV.7 (d)**, the *DSC* result as obtained for the irganox 1222 sample is shown. In this case, two endothermic peaks are found: 125 °C and 368 °C. The first peak may be addressed to the sample melting while the second peak is a boiling event. The predicted boiling temperature of irganox 1222 is estimated of about 417.0±33.0 °C at 760 mmHg [143]. Literature data showed that the main product of irganox 1222 decomposition is 3,5-di-tert-butyl-4-hydroxybenzaldehyde [144] at higher temperature (700 °C). *DSC* curve of glucose (**Figure IV.7 (e)**) shows the presence of two main peaks: the former endothermic peak (190 °C) is related to melting while the latter exothermic peak (270 °C) to the occurrence of an oxidative decomposition process.

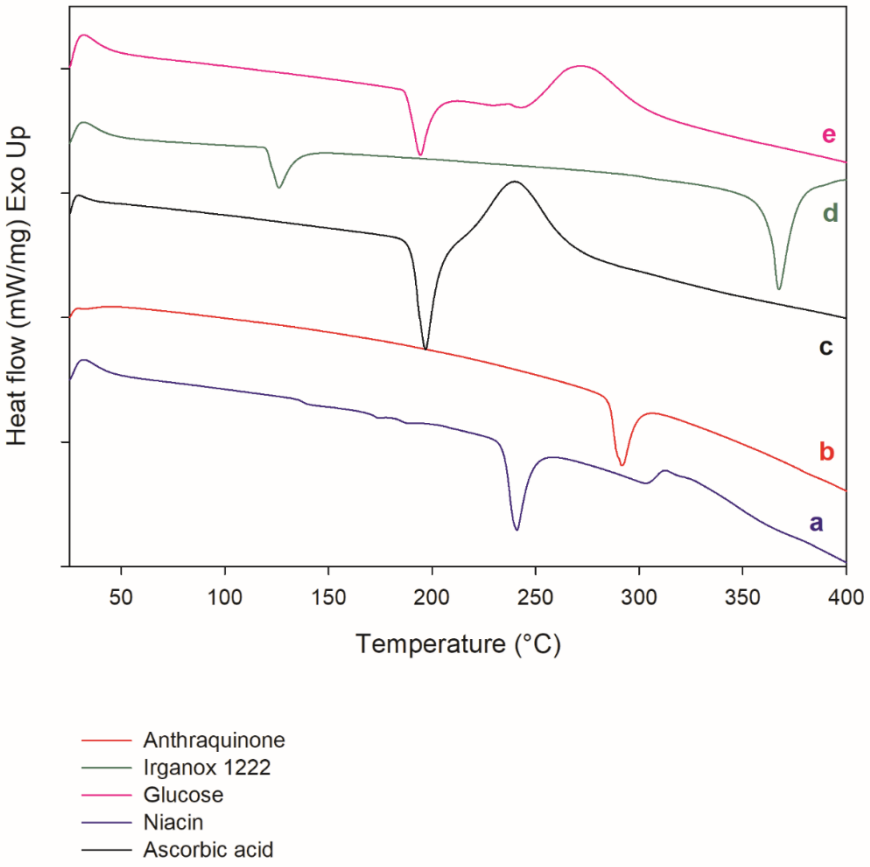

Figure IV.7 *DSC curves for all investigated pure dusts* [138]

Table IV.8 reports the peaks temperatures for each investigated sample. On the basis of thermal evolution behaviour, driven from thermograms we can divide the dusts into two classes:

a. Class A: dusts which undergo physical transformation (melting/boiling);
b. Class B: dusts which undergo physical transformation overlapped to a thermal decomposition.

According to our results, we classified the samples analysed as shown in **Table IV.8**. The combustion reaction path of the dusts differs depending on the class, as shown in **Figure IV.8**.

Table IV.8 *Peak temperature and nature* [138]

Dust	1st peak *(endothermic)*	2nd peak *endothermic*	2nd peak *exothermic*	Class
Niacin	233	-	303	B
Anthraquinone	290	-	-	A
Ascorbic Acid	190	-	250	B
Irganox	125	368	-	A
Glucose	190	-	270	B

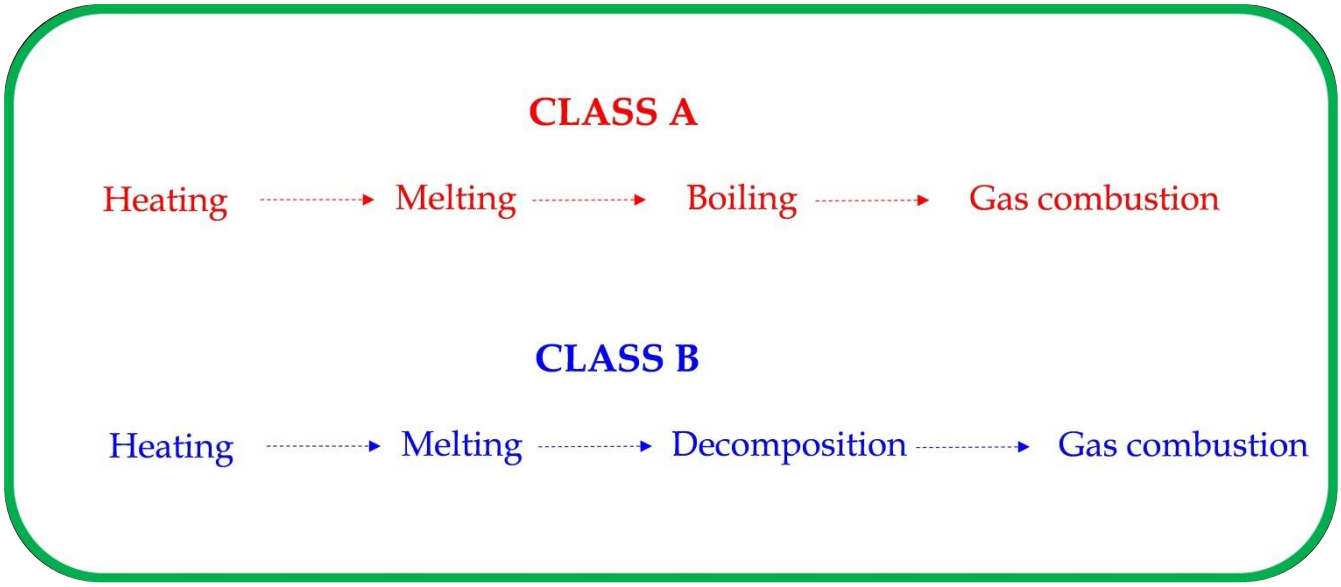

Figure IV.8 *Reaction path of dusts* [138]

In the following, the results of the measurements of the flammability and explosion parameters of binary dust mixtures are discussed. For all parameters, the weight average value is also computed according to the Le Chatelier rule (i.e., Equation (46) for *MIE*):

$$MIE_{mix} = \frac{1}{\left(\frac{x_A}{MIE_A} + \frac{1-x_A}{MIE_B}\right)} \tag{46}$$

where x_A is the mass fraction of component (A), MIE_A is the minimum ignition energy of component A and MIE_B is the minimum ignition energy of component B in the mixture. **Table IV.9** shows the list of investigated mixtures.

Table IV.9 *Investigated mixtures* [138]

Mixtures
niacin/anthraquinone
ascorbic acid/glucose
ascorbic acid/irganox 1222
ascorbic acid/niacin

MIE values of the niacin/anthraquinone mixture are shown in **Figure IV.9 (a)**. At all values of the mixture composition, the *MIE* value is constant (1.4 mJ) and equal to the values of the pure dusts. The only exception is shown by the 50 % mixture, but the difference is very small (1.6 mJ). In **Figure IV.9 (b)**, the *MIE* values of the ascorbic acid and glucose are shown. In this case, the *MIE*

values are between those of the pure ones and the trend is well predicted by the Le Chatelier equation. In the case of the ascorbic acid/irganox 1222 mixtures (**Figure IV.9 (c)**), a different behaviour is observed. In particular, *MIE* values are always higher (and consequently safer) than those predicted by the Le Chatelier equation. A complex non-linear behaviour is observed. The strong deviation from the Le Chatelier curve could be addressed to the different chemical structure of the pure dusts. For this reason, the energy supplied to the system is not sufficient to trigger ascorbic acid because it is largely absorbed by the heavier irganox. Given the same amount of sample, a greater energy amount than previously analyzed mixture (ascorbic acid-glucose) must be absorbed by ascorbic acid-irganox mixture to make the same temperature jump. Therefore, the higher the irganox fraction, the higher the energy supplied to get ignition. In the case of the ascorbic acid/niacin mixtures (**Figure IV.9 (d)**), *MIE* values are always higher (and consequently safer) than those predicted by the Le Chatelier equation. The addition of even a small amount of ascorbic acid increases *MIE* value (about 7mJ) compared to that of pure niacin (1.4 mJ) while 25 % of niacin does not affect ascorbic acid *MIE* value. This suggests that ascorbic acid is the substance among these pure dusts that controls *MIE* trend.

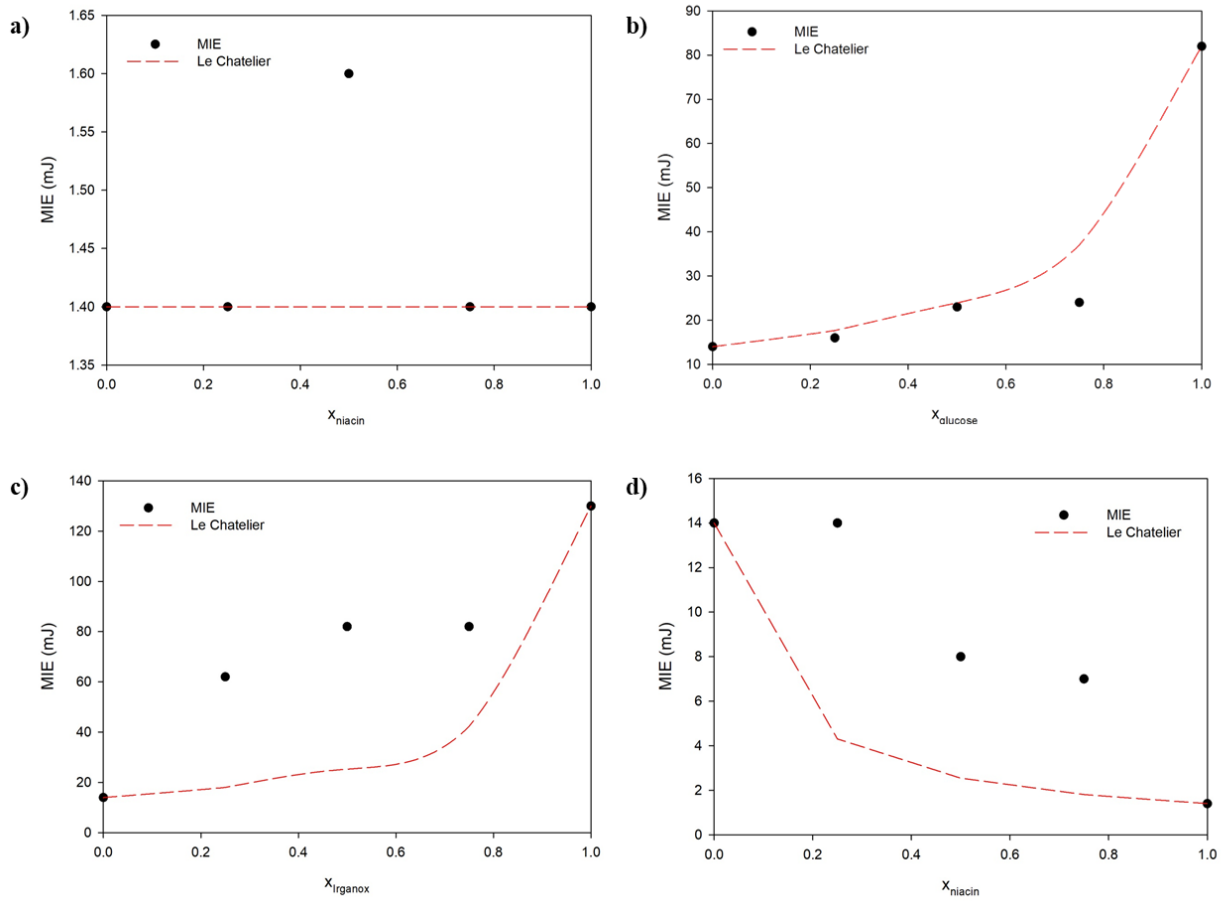

Figure IV.9 *MIE of niacin-anthraquinone (a), ascorbic acid-glucose (b), ascorbic acid-irganox 1222 (c) and ascorbic acid-niacin (d) mixtures* [138]

In **Figure IV.10 (a)**, the *MIT* values of the niacin/anthraquinone mixture are plotted. It is found that at all concentrations, the *MIT* values are dominated by the niacin *MIT* values. This result suggests that in the presence of niacin, the auto-ignition of the mixture is controlled by niacin reaction. Actually, at all investigated concentrations, the *MIT* value of the mixture is higher or equal to that of pure niacin. It is also worth noting that the *MIT* values are always lower (and more dangerous) than the value predicted by the Le Chatelier Rule. In the case of the glucose/ascorbic acid mixture (**Figure IV.10 (b)**), the *MIT* values are higher than the values predicted by the Le Chatelier equation. In this case, mixtures show a safer behavior that that expected from the Le Chatelier curve. In **Figure IV.10 (c)**, the *MIT* values are plotted as measured for ascorbic acid-irganox 1222 mixtures. *MIT* of the pure samples are the same and they are equal to 460 °C. Surprisingly, the *MIT* values of the mixtures are lower than 460 °C, at all the concentrations investigated. This result suggests that a chemical and/or physical interaction between the two

samples is established, generating a more severe behavior. Therefore, if safe measures are designed by taking into account the *MIT* values of the pure sample and ascorbic acid and irganox 1222 come into contact, the probability of generating random explosion is extremely high due to a higher temperature than the safe upper limit for the hot surfaces. In **Figure IV.10 (d)**, the *MIT* values of the niacin/ascorbic acid mixtures are plotted. It is also worth noting that the *MIT* values are always lower (and more dangerous) than the value predicted by the Le Chatelier Rule. Actually, at all investigated concentrations, the *MIT* value of the mixtures is higher or equal to that of pure ascorbic acid.

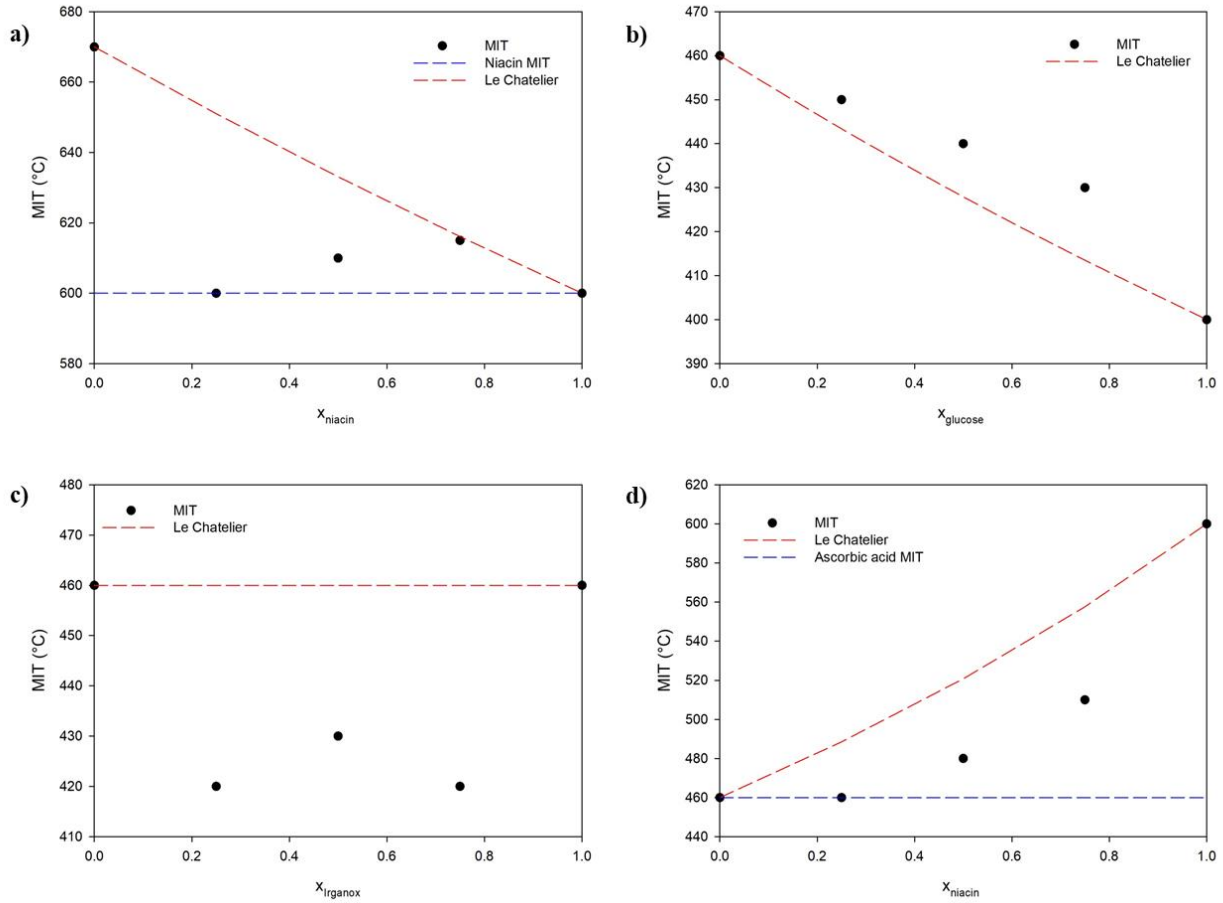

Figure IV.10 *MIT of niacin-anthraquinone (a), ascorbic acid-glucose (b), ascorbic acid-irganox 1222 (c) and ascorbic acid-niacin (d) mixtures* [138]

Explosion tests were performed to evaluate the maximum pressure (P_{max}) and the deflagration index (K_{St}). The evaluation of these parameters in the Siwek sphere for niacin/anthraquinone mixtures have not been carried out due to the difficulties encountered in cleaning the sphere

following a test involving anthraquinone. In **Figure IV.11 (I)**, the P_{max} (a) and K_{St} (b) are plotted versus the glucose amount in the ascorbic acid-glucose mixtures. At all dust mixtures compositions ($x_{glucose}$), the deflagration index is lower than the values of the K_{St} of the pure ascorbic acid dust, except at $x_{glucose}$ = 0.5 where the deflagration index is equal to the value of pure ascorbic acid. It is worth noting that the explosion phenomenon is controlled by ascorbic acid explosion since the K_{St} values are very similar to that of pure ascorbic acid, even at high glucose concentration ($x_{glucose}$ = 0.8). In all cases, the K_{St} is always higher that the values predicted by Le Chatelier equation (LC). In **Figure IV.11 (II)**, the explosion parameters are shown as obtained for the mixtures irganox-ascorbic acid at total dust concentration equal to 500 g/m^3. On increasing the irganox concentration, both maximum pressure and deflagration index overcome the pure values, suggesting that some physical and/or chemical reactions are playing a role. In the case of the niacin/ascorbic acid mixture, a significant increase of the explosion parameters compared to the pure dusts values is found (**Figure IV.11 (III)**).

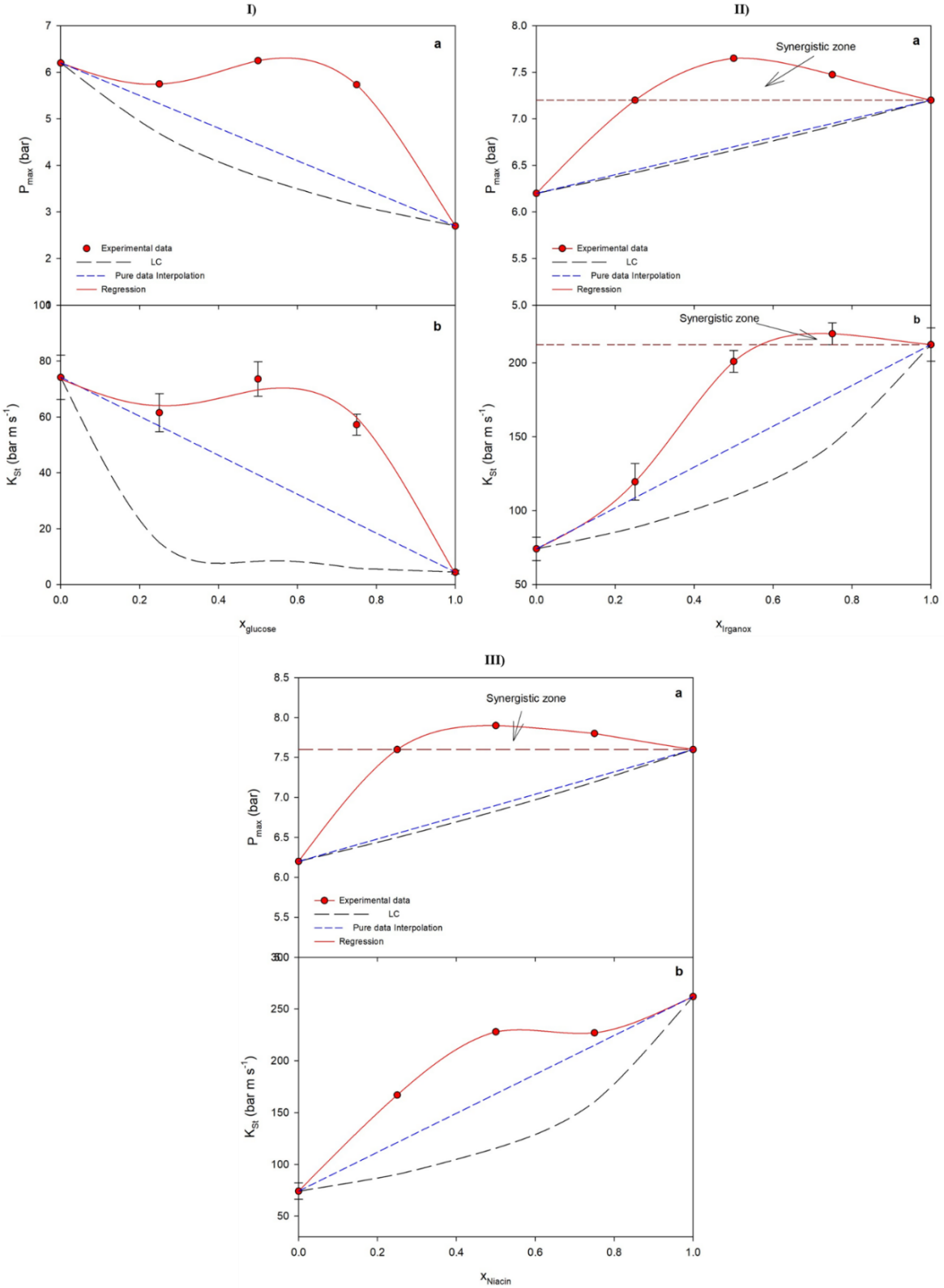

Figure IV.11 *P_{max} (a) and K_{St} (b) as function of mixture composition. C_{dust} = 500 g/m^3, ascorbic acid-glucose (I), ascorbic acid-irganox (II) and ascorbic acid-niacin (III)* [138]

In the following the *DSC* analysis results are discussed as obtained for niacin/anthraquinone, ascorbic acid/glucose, ascorbic acid/irganox 1222 and niacin/ascorbic acid mixtures.

As regards niacin and anthraquinone mixtures, it is worth noting that a synergistic behaviour within niacin/anthraquinone mixtures was already found in a previous work [22]. Precisely, it was assessed the mixture niacin/anthraquinone (25/75) had a significantly lower *VP* (170 °C) than pure niacin (198.5 °C) and pure anthraquinone (194.8 °C) [22]. **Figure IV.12** shows the *DSC* curves obtained for niacin/anthraquinone 25%/75% mixture. The first peak can be ascribed to the niacin phase transition and it shifts towards lower temperatures when adding anthraquinone. Similarly, the second *DSC* peak, correspondent to anthraquinone phase change, shifts to lower temperatures, when adding niacin. We may then conclude that the mixtures present a lower transition point than pure dusts.

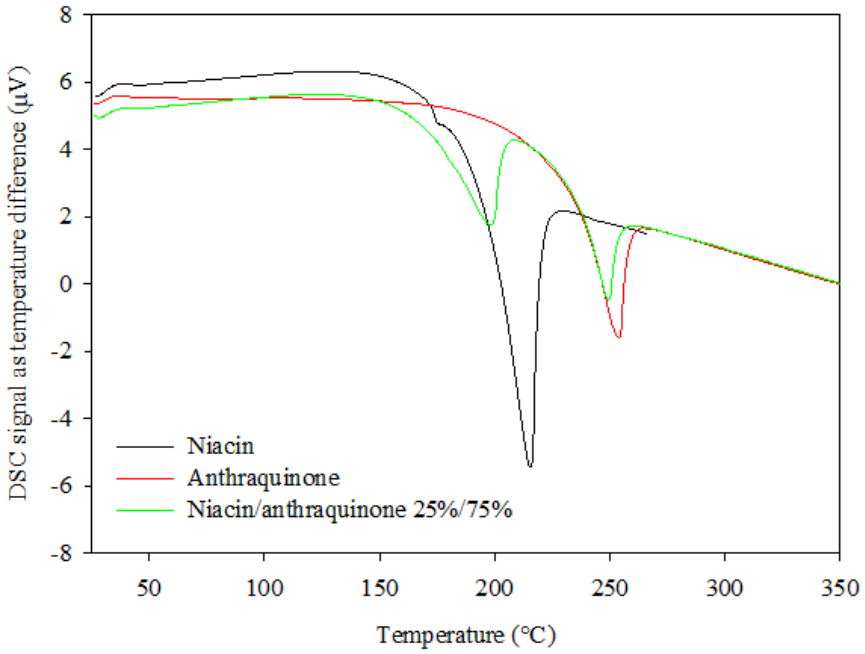

Figure IV.12 *DSC curves of niacin, anthraquinone and their mixture at 25% niacin/75% anthraquinone* [145]

To better understand the nature of the transformations resulting in thermal effects and weight loss during *DSC* analysis, *FTIR* spectroscopy was carried out on solid samples before (**Figure IV.13**) and after the thermal treatment (**Figure IV.14**) in *DSC* apparatus up to the first *DSC* peak, to check any presence of chemical species due to the decomposition of niacin and/or anthraquinone. **Figure IV.14** shows that niacin is no longer present in the sample since the *FTIR* spectrum of treated samples, completely matches with that of pure anthraquinone. This result allows addressing the

first weight loss and *DSC* peak to physical phenomena, exclusively involving niacin, that undergoes to melting-evaporation or sublimation in that temperature range. Furthermore, it is worth noting that, in the presence of anthraquinone, the niacin phase transformation occurs at a lower temperature than pure niacin.

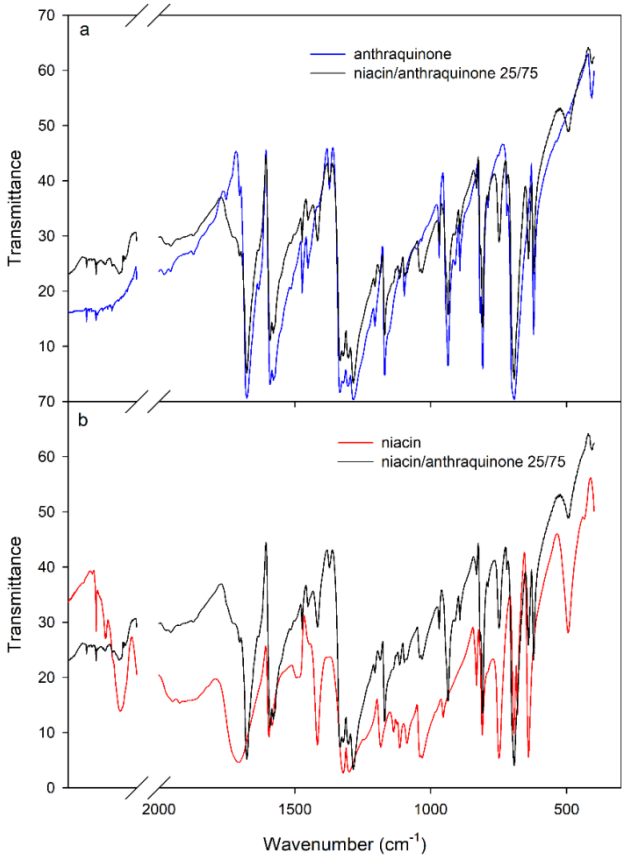

Figure IV.13 *FTIR spectra of the niacin-anthraquinone mixture (25/75) in comparison with pure anthraquinone (a) and pure niacin (b)* [145]

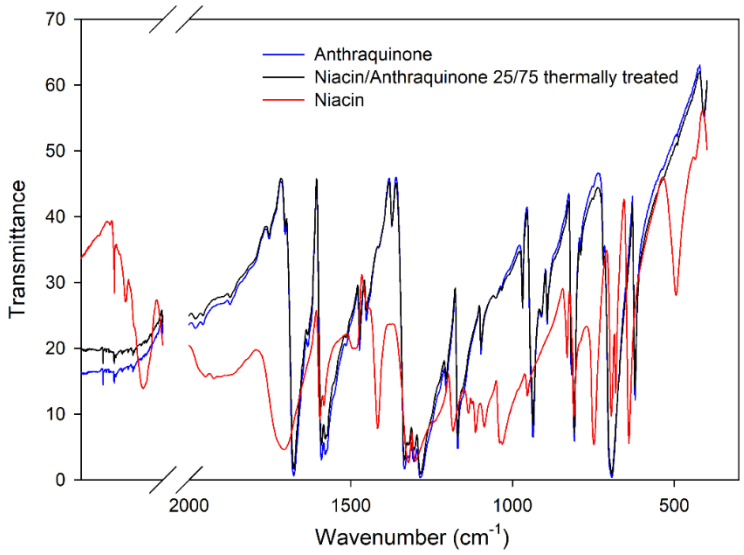

Figure IV.14 *FTIR spectra of the thermal-treated mixture anthraquinone/niacin 75/25* [145]

This analysis, performed for different compositions and also in closed cup apparatus, revealed the presence of a eutectic point which leads to a significant reduction of the melting point and/or of the sublimation/boiling point. **Figure IV.15** shows temperature-concentration phase diagram of the niacin/anthraquinone mixture built from *DSC* data. The presence of a eutectic point justifies lower temperatures at which vapors are formed both by sublimation and by melting/boiling for the investigated solid mixtures. As a result, their *VPs* are lower than the ones recorded for the pure compounds. Moreover, this phenomenon has the flammability parameters markedly deviated from the Le Chatelier curve (**Figure IV.10 (a)**). Due to, during the thermal treatment, niacin abandoned the system at a temperature lower than that of pure niacin, niacin was responsible of the production of volatiles at low temperature and, obviously, *MIE* of mixtures is equal to that of niacin (**Figure IV.9 (a)**) [145].

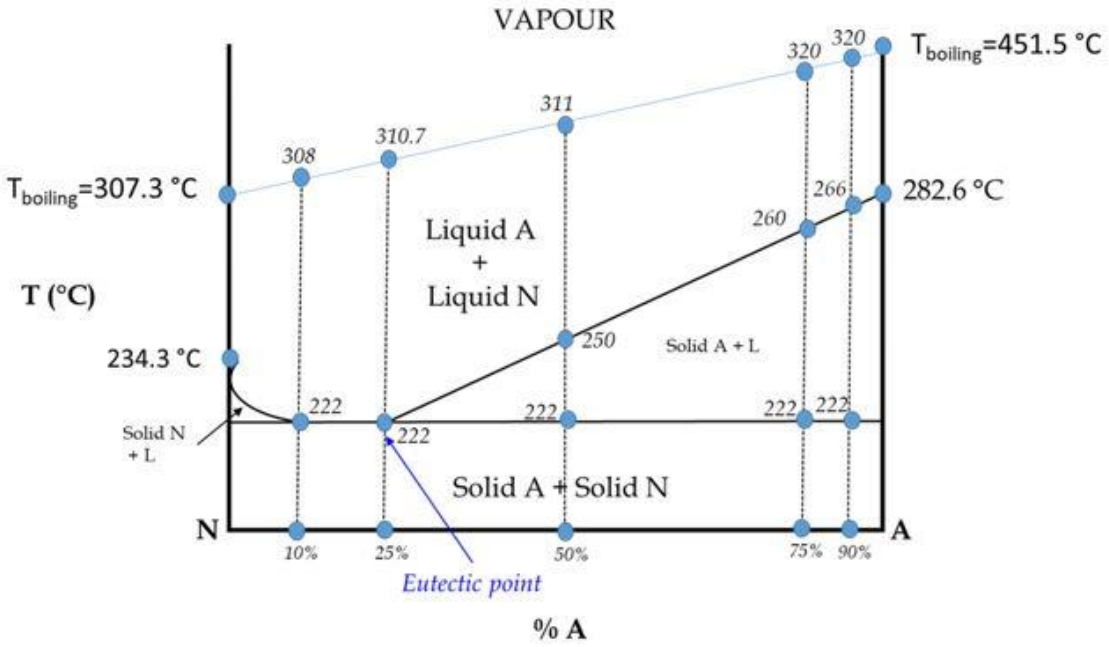

Figure IV.15 *State diagram of niacin/anthraquinone mixtures* [145]

Figure IV.16 (a) shows the DSC curves obtained for ascorbic acid/glucose mixtures, at changing the mixture composition. Ascorbic acid and glucose have the same melting temperature. Two main zones are found: the former is related to endothermic phenomena, while the latter to an exothermic process. In the endothermic zone, three peaks are superimposed in the same low temperature range: the first peak is always found at about 155 °C, which is lower than the fusion temperature of pure dusts (190 °C). It is reasonable to assume that even in this mixture a eutectic point may be present at about 155°C for a mixture containing 25% of ascorbic acid, thus a physical interaction between pure dusts occurs. After the endothermic zone, whatever the content of glucose, a marked decrease is observed for oxidative decomposition peaks, suggesting a decrease of its amount in the condensed phase. Therefore, the occurrence of a eutectic point and an endothermic reaction in the same temperature range has to be taken into account. Actually, the formation of furan (volatiles) from sugars, ascorbic acid, and organic acids as affected by thermal treatments was deeply investigated ([146], [147]). To assess the presence of a chemical reaction within the endothermic zone, a sample of ascorbic/glucose mixture at 50 % of glucose was treated up to 190 °C (end of endothermic zone) and rapidly quenched. The solid residue was tested through infrared analysis (ATR-FTIR) (**Figure IV.16 (b)**). After thermal treatment, the spectrum is different from the initial one. The spectrum of the treated mixture appears more smoothed and intense than the pure mixture. Notably, bands in the range 3000-3500 cm^{-1} and 1000-1500 cm^{-1} grow more intense and smoother,

as typical of oligosaccharide moieties. These features suggest glucose polymerization occurred during thermal treatment [148]. As a further support, recovered solid residue appeared in molten form, amber in colour with a consistency similar to caramel. The IR spectra and the aspect of the treated sample show the occurrence of a chemical process within the endothermic zone. Thus, the deviation from the theoretical behaviour is caused by physical and, more deeply, by chemical reaction within the endothermic zone.

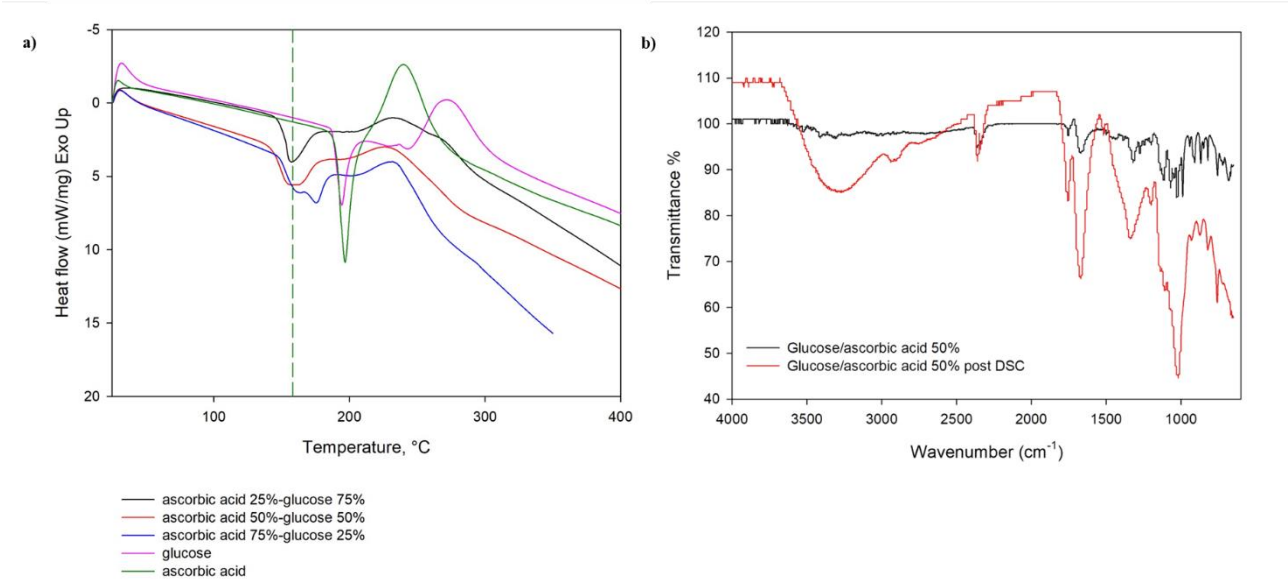

Figure IV.16 *DSC curves, ascorbic acid/glucose, all mixtures (a) and ATR spectra of 50 % glucose/ascorbic acid mixture before and after the thermal treatment (b)* [138]

In **Figure IV.17** the DSC curves obtained for the ascorbic acid and niacin mixture are shown, at changing the mixture composition. With only 25% of vitamin C, the DSC profile is completely mutated when compared to that of pure niacin. It can be seen the appearance of three different endothermic peaks that are at temperatures slightly lower than that of ascorbic acid endothermic peak. The first endothermic peak can be associated to the occurrence of a eutectic. Immediately after the third endothermic peak, an exothermic one appears, anticipating the exothermic phenomenon of pure vitamin C. In this exothermic zone, pure dusts react: increasing ascorbic acid concentration, the second peak of niacin disappears due to its total consumption. By increasing the content of ascorbic acid, the peak intensities increase, and the exothermic peaks are incorporated in a single peak.

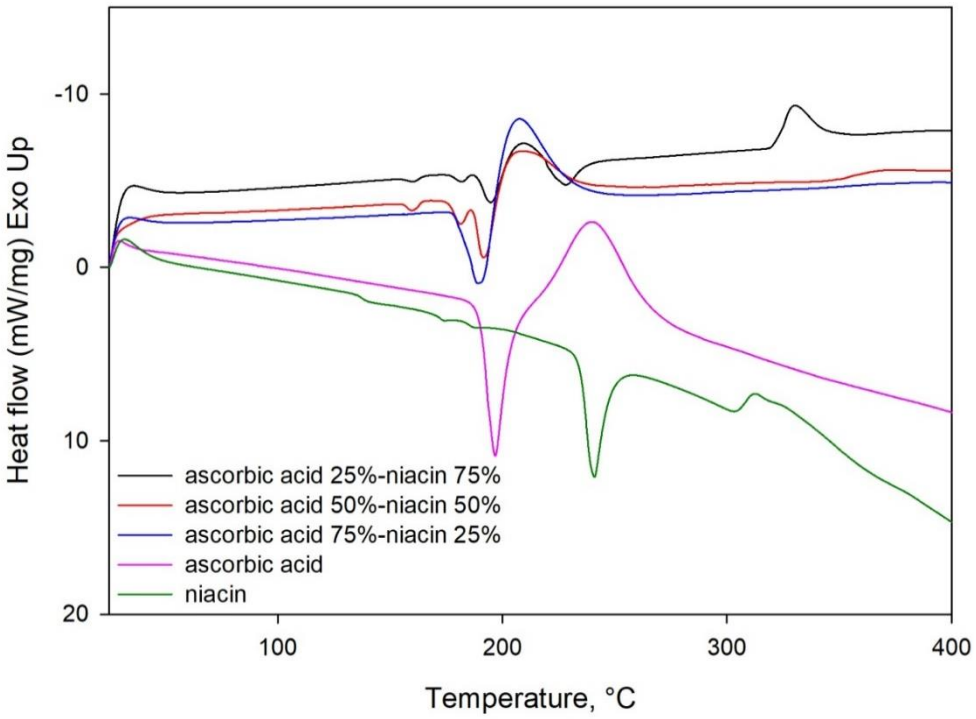

Figure IV.17 *DSC curves, ascorbic acid/niacin, all mixtures* [138]

To assess the occurrence of chemical reaction within the endothermic zone of DSC curve, a sample containing the 50% of niacin wat treated up to 190 °C and then rapidly quenched. The solid residue was then analyzed through HPLC analysis. The characteristic retention times are respectively 1.70 min (ascorbic acid), 2.20 min (niacin) and 1.53 min (ascorbic acid impurity). Comparing the HPLC spectra, no difference can be seen between the mixture before and after the thermal treatment. Thus, no chemical reaction occurs within the endothermic zone (**Figure IV.18 (a)**). Surprisingly, by analysing a sample treated up to 190 °C and kept at this temperature for 5 minutes, a change can be observed (**Figure IV.18 (b)**). In this new spectra, ascorbic acid characteristic peak disappears (1.70 min), leaving the niacin peak unchanged. The liquid solution, created by the fusion of niacin and ascorbic acid, favoured the decomposition of ascorbic acid into volatiles at lower temperature than ascorbic acid alone.

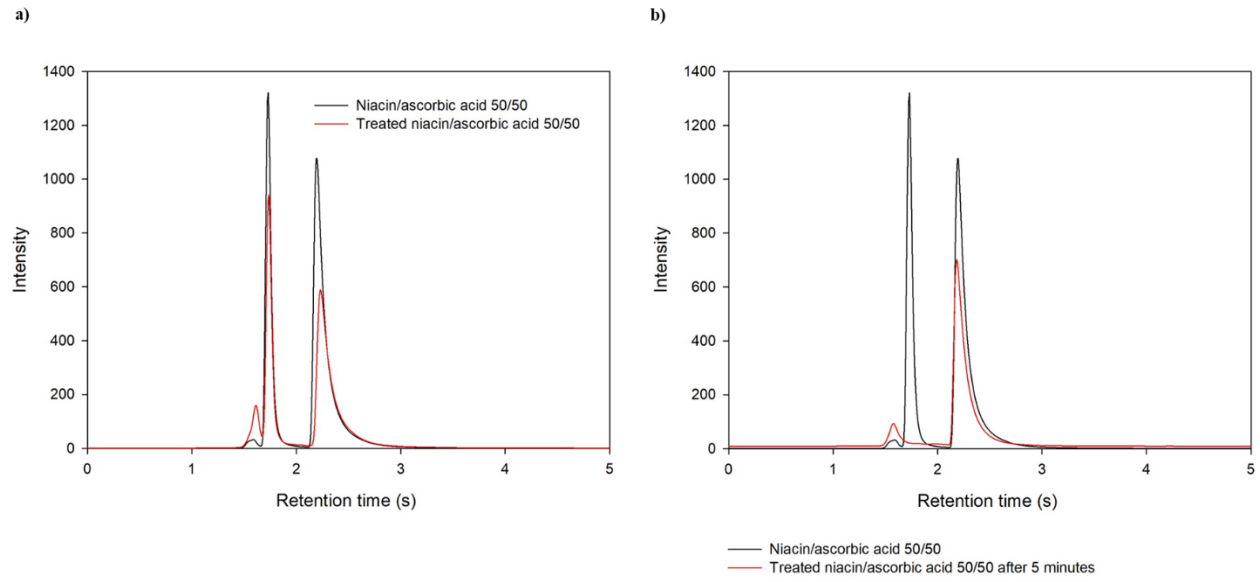

Figure IV.18 *Retention times profile for 50% niacin/ascorbic acid mixture, before and after the thermal treatment (a) and retention times profile for 50% niacin/ascorbic acid mixture, before and after the heating up to 190 °C and isotherm for 5 minutes (b)* [138]

Figure IV.19 shows the *DSC* curves of ascorbic acid/irganox mixtures. Four phenomena may be highlighted: three endothermic ones and one exothermic peak. The first endothermic peak, related to irganox melting, has a soft anticipation. In each of the three intermediate analyzed mixtures, the temperature is lower than that of irganox of about 6-7 °C for freezing-point depression. On the contrary, the second endothermic peak, caused by the ascorbic acid melting, does not show any incisive change in peak temperature. Instead, considering the exothermic peak, related to ascorbic acid decomposition, it is possible to notice how, as the irganox concentration increases, the peaks positions tend to shift to higher temperatures and the peak intensity decreases. This peak appears to be associated principally to the content of irganox, modifying the characteristic temperature of the following endothermic peak. This peak tends more and more to anticipate towards lower temperatures by decreasing irganox 1222 content. The difference between the temperature of the irganox boiling peak and the last endothermic peak of mixtures is of about 70 °C. This anticipation could be caused by a process that occurs within the exothermic peak. This probably corresponds to ascorbic acid decomposition. Furthermore, the shape change of exothermic peak, suggests that irganox 1222 also undergoes to chemical transformation, generating products with different boiling temperature. Actually, the formation of polymorphs of antioxidants, such as irganox 1076, when subjected to thermal treatments, has been studied [149].

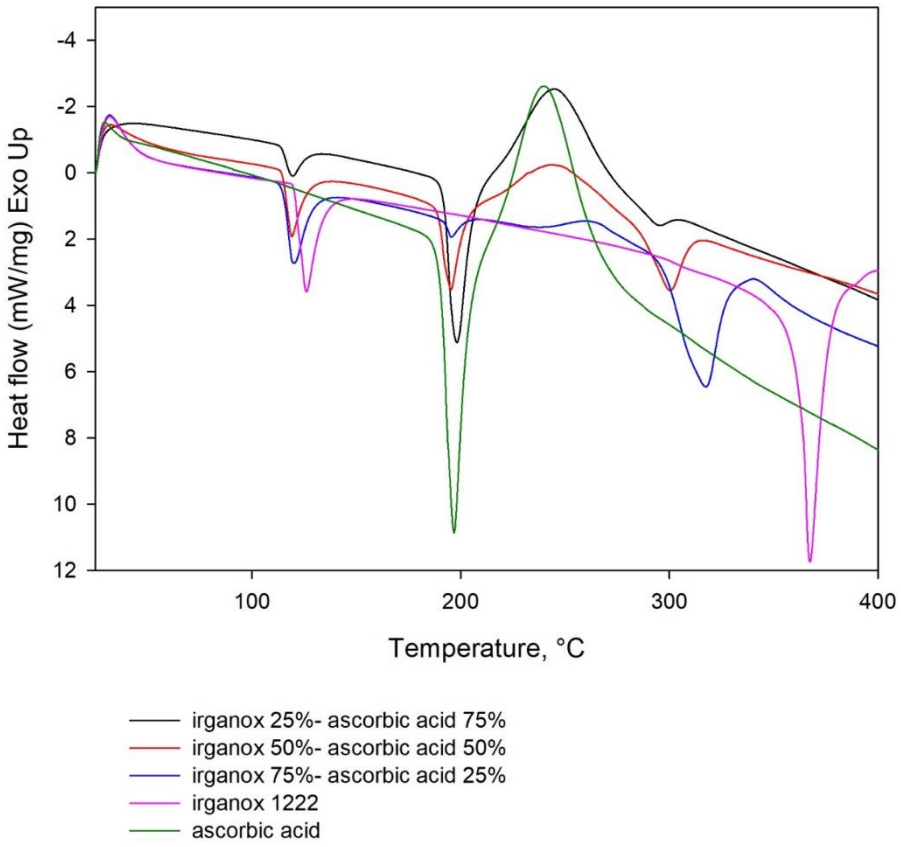

Figure IV.19 *Ascorbic acid-irganox 1222 mixtures DSC curves* [138]

In order to assess the occurrence of chemical processes, *HPLC* analyses were performed on ascorbic acid-irganox 1222 samples. First of all, the mixture containing 50% irganox before the thermal treatment was analyzed (**Figure IV.20**). The characteristic retention times are respectively 1.70 min (ascorbic acid), 2.23 min (irganox) and 1.53 min (ascorbic acid impurities). Then the dust samples were first subjected to thermal treatment with *DSC*, heated up to the exothermic peak temperature and then rapidly quenched to room temperature with a rate of 50°C/min. The obtained product was dissolved in acetonitrile (ACN) and analyzed with HPLC using 100% ACN flow as eluent. **Figure IV.21** shows the retention time profile for a mixture containing 25% of irganox and the mixture before the thermal treatment as reference. The retention time of the individuated substances are respectively: 1.531 min, 1.767 min, 2.229 min, 2.364 min, 3.164 min, 3.692 min. Different peaks appear compared to the reference, suggesting the occurrence of a chemical process with formation of new moieties. The signals of the mixtures at 50% and 75% of irganox have different intensities and retention times compared to the precedent profiles, suggesting the presence of different species (not reported). Unfortunately, it was not possible to determine the

nature of the detected substances due to lack of reference spectra. Hypothesizing a probable chemical reaction mechanism between the two constituents is very difficult. Similitudes among the detected spectra and those of Irgafos 168 [150] and butylated hydroxyanisole [151] were found. Both substances are antioxidants and could be produced through decomposition of Irganox 1222, protonation of the ascorbic acid and subsequent condensation of the decomposition products.

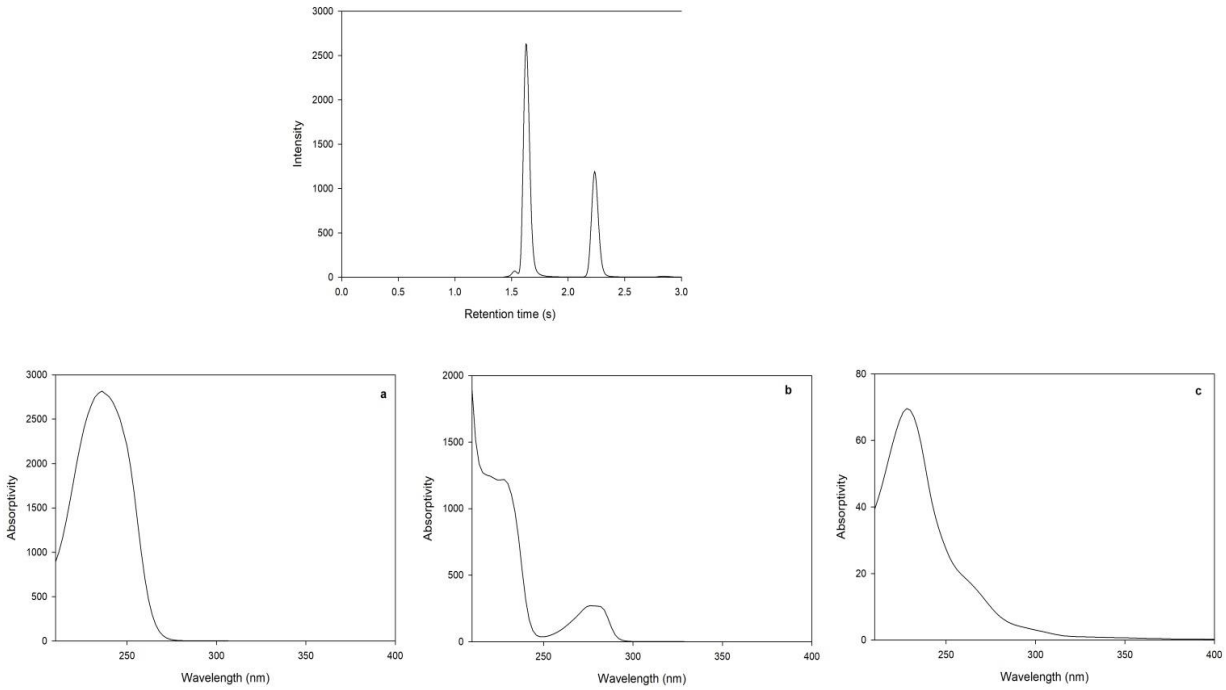

Figure IV.20 *Ascorbic acid (a), irganox 1222 (b) and ascorbic acid impurity (c) reference UV-spectra and retention time profile* [138]

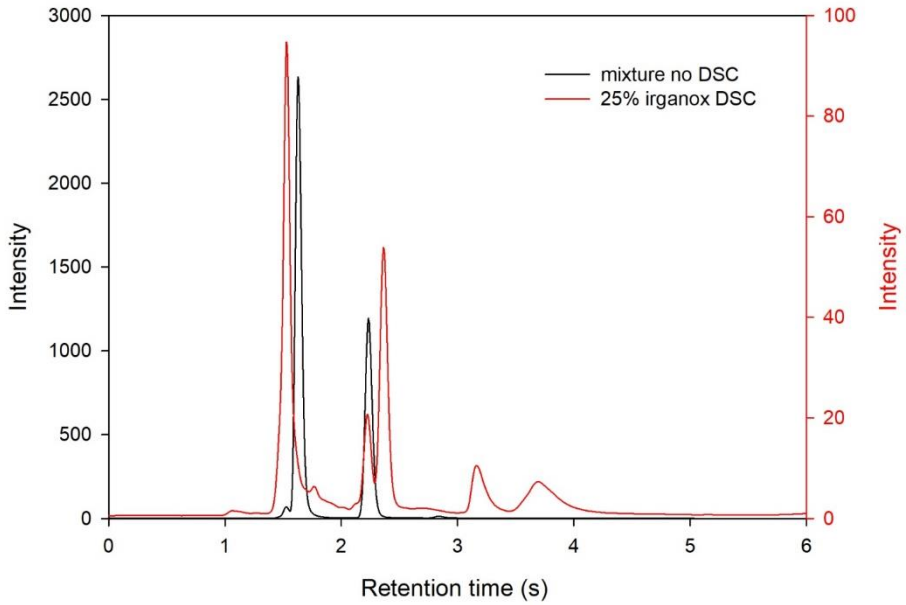

Figure IV.21 *Retention times profile for 25% irganox mixture before and after the thermal treatment* [138]

Different behaviours were found for each mixture and safety parameter. Each investigated mixture shows at least a slight synergistic effect between the pure dusts the mixture is composed of, resulting in a deviation from the theoretical Le Chatelier Law trend. Niacin/anthraquinone and ascorbic acid/glucose mixtures exhibited slight synergistic behaviors of different nature. For niacin/anthraquinone mixtures, the physical synergistic effect lowers MITs values compared to that predicted by Le Chatelier Law. In the case of ascorbic acid/glucose mixtures, the physical-chemical synergistic behavior deviates both P_{max} and K_{St} from ideality (Le Chatelier Law), with the highest deviation at 50 % of glucose, where P_{max} and K_{St} are equal to that of the most dangerous pure dust (ascorbic acid). Ascorbic acid/irganox 1222 and ascorbic acid/niacin mixtures shown strong synergistic behaviors that generated more severe conditions than in the case of pure dusts. Based on the obtained results, we identified three mixtures safety classes (*MSC*):

1) no chemical-physical interaction, ideal behavior of the dusts, in agreement with Le Chatelier law (*MSC* 0);
2) physical-chemical interactions that affect the safety parameters of the mixture. However, the safety parameters belong to the variation range of that of pure dusts (*MSC* 1);
3) physical-chemical interactions that affect the safety parameters of the mixture (*MSC* 2).

In the case of behavior 2) the mixture exhibits a slight synergistic behavior leading to a deviation from the flammable/explosion parameters compared to that predicted by Le Chatelier Law. However, since those parameters values are equal or lower than those of the most dangerous pure dust, *MSC* 1 mixtures do not require stronger safety measures than that for the pure dusts.

In the case of behavior 3) the mixture exhibits a strong synergistic behavior eventually leading to a shift of the flammable/explosion parameters to more severe conditions than the pure dusts.
On this basis, we classified the dust mixtures studied in this work (**Table IV.10**).

Table IV.10 *Classification of the investigated mixtures* [138]

Component	Class
niacin-anthraquinone	*MSC 1*
ascorbic acid-glucose	*MSC 1*
ascorbic acid-irganox 1222	*MSC 2*
ascorbic acid-niacin	*MSC 2*

IV.2.3. Final remarks

Measurements of the flammable and explosion parameters of mixtures of flammable dusts show that these parameters are not always the combination of the pure values and then it is not possible to predict *a priori* the behaviour of the parameters of flammability and explosibility of the mixture. Indeed, significant physical–chemical interactions may arise among the powders, leading to unexpected and sometimes worse behaviours than those of pure compounds. From the thermal analysis results, we may conclude that the physical interactions may be related to the formation of a eutectic point which reduces the temperature with respect to the pure dust at which melting and then boiling occur. Thermal analysis results combined with chemico-physical characterization also show the possibility of chemical reactions that lead to the formation of volatiles, which contribute to the explosion phenomenon. On this basis, we propose a classification of mixture of dusts in three mixtures safety classes (*MSC* 0; *MSC* 1; *MSC* 2). From these results, it may be concluded that in order to characterize the dust as well as mixtures flammability and explosion behaviour, a complete thermal scanning is advisable.

IV.2.4. Published articles

Results discussed in this section have been published in peer-reviewed scientific journals ([138], [145]):

- M. Portarapillo, G. Luciani, R. Sanchirico, and A. Di Benedetto, "Ignition mechanism of flammable dust and dust mixtures: An insight through thermogravimetric/differential scanning calorimetry analysis," *AIChE J.*, vol. 66, no. 8, 2020.
- L. Centrella, M. Portarapillo*, G. Luciani, R. Sanchirico, and A. Di Benedetto, "Synergistic behavior of flammable dust mixtures: A novel classification," *J. Hazard.*

Mater., vol. 397, no. January, p. 122784, 2020.

IV.3. Chemico-physical and thermal analysis of non-traditional dusts

The same approach presented in the previous section was applied to non-traditional dusts. In particular, different nylon fibres were tested in order to highlight the essential chemical-physical differences capable of modifying flame propagation and explosive behavior. Moreover, a grape pomace sample was analyzed to understand the role of lignocellulosic components and sample aging on flammability and explosibility.

IV.3.1. Methodologies

Nylon fibres

Five nylon 6.6 samples with different properties summarised in **Table IV.11** were investigated. Usually, nylon 6.6 fibres are covered by a thin layer of surfactant for production reasons. Consequently, they are sticky and do not disperse easily in the air. To remove the sticky layer, fibres are coloured and activated through a wet process. Moreover, the activation process alters the fibre surface and makes the fibres easily to suspend [75].

Table IV.11 *Properties and labels of nylon 6.6 samples*

Sample	**Linear density (Dtex)** [82]	**Activation**	**Colour**	**Label**
Nylon 6.6	1.9	Yes	Blue	1
Nylon 6.6	3.3	Yes	No	2
Nylon 6.6	6.7	No	Dark blue	3
Nylon 6.6	6.7	Yes	Brown	4
Nylon 6.6	0.9	No	Dark blue	5

To confirm the chemical nature of the substances, an *FTIR* solid (KBr grade), disk 1%, resolution 4 cm^{-1}, range 4000-400 cm^{-1} was carried out with Nicolet 5700 *FTIR*. *SEM* analysis was carried out through Philips mod. XL30 at magnifications from 100x to 6000x. From these images, the shape of the dust was identified. In addition, ImageJ was used to estimate particle sizes by means of a statistical analysis. To determine both the crystallographic structure and the degree of crystallinity, *XRD* analysis was carried out through *XRD* diffractometer PANalytical X'Pert Pro using Cu Kα radiation (1.5406 Å). The range of variability of 2θ is [5°; 79.99°] with a step size of 0.013° and a scan step time of 8.67 s. *BET* theory aims to explain the physical adsorption of gas molecules on a solid surface and serves as the basis for an important analysis technique for the measurement of the specific surface area of materials. During this analysis, the density of the material can also be evaluated. To evaluate thermal properties and characteristic temperatures of

the samples and explain the trend of minimum ignition energy, thermogravimetric analyses were carried out with *TGA/DSC* TA instrument Q600SDT. 5 mg sample were loaded into an alumina pan and were tested up to 1000 °C (heating rate 10 °C/min) in both inert (N_2) and oxidative (air) atmosphere (flow rate 100 mL/min). From *TGA*, the proximate analysis determined the moisture content (*M*), volatile matter (*VM*), ash (*A*) and the calculation of fixed carbon (*FC*) in the analysis of samples tested in N_2 atmosphere [129]. To analyse gases product from samples degradation, an *FTIR* gas was carried out through *TGA/FTIR* interface linked by transfer line to *TGA* furnace. The cell and transfer line of the *TGA/FTIR* interface were heated and kept at 220 °C. In this way, product gases from samples degradation could not condense. The output of this analysis is a Gram-Schmidt diagram. The device MIKE3 was used to estimate minimum ignition energy of dust samples [152]. In this work, the standard delay time was used (120 ms). Each sample was submitted to a maximum of ten ignition attempts at different concentrations and delivered energy.

Vinery waste

The sample analyzed in this work is a grape pomace coming from the waste stream of a wine distillery in Northern Italy. The sample is characterised by a heterogeneous morphology (**Figure IV.22**), mainly composed of aggregates, ligneous fibres, and fine particles. The size distribution is reported in **Table IV.12**. The heterogeneity in shapes could play an essential role in the explosive behavior of the sample: it is affected by handling and processing of the original material mixture, which behaves differently due to the different components "resistance" to mechanical operations (grinding/crushing/milling etc.). The components of the original sample (grape skins, seeds and other residues) generate particles with different shapes and with likely different sensitivity to ignition due to their chemical nature, as already observed for olive pomace in [153]).

Table IV.12 *PSD through laser granulometry and mechanical sieving (*[154], [155]*)*

Particle size distribution			
Laser granulometry [µm]		**Sieving granulometry (% wt.)**	
D_{10}	69.57	x>2000 um	0.04
D_{50}	302.852	2000 um<x<1000 um	3.66
D_{90}	633.752	1000 um<x<500 um	25.0
		x<500 um	71.3

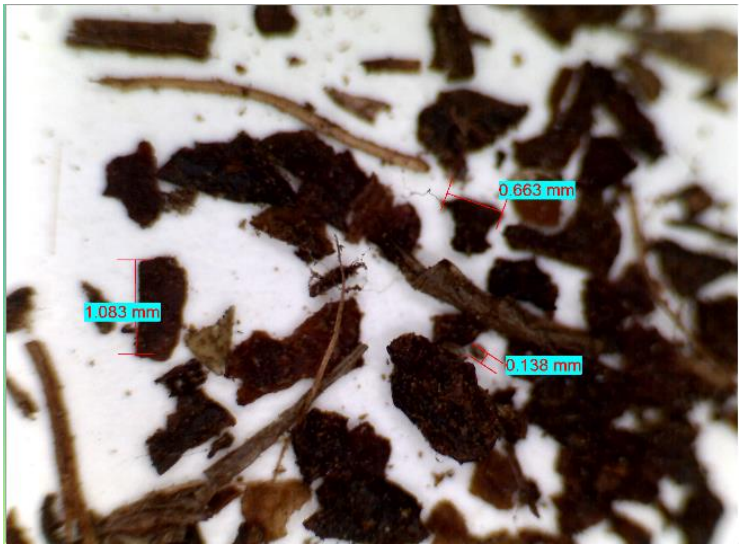

Figure IV.22 *Sample morphology through optical microscopy* ([154], [155])

FTIR was also performed to get early information on the sample chemical composition and nature. The spectrum was compared to those of the main biomass elements: lignin, cellulose, hemicellulose.

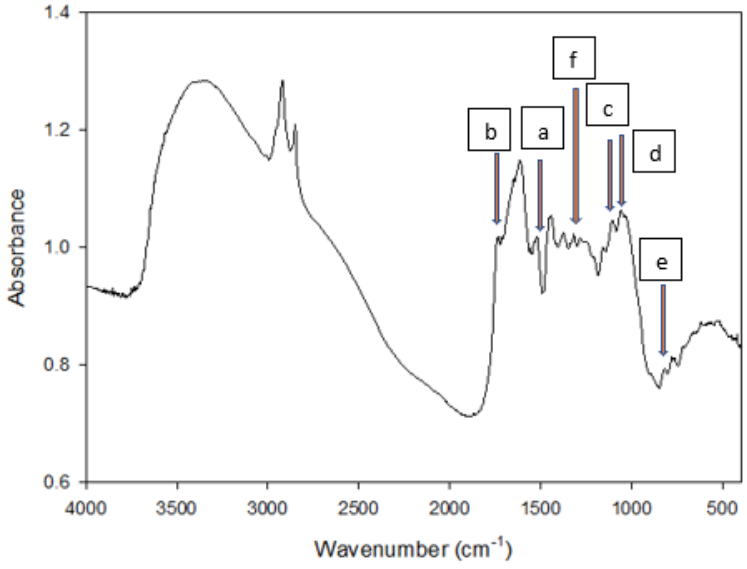

Figure IV.23 *FTIR spectra of the sample* ([154], [155])

From the spectra, it is recognisable: a) the Lignin associated C=C stretching (1510 cm^{-1}), b) the Hemicellulose associated C=O stretching (1740 cm^{-1}), c), d), e) the C-O stretching and C-H deformation associated to cellulose (1161,1120,890 cm^{-1} respectively), f) the symmetric C-H bending associated to cellulose and polysaccharides (1420 cm^{-1}). Similar considerations were

reported by Bekiaris et al. (2020) in their work on biomass substrates identification [156]. Moreover, the typical lignin fingerprint (1000-2000 cm^{-1}) is observed [157]. As expected, due to the freshness of the residue, the main lignocellulosic components seems to be lignin. **Table IV.13** reports the tests performed and the main outputs and considerations based on them. *TGA/DSC* TA Instrument Q600SDT was used to perform *TGA/DSC* and proximate analysis, following the ASTM D7582-15 [129], while as for *TGA/DSC* in an oxidative atmosphere, the sample was heated up to 1000 °C (heating rate: 10 °C/min) under airflow (100 mL/min).

Table IV.13 *Analytical methods used in this section (*[154], [155]*)*

Analysis	Output parameters	Aim	Standard
Thermogravimetric analysis (TGA) – Inert atmosphere	*DTG*	Estimate the pseudo-components % (lignin, cellulose, hemicellulose) through deconvolution of DTG curve	-
Differential Scanning Calorimetry	Characteristic temperatures and enthalpies	Evaluate the Temperature step of different phases (pyrolysis)	-
Proximate analysis	*VM, A, M, FC*	Compare volatiles and moisture content to other biomasses	ASTM D7582-15 [129]
Ultimate analysis	C%,H%,N%,O%	Estimate the C, O, N and H content	ASTM D3176 − 15 [158]
Thermogravimetric analysis (TGA) – Oxidant atm	T_{onset}, T_{offset}	Identify the magnitude of the exothermic reaction	-

A deconvolution procedure of the *DTG* curve is used to estimate the main components of lignocellulosic materials. The area beneath those curves will represent the percentage of each component (cellulose, hemicellulose and lignin). Fraser-Suzuki deconvolution [159] was used in this study, and the approach efficiently fit the experimental curves (R^2 equal to 0.99). Besides this, an ultimate analysis (according to ASTMD3176-15, [158]) was effectuated to quantify the sample's elemental composition. *FTIR* was used to analyse the product gases from samples degradation. A *TGA/FTIR* interface linked by a transfer line to the *TGA* furnace was used for this aim. The cell and transfer line of the *TGA/FTIR* interface is heated and kept at 220 °C to avoid condensation of the product gases. The background was KBr, resolution 8 cm^{-1}, range 4000−400 cm^{-1}. The output of this analysis is a Gram-Schmidt diagram.

Hydrothermal treatment is one method for the accelerated ageing of wood and lignocellulosic material. The ageing may reduce hygroscopicity, enhance stiffness and brittleness and cause

changes in the chemical composition [160]. Consequently, it may affect the flammable/explosible behaviour of the sample. The physical/chemical modifications due to hydrothermal treatment included both reversible and irreversible effects [161]. The reversible effects can be annulled once the sample is re-moistened. The irreversible chemical changes consist of decomposition, cross-linking, and recrystallisation of wood constituents [162]. To reproduce aged wood by hydrothermal treatments, both the effects must be considered, and the temperature and the relative humidity during heating (RHh) play a crucial role. According to Chedeville et al. (2012) [163], the chemical reactions induced by heating at 150 °C or higher are qualitatively different from those at 130 °C or lower. Therefore, 120 °C was employed as the treatment temperature because the final goal was to reproduce naturally aged wood [163]. Regarding humidity, industrial hydrothermal treatments are usually conducted either in the absence of moisture (0% RHh) or in steam (100% RHh). However, to consider both reversible and irreversible effects, an intermediate value of relative humidity must be used [161]. In this work, the sample was hydrothermally treated at 120 °C and RH 60% for 7 days in an autoclave [161]. The RH was calculated from the deionised water vapour pressure in the autoclave.

IV.3.2. Results

Nylon fibres

In the following the results obtained on the nylon 6,6 are discussed. First the flammability behaviour of all samples is tested. Then the chemical/physical and thermal characterization is shown. The hazard risk of nylon 6.6 was investigated, by measuring the minimum ignition energy in the Hartmann tube. In **Table IV.14**, *MIE* or E_s values are reported, as measured for all the nylon 6.6 samples. Notably, the values shown in **Table IV.14** are minimum ignition energies evaluated with a single delay time and inductance condition. Generally, in these conditions the lowest values of ignition energy are found.

Table IV.14 *Minimum Ignition Energy of nylon 6.6 samples. tv= 120 ms, L=1 mH* [164]

Sample	E_1 (mJ)	E_s (mJ)	E_2 (mJ)
1	300	471	1000
2	-	-	>1000
3	-	-	>1000
4	-	-	>1000
5	100	228	300

Samples 2, 3 and 4 did not ignite for ignition energy equal up to 1000 mJ. Sample 5 has the smallest MIE value followed by sample 1. In order to better clarify the reason why sample 5 is the most reactive, we performed a full chemico-physical and thermal screening and evaluated the step controlling the sample ignition/explosion.

All the samples have been characterized by FTIR analysis to identify the chemical nature. In **Figure IV.24** the FTIR spectra are shown as obtained for all samples. The spectrum of Nylon 6,6 is also shown for comparison.

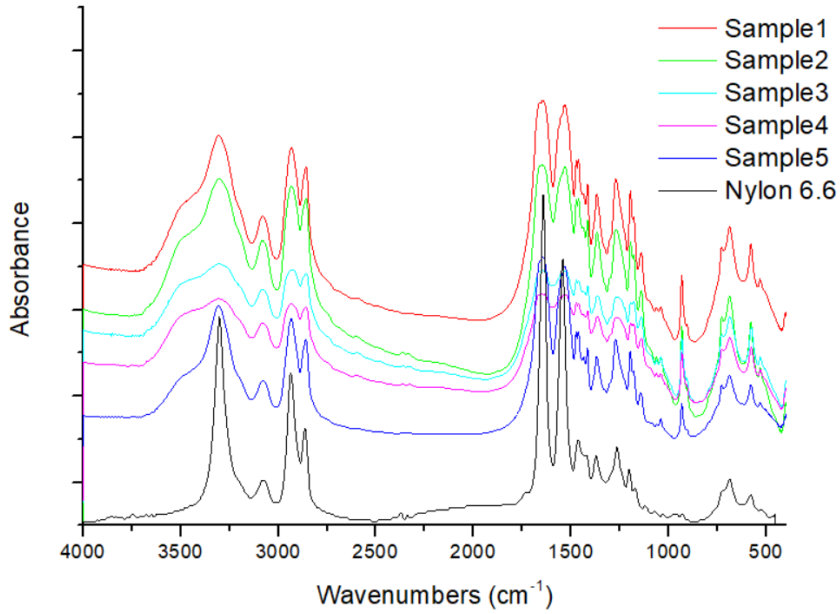

Figure IV.24 *FTIR spectra of nylon 6.6 (black), sample 1 (red), sample 2 (light green), sample 3 (light blue), sample 4 (magenta) and sample 5 (blue)* [164]

The bands of the spectra are given in **Table IV.15**. The spectra of all samples (1-5) correspond to the spectrum of nylon 6.6 (Hummel Polymer Sample Library of OMNIC software).

In **Figure IV.25**, SEM images are shown for all dusts investigated at different magnifications. All the samples are composed by fibres with a cylindrical shape. From these images, it is not possible to notice the differences due to the dying. Conversely, the effects of the activation process are recognizable. Fibres of samples 1, 2 and 4 appear well separated because the thin layer of surfactant has been removed by the wet activation process. Conversely, samples 3 and 5 particles, both not activated, seem more compact. Especially in 200x SEM image of sample 3 (**Figure IV.25 (c)**), a sticky group of particles is easily visible.

Table IV.15 *Absorption bands of FTIR solid of nylon 6.6 samples* [164]

Wavenumber (cm^{-1})	**Bands**
3182	NH stretching
3080	Asymmetrical stretch of CH
3020	Symmetrical stretch of CH
2958	Asymmetrical stretch of CH_2
2841	Symmetrical stretch of CH_2
1745	C=O stretching
1660	Amide I band
1541	Amide II band/CH_2 asymmetrical deformation
1447	NH deformation/CH_2 scissoring
1354	Amide III band/CH_2 wagging
1149	CCH symmetric bending/CH_2 twisting
1128	CCH symmetric bending
959	C-C stretching
755	N-H wagging/CH_2 rocking
606	C-C bending
549	O=C-N bending

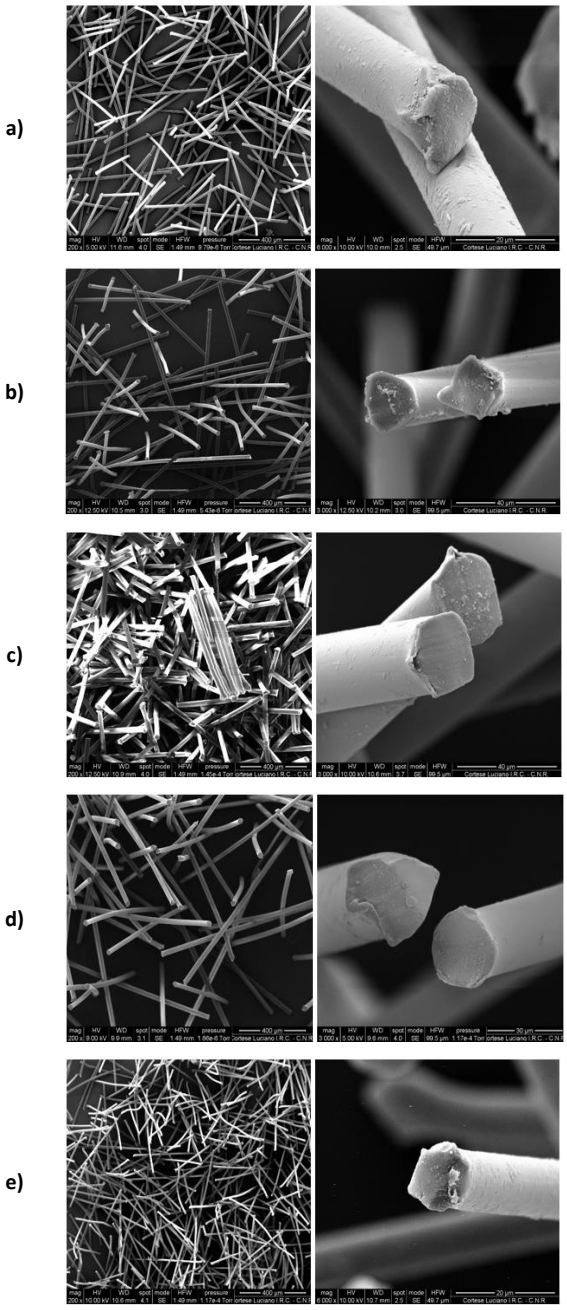

Figure IV.25 *SEM images of sample 1 (a), sample 2 (b), sample 3 (c), sample 4 (d) and sample 5 (e) investigated at 200x (left) and 6000x (right) magnification* [164]

From the SEM results, average length and diameter of fibres were calculated by statistical analysis using ImageJ program [165] (**Table IV.16**).

Table IV.16 *Average length and diameter of nylon 6.6 fibres* [164]

Sample	Length, L (μm)	Diameter, d_f (μm)	D_{eq} (μm)
1	393	15	87
2	520	20	115
3	540	30	144
4	933	30	189
5	319	10	64

The fibre diameter and length ranges from 10 up to 30 μm and 319 up to 933 μm, respectively. The smallest samples in terms of both diameter and length are sample 1 and 5. In **Table IV.16**, the equivalent particle diameters, D_{eq} is also reported as calculated according to the following formula [123]:

$$D_{eq} = 2\sqrt{\frac{d_f L}{\pi}} \tag{47}$$

The smallest value of the equivalent diameter is found for sample 5.

Then, *XRD* analysis has been carried out to assess crystal sizes and degree of crystallinity of each sample. *XRD* patterns of samples are shown in **Figure IV.26**. According to Diaz-Alejo et al. (2013) [166], the samples show a similar diffraction pattern of a predominant amorphous material with some crystallinity degree. The bands at around $2\theta = 19°$ and $2\theta = 26°$ correspond to the reflection of (100) and (010,110) doublet of the α phase of nylon 6.6 crystals oriented in a triclinic cell. The peaks intensity is related to the crystalline degree. The higher the intensity of the peak, the higher the crystalline degree. Sample 1 and 5 have the lowest crystalline degree.

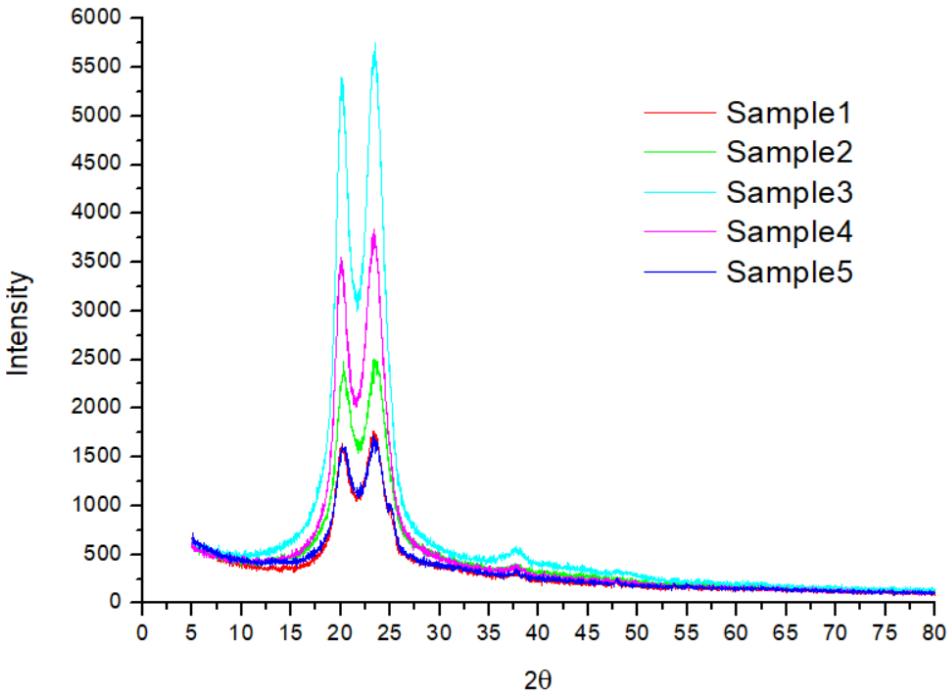

Figure IV.26 *XRD profiles of the nylon 6.6 samples* [164]

From this analysis, average crystal size (D) and interplanar spacing (d) were calculated by Debye-Scherrer equation [167] and Bragg law [168], respectively. These parameters are given in **Table IV.17**.

Table IV.17 *Average crystal size and interplanar spacing of nylon 6.6 samples* [164]

Sample	Main peak (2θ°)	*d* (Å)	*D* (Å)
1	19.9721	4.4	197.1
2	20.3901	4.3	215.7
3	23.4690	3.8	396.6
4	19.9259	4.4	143.7
5	25.3238	3.5	176.9

The interplanar spacing lies between 3.5 and 4.5 Å while the average crystal size changes a lot from sample to sample. Sample 5 shows the lowest pair of parameters. The evaluation of the crystallinity degree is very important since it has been shown that amorphous materials have oxygen diffusion coefficient much higher than crystalline materials [169], thus increasing the reaction rate of the heterogeneous path which is mainly controlled by O_2 diffusion. As a consequence, dust with decreasing the crystalline degree may be more reactive.

In **Table IV.18** the specific surface area (SSA) values measured through BET analysis are given. Density is also reported.

Table IV.18 *Specific surface area and density of nylon 6.6 samples* [164]

Sample	SSA (m^2/g)	Density (g/cm^3)
1	10.5	1.23
2	10.4	1.07
3	3.9	1.11
4	10.8	1.05
5	14.3	1.06

SSA are quite similar except for sample 3 and 5 which exhibit the lowest and the highest specific surface area, respectively. The densities of each sample are comparable except sample 1 one which is slightly higher.

From these first analyses, the explosive behaviour seems to strongly depend on the sizes of the fibres. Small sizes make fibre dispersion easier and more effective. This phenomenon makes the formation of an explosive cloud more probable. The crystalline degree and the surface area also play a role. The specific surface area (SSA) is a key parameter significantly affects the heat transfer rate, the volatilization rate, the heterogeneous combustion and most importantly the O_2 diffusion. Moreover, a low crystalline degree (amorphous material) promotes the diffusion of oxygen that can sustain the combustion reaction then supporting the flame propagation. Instead, activation ad coloration seems to have no effect on the explosive character. In particular, sample 5 is the most reactive even if its dispersibility should be worse due to the absence of the activation process. It can be stated that in the case of sample 5 the dispersion is effective despite the absence of the activation process due to the small size which plays a fundamental role. Therefore, activation ad coloration will not be taken into account in the rest of the study. To make the study complete, it is interesting to assess how these different properties influence thermal behaviour of nylon 6.6 samples in N_2 and oxidative atmosphere.

For all samples, proximate analysis was performed to quantify the volatile (V), the humidity (M), the ash (A) and the fixed carbon (F) contents [129]. In **Table IV.19**, the results are given for all samples. The moisture percent is about 1 % for all samples. The volatile percentage is very high ranging from 90 to 98 %. The ash content is lower than 10 % for all samples, while fixed carbon is not present. From these data we may conclude that all the samples have a very high volatile content.

Table IV.19 *Proximate analysis of nylon 6.6 samples* ([129], [164])

Sample	M%	V%	A%	F%
1	0.3	98.7	1.0	0
2	1.1	96.5	2.4	0
3	1.1	98.7	0.2	0
4	0.4	91.0	8.6	0
5	0.7	92.3	7.0	0

In our previous papers, we showed that the dust response to the temperature increase is very useful for understanding the phenomena controlling the flammability/explosion behaviour of dusts [138], [145]. In this work, we performed thermogravimetric analysis of all samples, in both N_2 and air atmosphere. The temperature has been varied up to 600°C, at a heating rate equal to 10°C/min.

N_2 atmosphere

In **Figure IV.27**, the TG curves in terms of weight loss as function of temperature are shown as obtained for all the samples.

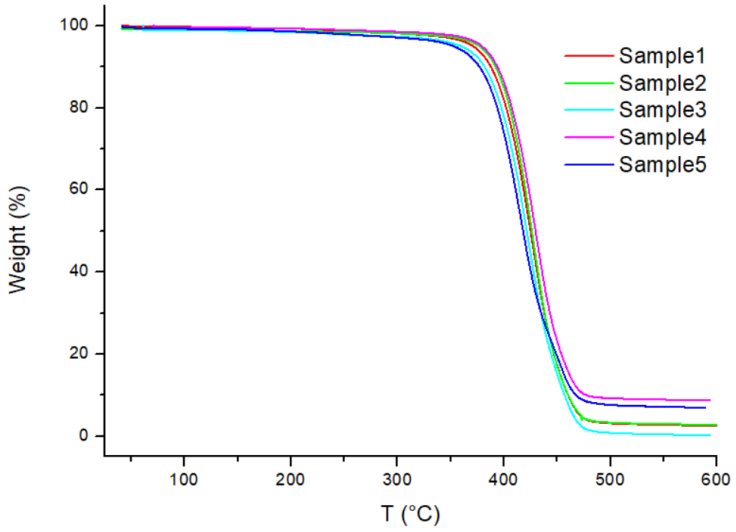

Figure IV.27 *TG curves of nylon 6.6 samples in N_2 atmosphere* [164]

From these profiles, characteristic temperatures were calculated: the temperature at which weight loss starts (T_{onset}), the inflection temperature at which there is the maximum rate of weight decrease (T_{flex}) and the temperature at which the weight loss ends (T_{offset}). The calculated values are given in **Table IV.20**.

Table IV.20 *Characteristic temperatures from TG curves in N_2 atmosphere* [164]

Sample	T_{onset} (°C)	T_{flex} (°C)	T_{offset} (°C)
1	390	427	510
2	391	429	495
3	387	425	507
4	392	430	493
5	380	417	510

Sample 5 has an early thermal degradation (380 °C) compared to others (≈ 390 °C). This could be due to the lowest fibre sizes. The maximum degradation rate is also reached earlier (T_{flex}), about 10 °C, by sample 5. In addition to the TG curves, DSC curves are reported in **Figure IV.28**.

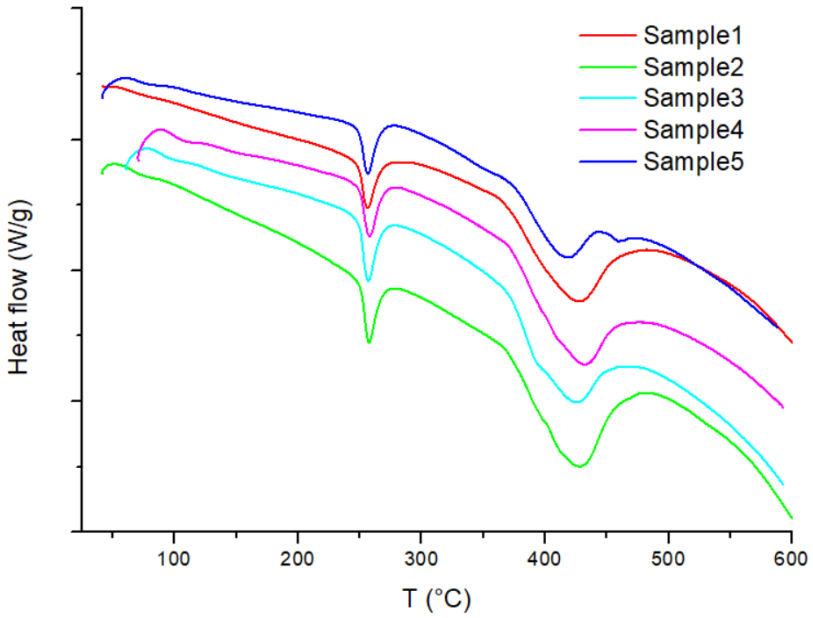

Figure IV.28 *DSC curves of nylon 6.6 samples in N_2 atmosphere* [164]

Two endothermic peaks are found for all samples. The first peaks (256 °C) can be addressed to the melting of the crystalline material. The temperature of the second (endothermic) peak is slightly different for all samples and it is equal to the flex temperature (T_{flex}). This peak has been addressed to the occurrence of a chemical reaction and to a pyrolysis reaction. In the Gram smith diagram (not reported), all samples exhibit a single peak which corresponds to the temperature of the second peak in the DSC diagrams (**Figure IV.28**), confirming the occurrence of the pyrolysis reaction. At each peak of Gram-Schmidt diagram corresponds a spectrum shown in **Figure IV.29**. All curves have the same main peaks. Noteworthy, all the samples lead to the formation of the same volatile substances.

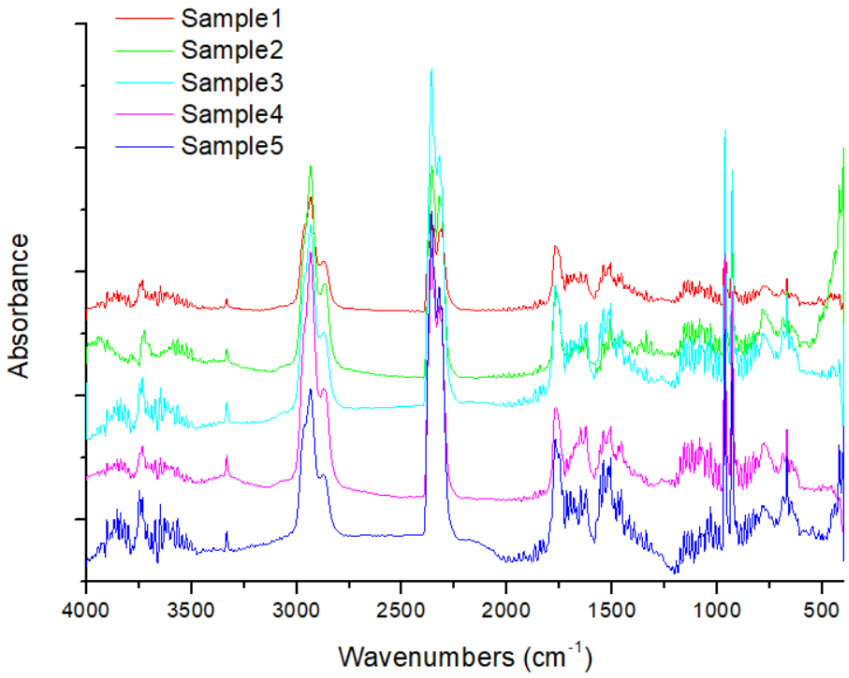

Figure IV.29 *Spectra of product gases during pyrolysis of nylon 6.6 samples* [164]

The HR Nicolet TGA Vapor Phase library of OMNIC software has been used to recognize the product gases. From this result, CO_2 (peaks between 2400 and 2200 cm^{-1} and at 669 cm^{-1}), NH_3 (peaks at 3330 cm^{-1} and between 2000 and 600 cm^{-1}) and H_2O (peaks in bands 4000-3000 cm^{-1} and 2200-500 cm^{-1}) are the main products in the N_2 atmosphere measurements. The two peaks at 2934 and 2866 cm^{-1} are due to C-H bond, so they indicate a hydrocarbon chain while the peak at 1766 cm^{-1} is related to C=O bond, related to the production of cyclopentanone [170].

Air atmosphere

The tests in air have been carried out up to 600°C with heating rate equal to of 10 °C/min. TG curves for all samples are shown in **Figure IV.30**.

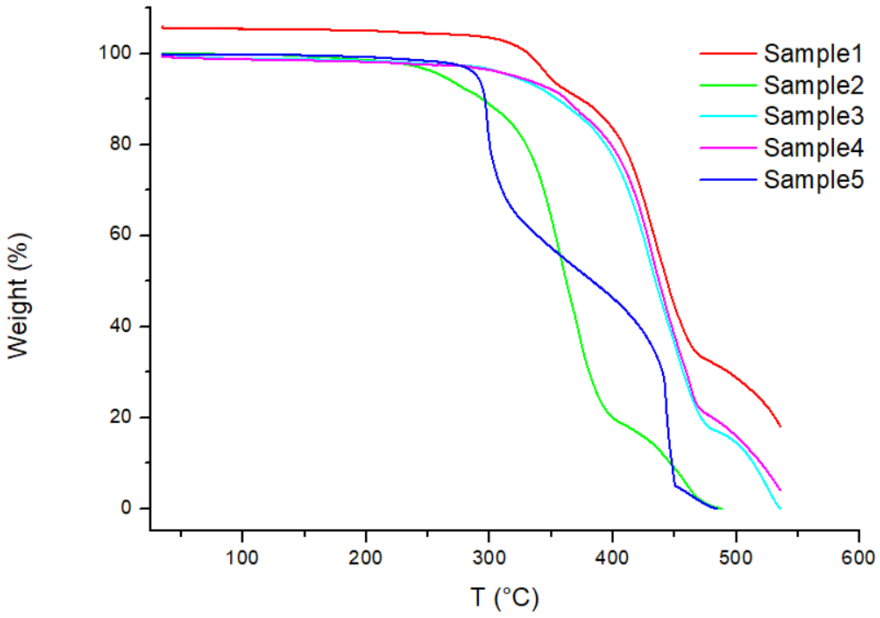

Figure IV.30 *TG curves of nylon 6.6 samples in oxidative atmosphere* [164]

The TG curves in oxidative atmosphere are significantly different form the profiles obtained in N_2. Several peaks of weight losses are observed. In addition to the temperature T_{onset}, T_{flex} and T_{offset}, we calculated T_1 and T_2 which are the temperatures at which the second and the third weight loss (before inflection temperature) occurs, respectively (**Table IV.21**).

Table IV.21 *Characteristic temperatures from TG curves in oxidative atmosphere* [164]

Sample	T_{onset} (°C)	T_1 (°C)	T_{flex} (°C)	T_2 (°C)	T_{offset} (°C)
1	305	364	440	479	608
2	317	-	438	487	560
3	308	-	430	480	540
4	300	-	435	473	560
5	303	327	347	485	505

Only samples 1 and 5 show a weight loss peak before the inflection temperature. In **Figure IV.31**, the corresponding DSC curves are shown as obtained for each sample.

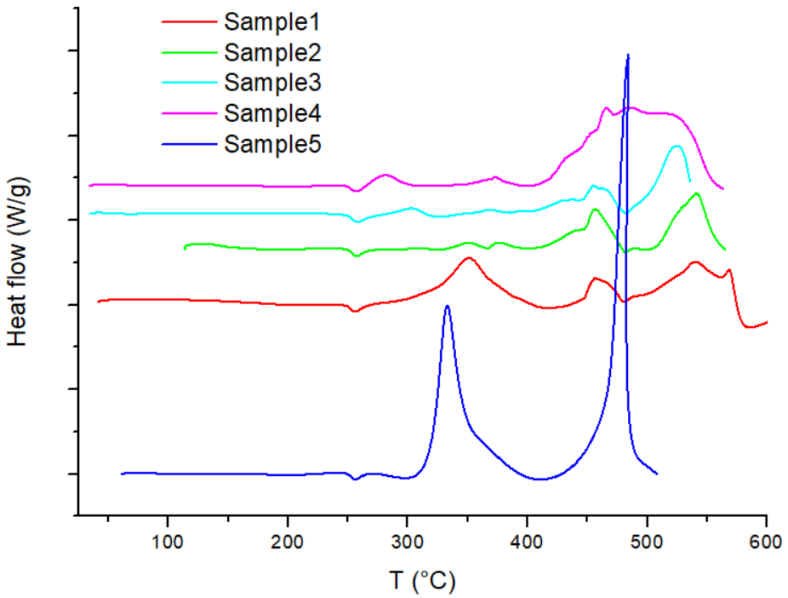

Figure IV.31 *DSC curves of nylon 6.6 samples in oxidative atmosphere* [164]

All samples exhibit a first endothermic peak which can be addressed to the crystalline melting of the material (as in the N_2 measurement). Differently form the TG in N_2 atmosphere, exothermic peaks are present. In the case of sample 5 these peaks are higher than in the other samples. In **Table IV.22** the temperature ($T_{Iexopeak}$) and the heat released ($\Delta H_{Iexopeak}$) in correspondence of the first exothermic peak are given, for all samples.

Table IV.22 *Temperatures and heat released at first exothermic peak of each sample. The equivalent diameter is also reported* [164]

Sample	D_{eq} (µm)	$T_{Iexopeak}$ (°C)	$\Delta H_{Iexopeak}$ (J/g)
1	87	351	-233.0
2	115	350	-12.6
3	144	305	-14.4
4	189	282	-27.4
5	64	334	-508.6

It is worth noting that the heat released at the first peak, increases by decreasing the characteristic fibre dimension (D_{eq}). To assess the chemical nature of the residual after the first exothermic peak, FTIR solid was performed. For samples 1, 2, 3, 4, the residue had a very resistant and difficult to pulverize shell. However, inside the shell, the substance present is still nylon 6.6 (spectra not reported). The residue of sample 5 had a porous and easy to pulverize shell. As can be seen in **Figure IV.32**, the spectrum of sample 5 after the first exothermic peak, (Sample5_afterIexopeak)

is significantly different from that of nylon 6.6 and very similar to char one [171], suggesting that a chemical transformation has occurred.

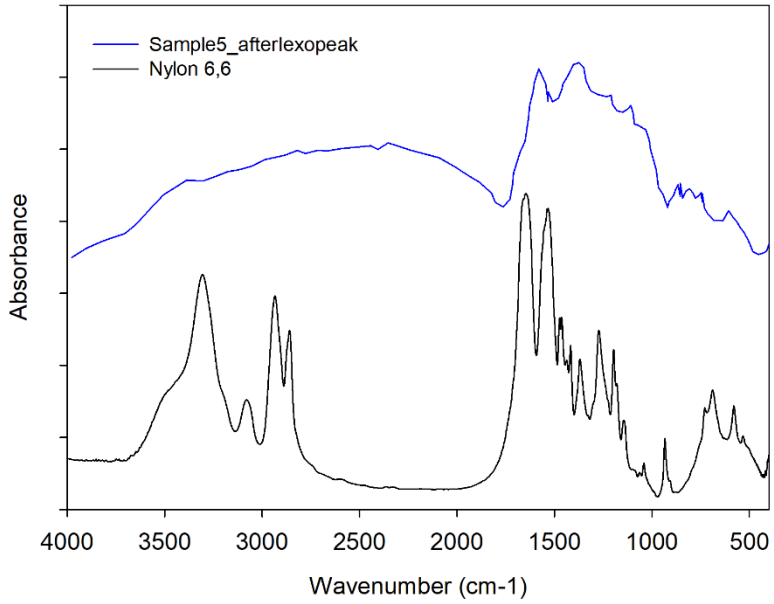

Figure IV.32 *Spectra of nylon 6.6 TQ (black) and sample 5 (blue) after the first exothermic peak* [164]

Moreover, as can be seen in **Figure IV.31**, samples 2,3 and 4 restart reacting with oxygen from 400 °C onwards. After the first peak, the hard shell isolates the nylon core until, at high temperatures, the shell breaks allowing the diffusion of oxygen and the heterogeneous reaction. To evaluate the chemical nature of the gaseous substances released during the first peak, FTIR gas was carried out. All Gram-Schmidt diagrams (not reported) show two main peaks. The first peak corresponds to the occurrence of the exothermic phenomenon. The spectra corresponding to the first peak of Gram-Schmidt are shown in **Figure IV.33**.

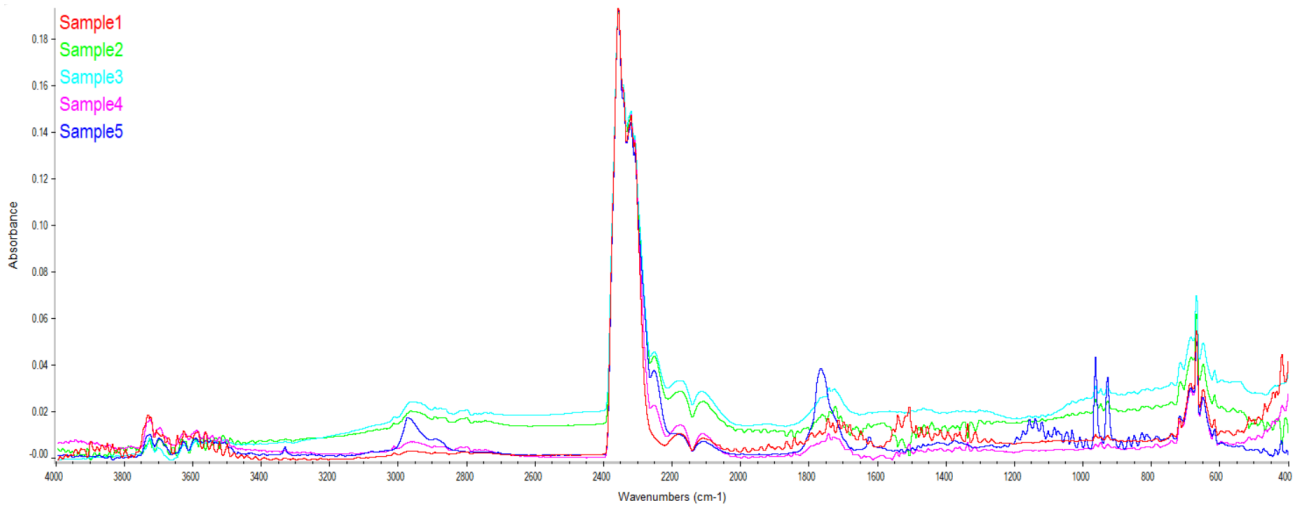

Figure IV.33 *Spectra of product gases at first exothermic peak of nylon 6.6 samples* [164]

In oxidative atmosphere, there are some differences about gas production of nylon 6.6 samples. The HR Nicolet TGA Vapor Phase library of OMNIC software was used to identify the product gases. As regards sample 1 (spectrum not shown), CO_2 (at 2400-2200 cm^{-1}) and H_2O (at 4000-3400 cm^{-1} and 2000-1200 cm^{-1}) are the main products, with CO in trace (at 2200-2000 cm^{-1}). Differently from the results under N_2 atmosphere, cyclopentanone was not found. In the spectra of samples 2, 3 and 4 (not reported), the main product is CO_2. The peaks at 2960 cm^{-1} and at 2252 cm^{-1} can be addressed to metyl-isocyanate (C_2H_3NO) while peaks at 2181 and 2106 cm^{-1} suggest the presence of CO. The peaks at about 1750 cm^{-1} suggest the presence of small amount of cyclopentanone. In the case of Sample 5 (spectrum not reported), the formation of CO (green) and NH_3 (red) is detected. The peak at 1766 cm^{-1} is related to C=O bond (production of a significant amount of cyclopentanone) while peaks at 2181 and 2106 cm^{-1} are due to CO. As for samples 2, 3 and 4, the peaks at 2960 cm^{-1} and at 2252 cm^{-1} are attributable to metyl-isocyanate (C_2H_3NO). The interaction with oxygen of Sample 5 at low temperature (the onset temperature in oxidative atmosphere is about 300 °C) leads to the generation of combustible volatiles (CO, NH_3, C_2H_3NO and cyclopentanone). It is worth noting that although in the oxidizing environment the main products are those typical of complete combustion (CO_2 and water) due to the presence of the combustion reaction in the heterogeneous phase, there is still the formation of flammable gaseous species produced by thermal decomposition of the fibres that can take part to combustion in the homogeneous phase. In order to better clarify the reason why sample 5 is the most reactive, we evaluated the step controlling the sample ignition/explosion.

In our previous paper we showed that the explosion mechanism of dust occurs through the following network of series/parallel steps (**Figure IV.34**).

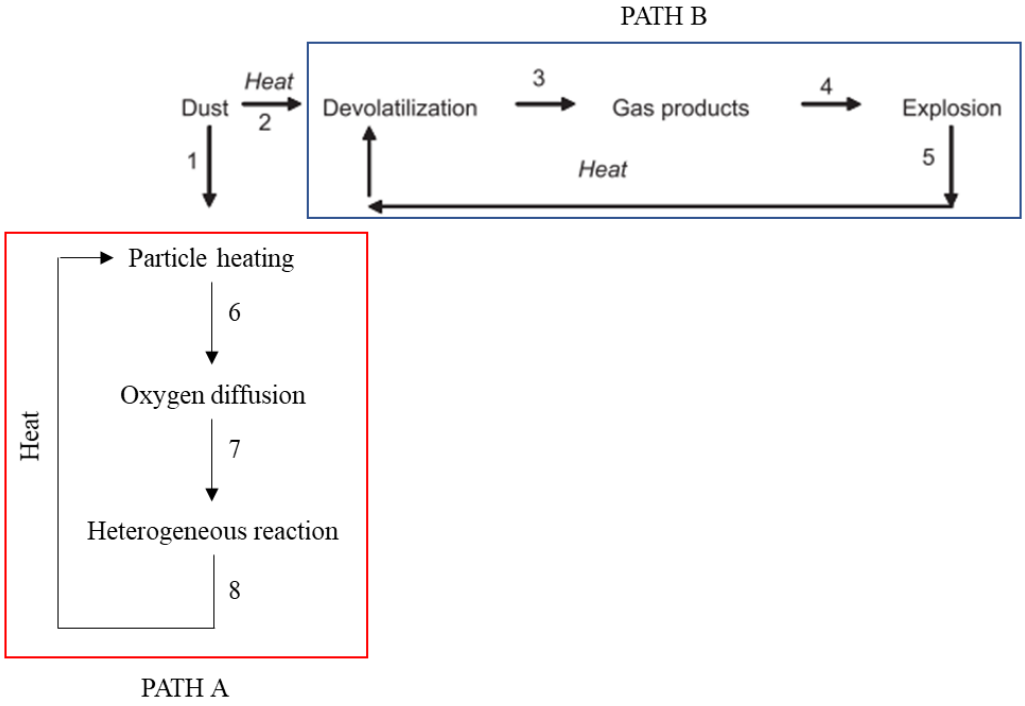

Figure IV.34 *Schematic representation of the paths occurring during dust explosion* [28]

The explosion/flammability behaviour depends on the controlling step. In order to get insights into the different behaviour of the nylon 6,6 samples here analysed, we calculated dimensionless numbers to identify the controlling step, according to the model developed by Di Benedetto et al. (2010) [41].

To quantify the role of particle heating, we calculated the Biot number (*Bi*), which is the ratio between the internal heat conduction time (t_c) with respect to the external heat transfer time (t_e) (Equation (5)). The evaluation of the comparison between heat transfer and devolatilization reaction was performed by calculating the Damköhler number (*Da*), which is the ratio between the external heat transfer time (t_e) and the devolatilization chemical time (t_{pyro}) (Equation (6)). The thermal Thiele number (*Th*) allow the comparison between the conduction heat transfer time (t_c) and the pyrolysis chemical time (t_{pyro}) (Equation (7)). Biot number is equal to 1 for all the samples, suggesting that external and conduction (internal) heat transfer time are comparable. *Da* and *Th* numbers are found to be both much lower than 1, for all samples. Therefore, we may affirm that the controlling step is the pyrolysis reaction. The evaluation of the controlling step has to be performed by comparing the volatile combustion time to the pyrolysis time. To this end we calculated the *Pc* number as the ration of the volatile combustion time (t_{comb}) and the pyrolysis time (t_{pyro}) (Equation (8)). The *Pc* number has been calculated by assuming $S_l = 0.2$ m/s.

Moreover, we considered two additional dimensionless numbers able to take into account the oxygen diffusion. More precisely, the Thiele modulus (Φ_{Th}) indicates the rate of reaction with respect to the rate of diffusion while the Sherwood number (*Sh*) represents the ratio of the convective mass transfer to the rate of diffusive mass transport. The Sherwood number can be expressed also as a function of the Reynolds and Schmidt dimensionless numbers ([172], [173]). The formula are reported as in the following:

$$\phi_{Th} = D_{eq}\sqrt{\frac{k_{in}}{D_{O_2}}} \tag{48}$$

The Sherwood number is a function of the Reynolds and Schmidt dimensionless numbers ([26,27]):

$$Sh = Kc \cdot \frac{D_{eq}}{D_{O_2}} = 2 + 0.69Re^{\frac{1}{2}}Sc^{\frac{1}{3}} \tag{49}$$

Where k_{in} (s^{-1}) is the intrinsic kinetic constant for the first exothermic peak found in oxidative atmosphere, D_{O2} (m^2/s) is the effective oxygen diffusivity, *Kc* (m/s) is the external mass transfer coefficient and *Sc* (-) is the Schmidt number defined as

$$Sc = \frac{\mu}{\rho D_{O_2}} \tag{50}$$

The overall (apparent) reaction rate was calculated by using the Arrhenius formula where the kinetic parameters were obtained from the constant heating rate approach based on the Flynn & Wall method [174] (**Table IV.23**). The intrinsic kinetic constant (k_{in}) was then evaluated by considering the effectiveness factor and the Weisz–Prater module Φ, so that the effect of mass transfer can be evaluated and eliminated [175].

Table IV.23 *Kinetic parameters relative to the first exothermic peak in oxidative atmosphere for each sample* [164]

Sample	D_{eq} (µm)	E_a (J/mol)	Z (s^{-1})
1	87	19665.5	0.02
2	115	101853.5	430567
3	144	99869.5	357102
4	189	87131	36251
5	64	40896.5	8.55

Sh was calculated assuming Reynolds number equal to 2000 (i.e., the maximum value allowable by Equation (49) by [172], [173]). The effective oxygen diffusivity was set for each sample starting

from the value of $1.70 \cdot 10^{-10}$ m^2/s [176], found in literature for the amorphous polyethylene, and calculating the values by considering the following equation

$$D_{O_2,i} = \left(\frac{100 - X_c}{100}\right)^2 D_a \quad (51)$$

Where X_c is the crystalline fraction within the sample and D_a (m^2/s) is the oxygen diffusion coefficient in the amorphous material (Xc=0). To estimate X_c, we calculated the fusion heat ΔH_{sample}^{fus} from the DSC analysis for each sample:

$$\mathrm{X_c} = \frac{\Delta H_{sample}^{fus}}{\Delta H_{nylon}^{fus}} \quad (52)$$

Where ΔH_{nylon}^{fus} (J/g) is the heat of fusion of crystalline nylon 6,6 (175.6 J/g) [177]. In **Table IV.24**, the external heat transfer coefficient, the fibre equivalent diameter and the effective oxygen diffusivity are reported for each sample. In **Table IV.25** the values of *Bi*, *Da*, *Th* and Pc as calculated for all samples are given.

Table IV.24 *Hydraulic diameter and heat transfer coefficient of nylon 6.6 samples* [164]

Sample	L (µm)	d_f (µm)	D_{eq} (µm)	h_c (W/m² K)	ΔH_{sample}^{fus} (J/g)	X_c (-)	D_{O2} (m^2/s)
1	393	15	87	2499.0	63.94	0.36	$6.87 \cdot 10^{-11}$
2	520	20	115	2172.5	68.57	0.39	$6.32 \cdot 10^{-11}$
3	540	30	144	1740.7	69.28	0.39	$6.23 \cdot 10^{-11}$
4	933	30	189	1324.3	70.76	0.40	$6.06 \cdot 10^{-11}$
5	319	10	64	3922.7	53.27	0.30	$8.25 \cdot 10^{-11}$

Where $h_c = \frac{\lambda}{D_{eq}}$ is the heat transfer coefficient with the model of pipe wall. The other parameters to calculate dimensionless number are [178]:

- Cp_{dust} = 1670 J/kg K
- λ_{dust} = 0.25 W/m K
- ε_λ = 0.88
- ΔT = 0.5 K value chosen due to the fibres size
- σ= $5.67 \cdot 10^{-8}$ W/m^2 K^4

All the dimensionless numbers have been calculated and reported in the following **Table IV.25**:

Table IV.25 *Dimensionless numbers for all samples* [164]

Sample	Bi	Da	Th	Pc	Φ_{Th}	Sh
1	1	$1.54 \cdot 10^{-4}$	$1.54 \cdot 10^{-4}$	$1.04 \cdot 10^{2}$	$7.08 \cdot 10^{-2}$	$1.80 \cdot 10^{3}$
2	1	$2.18 \cdot 10^{-4}$	$2.18 \cdot 10^{-4}$	$9.73 \cdot 10^{1}$	$7.69 \cdot 10^{-2}$	$1.85 \cdot 10^{3}$
3	1	$2.82 \cdot 10^{-4}$	$2.82 \cdot 10^{-4}$	$1.18 \cdot 10^{2}$	$9.21 \cdot 10^{-2}$	$1.86 \cdot 10^{3}$
4	1	$4.77 \cdot 10^{-4}$	$4.77 \cdot 10^{-4}$	$1.20 \cdot 10^{2}$	$1.18 \cdot 10^{-1}$	$1.87 \cdot 10^{3}$
5	1	$1.96 \cdot 10^{-4}$	$1.96 \cdot 10^{-4}$	$3.32 \cdot 10^{1}$	$8.77 \cdot 10^{-2}$	$1.69 \cdot 10^{3}$

From the values of *Pc* (>>1) we may conclude that the pyrolysis time is much higher than the volatile combustion time then identifying the pyrolysis of nylon 6,6 as the controlling step of the flame propagation. However, the pyrolysis time strongly depends on the fibre size. In **Figure IV.35** the pyrolysis time ($t_{pyr}=rp/\rho_{dust}$) is shown for each sample. It is worth noting that r_p used for the pyrolysis time calculation is the maximum i.e. relative to the main peak of *TG* curve in inert atmosphere. From the plot we may observe that the pyrolysis time is much lower for Sample5 with respect to the other samples. Sample5 is the most flammable (lowest value of the MIE). As a result, when the pyrolysis is faster, the dust is more flammable/explosive.

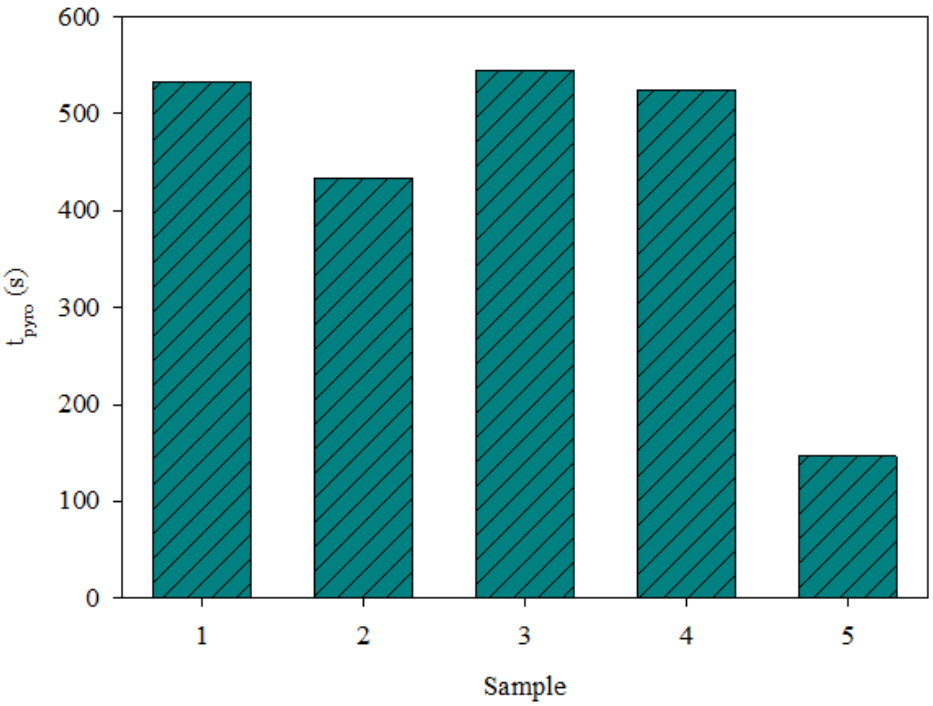

Figure IV.35 *Pyrolysis time as function of the samples* [164]

From the obtained values of Φ_{Th} (<<1), we may conclude that the heterogeneous flame propagation path is controlled by the heterogeneous intrinsic reaction. Consequently, the main effect is played by the specific surface area. Sample5, that is characterized by the highest value of *SSA* reacts faster and at lower temperature compared to the other samples.

Vinery waste

Figure IV.36 (a) shows the weight percentage and derivative thermogravimetric (*DTG*) curves as a function of temperature for *TG/DSC* analysis in N_2 flow. *DTG* curve exhibits two main peaks:

the former at low temperature (<200 °C) is related to the moisture loss while the latter to the pyrolysis of lignocellulosic components. Following the standard test method, we carried out the proximate analysis from the weight loss curve, whose results are presented in **Figure IV.36 (b)**. It is worth noting that the volatile content is very high, so it is reasonable to assume that if dispersed in air, the sample will be subject to homogeneous combustion controlled by the devolatilization process. However, it is worth noting that the peak temperature corresponding to the pyrolysis step activation is very high (about 380°C). This data suggests that the onset of the pyrolysis could control the explosion.

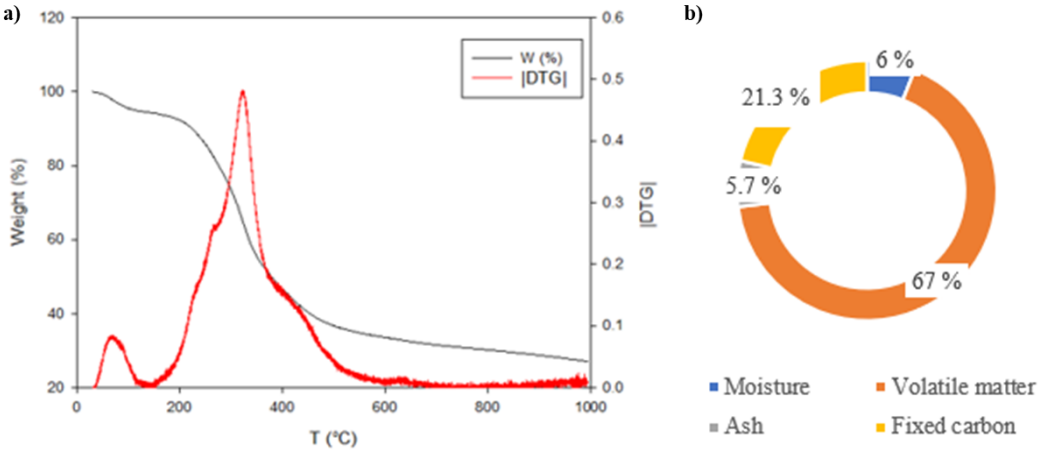

Figure IV.36 *TG/DTG analysis, 10°C/min, 100 ml/min N_2, 10 mg sample: weight % and DTG as a function of temperature (a) and proximate analysis results (b)* ([154], [155])

As the production of volatile species is remarkable, an *FTIR* gas has been carried out to evaluate which substances are released during pyrolysis. Gram-Schmidt diagram (**Figure IV.37**) shows a single prominent peak. The time at which the peak occurs corresponds to the *DTG* peak temperature (320 °C). Notably, at each Gram-Schmidt diagram point corresponds a *FTIR* spectrum. As a result of the *FTIR* spectra analyses, the diagram may be divided into three zones: the first corresponding to the water desorption (*FTIR* spectrum not reported), the second zone is related to the decomposition, while the last section relates to the residual gas produced by the decomposition still present inside the transfer line. **Figure IV.38** shows the *FTIR* spectrum at the Gram-Schmidt main peak. The thermal decomposition of the sample leads to the formation of different species, including flammable ones such as hydrocarbon chains (from C3), carboxylic acids and CO.

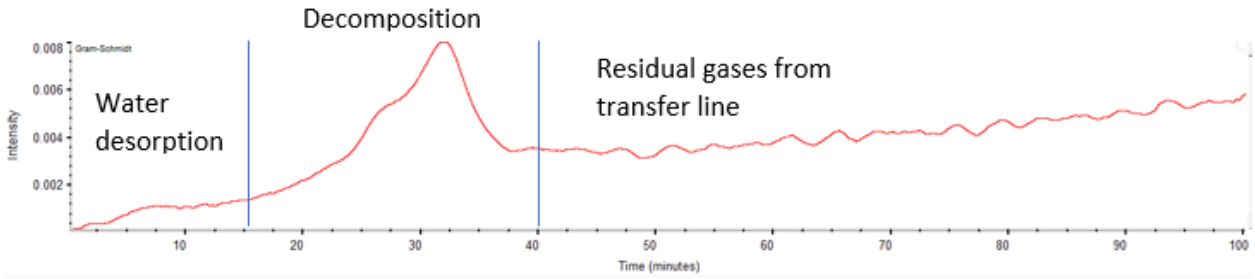

Figure IV.37 *Gram-Schmidt diagram related to the TG/DTG analysis, 10°C/min, 100 ml/min N_2, 10 mg sample* ([154], [155])

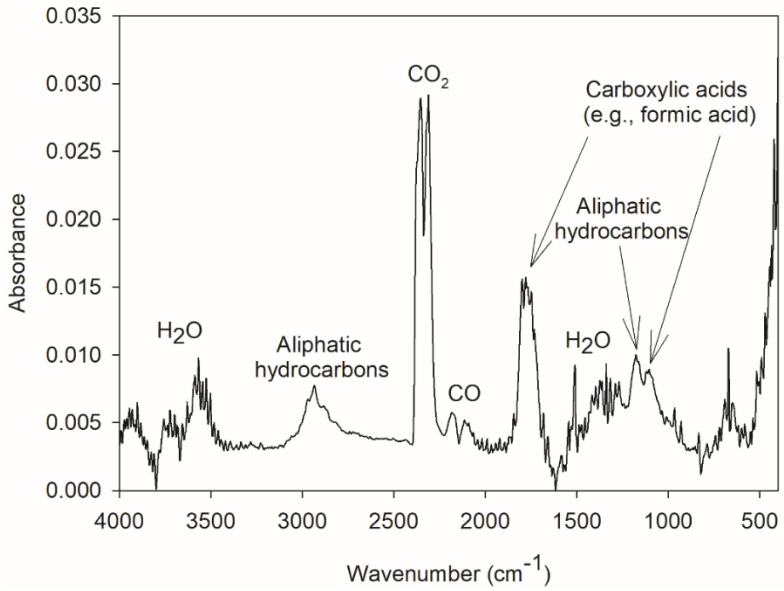

Figure IV.38 *FTIR spectrum at the Gram-Schmidt diagram main peak* ([154], [155])

Sheng and Azevedo reported an analytical correlation to associate proximate and ultimate analyses values to the content in lignin and cellulose for many biomasses [179]:

$$Cellulose = -1019.07 + 293.81 \cdot (O/C) - 187.639 \cdot (O/C)^2 + 65.1426 \cdot (H/C) - 19.3025 \cdot (H/C)^2 + 21.7448 \cdot VM - 0.132123 \cdot (VM)^2 \quad (53)$$

$$Lignin = 612.099 + 195.366 \cdot (O/C) - 156.535 \cdot (O/C)^2 + 511.357 \cdot (H/C) - 177.025 \cdot (H/C)^2 - 24.3224 \cdot VM + 0.145306 \cdot (VM)^2 \quad (54)$$

The analytical estimate of the pseudo-components amount was obtained from the equations above. The cellulose and lignin contents were estimated respectively as 5% and 61%. As observed from the *FTIR* spectrum, the sample mainly consists of lignin and contains a small amount of cellulose. **Figure IV.39 (a)** shows the *DTG* and the hemicellulose, cellulose, and lignin peaks as a temperature function, as obtained through the Fraser-Suzuki equation. The amount of each

component is reported in **Figure IV.39 (b)**. The results of the deconvolution are almost in agreement with the evaluation made with the above equations.

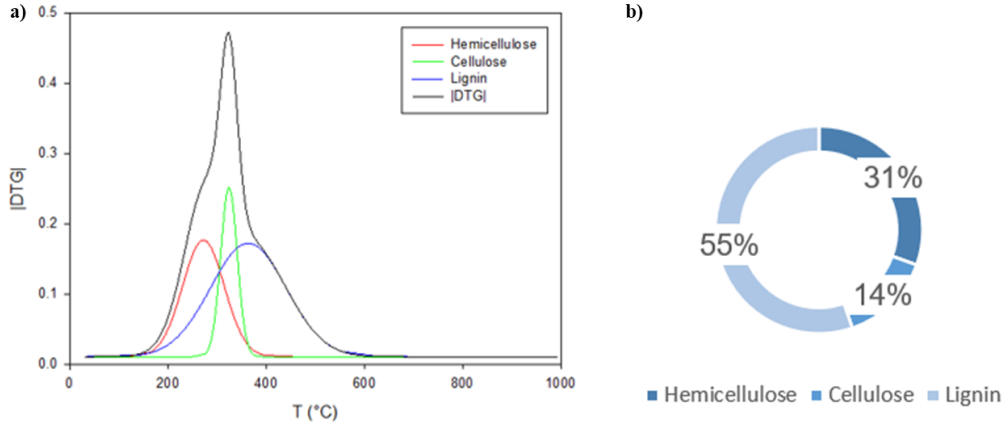

Figure IV.39 *Deconvolution through Fraser-Suzuki equation of DTG curve (a) and lignocellulosic components amounts (b) of the sample* ([154], [155])

Figure IV.40 shows the weight percentage and *DTG* curves as a function of temperature for TG/DSC analysis in airflow. In this case, the *DTG* curve exhibits three prominent peaks. The first peak is relative to the hemicellulose exothermic reaction (peak temperature 300 °C). The second is very sharp and is related to cellulose combustion (peak temperature 426 °C). The third peak relates to the lignin reaction (peak temperature 460 °C). This result makes the effect of the relative content of the three components, which have different reaction temperatures, on the flammability/explosibility parameters more understandable. The exothermic process starts at 200 °C (T_{onset}) and finishes at 525 °C (T_{offset}), with a final solid residual of 10%, attributable to char.

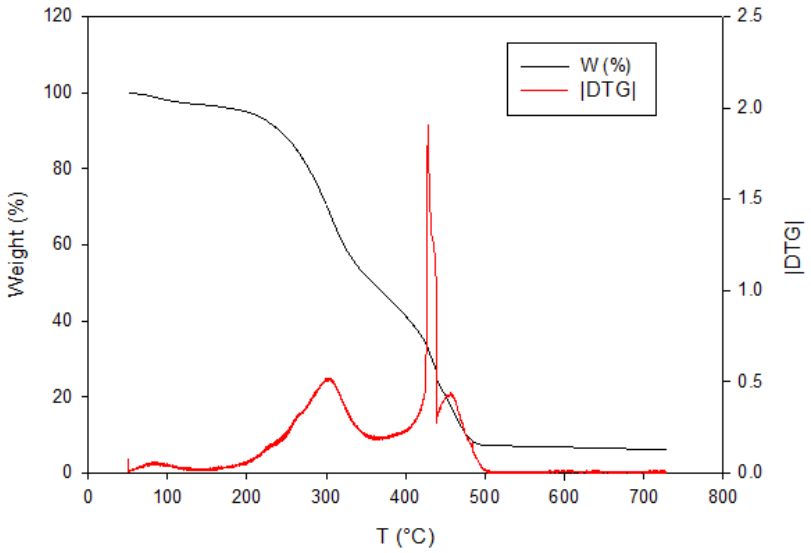

Figure IV.40 *TG/DTG analysis, 10°C/min, 100 ml/min air, 10 mg sample: weight % and DTG as a function of temperature* ([154], [155])

FTIR gas was carried out to evaluate which substances are released during combustion. Gram-Schmidt diagram (**Figure IV.41**) shows three peaks, as the *DTG* curve reported in **Figure IV.40**. *FTIR* spectra (not reported) at the Gram-Schmidt peaks mainly show the peaks relative to water and CO_2 with CO traces in the hemicellulose combustion peak (i.e., first weight loss).

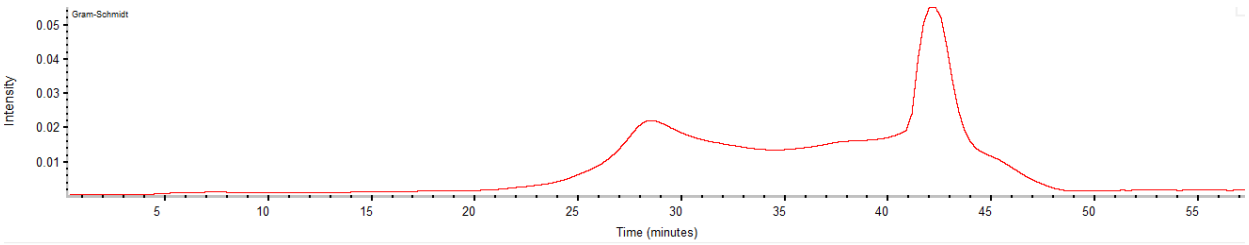

Figure IV.41 *Gram-Schmidt diagram related to the TG/DTG analysis, 10°C/min, 100 ml/min airflow, 10 mg sample* ([154], [155])

To assess the ageing effect on the thermal, physico/chemical and flammable properties, the sample was hydrothermally treated at 120 °C and RH 60% for seven days in an autoclave. Regarding the sample's appearance, analysis with an optical microscope (**Figure IV.42**) shows browning of the aged sample and a simultaneous reduction of flakes.

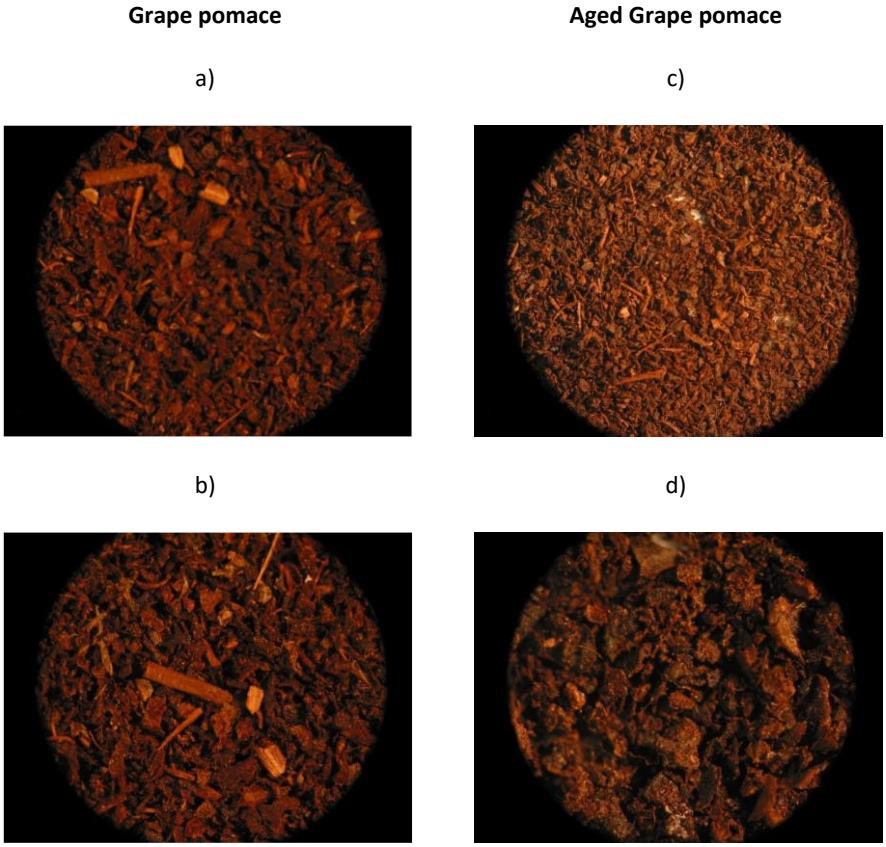

Figure IV.42 *Optical microscope images with different details of the grape pomace sample (a and b) and the aged sample (c and d)* ([154], [155])

Figure IV.43 shows *FTIR* spectra of the grape pomace sample (blue line) and the aged sample (red line), while in **Table IV.26**, the information of the bands most affected by the ageing process is reported. In the aged sample, there is a band restriction relative to hydroxyls (probably due to a water loss) and a reduction of several peaks within the wavenumbers range 1800-1200 cm^{-1}. As shown in **Table IV.26**, the aged sample presents reduced intensity of the peaks related to lignin presence (and some related to hemicellulose). The lignin and hemicellulose content decrease with the harvesting age was expected [180], reflecting an increase in the cellulose content not found from a qualitative point of view by *FTIR* spectrum.

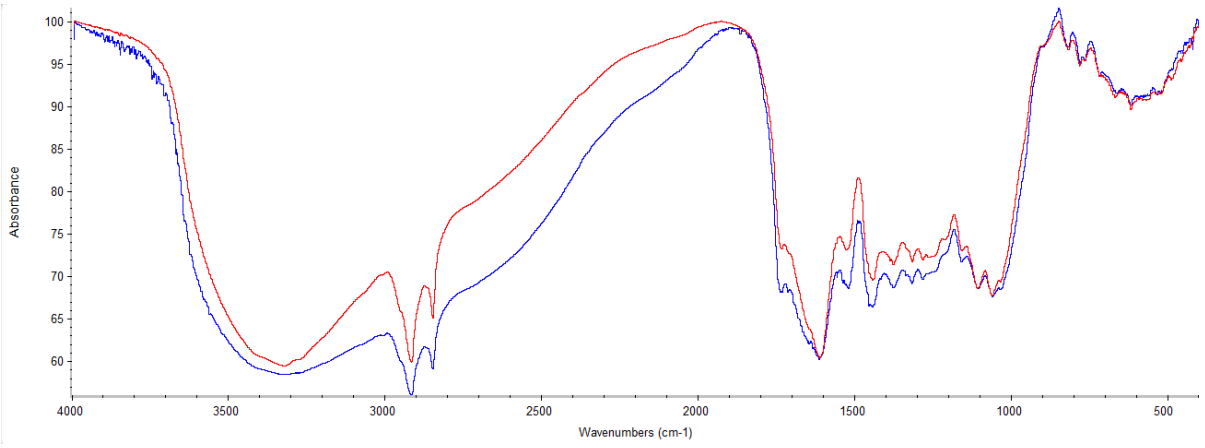

Figure IV.43 *FTIR spectra of the sample (blue line) and the aged sample (red line)* ([154], [155])

Table IV.26 *Wavenumbers with relative vibration and attribution affected by the ageing process* ([154], [155])

Wavenumber (cm^{-1})	**Vibration**	**Functional group and/or compound**
Hydroxyl band	O–H stretching	Water, alcohols and phenols
1740	C=O stretching	Ketones, aldehydes and carboxylic acids; associated with hemicellulose
1650	Absorbed O–H Conjugated C–O stretching Carbonyl C=O stretching	Water, carbohydrates, primary and secondary amides (amide I region)
1510	C=C stretching	Lignin
1420	Symmetric C–H bending O–H deformation /C–O stretching	Lignin and polysaccharides plant biomass, phenolic compounds
1365	Symmetric CH_3 bending	Polysaccharides and lignin
1320	C–N stretching	Secondary amides (amide III region)
1244	C–O stretching	Hemicellulose or syringyl ring in lignin in plant biomass and wood

Figure IV.44 shows the weight percentage curves as a function of the temperature of the sample and the aged sample in N_2 flow (a) and in airflow (b). Following the standard test method, we carried out the proximate analysis from the weight loss curve, which results in **Table IV.27**. It is worth noting that profiles are almost similar except for the moisture content within the aged sample.

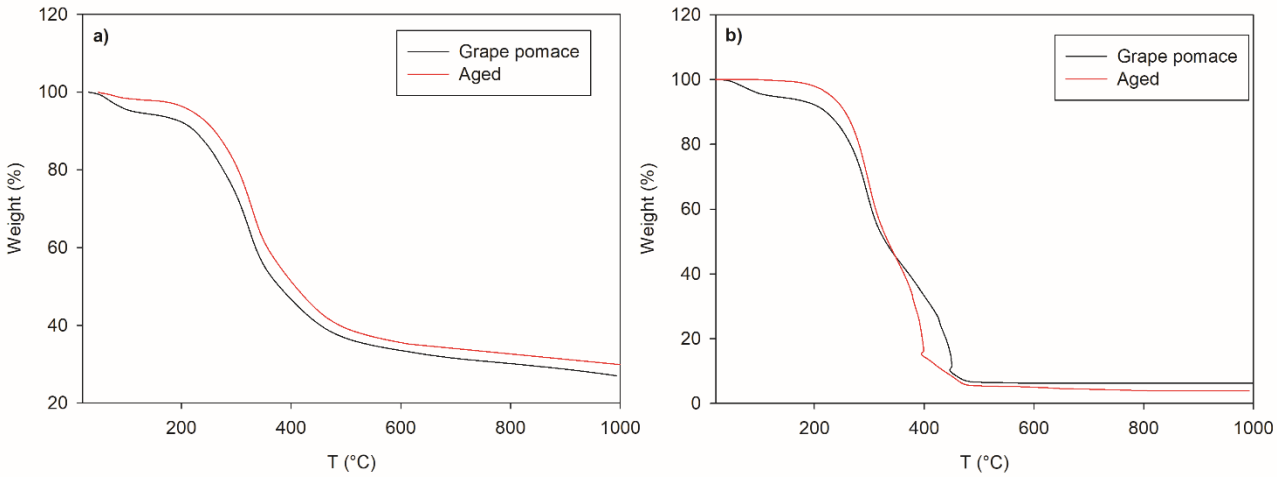

Figure IV.44 *Weight % curves as a function of the temperature of the sample and the aged sample in N_2 flow (a) and in airflow (b)* ([154], [155])

Table IV.27 *Proximate analysis results for grape pomace and the aged sample* ([129], [154], [155]**)**

Samples	*M*%	*VM*%	*A*%	*FC*%
Grape pomace	5.64	67.38	5.70	21.28
Aged grape pomace	≈0	70.10	5.00	24.90

Figure IV.45 (a) shows the *DTG* and the hemicellulose, cellulose, and lignin peaks as a temperature function, as obtained through the Fraser-Suzuki equation. The amount of each component is reported in **Figure IV.45 (b)**. As qualitatively shown through the *FTIR* spectrum, ageing reduces the lignin (from 55% to 48%) and the hemicellulose (from 31% to 29%) content and increases the cellulose (from 14% to 23%).

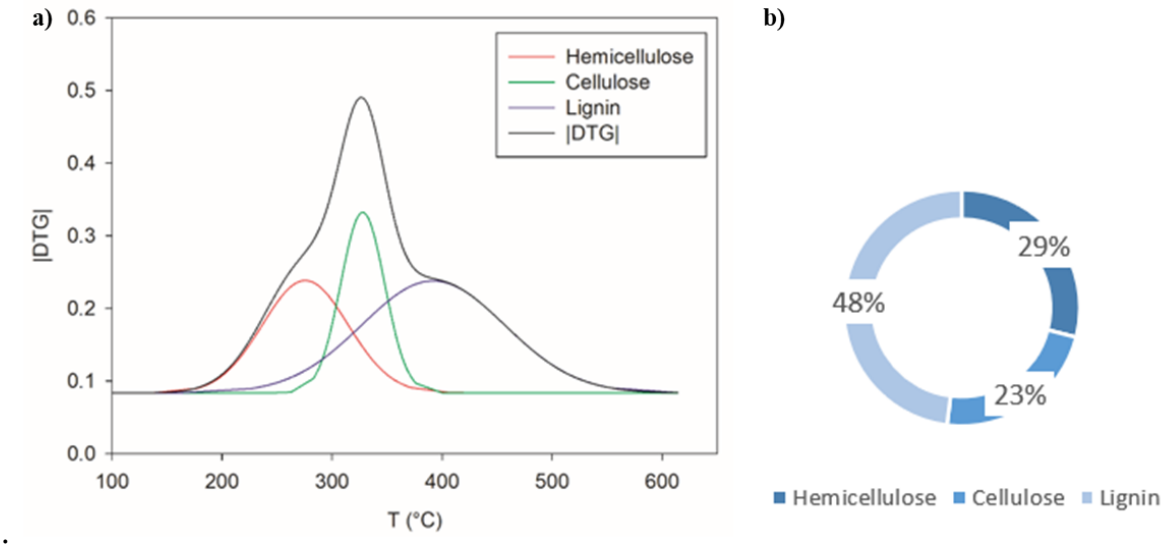

Figure IV.45 *Deconvolution through Fraser-Suzuki equation of DTG curve (a) and lignocellulosic components amounts (b) of the aged sample* ([154], [155])

Table IV.28 *Result of proximate and ultimate analysis for the sample and the aged sample* ([154], [155])

Sample	C %	H %	N %	O %	Hemicellulose %	Cellulose %	Lignin %	H/C	O/C
Sample	51.96	5.73	1.98	40.33	31	14	55	1.32	0.58
Aged	50.45	5.52	2.73	41.29	29	23	48	1.31	0.61

Table IV.29 shows the flammability/explosibility parameters of the grape pomace sample. *MIE* analysis showed that the sample was not sensitive to be ignited by an electrical spark with associated energy lower than 1 J. Despite the high volatile content, the volatile point is > 300 ° C. Regarding *MIT*, no flame instantaneously came out from the apparatus, but instead, the flame appeared after 2-3 seconds from the injection of the powder, maybe due to the off-gases ignition into the chamber (flash fire). Finally, from the explosibility parameters, the dust can be classified in the *St-1* class. *MIE* analysis was carried out on the aged sample, and the comparison with the grape pomace sample was reported in **Table IV.30**. As can be seen, ageing leads to a reduction in the minimum ignition energy. Moreover, after the electric spark ignition, the sample shows widespread hot spots (both embers and sparks) even without flame propagation at each tested concentration. This inflammable behaviour change is connected to the combined effect of reduced moisture of the aged sample and the decrease in the hemicellulose content, whose decomposition occurs at low temperature but generates CO_2, not really contributing to the propagation of the explosion/flammability process of the dust. In addition, this result may be attributable to the sample morphological variation, which shows a lower presence of flakes. To evaluate the effect

of the diameter, we used laser diffraction granulometry (Malvern Instruments Mastersizer, 2000) to characterise the granulometric distribution on both the samples, before and after the dispersion within the MIKE3 instrument used for the *MIE* evaluation. Indeed, in **Table IV.30**, the volume-weighted mean diameters (*D(4,3)*) are also reported. Although there is no ageing effect on the diameter, this process increases the particle cohesion (*D(4,3)* after the dispersion at the walls of the MIKE3 tube after dispersion. The greater cohesive behaviour of the non-aged sample can be caused by its morphological nature but, above all, by the higher moisture content. The formation of larger agglomerates further explains the insensitivity to be ignited by an electrical spark.

Table IV.29 *Explosibility and flammability properties of the grape pomace sample* ([154], [155])

Parameter	Value
Minimum ignition temperature in the cloud (MIT), °C	480
Layer ignition temperature (LIT), °C	290
Minimum ignition energy (MIE), mJ	>1000
Maximum explosion pressure, bar	6.2
Deflagration index, bar/ m s	57.8
Lower explosivity limit, g/m^3	625

Table IV.30 *MIEs and volume-weighted mean diameters (pre and post dispersion) of both the samples* ([154], [155])

Sample	*MIE* (mJ)	*D(4,3)* (μm)	*D(4,3)* post dispersion (μm)
Grape pomace	1000	208	324
Aged grape pomace	740*	211	254

* Sparks and embers at each concentration

IV.3.3. Final remarks

In this section, the flammability/explosibility analyses of non-traditional dust was effectively coupled with the chemico-physical and thermal characterization to understand the different behavior of nylon fibres and the effect of the content of lignocellulosic components and aging on a grape pomace. As regards the nylon fibres, the size of nylon 6.6 fibres, considered in terms of equivalent diameter, is the main feature to be considered in the flammability and explosibility risk. Fibres with smaller equivalent diameter can be easily dispersed thus driving more easily the formation of a flammable cloud. In addition, smaller samples have a faster thermal degradation as observed both in inert and oxidative atmosphere. The higher reactivity exhibited in the thermal tests was confirmed in the flammability tests as shown by the measured values of the minimum ignition energy. Dimensionless analysis allowed the evaluation of the step controlling the fibre

reaction paths. It was found that both the homogeneous and the heterogeneous reactive paths play a significant role in affecting the reactivity of the samples. In the homogeneous path, the pyrolysis controls flame propagation path while the heterogeneous combustion path is controlled by the intrinsic kinetic and then mainly affected by the specific surface area. All these results suggest that to reduce reactivity/flammability the key phenomena affecting the reaction progress have to be identified and quantified. As regards the grape pomace sample, the thermal analysis allowed the calculation of the contribution of the lignocellulosic components. The hemicellulose is the main component and the major contributor to volatiles. However, it generally gives mainly CO_2 and not really contributing to the propagation of the explosion/flammability process of the dust. Conversely, lignin generates CH_4 at high temperature and cellulose generates CO. As a result of the aging process, the sample is richer in cellulosic component at the expense of the lignin content, a typical component of fresh biomass, and without moisture. The degradation of lignin to cellulose makes the sample intrinsically more reactive while the lack of humidity makes the sample more dispersible. In addition, it is possible to notice a morphological difference between the pre and post-aging sample with a reduction of flakes. Consequently, analyzed at MIKE3, the aged sample is susceptible to electric discharge compared to the pre-aging sample also thanks to a reduction in post-dispersion mean diameter in MIKE3 due to a greater fragility of the aged sample.

IV.3.4. Published articles

Results discussed in this section have been published in peer-reviewed scientific journals ([154], [155], [164]):

- M. Portarapillo, E. Danzi, R. Sanchirico, L. Marmo, and A. Di Benedetto, "Energy recovery from vinery waste: dust explosion issues," *Appl. Sci., 11*(23), 11188, 2021.
- E. Danzi, A. Di Benedetto, R. Sanchirico, M. Portarapillo, and L. Marmo, "Biomass from Winery Waste : Evaluation of Dust Explosion Hazards," *Chem. Eng. Trans.*, vol. 86, 2021.
- M. Portarapillo* *et al.*, "Chemico-physical and thermal characterization of flammable nylon 6,6 dusts," *Submitt. to Fuel*, 2021.

IV.4. CFD simulation of the dispersion of binary dust mixtures in the 20 L vessel: effect of dust diameter and density

As specified in Section II.5, there are at least two main requirements for repeatable and reliable measurements of flammability and explosibility parameters of dusts: a uniform dispersion of solid particles inside the test vessel and a homogeneous degree of turbulence. In literature, it has been shown that in the standard 20 L sphere these requisites are not satisfied. Moreover, the dust dispersion and the pre-ignition turbulence level is strongly affected by dust properties (size, density, shape and moisture) that, as said in the previous sections, influence also qualitatively the flame propagation and the step controlling it. In this section, we simulated the dust dispersion of a binary dust mixture in the 20 L vessel in order to evidence the segregation phenomena caused by the different properties of the involved gases. Moreover, we carried out a simulative campaign to evaluate the contribution of the sedimentation phenomenon at varying density and diameter.

IV.4.1. Methodologies

CFD simulation of the dispersion of binary dust mixtures in the 20 L vessel

In this work, we aimed at investigating the dust dispersion and turbulence generation in the 20 L sphere for the case of dust mixtures. To this end, simulations for nicotinic acid/anthraquinone mixtures were performed with a validated three-dimensional *CFD* model. These two dusts were chosen since, in recent investigations, it has been found the occurrence of synergistic effects between niacin and anthraquinone that affect the flammability and explosibility parameters ([22], [138], [145]). Detailed model description was given in a previous paper [122]. Parallel calculations were performed by means of the segregated pressure-based solver of the code ANSYS Fluent (Release 19.0). Simulation conditions and dust properties are given in **Table IV.31** and **Table IV.32**, respectively.

Table IV.31 *Simulation conditions* [181]

Parameter	Value
Dust container volume (L)	0.6
Sphere volume (L)	20
Initial pressure of the container (bar)	21
Initial pressure of the sphere (bar)	0.4
Dust concentration (g/m^3)	250

Table IV.32 *Dust properties used for simulation* [181]

Property	Niacin	Anthraquinone
Density (kg/m^3)	1470	1310
Diameter (μm)	41.4	26.9

We performed simulations of mixtures of niacin and anthraquinone (25 % w/w, 50 % w/w, 75 % w/w of niacin/total dust) to test the effects of varying particle size and density.

Effect of dust diameter and density on feeding and sedimentation

Moreover, to study the effect of diameter and density on the fraction of fed dust that remains dispersed in the sphere at the ignition delay time t_d, a simulation campaign was carried out, in which the dispersion of the dust in the 20 L sphere was simulated under the operating conditions contained in **Table IV.33** with a nominal dust concentration set at 250 g/m^3. Theoretically, the effect of concentration should also be investigated. Indeed, the dust concentration does not seem to have a direct effect on the sedimentation phenomenon but indirectly affects it by modifying the flow field of the continuous phase.

It is worth underlining that the dust aliquot that remains dispersed in the form of a cloud inside the sphere is the one that, once triggered the explosion, contributes to it. The rest of the powder will form a layer on the base of the vessel and on the rebound nozzle.

To this aim, the mass fractions of dispersed (y_{disp}) and deposited (y_{dep}) dust present in the sphere at different instants of time (0.02,0.04,0.06 s) were calculated as a function of the dimensionless relaxation time τ^+. y_{disp}, y_{dep} and τ^+ were defined as

$$y_{disp} = \frac{m_{disp}}{m_{tot}} = \frac{m_{disp}}{C_{nom} \cdot V} \tag{55}$$

$$y_{dep} = \frac{m_{dep}}{m_{tot}} = \frac{m_{dep}}{C_{nom} \cdot V} \tag{56}$$

$$\tau^+ = \frac{\tau}{t_d} = \frac{\rho_p d_p^2}{18 \cdot \mu \cdot t_d} \tag{57}$$

where τ (s) is the relaxation time, m_{disp} (kg) is the dispersed dust mass within the 20 L sphere and m_{dep} (kg) is the deposited dust mass. It is the characteristic time for the particle to approach steady motion. It characterizes the time required for a particle to adjust or "relax" its velocity to a new condition of forces. It is an indication of the particle ability to quickly adjust to a new environment or condition. Since relaxation time is proportional to the square of particle diameter, it increases rapidly with the increase of particle size. Usually, small particles "relax" to new environments (i.e., following the flow well) in a very short time, while larger particles are more "stubborn" and tend

to stick to their original path.

Table IV.33 *Dust properties used for simulation* [181]

Diameter (μm)	Density (kg/m^3)
10	500, 1000, 2000, 3000, 4500, 7000
60	500, 1000, 2000, 3000, 4500, 7000
100	500, 1000, 2000, 3000, 4500, 7000
200	500, 1000, 2000, 3000, 4500, 7000
400	500, 1000, 2000, 3000, 4500, 7000

IV.4.2. Results

CFD simulation of the dispersion of binary dust mixtures in the 20 L vessel

Figure IV.46 shows the pressure-time profiles as computed in the sphere and in the dust container for both niacin and anthraquinone. From these profiles, the phase during which the dust-air mixture goes from the container to the sphere (i.e., the injection phase) can be identified as a phase lasting 40 ms. Indeed, after 40 ms, the pressure in the sphere reaches 1 bar and, thus, further injection of dust-air becomes substantially negligible. Moreover, almost identical curves are simulated for both niacin and anthraquinone, meaning that the pressure-time profile is not affected by the differences in dust density and diameter. In **Figure IV.46**, the model results in terms of pressure-time profiles inside the sphere are compared to literature experimental data [64]. A rather good agreement between experimental data and model predictions is found, providing a model validation. The comparison shows that, in the first 25 ms, the experimental data are slightly higher (about 11 %). The simulated values need about 10 ms more to reach 1 bar. As a consequence, it is likely that, in the simulation, the dust amount that remains in the container is slightly lower.

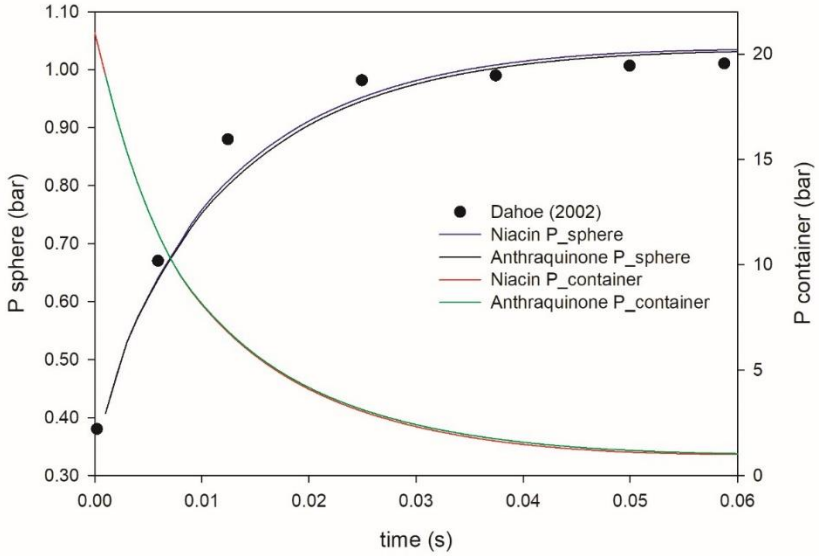

Figure IV.46 *Pressure-time profiles computed in the sphere and in the container for pure dusts* [181], *and literature data for the sphere* [64]

In **Figure IV.47**, the temporal trends of the root mean square velocity (*RMS*) in the case of only air, niacin and anthraquinone are shown as computed in the center of the sphere. The *RMS* was calculated from the turbulence kinetic energy *k* assuming an isotropic flow field:

$$k = \frac{3}{2}(u')^2 \tag{58}$$

Experimental data measured by Dahoe et al. (2002) are also shown [64]. In particular, these are data related to both vertical and horizontal velocity component fluctuations from experiments with only air. From **Figure IV.47**, it appears that there is a short time-period of turbulence build-up followed by a much longer time-period of turbulence decay. Turbulence starts decaying few milliseconds after the opening of the valve, well before the end of the injection phase. It is found that the *RMS* curves differ in the first 30 ms, while differences decrease after 30 ms. In the first part (t < 30 ms), the combined effects of dust concentration and dust diameter affect the spatio-temporal distribution of flow velocity and turbulence kinetic energy. Indeed, the flow development is affected not only by the dust concentration, but also by the particle size. The values of *RMS* for dusts are lower than the experimental values for only air. In going from anthraquinone to niacin and, thus, increasing the dust diameter, a further decrease in *RMS* is found.

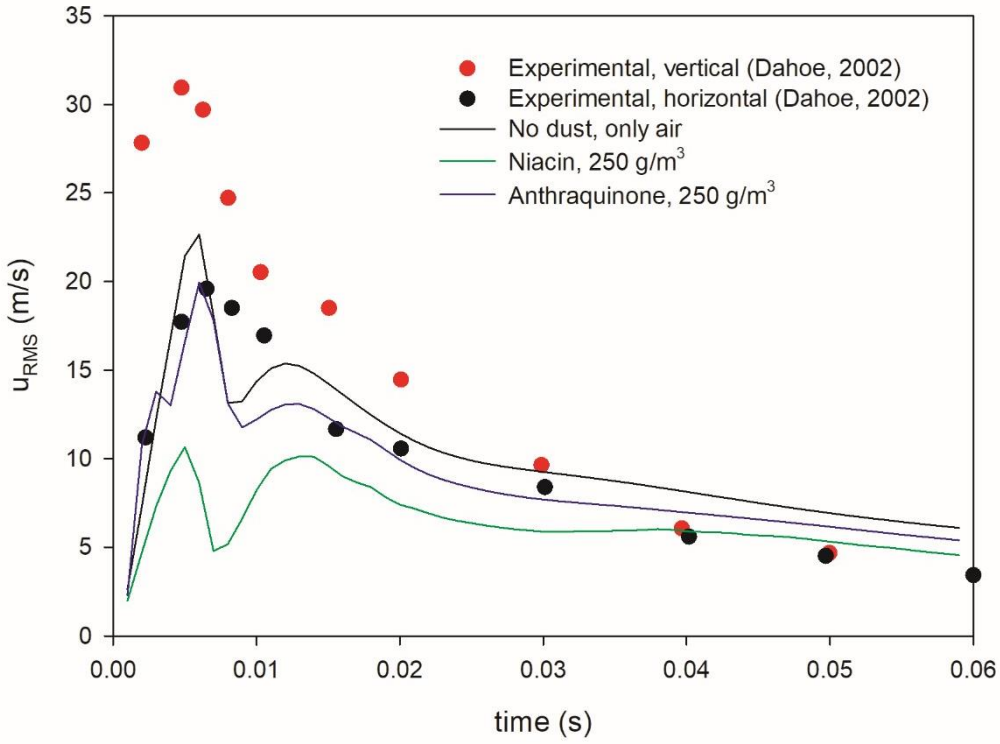

Figure IV.47 *Temporal trends of root mean square velocity for only air, niacin and anthraquinone: simulations* [181] *and literature data (these latter are for only air)* [64]

In **Figure IV.48** and **Figure IV.49**, the time sequence of the maps of (flow) velocity vectors colored by the (flow) velocity magnitude is shown as computed over the frontal x-y plane of the sphere (more clearly shown in the empty images of each figure) for pure niacin and pure anthraquinone, respectively. It can be seen that vortex structures form starting from 20 ms. Such structures become well-defined at 60 ms. In both cases, asymmetric fields are simulated, especially at t = 60 ms. This behavior has also been previously found ([122], [182]). In particular, Kartushinsky et al. (2011) developed a three-dimensional model of particulate flow in a horizontal pipe using the Reynolds-Averaged Navier-Stokes method. Simulation results showed that, in spite of the geometric symmetry, the presence of solid particles in the flow may return asymmetric fields due to the gravitational effect on the particles and particle sedimentation. It is worth noting that the particle-induced asymmetry of the flow field is more evident in the case of niacin (**Figure IV.48**), which is characterized by higher values of diameter and density than anthraquinone and, thus, by a higher value of sedimentation velocity [183].

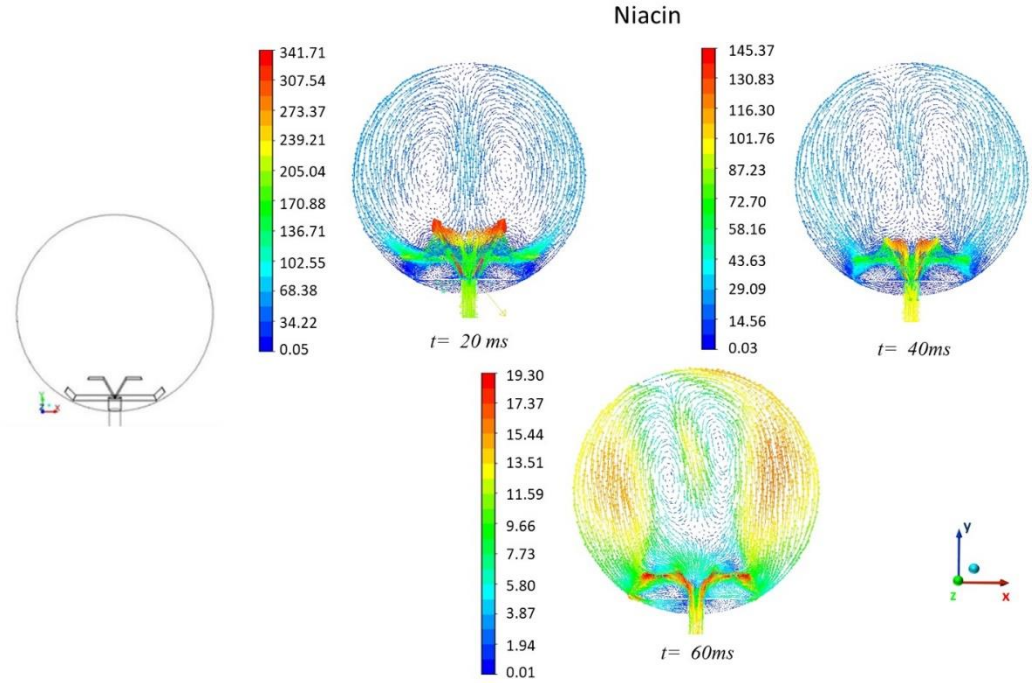

Figure IV.48 *Time sequence of maps of velocity vectors colored by velocity magnitude (m/s): niacin (frontal view)* [181]

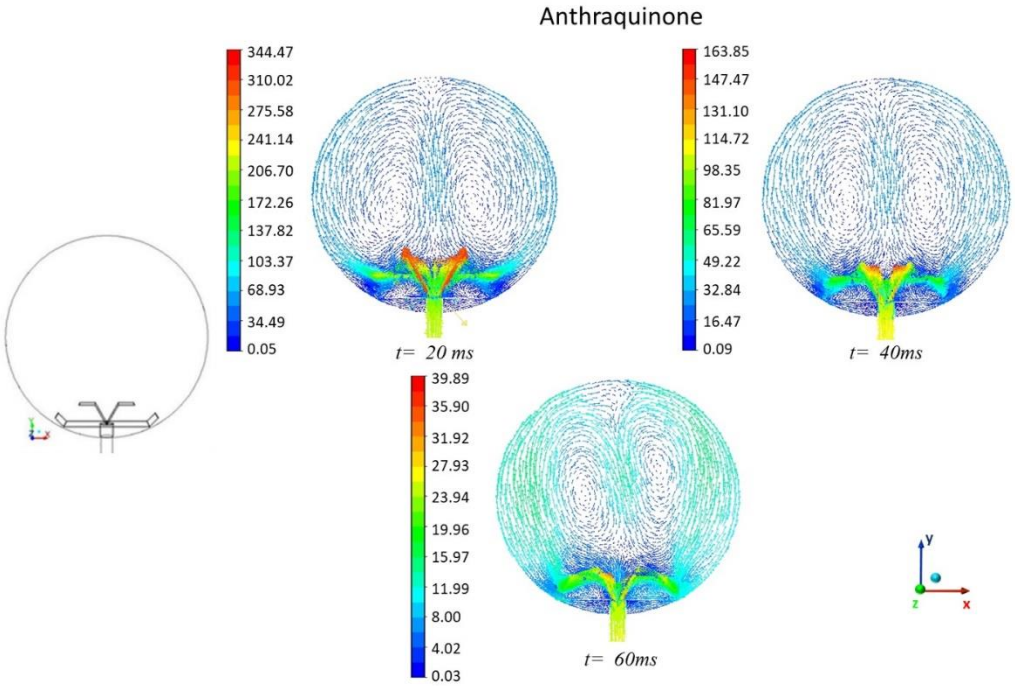

Figure IV.49 *Time sequence of maps of velocity vectors colored by velocity magnitude (m/s): anthraquinone (frontal view)* [181]

In **Figure IV.50** and **Figure IV.51**, the time sequence of the maps of turbulence kinetic energy is shown as computed over the frontal x-y plane for pure niacin and pure anthraquinone, respectively. As already found for the velocity vector maps, the presence of dust gives rise to an asymmetric distribution of turbulence kinetic energy. Anthraquinone shows fields characterized by higher velocity and more intense turbulence than niacin, and this can be attributed to its smaller diameter.

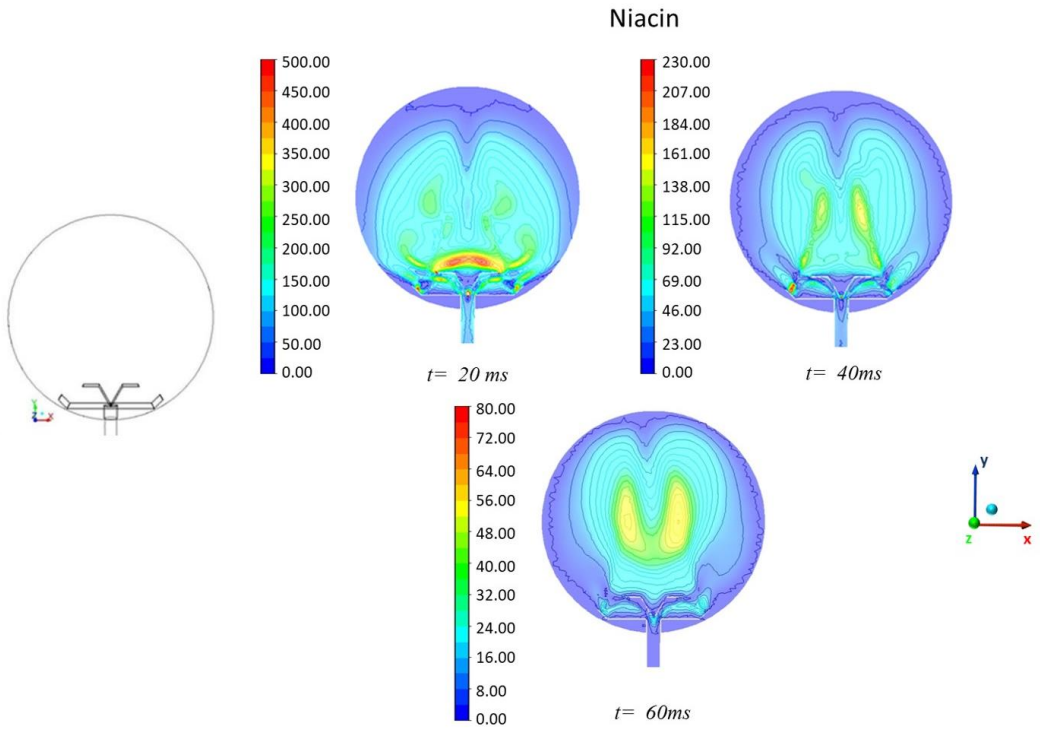

Figure IV.50 *Time sequence of maps of turbulence kinetic energy (m^2/s^2): niacin (frontal view)* [181]

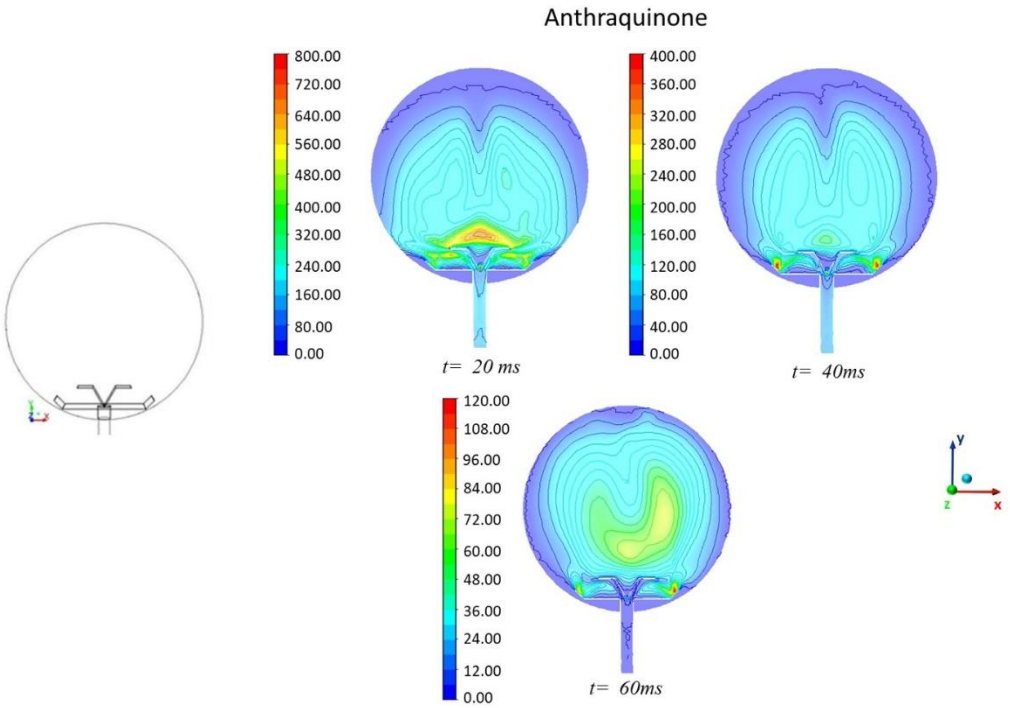

Figure IV.51 *Time sequence of maps of turbulence kinetic energy (m^2/s^2): anthraquinone (frontal view)* [181]

The spatio-temporal distribution of dust concentration inside the sphere is shown in **Figure IV.52**, through the time sequence of particle tracks colored by the ratio χ between the local dust concentration and the nominal dust concentration (250 g/m^3), for (a) pure niacin and (b) pure anthraquinone. Due to the presence of vortices, it appears that the highest values of dust concentration are attained close to the wall and, more generally, at the edge of the vortices. This suggests that the solid particles are not entrained by the fluid flow and, thus, the vortices represent dead volumes for the dust. In the case of niacin (**Figure IV.52 (a)**), the accumulation of dust particles gives rise to the formation of a three-dimensional cross, which is well evident at the ignition time (t = 60 ms). At this time, the particles are highly concentrated at the sphere wall, and values of dust concentration much higher than the nominal value are attained ($\chi = 2$; C = 500 g/m^3). This result is in agreement with the findings by Kalejaiye et al. (2010) [121], who measured the values of transmission in different positions inside the 20 L sphere. Lower values of transmission (and, thus, higher values of concentration) were found in correspondence to the probes inside. In the case of anthraquinone (**Figure IV.52 (b)**), due to their smaller diameter, the dust particles are better entrained by the fluid flow and, thus, the cross-shaped structure is not predicted.

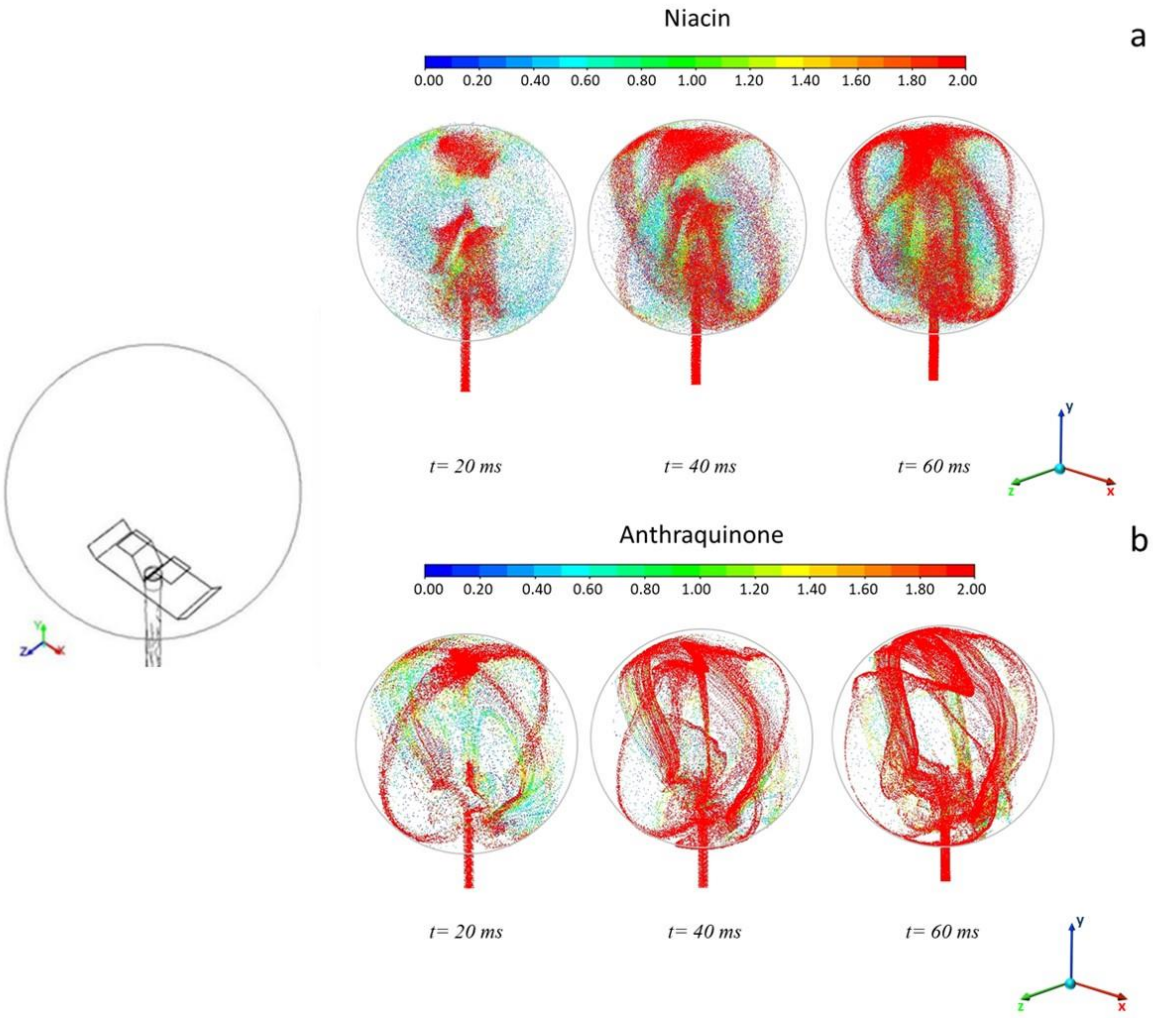

Figure IV.52 *Time sequence of particle tracks colored by χ (ratio between local dust concentration and nominal dust concentration) as computed for (a) niacin and (b) anthraquinone (isometric view)* [181]

The temporal trend of dust concentration in the center of the sphere is shown in **Figure IV.53** for (a) niacin and (b) anthraquinone. At t = 60 ms (ignition time), the concentration of niacin in the center is equal to 500 g/m^3, which is the same value as close to the wall. This is a result of the fact that niacin particles are located mainly at the edge of the vortices. Conversely, at t = 60 ms, the concentration of anthraquinone in the center is equal to zero. In this case, beyond diameter, density plays a role. The higher the density ratio between dust and gaseous medium, the lower the capability of the vortices to entrain the solid particles. Niacin is more dense than anthraquinone and, thus, niacin particles are concentrated mainly at the edge of the vortices [184], while anthraquinone is dispersed in the internal zone of the vortices. For both the pure dusts, the value

of concentration in the center at the ignition time differs from the nominal value, and the distribution of particles is strongly non-uniform.

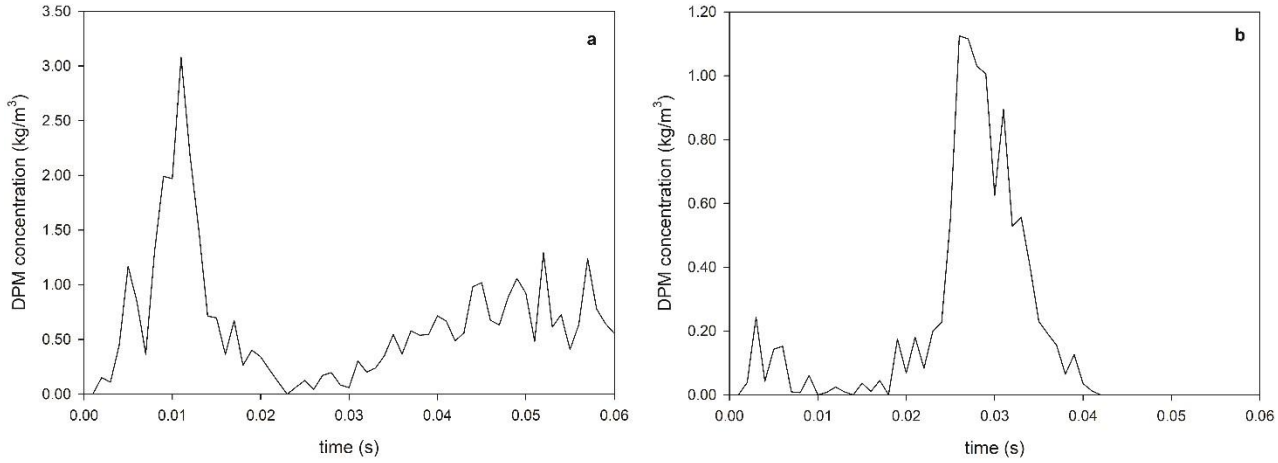

Figure IV.53 *DPM concentration in the center of the sphere versus time for (a) niacin and (b) anthraquinone* [181]

In **Figure IV.54**, the time sequences of the maps of (flow) velocity vectors colored by the (flow) velocity magnitude are shown as computed over the frontal x-y plane of the sphere (more clearly shown in the empty images of each figure) for niacin/anthraquinone mixtures at different compositions. As in the case of pure dusts, due to the presence of vortices, the highest values of dust concentration are attained close to the wall and, thus, in zones external to the vortices themselves. This suggests that the solid particles are not entrained by the fluid flow and, thus, the vortices are dead volumes for the dust.

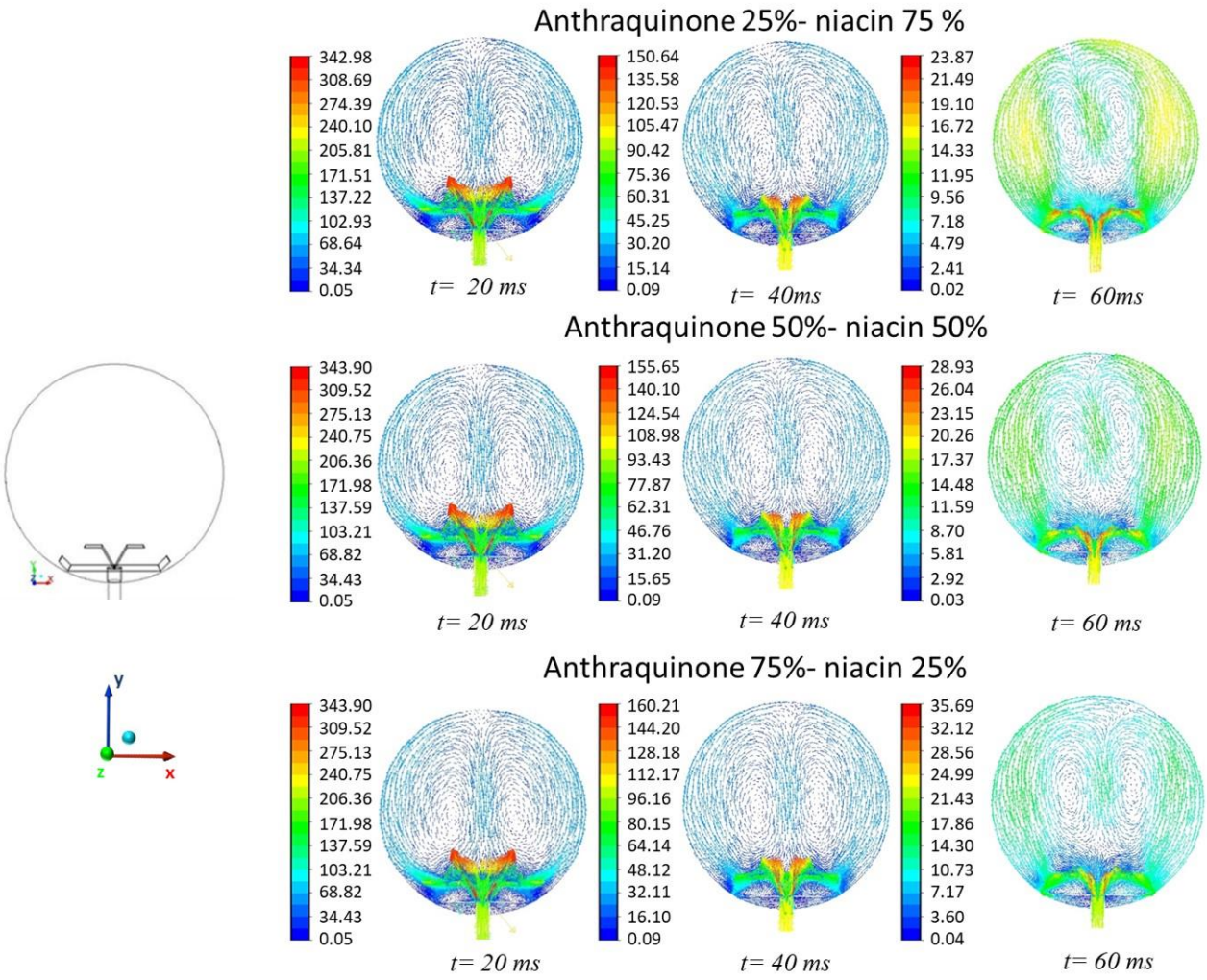

Figure IV.54 *Time sequences of maps of velocity vectors colored by velocity magnitude (m/s) for niacin/anthraquinone mixtures at different compositions (frontal view)* [181]

In **Figure IV.55**, the time sequences of the maps of turbulence kinetic energy are shown as computed over the frontal x-y plane for niacin/anthraquinone mixtures at different compositions. Even in the case of dust mixtures, an asymmetric distribution of turbulence kinetic energy is simulated. As discussed above, due to the smaller particle diameter, anthraquinone shows fields characterized by higher velocity and more intense turbulence than nicotinic acid. Thus, as the concentration of anthraquinone in the dust mixture is increased, the turbulence kinetic energy increases. This is confirmed by **Figure IV.56** showing the values of turbulence kinetic energy in the center of the sphere at 60 ms (ignition time) for air, pure dusts, and dust mixtures at different compositions. **Figure IV.56** clearly shows the trend of increasing turbulence kinetic energy with increasing concentration of anthraquinone in the dust mixture (i.e., in going from pure niacin to

pure anthraquinone). However, the highest value of turbulence kinetic energy is attained in the case of air without dust.

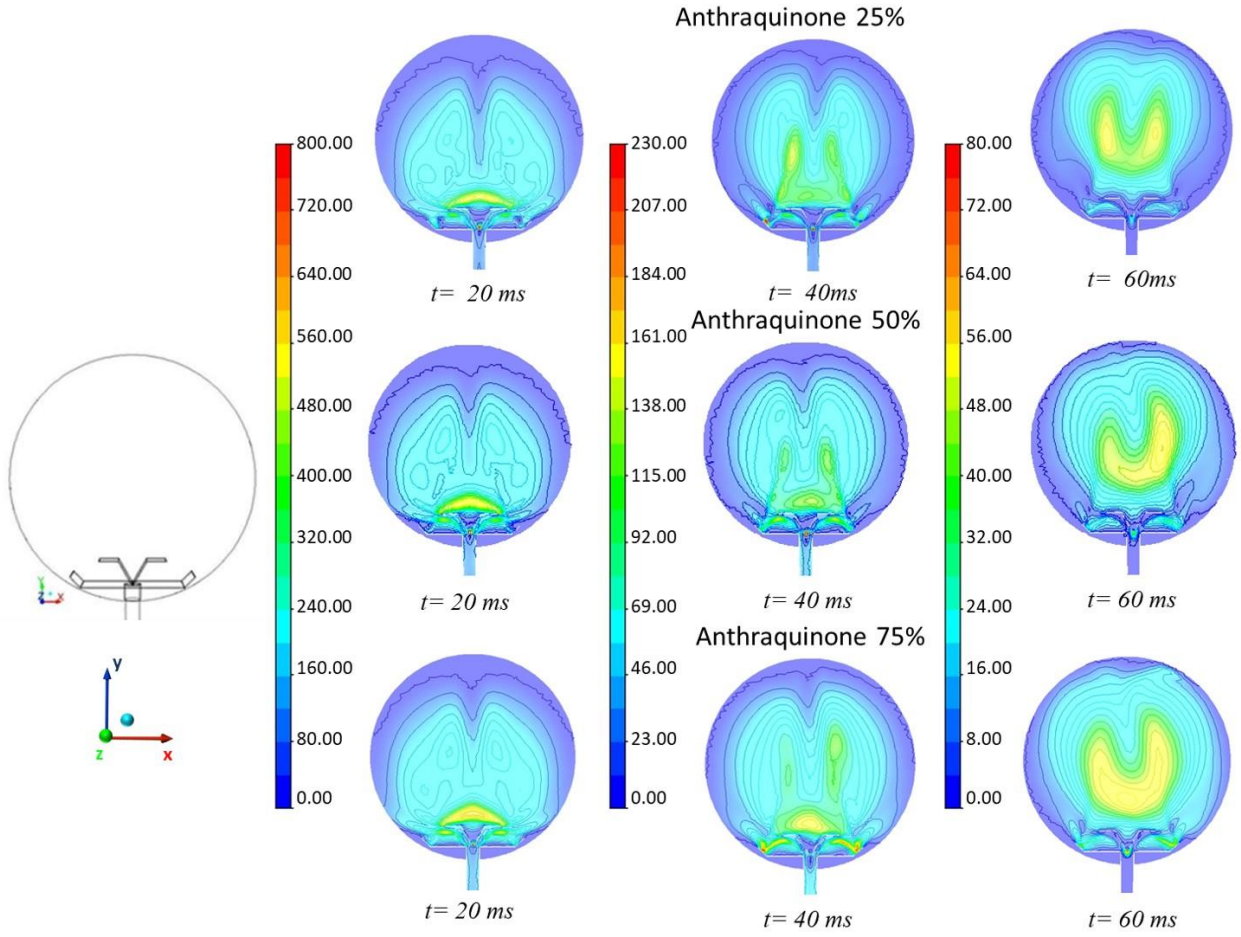

Figure IV.55 *Time sequences of maps of turbulence kinetic energy (m^2/s^2) for niacin/anthraquinone mixtures at different compositions (frontal view)* [181]

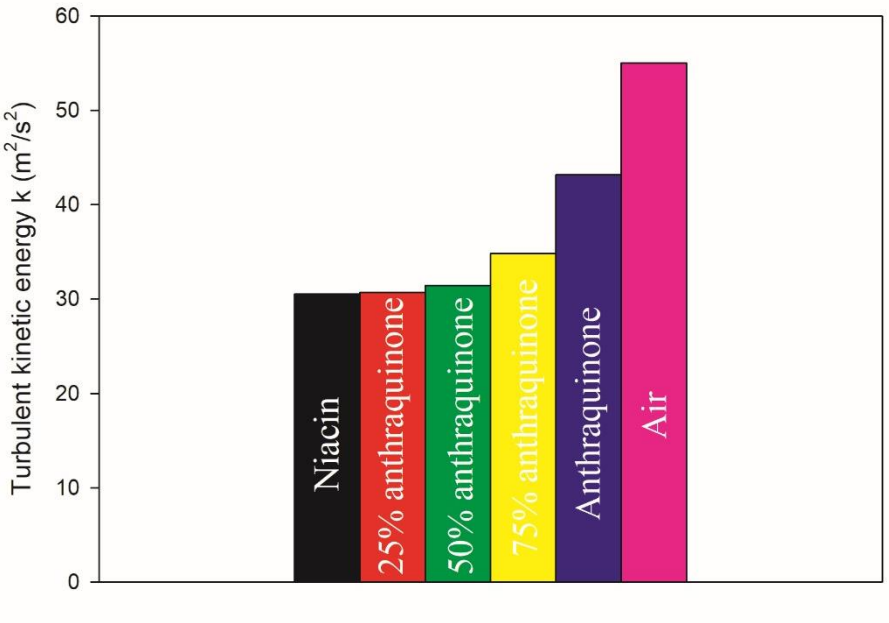

Figure IV.56 *Values of turbulence kinetic energy as computed in the center of the sphere at 60 ms (ignition time) for air, pure dusts, and dust mixtures at different compositions* [181]

The spatio-temporal distribution of dust concentration inside the sphere is shown in **Figure IV.57**, through the time sequences of particle tracks colored by the ratio χ between the local dust concentration and the nominal dust concentration (250 g/m^3), for dust mixtures at different compositions. This figure further confirms that the highest values of dust concentration are attained externally to the vortices. In particular, at the ignition time (t = 60 ms), the dust is highly concentrated at the sphere wall, and values of concentration higher than the nominal value are predicted (χ = 2; C = 500 g/m^3). Due to the higher ability of anthraquinone to be entrained by the fluid flow, the internal zone of the vortices is gradually filled by solid particles with increasing concentration of anthraquinone in the dust mixture.

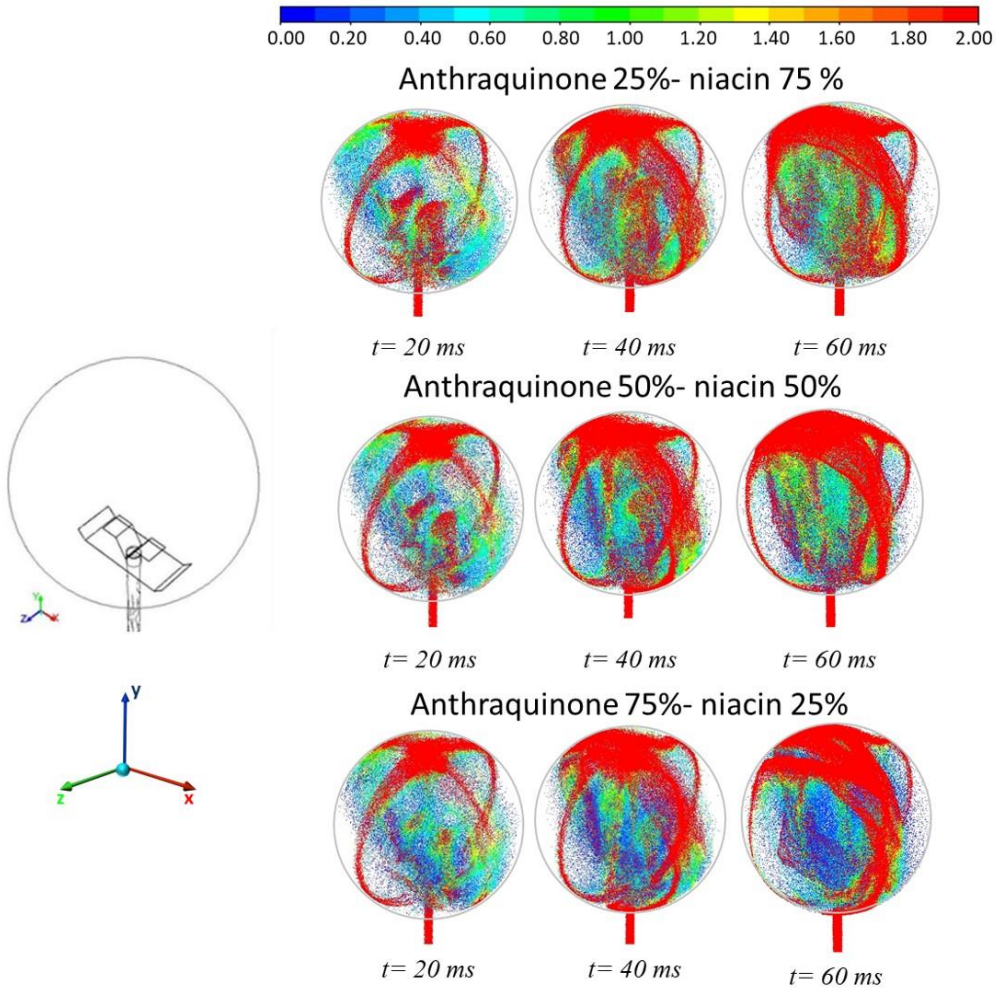

Figure IV.57 *Time sequences of particle tracks colored by χ (ratio between local dust concentration and nominal dust concentration) as computed for niacin/anthraquinone mixtures at different compositions (isometric view)* [181]

The temporal trend of dust concentration in the center of the sphere is shown in **Figure IV.58** for niacin/anthraquinone mixtures at different compositions. In particular, for each mixture composition, the temporal trends of total concentration and concentration of the two pure dusts are plotted. The total concentration is always different from the nominal one and, at the ignition time (t = 60 ms), only niacin is present at the center of the sphere. As a consequence, in the case of spark ignition, it is likely that only niacin will be ignited, anthraquinone concentration being almost zero. In the case of chemical igniters, due to the larger ignition volume, also anthraquinone will be involved in ignition. However, regardless of the ignition type, the strongly non-uniform dust distribution affects the flame speed and then, the pressure rise.

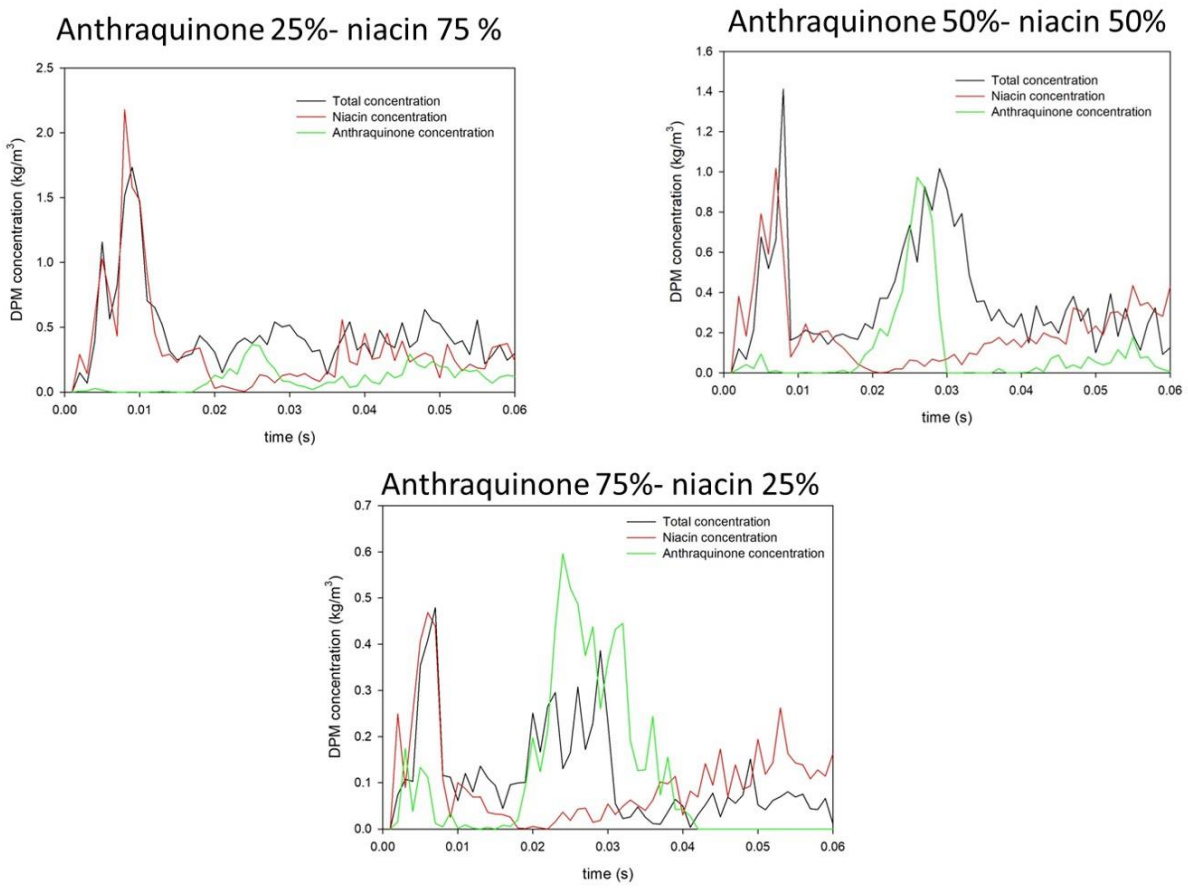

Figure IV.58 *DPM concentrations in the center of the sphere versus time for niacin/anthraquinone mixtures at different compositions* [181]

Global assessment of the results obtained for dust mixtures, thus, demonstrates that a new issue arises. Since pure dusts may have quite different properties (diameter, density, shape, etc.), in the case of dust mixtures, particles will follow preferential paths that are dictated by these differences, thus resulting in zones richer in a pure constituent and poorer in the other one and *vice versa*. This issue is further confirmed by **Figure IV.59** showing the particle tracks colored by (normalized) total and pure dust concentrations as computed at the ignition time for niacin/anthraquinone mixtures at different compositions. Due to the different properties, pure dusts are not homogenously mixed up within the sphere but, on the contrary, they tend to segregate. This issue negatively affects repeatability and reliability of experimental tests carried out in the standard 20 L sphere to evaluate safety parameters of dust mixtures.

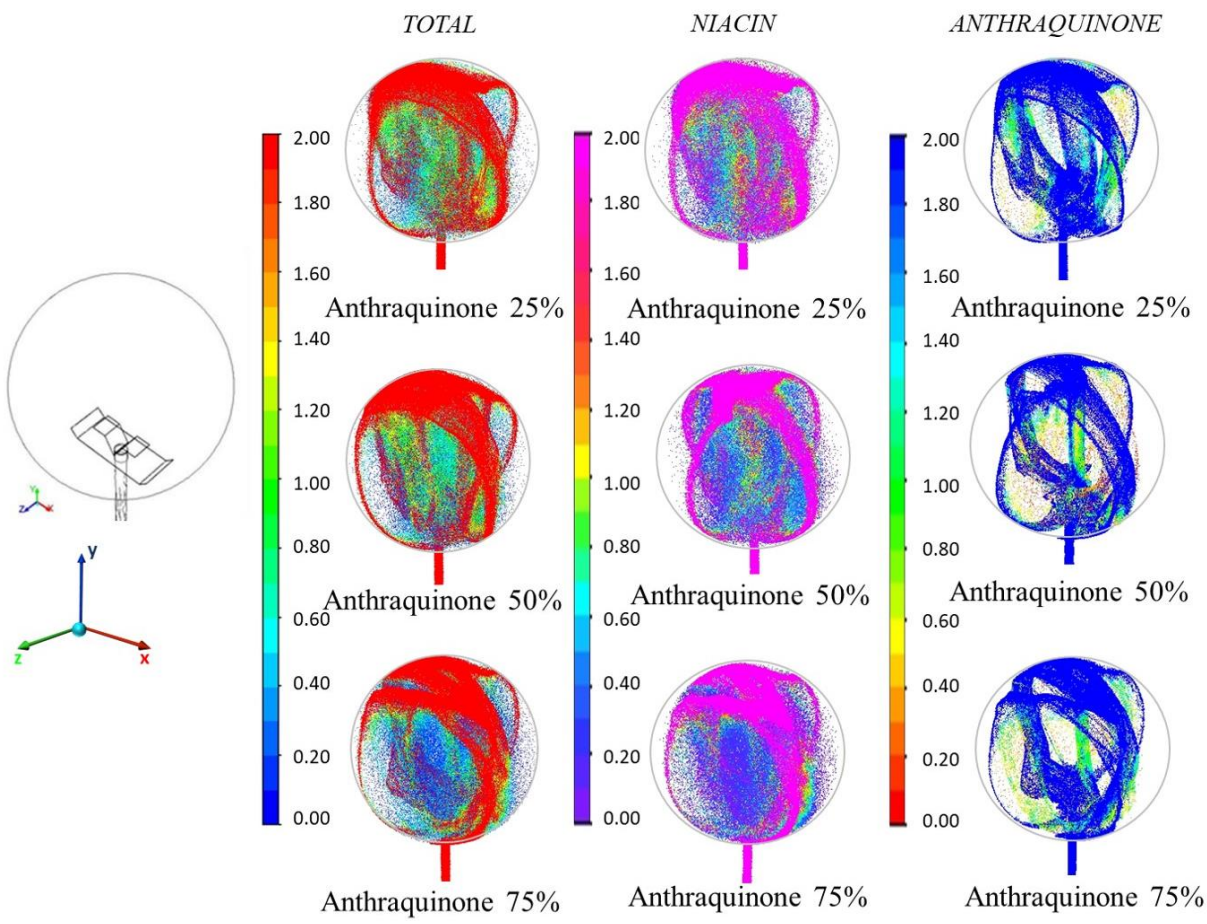

Figure IV.59 *Particle tracks colored by (normalized) total and pure dust concentrations as computed at 60 ms (ignition time) for niacin/anthraquinone mixtures at different compositions (isometric view)* [181]

Effect of dust diameter and density on feeding and sedimentation

As just discussed, in the case of dust mixtures having different properties, the issues already known regarding the dispersion of the powder inside the 20 L sphere are even more critical. In order to highlight the effect of diameter and density on feeding and on the sedimentation phenomenon, the results of a simulation campaign conducted with the same *CFD* model are reported in this section. As per definition, the trend of the dimensionless relaxation time is quadratic with respect to the diameter and linear with the density (**Figure IV.60**).

Figure IV.61 shows the mass-to-nominal mass ratio present within the vessel, the tube and the container at the ignition delay time, at different values of diameter and as function of density. As can be seen, at low value of diameter (<100 μm) the mass-to-nominal mass ratios within all the three parts of the whole domain are less sensitive to density variations. As the diameter increase, the dependence on the density is more relevant, the ratio in the explosion vessel decreases while

increases both in the tube and in the container. The same behaviour was found at low values of density (<1000 kg/m^3) where the mass-to-nominal mass ratios within all the three parts of the whole domain are less sensitive to diameter variations (**Figure IV.62**). The trends of y_{disp} within the explosion vessel are reported as function of density at different value of diameter (**Figure IV.63**) and as function of diameter at different value of density (**Figure IV.64**), parametric in time. These Figures are useful to better visualize the sedimentation phenomenon within the vessel. The following considerations can be performed:

- At fixed values of both dust density and diameter, the feeding phase can be observed. Indeed, the fraction of dust dispersed in the vessel increases from 0.02 s to 0.04 s
- At fixed values of both dust density and diameter, the sedimentation phase can be observed. Indeed, the fraction of dust dispersed in the vessel decreases from 0.4 s to 0.06 s
- y_{disp} dramatically decreases as density and diameter increase, starting from a maximum value equal to 0.86 and reaching a plateau value at 0.50

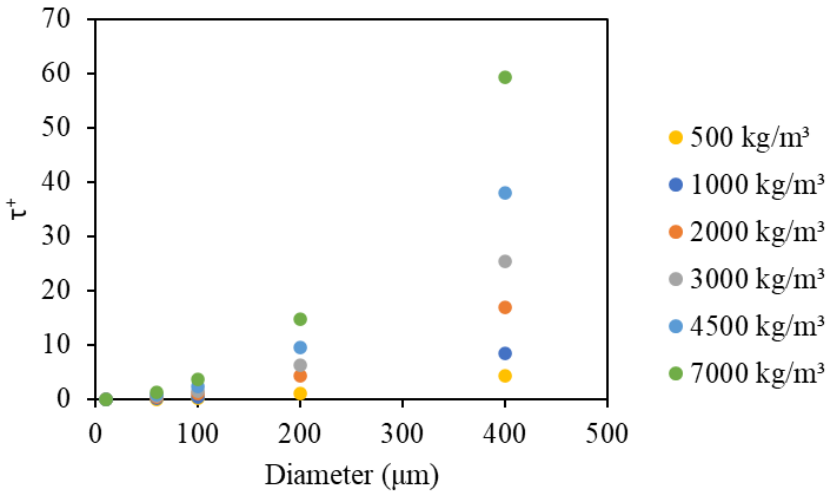

Figure IV.60 *Dimensionless relaxation time as a function of the diameter and parametric in the density*

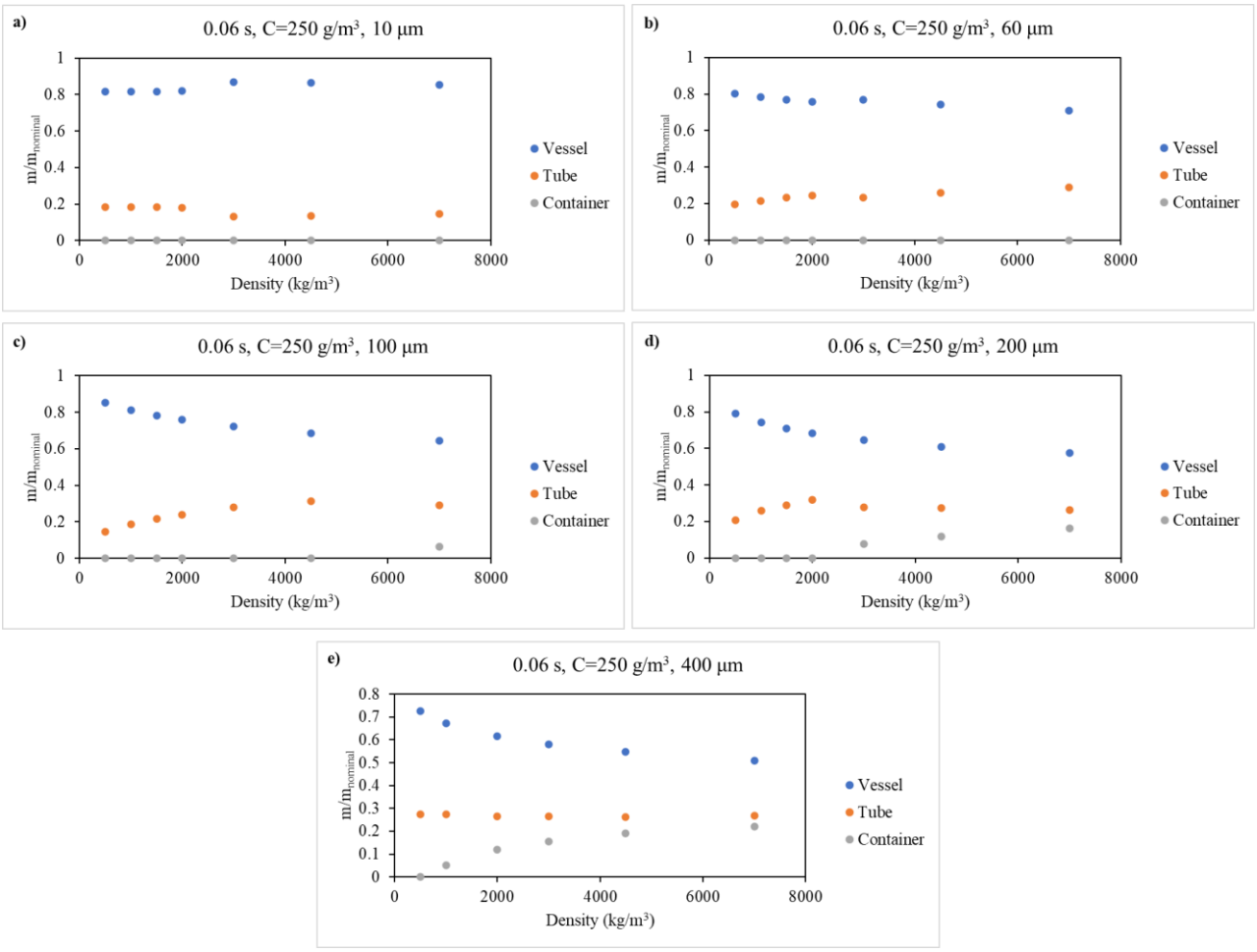

Figure IV.61 *Mass-to-nominal mass (C_{nom}=250 g/m^3) ratio at 10 µm (a), 60 µm (b), 100 µm (c), 200 µm (d), 400 µm (e) as a function of density at the ignition delay time in the vessel (blue scatter plot), the tube (orange scatter plot) and the container (grey scatter plot)*

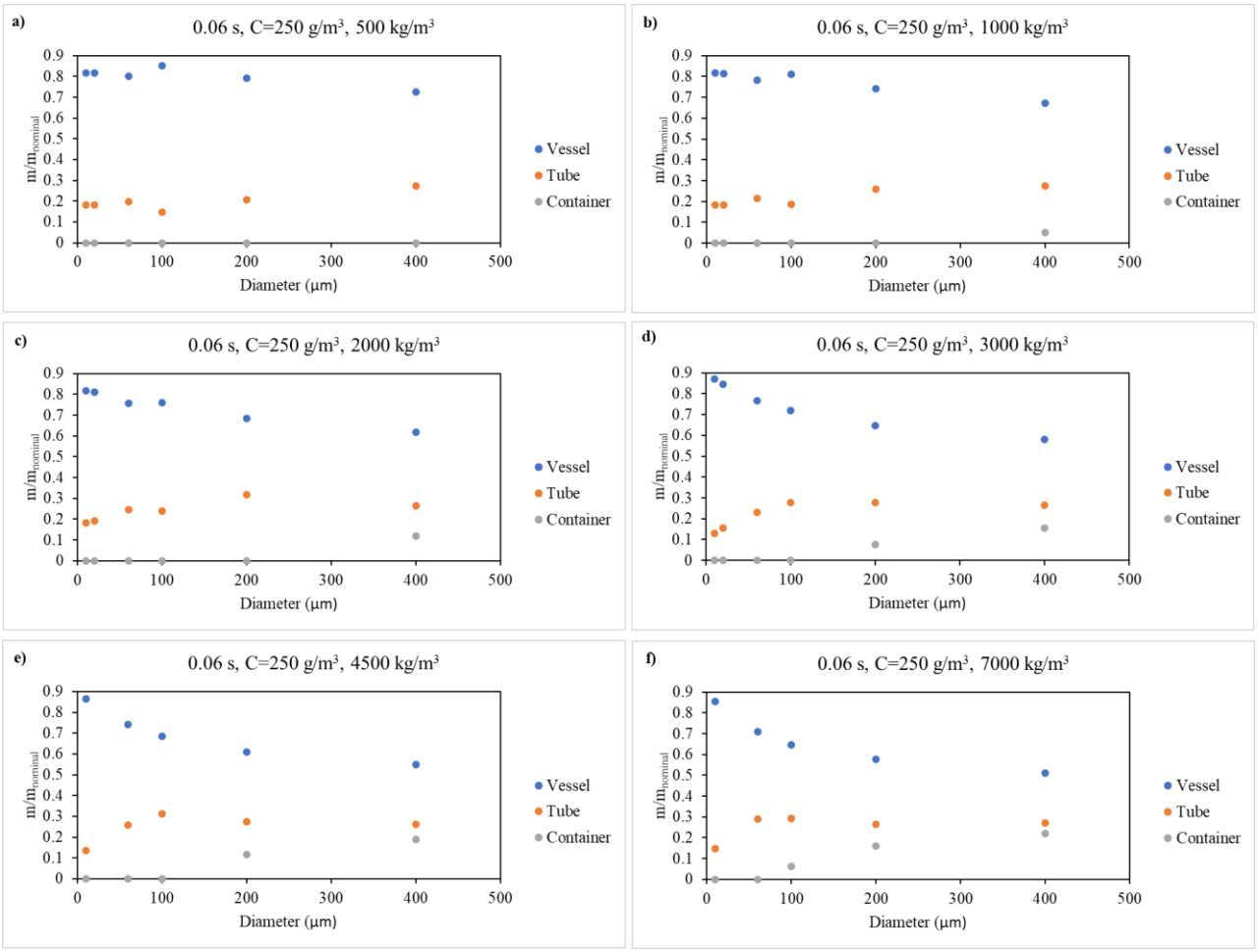

Figure IV.62 *Mass-to-nominal mass (C_{nom}=250 g/m^3) ratio at 500 kg/m^3 (a), 1000 kg/m^3 (b), 2000 kg/m^3 (c), 3000 kg/m^3 (d), 4500 kg/m^3 (e) and 7000 kg/m^3 (f) as a function of diameter at the ignition delay time in the vessel (blue scatter plot), the tube (orange scatter plot) and the container (grey scatter plot)*

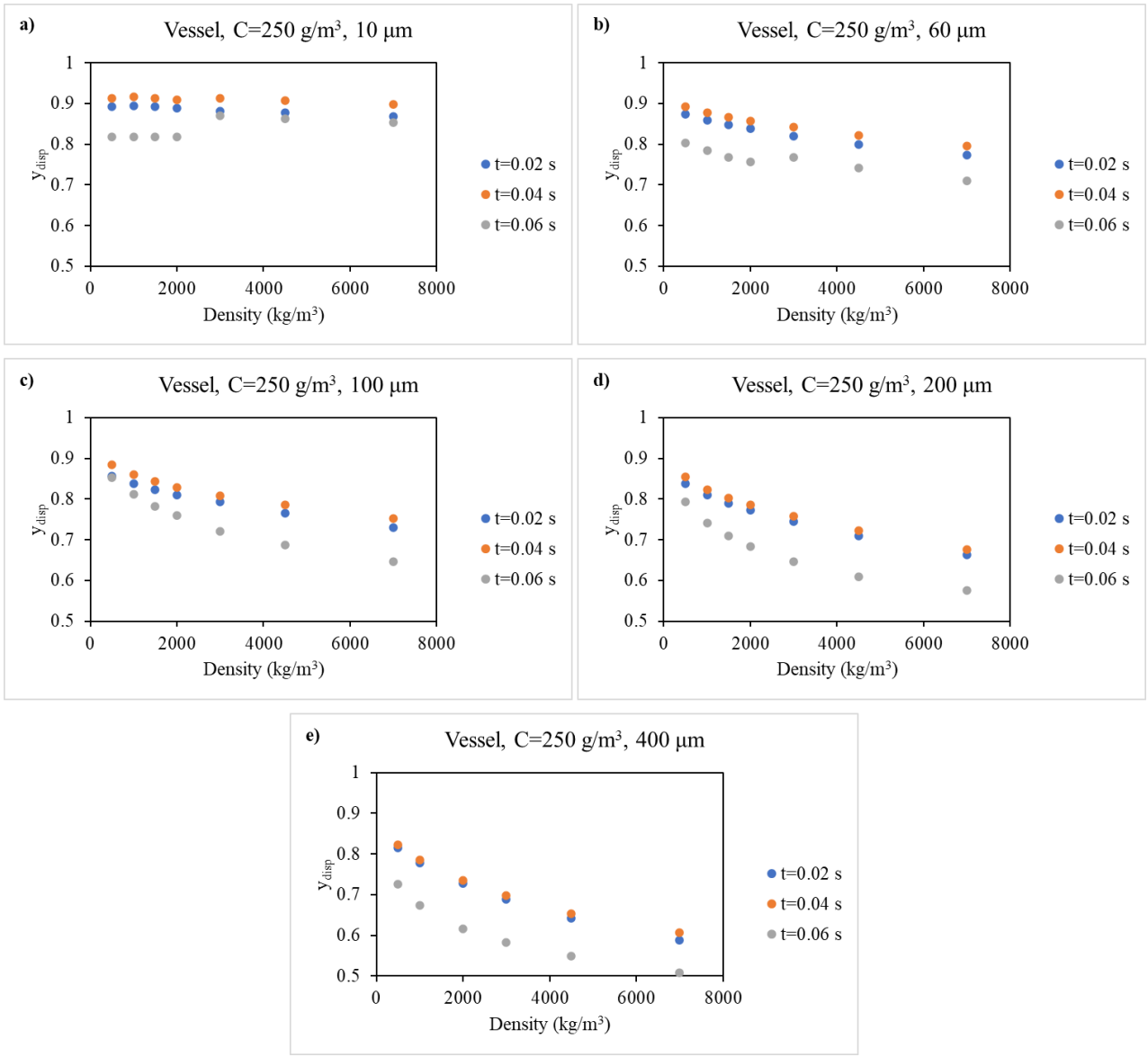

Figure IV.63 *y_{disp} (C_{nom}=250 g/m³) at 10 µm (a), 60 µm (b), 100 µm (c), 200 µm (d), 400 µm (e) as a function of density within the explosion vessel at 0.02 s (blue scatter plot), 0.04 s (orange scatter plot) and 0.06 s (grey scatter plot)*

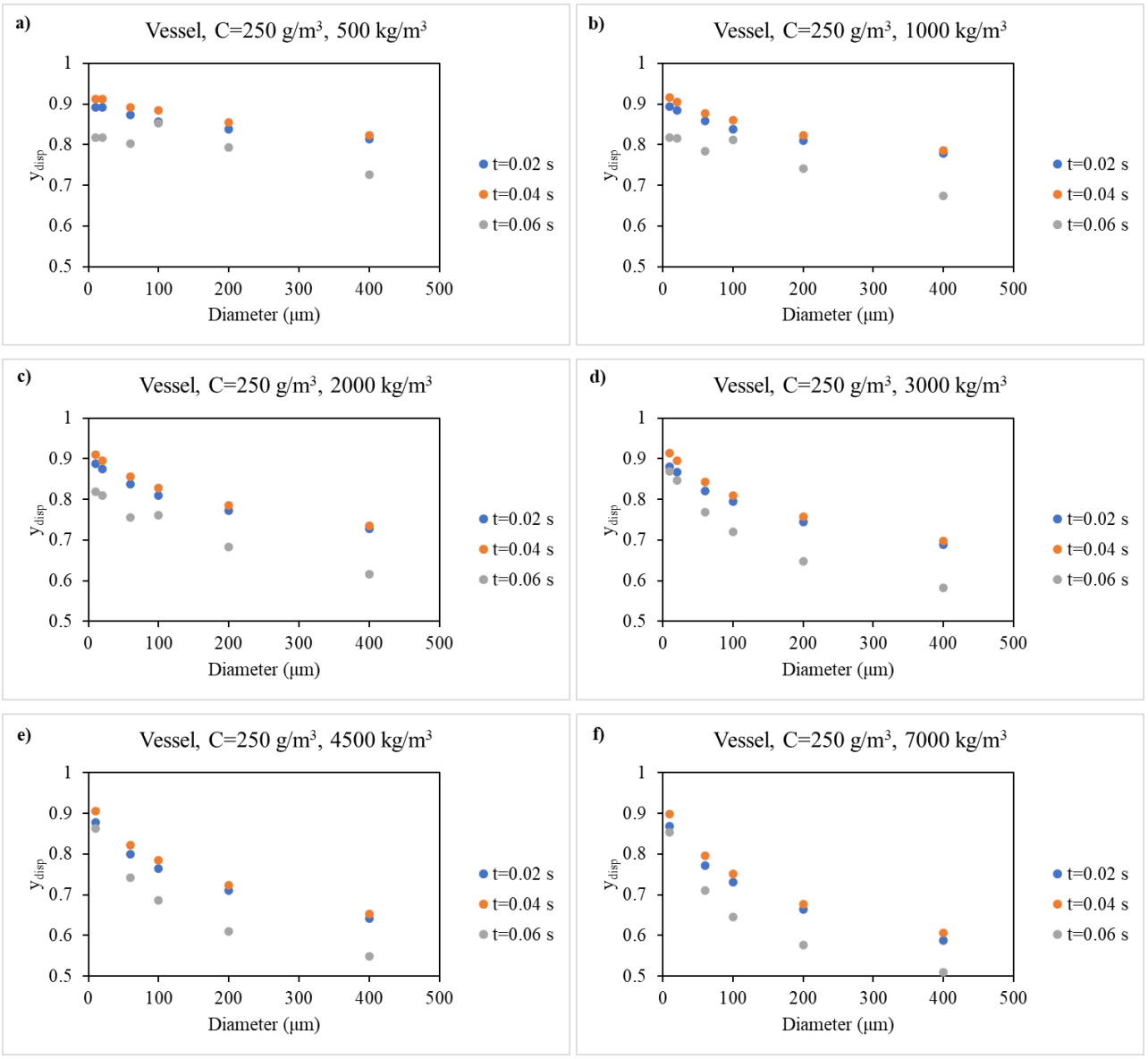

Figure IV.64 *y_{disp} (C_{nom}=250 g/m³) at 500 kg/m³ (a), 1000 kg/m³ (b), 2000 kg/m³ (c), 3000 kg/m³ (d), 4500 kg/m³ (e) and 7000 kg/m³ (f) as a function of diameter within the explosion vessel at 0.02 s (blue scatter plot), 0.04 s (orange scatter plot) and 0.06 s (grey scatter plot)*

Figure IV.65 shows the fraction of dust dispersed inside the vessel versus the dimensionless relaxation time, parametric in time. Notably, the fraction increases during the feeding phase (up to 0.04 s the pressure gradient still allows the dust to enter from the container and the tube within the 20 L vessel) and then decreases to 0.06 s due to sedimentation phenomenon. As can be seen in **Figure IV.65** and better in **Figure IV.66** the fraction of dust dispersed in the form of a dust cloud decreases as τ^+ increases: the higher the τ^+, the longer the time required for the fluid to involve the dust particles in the turbulent motion generated by the pressure gradient. If the dust is not involved in the swirling motion generated in the sphere, it will therefore tend to settle on the bottom of the

vessel and will not participate in the subsequent flame propagation. In the case of dusts characterized by high relaxation time values, the fraction dispersed at the ignition delay time is equal to only half of that which should be nominally. This turns out to be very critical both for the evaluation of P_{max} and K_{St} (which would be underestimated) but above all in the evaluation of the *MEC* which could be largely overestimated.

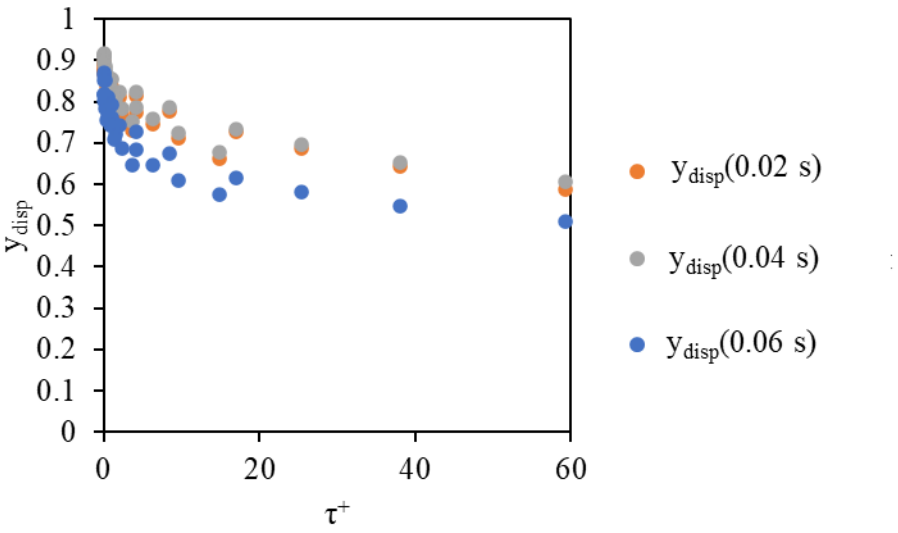

Figure IV.65 *Mass fraction of dispersed dust as a function of the dimensionless relaxation time and parametric in time*

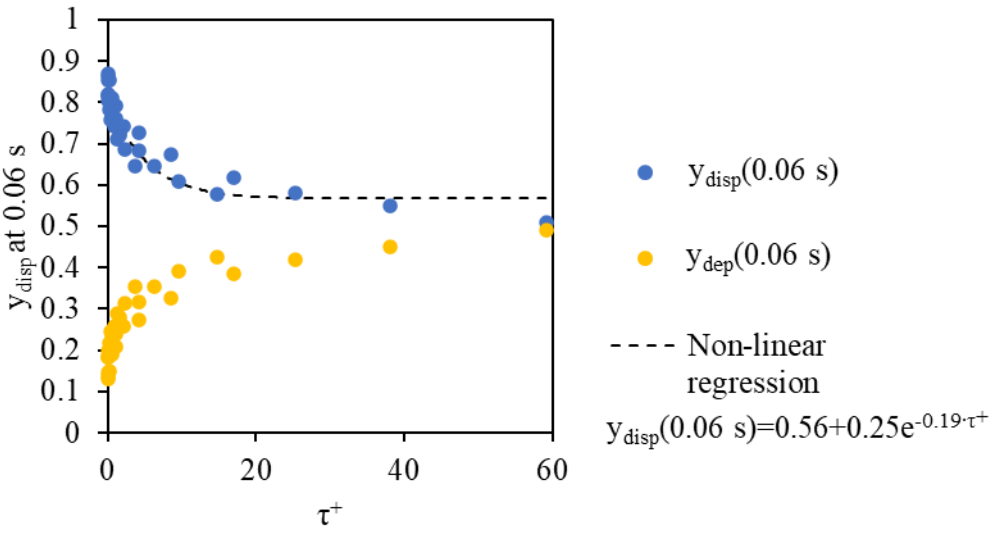

Figure IV.66 *Mass fraction of dispersed and deposited dust at 0.06 s as a function of the dimensionless relaxation time. A non-linear regression (3-factors exponential decay) for y_{disp} is also shown (R^2=0.91)*

IV.4.3. Final remarks

A validated three-dimensional CFD model was used to simulate the dust dispersion inside the 20 L sphere for niacin/anthraquinone mixtures at different compositions (i.e., pure dust ratios, while keeping the total dust concentration constant). Simulations for pure dusts were also performed. In the case of pure dusts, the time sequences of velocity vector maps show that multiple vortex structures are established inside the sphere, generating dead volumes for the solid particles, which are pushed towards the edges of the vortices. This is especially true for niacin. Due to its lower diameter and density, anthraquinone can be better entrained by the fluid flow. However, for each pure dust, the value of concentration in the center of the sphere at the ignition time (60 ms) differs from the nominal value. In the case of dust mixtures, the dispersion inside the sphere is strongly non-uniform, with zones richer in niacin and poorer in anthraquinone and *vice versa*. Overall, the obtained results demonstrate that, to perform a correct and reliable evaluation of flammability and explosibility parameters for dusts and dust mixtures, a different dispersion method has to be developed. When testing dust mixtures, this is needed not only to guarantee a uniform dispersion of the solid particles, but to also ensure the nominal mixture composition in each point of the sphere. The search for a new dust dispersion system also appears necessary to solve the problem related to the sedimentation of the powder, which is increasingly severe as the relaxation time of the powder increases. Due to sedimentation, a lower dust aliquot than the nominal one is tested and the results in terms of explosivity parameters cannot be considered reliable.

IV.4.4. Published articles

Results discussed in this section have been published in a peer-reviewed scientific journal ([181]):

- M. Portarapillo, V. Di Sarli, R. Sanchirico, and A. Di Benedetto, “CFD Simulation of the Dispersion of Binary Dust Mixtures in the 20 L Vessel,” *J. Loss Prev. Process Ind.*, vol. 67, no. April, p. 104231, 2020.

IV.5. CFD simulations of dust dispersion in the 1 m^3 explosion vessel

Due to the possibility of experimental measurements of turbulence level and dust concentration only in few points of the vessels, maps of velocity vectors, turbulence degree, and dust concentration cannot be derived from experimental analyses. Moreover, no simulation is available for 1 m^3 vessel which allows the quantification of these maps. The aim of this work was to develop a CFD model able to get insights into the fluid flow which is established inside the 1 m^3 vessel, when injecting either only air or dust-air mixtures, and to visualize the dust dispersion process. Moreover, we simulated the dust dispersion in the 1 m^3 vessel equipped with rebound and perforated annular nozzles get insight into the effect of these on turbulence (and consequently on flame propagation) and concentration. The simulation results of turbulent kinetic energy and dust concentration are compared to that simulated in the of 20 L sphere, to evidence similarities and differences.

IV.5.1. Methodologies

Perforated annular nozzle

The computational domain and mesh of 1 m^3 vessel were built and refined by means of the Design Modeler and Meshing packages of Ansys (Release 19). The sphere was modeled as three-dimensional and details of the annular ring nozzle were also reproduced. It is worth noting that although the perforated annular nozzle is rarely used in both vessels due to the partial feeding issue, it is still contained within the standards. In addition, the container with the feeding tube of the dust was included in the computational domain (**Figure IV.67**). The feeding tube length was set at the maximum allowable value (350 mm). In **Table IV.34**, geometrical details of the computational domain are given and in **Figure IV.68** a section of the unstructured and non-uniform mesh used is shown. Full model description for 20 L sphere used for the sake of comparison has been given in a previous paper [122]. The model used for dispersion simulation in 1 m^3 vessel consists of the time-averaged Navier-Stokes equations (Eulerian approach). Computations were performed for a dust with density and diameter equal to 2046 kg/m^3 and 250 µm, respectively. The simulation conditions for both standard vessels are summarised in **Table IV.35**.

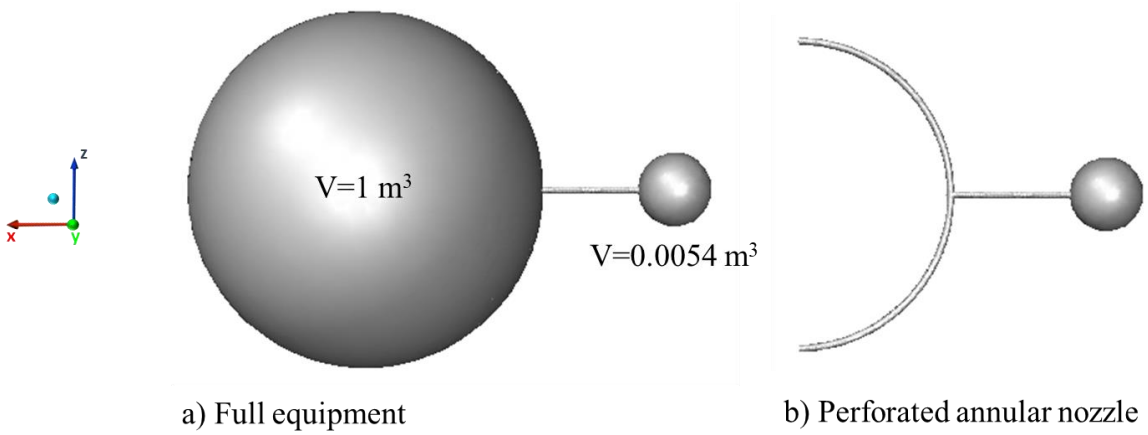

Figure IV.67 *Computational domain: full equipment (a) and perforated annular nozzle (b)* [185]

Table IV.34 *Geometrical details of the computational domain* [185]

Geometrical detail	Value
Container volume (m^3)	0.0054
Tube diameter (m)	0.02
Tube length (m)	0.35
Sphere volume (m^3)	1

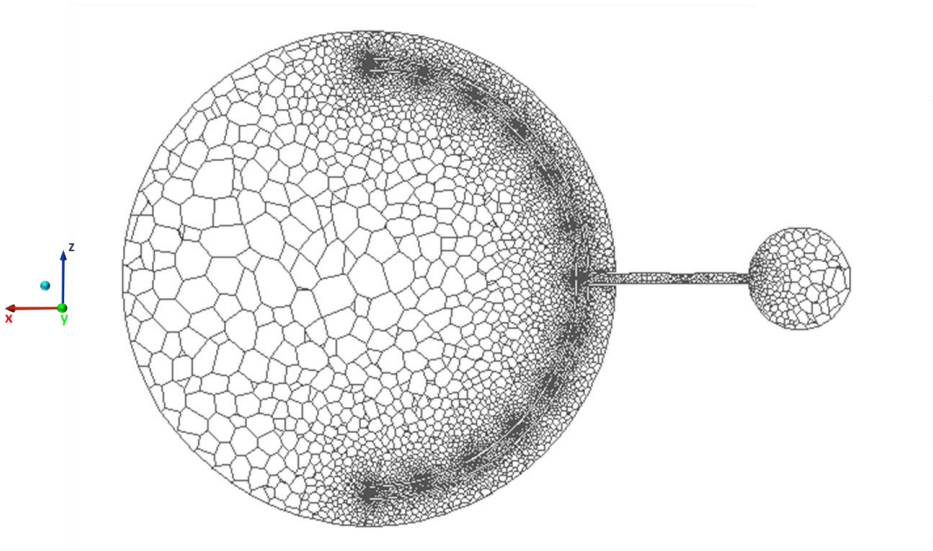

Figure IV.68 *Section of the unstructured and nonuniform mesh used, (x-z) central plane* [185]

Table IV.35 *Simulation conditions* [185]

Parameter	20 L sphere	1 m^3 sphere
Initial pressure of container (bar)	21	21
Initial pressure of sphere and container (bar)	0.4	1
Dust concentration (g/m^3)	100	100
Dust density (kg/m^3)	2046	2046
Dust diameter (μm)	250	250
Time step (s)	$1•10^{-4}$	$4•10^{-5}$
Number of time steps	600	15000

Effect of dust size

In this work, we aimed at extending our model to simulate the effect of dust size on the dust dispersion, turbulence level and theoretical deflagration index evaluation inside the 1 m^3 vessel equipped with the perforated annular nozzle. For the sake of comparison, CFD simulations were carried out with a previously developed and validated model of dust dispersion in 20 L sphere equipped with rebound nozzle [122]. Computations were performed for both the vessels for a dust with density equal to 2046 kg/m^3 and variable diameter (200 and 400 μm), using Ansys Fluent (release 2019R2). Although from the point of view of the explosion risk fine powders are more dangerous (<100 μm), for these simulations these diameter values have been chosen to allow to appreciate the effect of the presence of dust on the continuous flow field (visible in the case of 200 μm) and the sedimentation phenomenon in the case of coarser dust. However, these values are contained in the diameter range included in the definition of combustible dusts [2]. The simulation conditions for both standard vessels are summarized in **Table IV.36**.

Table IV.36 *Simulation conditions* [186]

Parameter	1 m^3	20 L
Initial pressure of container (bar)	21	21
Initial pressure of sphere and container (bar)	1	0.4
Dust concentration (g/m^3)	100	100
Dust density (kg/ m^3)	2046	2046
Dust diameter (μm)	200; 400	200; 400
Time step (s)	$4•10^{-5}$	$1•10^{-4}$
Number of time steps	15000	600

Rebound nozzle

In the standards, the nozzles are presented as interchangeable alternatives, without highlighting any kind of difference. In particular, in the standard procedure for the 1 m^3 dust explosion vessel the rebound nozzle is suggested as an alternative in the case of fibrous dusts testing ([9], [84]). In this work, we aimed at simulating the fluid flow evolution and dust dispersion process which is established inside the 1 m^3 vessel equipped with the rebound nozzle, when injecting either only air or dust-air mixtures, to compare the results with the case of the perforated annular nozzle in terms of turbulent kinetic energy and dust distribution [185]. CFD simulations of the dust dispersion in the standard 1 m^3 vessel apparatus were run ([39], [84], [106]). The equipment mainly consists of a spherical vessel of 1 m^3 and a dust container (5.4 L), closed by a fast-acting. The connecting tube between the fast-acting valve and the dust container must be no longer than 350 mm, as suggested in the standards ([39], [84], [106]). The container with the required amount of dust is pressurised to 21 bar while the vessel is left at ambient pressure. For dispersing the dust inside the vessel, a rebound nozzle is mounted inside the explosion vessel. The rebound nozzle was built following the drawing dimensions reported in UNI EN 14034-2 and UNI EN 14034-3 [84] (**Figure IV.69**). Noteworthy, discrepancies were found in those reported in UNI EN 14034-1, UNI EN 14034-4 and BS EN 14034-1 ([39], [84]). The ignition delay time (i.e., the duration of the dust dispersion) was set at (600±100) ms. CFD simulations of the vessel equipped with perforated annular nozzle were computed for the sake of comparison. The CFD model for this equipment was presented and validated in previous studies ([185]–[187]).

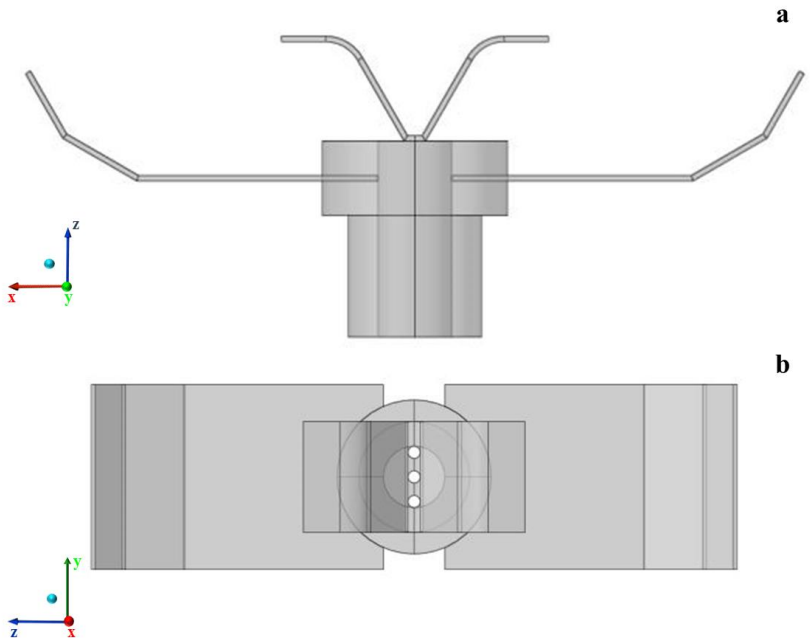

Figure IV.69 *Front (a) and top (b) view of the rebound nozzle used in 1 m^3 vessel* [188]

The computational domain and mesh of 1 m^3 vessel were built and refined by means of the Design Modeler and Meshing packages of Ansys (Release 2020 R2). In Table IV.37, geometrical details of the computational domain are provided. A section of the used unstructured mesh and a zoom close to the rebound are shown in **Figure IV.70**.

Table IV.37 *Geometrical details of the computational domain* [188]

Geometrical detail	Value
Container volume (m^3)	0.0054
Tube diameter (m)	0.02
Tube length (m)	0.35
Sphere volume (m^3)	1

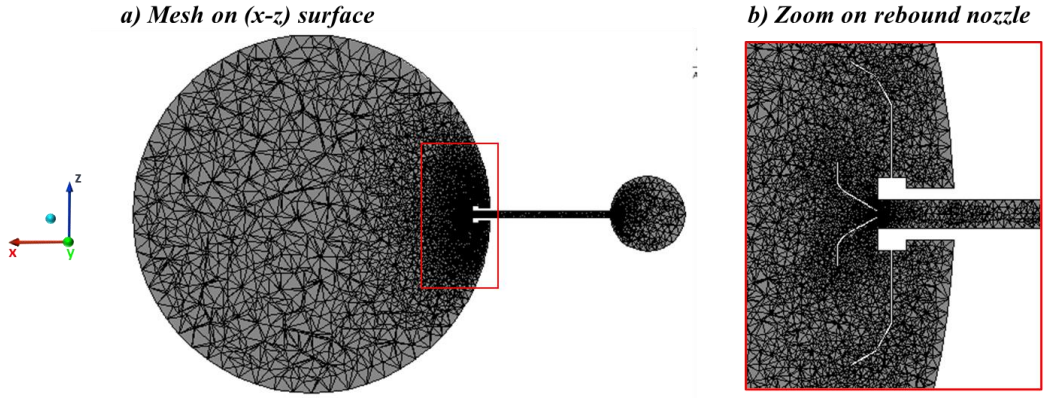

Figure IV.70 *Section of the unstructured and non-uniform mesh used, (x–z) central plane (a) and zoom on rebound nozzle zone (b)* [188]

The model used consists of the Reynolds-averaged Navier-Stokes equations (Eulerian approach). These were solved using the standard *k-ε* model with the standard wall function and considering compressibility effects [130]. The fluid flow equations were finite-volume discretized on the 3D tetrahedral unstructured grid (506805 elements), refined in correspondence of the rebound. The semi-implicit method for pressure-linked equations (SIMPLE) was used to solve the pressure-velocity coupled equations. First order schemes for convective terms and second order schemes for diffusion terms were used for the spatial discretization of the model equations. First-order scheme was used to discretize temporal derivatives (time step of $4 \cdot 10^{-5}$ s).

The flow of the dust was solved with the Lagrangian formulation using the Discrete Phase Model (*DPM*). The turbulent dispersion was considered activating the Discrete Random Walk model. In this way, the interaction of a particle with a succession of discrete fluid phase turbulent eddies is simulated [131]. The DPM model can be implemented when the second phase is dilute (i.e., volume fraction lower than 10-12%) enough to apply the two-way coupling approach [133]. In this work, the solid fraction was equal to $\alpha = 4.9 \cdot 10^{-5}$.

The unsteady particle tracking time step was taken equal to the fluid flow time step. Parallel calculations were performed through the segregated pressure-based solver of the code ANSYS Fluent (Release 2020 R2). All residuals were set equal to $1 \cdot 10^{-6}$ for convergence purpose. For 1 m^3 simulation, the fluid phase was air at atmospheric temperature and was modeled as an ideal gas. As initial conditions, we adopted that used in the standard tests: the dust container was initially at pressure equal to 21 bar (the spherical dust container was patched) while the connecting tube and the sphere were set to 1 bar. Computations were performed for a dust with a diameter equal 250 μm. Comparison with the previous results obtained with the perforated annular nozzle is also

performed [185]. The simulation conditions for both standard nozzles are summarised in **Table IV.38**.

Table IV.38 *Simulation conditions* [188]

Parameter	**1 m^3 sphere**
Initial pressure of container (bar)	21
Initial pressure of sphere and container (bar)	1
Dust concentration (g/m^3)	100
Dust density (kg/m^3)	2046
Dust diameter (µm)	250
Time step (s)	$4 \cdot 10^{-5}$
Number of time steps	15000

IV.5.2. Results

Perforated annular nozzle

In **Figure IV.71**, the pressure is plotted vs. time as computed in the centre of the dust container. From the pressure trends, the feeding phase during which air or dust-air mixture goes from the container to the sphere may be identified. This phase lasts 0.4 s. Indeed, after 0.4 s, the container pressure reaches 1 bar and the injection of air/dust-air comes to an end. The model results in terms of temporal profile of pressure inside the container are compared to experimental data available in the literature [189]. The comparison shows a very good agreement with a maximum deviation at 0.2 s between the experimental and the theoretical data of the dust/air mixture feeding equal to 20 %.

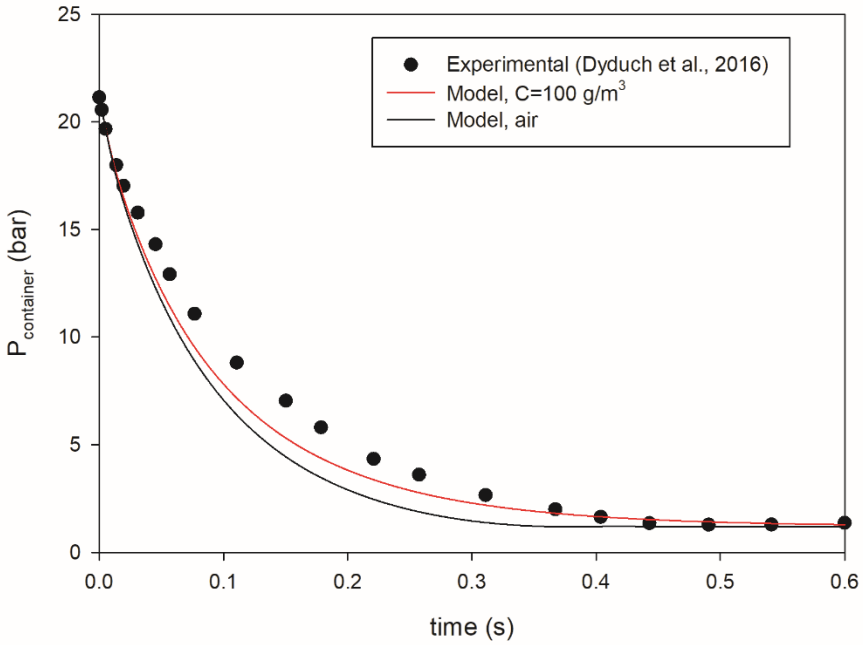

Figure IV.71 *Pressure time histories computed in the centre of the dust container for dust free air and dust-air mixture* [185]. *Literature data are also shown for the sake of comparison* [189]

In **Figure IV.72**, the corresponding temporal trend of the root mean square velocity (*RMS*) in case of dust-free air and dust at a concentration equal to 100 g/m^3 are shown as computed in the centre of the sphere. For the sake of comparison, the experimental data measured by Hauert and Vogl (1995) are also shown [119]. The experimental data were used only to compare the trend, but a direct comparison is not possible since the geometries of involved vessels are different (spherical in this work while cylindrical in the experimental data) as well as the considered dust (different diameter and density). To avoid a fast soiling on the optical measuring probes in the 1 m^3 cylindrical vessel, Hauert and Vogl (1995) used maize starch (diameter 15 μm, density of about 1000 kg/m^3) concentrations between 30 g/m^3 and 120 g/m^3.

From **Figure IV.72**, it appears that there is a short period of turbulence build up followed by a much longer period of turbulence decay. The turbulence decay starts after few milliseconds from the opening of the valve, well before the end of the injection phase. It is found that the computed u_{RMS} curves are different in the first 300 ms compared to the experimental data, while they show a similar trend after 300 ms, in the turbulence decay phase. Due to the low value of concentration, the flow development in the model is not strongly affected by the dust presence, resulting in overlapped RMS curves in the case of dust-free air and dust with a slight difference in the peak value.

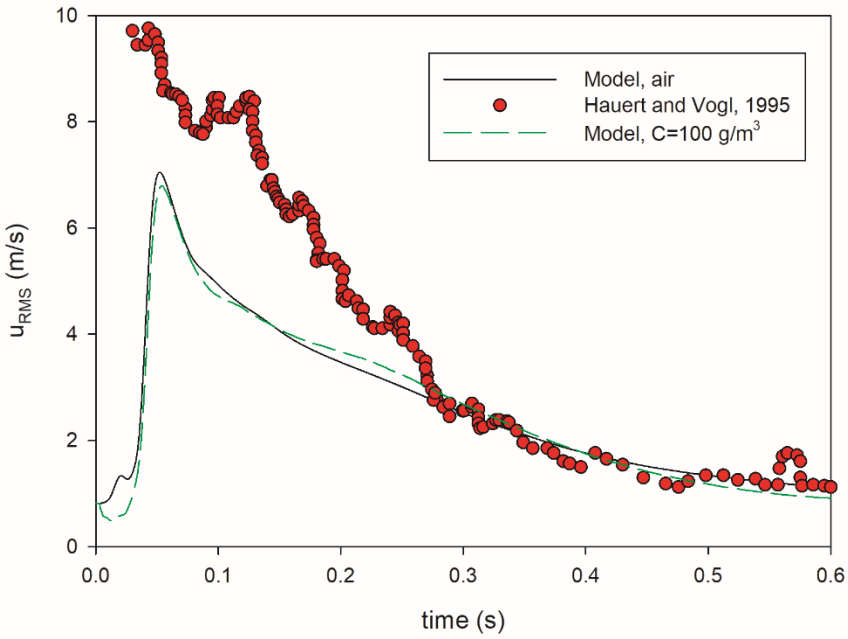

Figure IV.72 *RMS turbulence velocity (m/s) as a function of the time at the centre of the 1 m3 vessel for dust free air and dust-air mixture* [185]. *Literature data are also shown for comparison* [119]

In **Figure IV.73**, the temporal trend of the *DPM* concentration is shown as computed in the centre of the sphere. For the sake of comparison, the experimental data determined by measuring the light transmission using opto-electronic techniques by Hauert and Vogl (1995) are also shown [119]. Hauert and Vogl (1995) used maize starch (diameter 15 μm, density of about 1000 kg/m^3) at 120 g/m^3. Due to the different nature of involved dusts (different diameter and density), a direct comparison is not possible. As for the *RMS* trends, it is found that the *DPM* concentration as computed through the model are different in the first 300 ms compared to the experimental data, while the values fall in the same concentration range after 300 ms. It is worth noting that according to the model simulation, at the ignition delay time (0.6 s) the dust concentration computed at the centre of the sphere is very similar to the nominal value (C_{nom}=100 g/m^3).

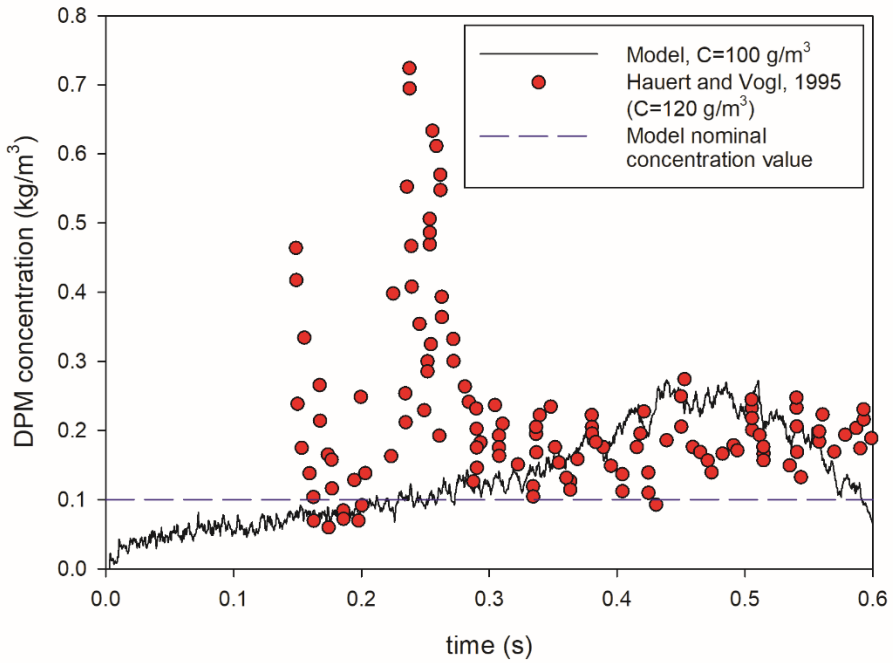

Figure IV.73 *DPM concentration (kg/m3) as a function of the time at the centre of the 1 m3 vessel* [185]. *Literature data are also shown for the sake of comparison* [119]

In **Figure IV.74** the time sequence of maps of the turbulent kinetic energy is shown as computed over the frontal (x-z) plane in case of dust-free air (a) and dust at 100 g/m^3 (b). It is worth noting that the maps at 400 ms and 600 ms with dust present non-symmetric fields, differently from the results obtained in the case of dust-free air (a). This behaviour has been previously found by Kartushinsky et al. (2011) [182]. They developed a three-dimensional *RANS* numerical method with the appropriate system of closure equations for the transport of gas–solids mixtures. The results showed that the presence of particles in the flow has a significant effect on all the flow variables. Most notably, the distribution of all the parameters becomes asymmetric, because of the gravitational effect on the particles and particle sedimentation [182]. Although the level of turbulence is not completely uniform within the sphere, showing a decay moving from the centre to the walls, the variation range of turbulent kinetic energy is very narrow (from 1.25 m^2/s^2 to 0 m^2/s^2).

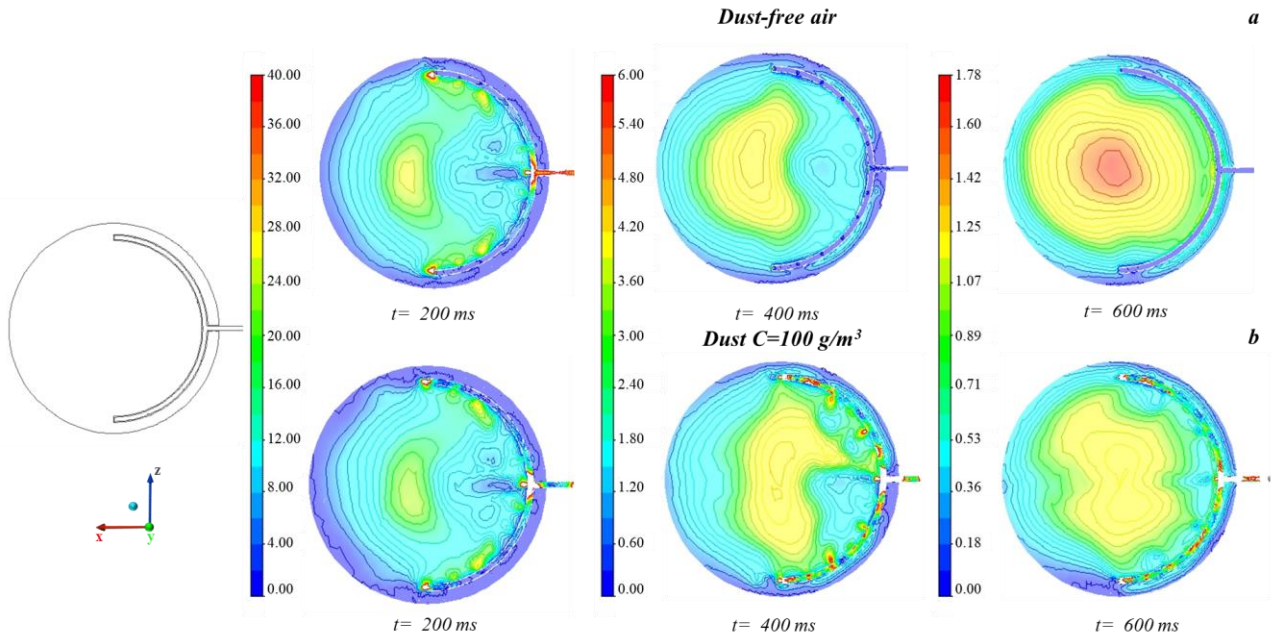

Figure IV.74 *Time sequence of computed maps of turbulent kinetic energy (m2/s2): dust-free air (a) and dust C=100 g/m3 (b), (x-z) plane* [185]

In **Figure IV.75** the time sequence of maps of the velocity vectors is shown as computed over the frontal (x-z) plane in case of dust-free air (a) and dust at 100 g/m^3 (b). While the pressure in the dust container falls, the gas velocity significantly decays in time. **Figure IV.75** also shows that two main vortices are formed at the centre of the sphere, they are well evident at 200 and 400 ms and appear to be almost dissipated at 600 ms. These vortex structures generally result in higher dust concentrations close to the walls and, thus, in regions external to the vortices. Conversely, at the centre of the vortices, the dust concentration is very low. This suggests that the dust is not entrained by the fluid and then the vortices are dead volume for the dust ([122], [124], [128]). In the case of dust dispersion (b), the maximum velocities correspond to the zone of perforated annular nozzle, in particular at the exit of the central hole and of holes in each end cap. In **Figure IV.76**, the area averaged velocity profiles at the exit of the central hole (mid) and of holes in each end cap (z+ and z-) are shown. As the time increases, each profile shows a decay due to the reduction of the pressure gradient from the dust container to the sphere. For each time, the velocity modulus is higher than the value recorded in the centre of the sphere.

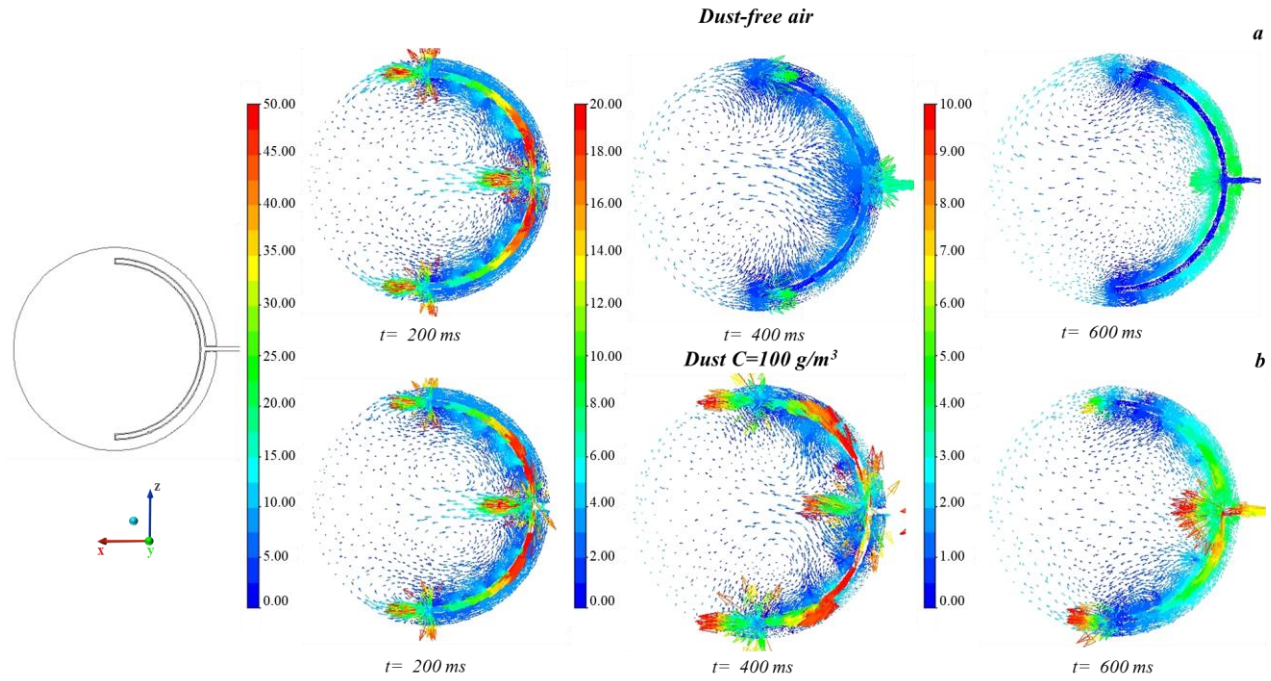

Figure IV.75 *Time sequence of computed velocity vectors (m/s): dust-free air (a) and dust C=100 g/m³ (b), (x-z) plane* [185]

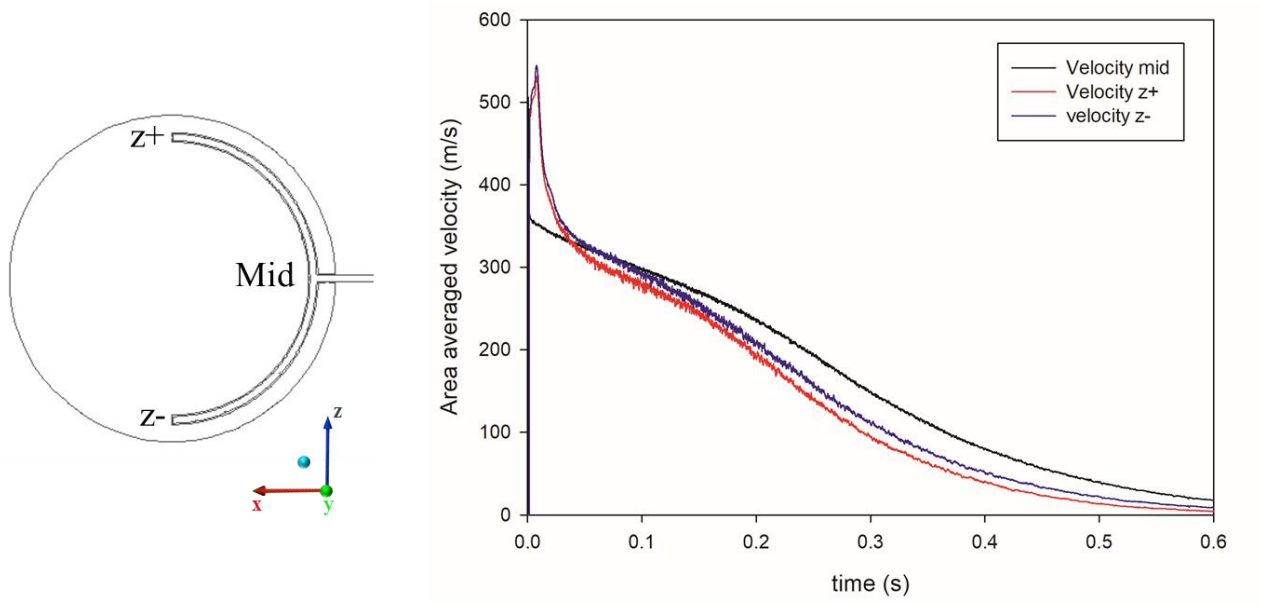

Figure IV.76 *Area-averaged velocity profiles at the exit of the central hole (mid) and of holes in each end cap (z+ and z-) for dust C=100 g/m³ simulation* [185]

The spatial-temporal distribution of dust concentration inside the sphere is represented through the ratio γ between the dust concentration and the nominal dust concentration (C_{nom}=100 g/m^3). In

Figure IV.77, the time sequence of the particle tracks coloured by γ is shown as obtained on the (x-z) plane (a) and in the whole sphere (b) oriented as in the empty image. This figure further confirms that the highest dust concentrations are attained externally to the vortices, whereas the dust concentration is very low inside the vortices. Indeed, the dust is highly concentrated at the sphere walls, reaching concentrations much higher than the nominal value (γ=2; C=200 g/m^3), while in the bulk of the sphere, the dust concentration is lower than the nominal value (γ<1; C<100 g/m^3). This result is qualitatively in agreement with the findings by Kalejaiye et al. (2010) [121]. Lower values of transmission (and then higher values of concentration) were found in correspondence to the probes close to the vessel walls with respect to those closer to the sphere centre. In particular, at each time, an accumulation close to the perforated annular nozzle on the (x-z) plane can be observed. Moreover, starting from 400 ms, the dust creates a three-dimensional cross inside the vessel. In particular, at the ignition time (t_d=600 ms), the cloud is not uniform, suggesting that the flame will start propagating in a stratified flammable mixture.

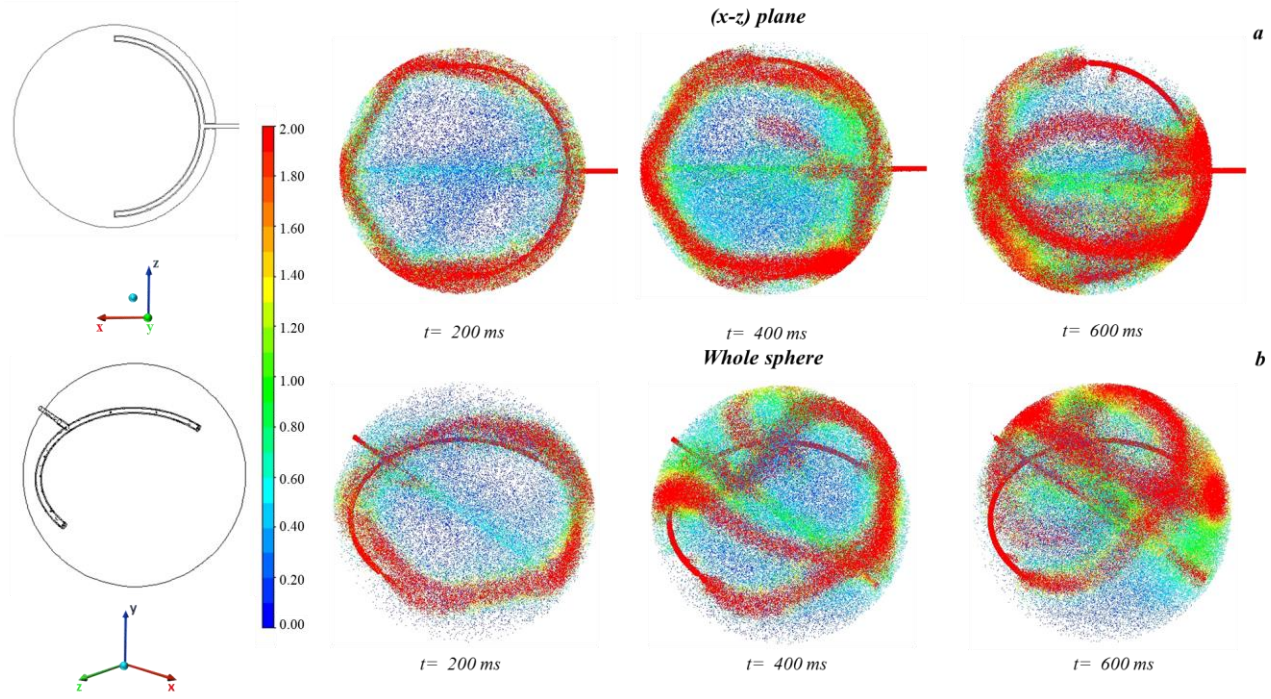

Figure IV.77 *Time sequence of particle tracks coloured by γ: (x-z) plane (a) and whole sphere (b)* [185]

According to the standard guidelines ([9], [39], [106]) and previous results ([1], [37], [38]) it is widely accepted that the 20 L and the 1 m^3 vessels would give the same values of the deflagration index, provided that the ignition time are 60 ms and 600 ms, respectively. In order to give the same value of the deflagration index, the same dust concentration and turbulent kinetic energy should

be established inside the vessels. To verify this, we performed the simulations of the same dust feeding inside the 20 L vessel.

We refer to the dimensionless time τ defined as the ratio between time and ignition delay time (t_d = 60 ms for 20 L vessel; 600 ms for 1 m^3 vessel).

In **Figure IV.78** the time sequence of the turbulent kinetic energy maps is shown as computed over the frontal (x-y) plane for the 20 L vessel (a) and for the 1 m^3 vessel (b). At all times, the turbulent kinetic energy computed in the 20 L vessel is higher than that found in the 1 m^3 vessel. Notably, the 20 L vessel shows a non-uniform degree of turbulence, resulting in not reliable and not repeatable measurements of the explosibility parameters ([122], [124], [125], [128]). This issue appears to be solved in the 1 m^3 vessel since the variation range of turbulent kinetic energy from the centre to the wall at the ignition delay time is very narrow (from 1.25 m^2/s^2 to 0 m^2/s^2). However, the values of the turbulent kinetic energy are quite different, even at the ignition delay times (τ = 1).

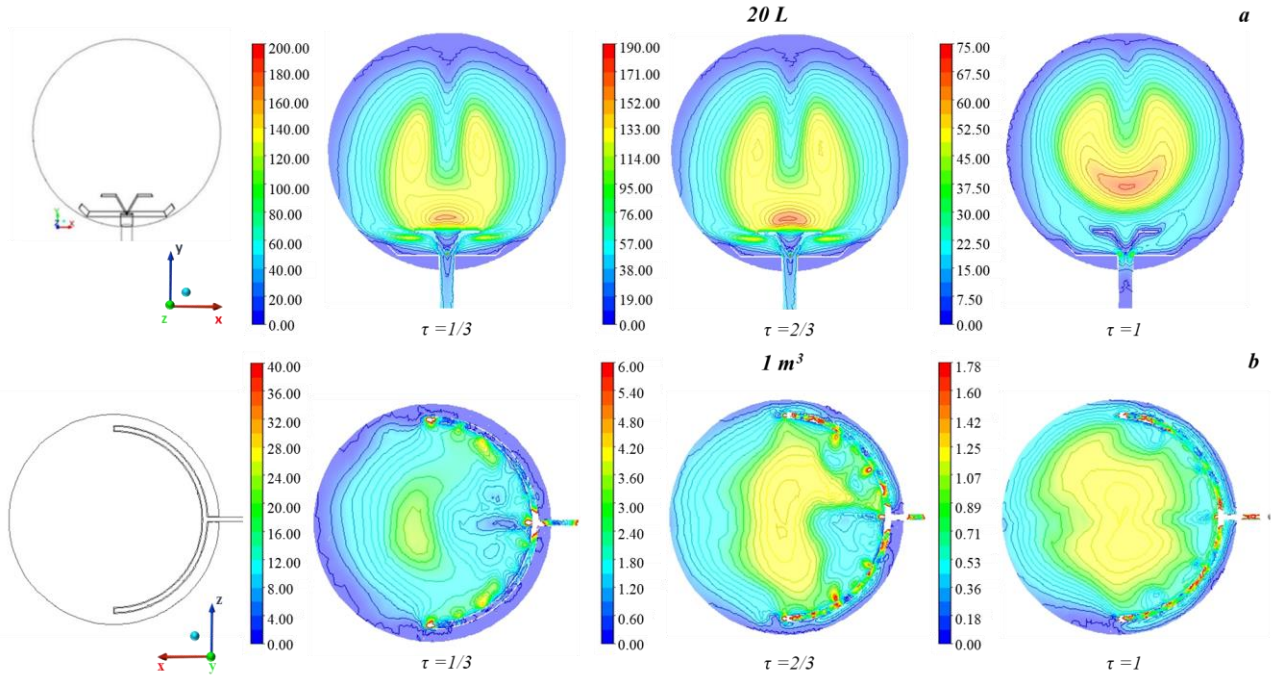

Figure IV.78 *Computed maps of turbulent kinetic energy (m^2/s^2) as function of the ratio τ: 20 L sphere (a) ((x-y) plane) and 1 m^3 vessel (b), (x-z) plane* [185]

The spatial-temporal distributions of dust concentration are represented in **Figure IV.79** through the ratio γ between the dust concentration and the nominal dust concentration (C_{nom}=100 g/m^3) as function of the ratio τ computed in the vessel (20 L (a), 1 m^3 (b)). In both the standard vessel, the

requirement of a uniform dust cloud within the test volume reported in several standard is not satisfied ([9], [19], [20], [39], [106]) and the dust distribution changes with dust diameter, nominal concentration and shape of the particles. This involves a variability of the results according to the boundary conditions even for the same dust. In particular, the highest dust concentrations are attained externally to the vortices, whereas the dust concentration is very low inside the vortices. Indeed, the dust is highly concentrated at the sphere walls, reaching concentrations much higher than the nominal value (γ=2; C=200 g/m^3), while in the bulk of the sphere, the dust concentration is lower than the nominal value (γ<1; C<100 g/m^3). In the case of 20 L vessel, dust accumulation in the centre of the sphere can be observed. Moreover, the perforated annular nozzle, used in the 1 m^3 vessel, does not allow the complete feeding of dust within the test volume, as already found in a previous work [128].

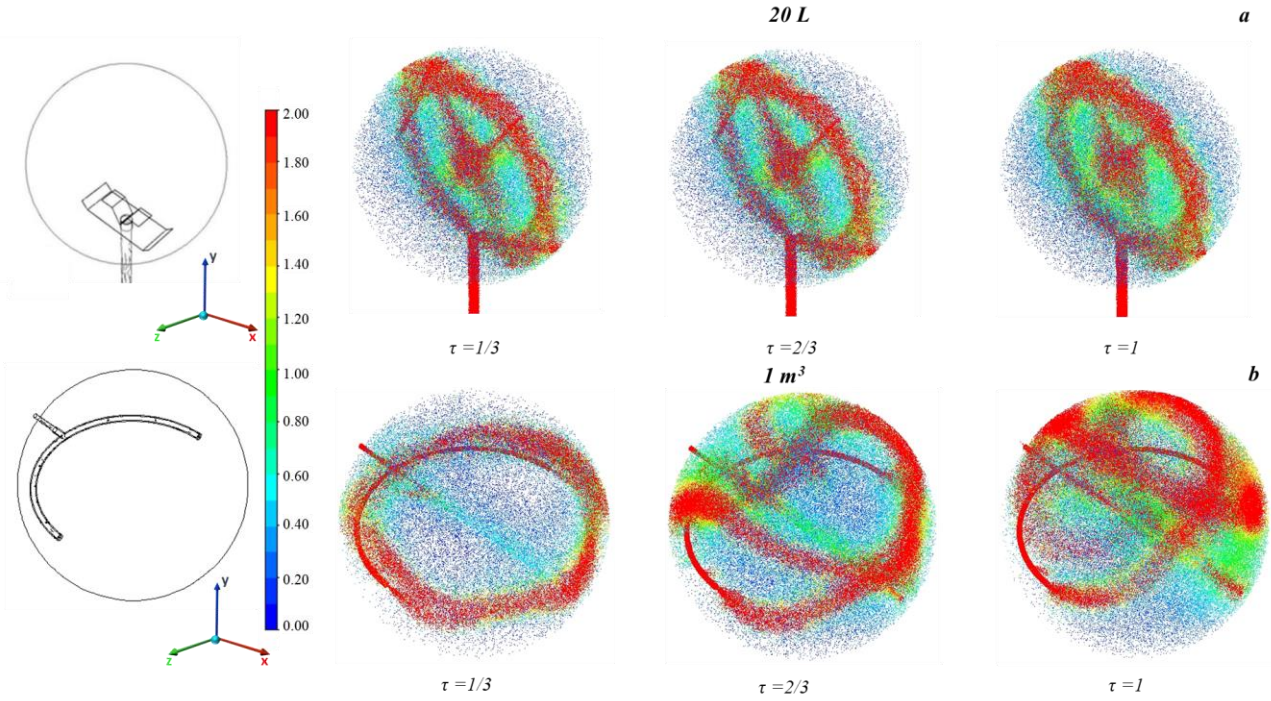

Figure IV.79 *Particle tracks colored by γ as function of the ratio τ computed in the whole spheres: 20 L sphere (a) and 1 m^3 vessel (b)* [185]

Figure IV.80 shows the temporal trend of the turbulent kinetic energy as computed in the centre of the vessels as a function of the dimensionless time τ. At each time in the ignition point, the vessels show values of turbulent kinetic energy very different from each other. In particular, at the ignition delay time (τ =1), the turbulent kinetic energy in the 20 L vessel is still high (42.30 m^2/s^2) and very different from that in 1 m^3 vessel (1.24 m^2/s^2). It suggests that after 60 ms the degree of

turbulence within the 20 L sphere is not uniform and not comparable to that found in the 1 m^3 vessel. This does not satisfy the necessary requirement of comparable level of turbulence at the moment of ignition in the two vessels presented in the standards and in the calibration procedures.

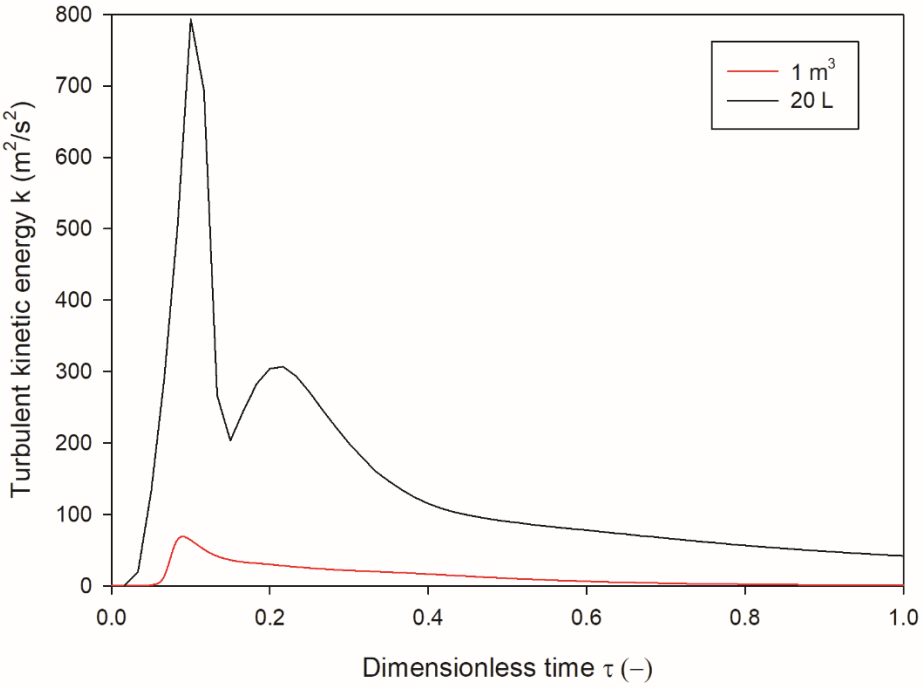

Figure IV.80 *Temporal trends of turbulent kinetic energy (m^2/s^2) as computed in the centre of the vessels for 20 L sphere and 1 m^3 vessel as a function of the dimensionless time τ* [185]

Figure IV.81 shows the temporal trend of the *DPM* concentration as computed in the centre of the vessels as a function of the dimensionless time τ. At ignition, the vessels show *DPM* concentration values very different from each other. In particular, in the 20 L vessel the dust concentration is higher than that found in the 1 m^3 vessel. At the ignition delay time (τ = 1), the *DPM* concentration in the 20 L vessel is still high (C = 990 g/m^3) and very different from the nominal value (C = 100 g/m^3) and from that in 1 m^3 vessel (C =70 g/m^3). The highest values of turbulent kinetic energy and dust concentration at the ignition delay time in the centre of the 20 L sphere (where ignition occurs) may explain the frequent overdriving leading to false positives in smaller explosion chambers, mostly in the case of weakly reactive and organic dusts [105].

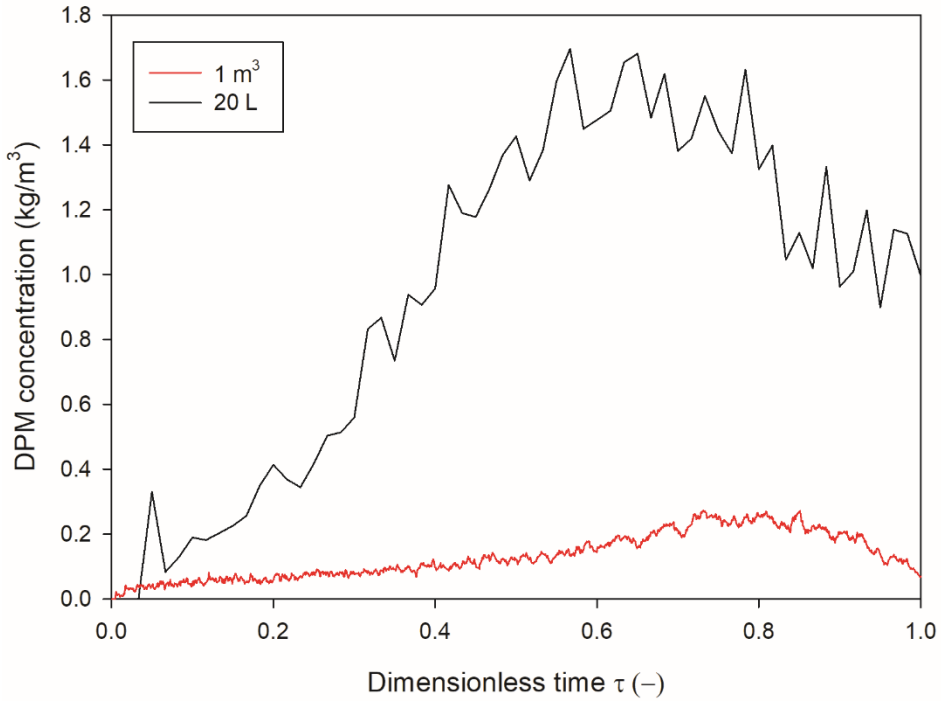

Figure IV.81 *DPM concentration as computed in the centre of the spheres for 20 L sphere and 1 m³ vessel as a function of the dimensionless time τ* [185]

To assess the effect of turbulence on the evaluation of deflagration index with the two standard vessels, we estimated the theoretical K_{St} through the thin-flame model by Dahoe et al. (1996) [190]. In this model, the content of the vessels consists of a spherical inner region of completely burnt material, encapsulated by an outer region of completely unburnt mixture. The model assumes that the laminar burning velocity S_l remains constant during the explosion (i.e., it does not depend on the dust concentration). As concern the maximum rate of pressure rise $(dP/dt)_{max}$ to be included in the formula of Lewis von Elbe (Equation (59)), it was computed maximizing the equation by Dahoe et al. (1996) [190], which link the pressure P and the turbulent burning velocity S_t to the rate of pressure rise (Equation (60)). The evaluation of the turbulent burning velocity as function of the turbulent fluctuations (u') was performed through the equation by Pocheau (1994) (**Table II.3**) [57].

The equations used are in the following:

$$K_{St} = \left(\frac{dP}{dt}\right)_{MAX} \left(\frac{4}{3}\pi r_{vessel}^3\right)^{\frac{1}{3}} \tag{59}$$

$$\frac{dP}{dt} = 3\frac{P_{MAX} - P_0}{r_{vessel}}\left[1 - \left(\frac{P_0}{P}\right)^{\frac{1}{\gamma}} \frac{P_{MAX} - P}{P_{MAX} - P_0}\right]^{\frac{2}{3}} \left(\frac{P}{P_0}\right)^{\frac{1}{\gamma}} S_t \tag{60}$$

Where P_{max} was set at 8 bar and P_0 (bar) is the initial pressure (assumed equal to 1 bar).

The results and the differences between the two vessels are summarized in **Table IV.39**. In the case of the 1 m^3 vessel, a controlled turbulence level is realized. Conversely, in the case of 20 L sphere, a non-uniform spatial distribution is found. The propagating flame will encounter zones with concentration much higher than the nominal value ($\gamma > 1$) and zones with concentration much lower than the nominal value ($\gamma < 1$). It was found that the K_{St} estimated in the 20 L vessel is 2.4 times higher than the value obtained in the 1 m^3 vessel. Therefore, turbulence level has a crucial role on the K_{St} assessment. The turbulence intensity seems weak and more or less the same in the 1 m^3 vessel at the delay time, whereas it may vary significantly in the 20 L sphere. If the K_{St} depended solely on the level of turbulence, the assessment within the 20 L vessel would always be more conservative than that in the 1 m^3 vessel. Conversely, other effects must be taken into consideration such as overdriving, preheating and thermal radiation ([99], [102], [104], [105]). When performing explosion/flammability tests by using chemical igniters (according to the standard procedure), the flame is overdriven by the igniters explosion and mainly controlled by them. Conversely, the effects of preheating, thermal radiation and turbulence level on the explosion parameters are not foreseeable as they strongly depend on the type of investigated dust. For this reason, the calibration cannot be generalizable to all types of dust but each one needs its own calibration to assess the relative turbulence level. However, the *ad hoc* calibration procedure would lead to the drop of the idea of a standardized procedure suitable for all the dusts.

The obtained results in the investigated case suggest that, whatever the volume of testing vessels, different explosion vessel configuration and dispersion method have to be developed to perform a correct and reliable evaluation of the flammability and explosibility parameters for dusts and dust mixtures.

Table IV.39 *Comparison between the 20 L and 1 m^3 vessels* [185]

	20 L sphere	**1 m^3 sphere**
Turbulence level and control	High turbulence level, not uniform in space	Low turbulence level, uniform in space
Turbulent kinetic energy in the centre (m^2/s^2) at $\tau = 1$	42.30	1.24
Dust concentration distribution	Not well mixed, low level of uniformity	Not well mixed, low level of uniformity
Dust concentration at the centre (g/m^3) at $\tau = 1$	990	70
Theoretical deflagration index (bar m/s)	92.40	37.80
K_{St} (20 L) / K_{St} (1 m^3)	2.4	

Effect of dust size on the dust dispersion

Figure IV.82 shows the time sequence of the turbulent kinetic energy maps as computed over the frontal (x-z) plane in case of dust-free air (a) and dust-air mixtures with concentration 100 g/m^3 and dust diameters of 200 μm (b) and 400 μm (c) in the 1 m^3 vessel. The maps of dust-free air turbulence level are symmetric while the maps obtained in the presence of dust are non-symmetric due to the dust entrainment by the fluid flow. The results showed that the presence of particles in the flow has a significant effect on all the flow variables. Most notably, the distribution of all the parameters becomes asymmetric, because of the gravitational effect on the particles and particle sedimentation [182]. In the case of dust size equal to 400 μm, at 600 ms, the flow field is more similar to that of dust-free air, likely due to the occurrence of a strong sedimentation phenomenon. In order to better visualise the preferential paths of the dust, we mapped the particle tracks. The spatial-temporal distribution of dust concentration inside the sphere is represented through the ratio (γ) between the dust concentration and the nominal dust concentration (C = 100 g/m^3) in the 1 m^3 vessel. In **Figure IV.83** and **Figure IV.84**, the time sequence of the particle tracks coloured by γ is shown as obtained on the (x-z) plane (a) and in the whole sphere (b) oriented as in the empty image in the case of dust at 200 μm and 400 μm, respectively. In the case of 200 μm (**Figure IV.83**), starting from 400 ms, the dust creates a three-dimensional cross inside the vessel due to the dust dispersion system and the formation of turbulence macro-vortices. In particular, at the ignition time (t = 600 ms), the cloud is not uniform. In the case of 400 μm (**Figure IV.84**), the three-dimensional cross structure does not form because it becomes more difficult for the fluid flow to entrain the dust which then follows a completely different path with respect to the fluid. Therefore, also in the 1 m^3 vessel, on increasing the dust diameter the preferential paths are much more evident suggesting that the dust dispersion is worst. It is worth noting that a large amount of dust is present on the sphere bottom, due to sedimentation. Moreover, a worse feeding is attained, with most of the dust trapped in the perforated annular nozzle on increasing dust diameter. Indeed, the averaged dust concentration in the 1 m^3 sphere is reduced by about 10% in the case of dust with diameter of 400 μm.

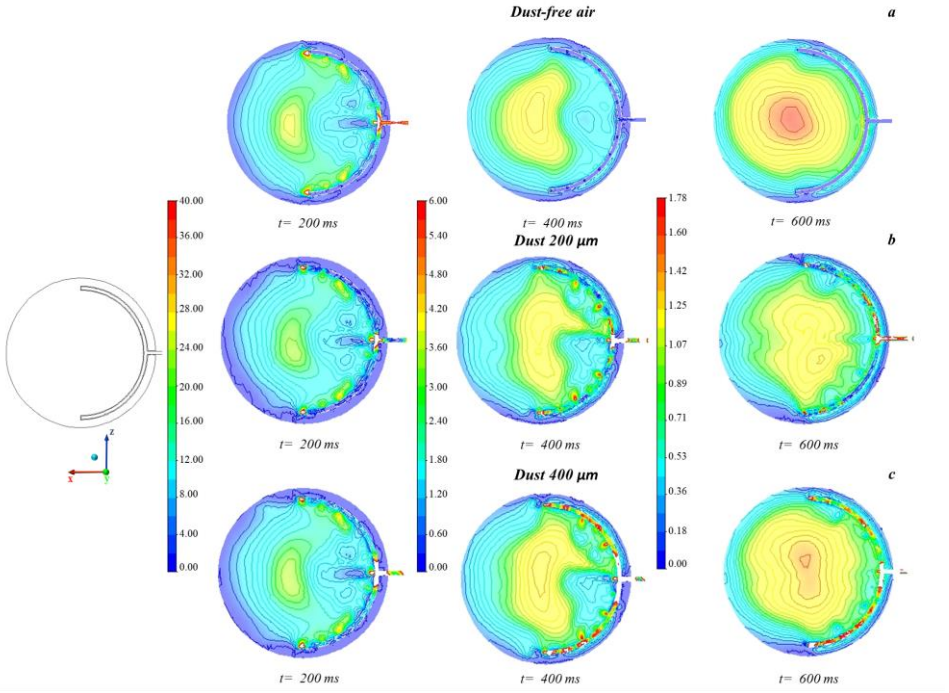

Figure IV.82 *Time sequence of computed turbulent kinetic energy maps (m^2/s^2) in the 1 m^3 vessel: dust-free air (a), dust at C=100 g/m^3 and d=200 µm (b) and dust at C=100 g/m^3 and d=400 µm (c), (x-z) plane* [186]

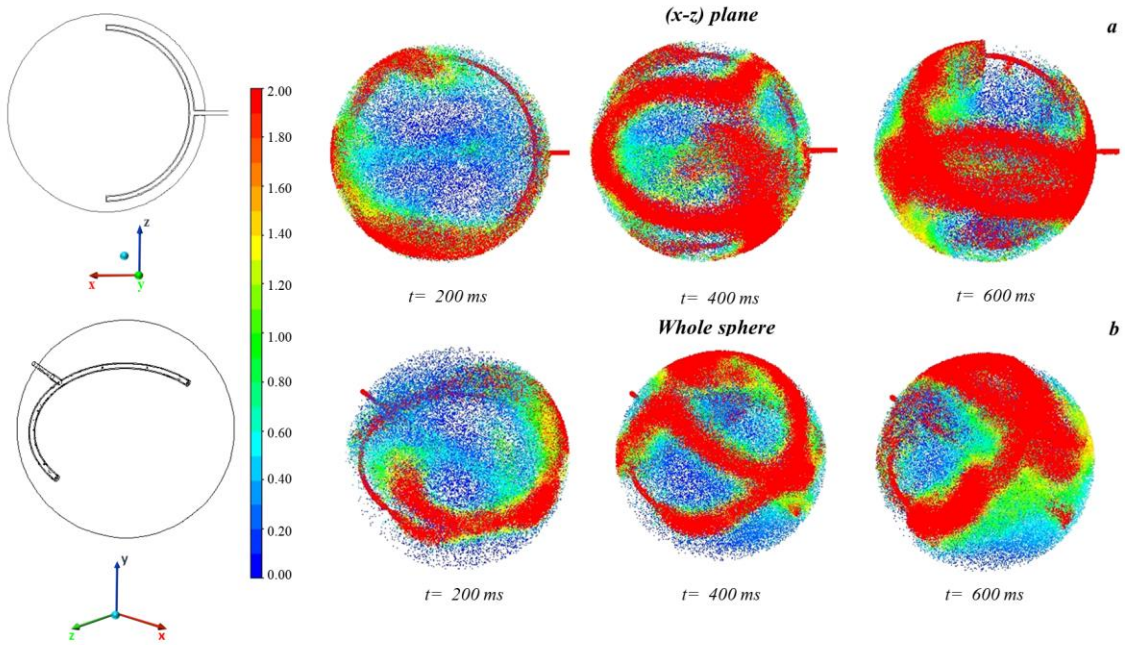

Figure IV.83 *Time sequence of particle tracks coloured by γ in the 1 m^3 vessel: (x-z) plane (a) and whole sphere (b), C=100 g/m^3 and d=200 µm* [186]

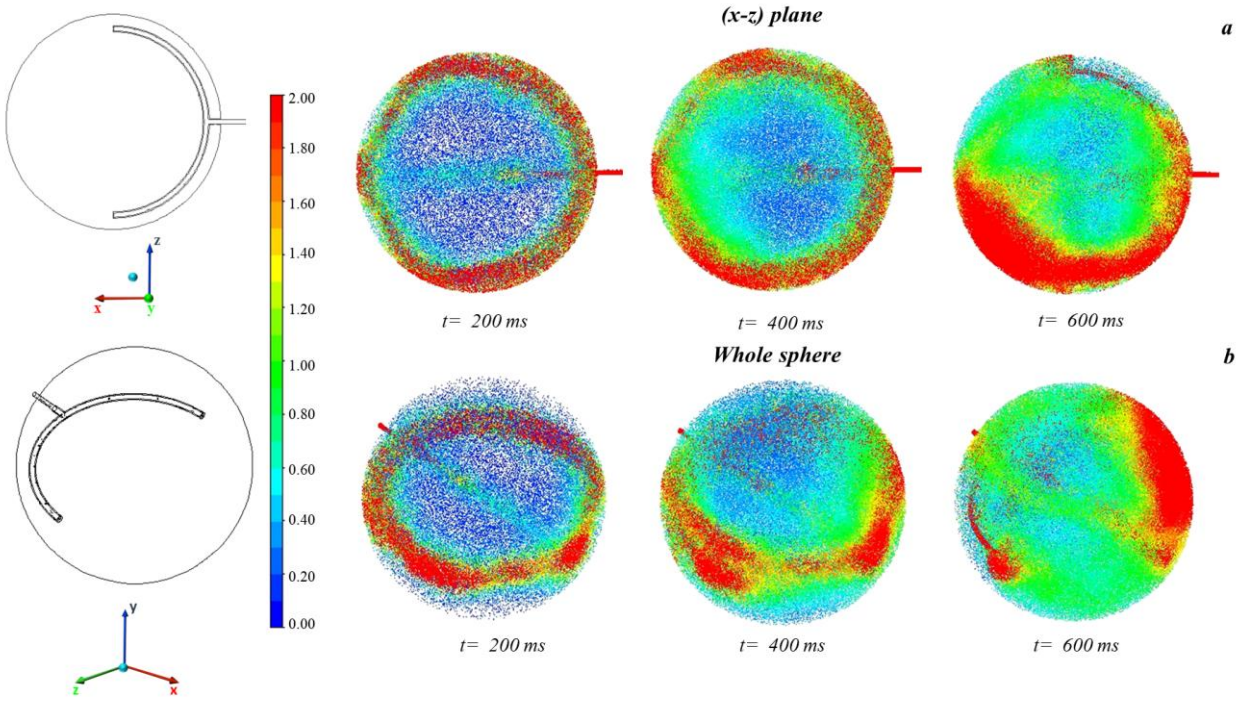

Figure IV.84 *Time sequence of particle tracks coloured by γ in the 1 m³ vessel: (x-z) plane (a) and whole sphere (b), C=100 g/m³ and d=400 μm* [186]

Figure IV.85 shows the temporal trend of the DPM concentration as computed in the centre of the 1 m^3 vessel as a function of time for dust dispersion at d=200 μm (black line) and d=400 μm (red line). At the ignition delay time (t=600 ms), the 200 μm dust shows a concentration in the centre equal to 66 g/m^3 while dust at 400 μm shows a concentration equal to the nominal value, C_{nom}=100 g/m^3. It is worth noting that in this last case, as discussed above, the quantity of dispersed dust is very low due to both the trapping in the perforated annular nozzle and the sedimentation. Indeed, the red line in **Figure IV.85** shows a continuous increase in the concentration value, but it rapidly decays starting from 500 ms due to the sedimentation phenomenon. However, the concentration in the case of dust at 400 μm is always higher than the 200 μm case (**Figure IV.86**). In the former case, the dust leaves the perforated annular ring and, once the turbulence decays, begins to settle occupying the entire sphere and therefore also its centre. In the latter, the particles accumulate on the walls of the sphere due to the presence of macro-vortices (generated by the dust dispersion method), forming the cross structure seen in **Figure IV.83** and leaving the internal zone at low concentration values. **Figure IV.87** shows the turbulent kinetic energy (m^2/s^2) profiles on a cut line (indicated on the left side) for 1 m^3 vessel (a) and 20 L vessel (b) in the case of dust-free air

(black line), and dust/air mixtures with dust size d=200 μm (red line) and d=400 μm (blue line). In both vessels, dust-free air case is characterized by the highest turbulence level. As reported in the literature, as long as the diameter is small (<100 μm), dust particles are partially entrained by the fluid flow [122]. On increasing the dust diameter (e.g., d≥200 μm), it becomes more difficult for the fluid flow to entrain the dust which then follows different paths with respect to the fluid and, consequently, different turbulent kinetic energy profiles are establish (see red line in **Figure IV.87**). Further increasing the dust diameter (e.g., 400 μm), the sedimentation phenomenon becomes more severe as the turbulence dissipates, the air cannot support the dust dispersion that, once left the perforated annular nozzle, falls down leaving the velocity flow field similar to that of the dust-free air case. To assess the effect of turbulence on the evaluation of deflagration index with the two standard vessels at 100 g/m^3, we estimated the theoretical K_{St} as shown elsewhere [185]. Considering only the effect of turbulence, whatever the diameter, the dust is classified always St-1 in the 1 m^3 vessel. Conversely, in the 20 L vessel, starting from the most dangerous condition in which the flow field is similar to that of the dust-free air case (St-3), the classification could significantly vary according to the particles-fluid flow interaction. Therefore, given the great non-uniformity of turbulence degree, the measurement in the 20 L is more susceptible/sensitive to variations in the properties of the dust particles, reducing the repeatability/reliability of the measurements of the explosivity parameters.

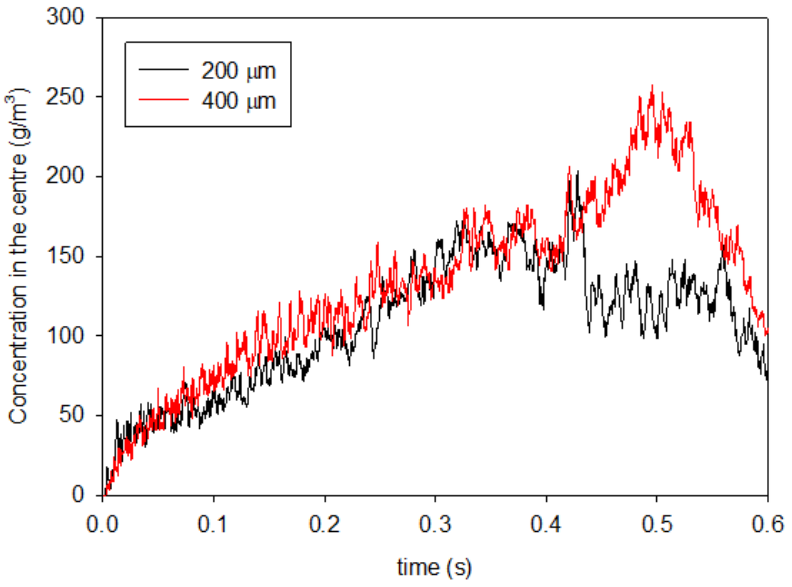

Figure IV.85 *DPM concentration as computed in the centre of the 1 m^3 vessel as a function of time for dust dispersion at d=200 μm (black line) and d=400 μm (red line) C=100 g/m^3* [186]

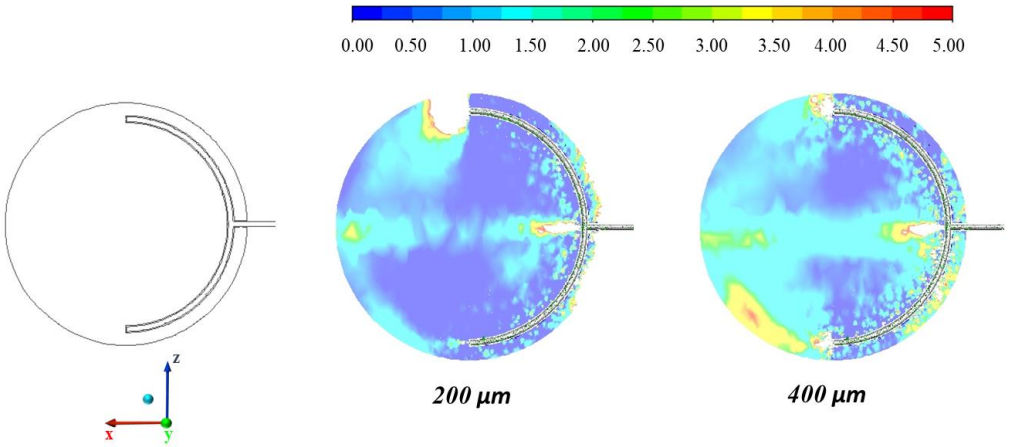

Figure IV.86 *Computed maps of DPM concentration at 600 ms for dust dispersion at d=200 µm (left) and d=400 µm (right), (x-z) plane* [186]

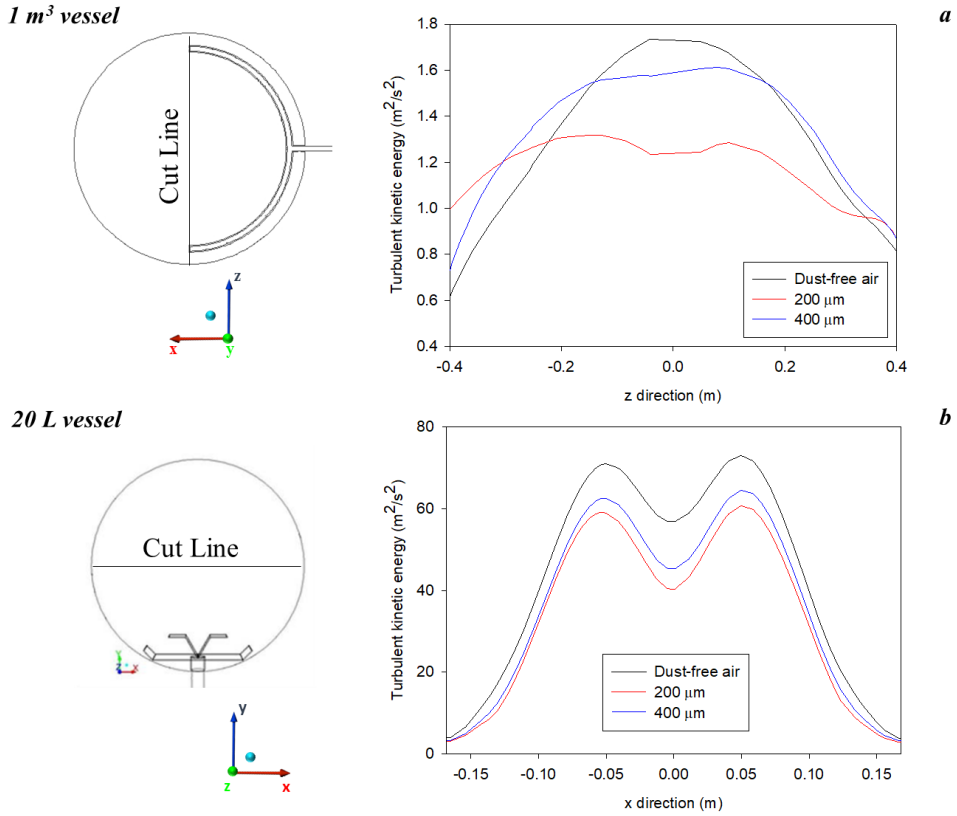

Figure IV.87 *Turbulent kinetic energy (m^2/s^2) profiles on a cut line (indicated on the left side) for 1 m^3 vessel (a) and 20 L vessel (b): dust-free air (black line), dust dispersions at d=200 µm (red line) and d=400 µm (blue line)* [186]

Rebound nozzle

Figure IV.88 shows the temporal pressure trend as computed in the centre of the dust container, in the case of dust-free air and dust at C = 100 g/m^3. As exhibited by the pressure trends, the feeding phase lasts 0.4 s in which the dust container reaches 1 bar and the injection of air/dust-air comes to an end. The temporal pressure trend was compared to experimental data available in the literature to validate the *CFD* model [189]. Dyduch et al. (2016) measured the pressure trend and the transient flow velocity generated by air outflow from the dust dispersion system inside the standard 1 m^3 vessel equipped with the rebound nozzle. The comparison shows a very good agreement.

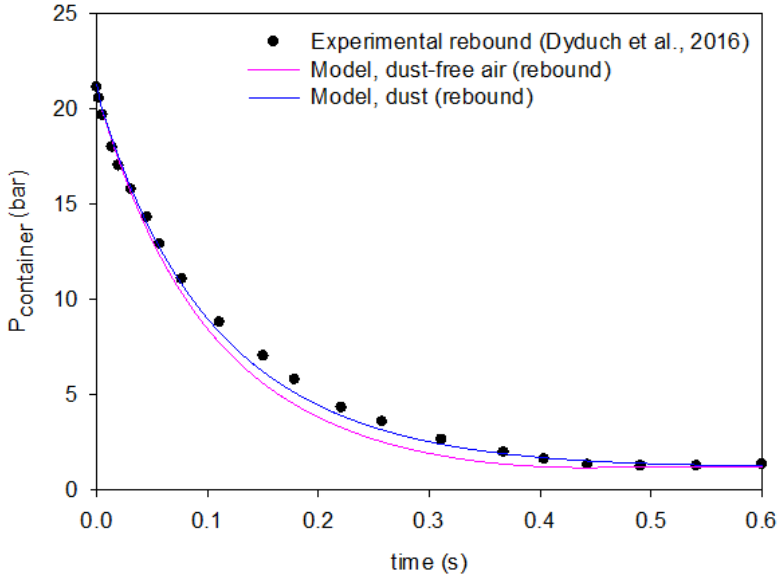

Figure IV.88 *Pressure time histories computed in the centre of the dust container for dust-free air (pink line) and dust-air mixture (blue line)* [188]. *Literature data are also shown for the sake of comparison (black scatter plot)* [189]

In **Figure IV.89** the root mean square velocity (*RMS*) temporal trend in the case of dust-free air and dust at a concentration equal to 100 g/m^3 are shown as computed in the centre of the sphere. The RMS velocity was calculated from the turbulent kinetic energy by considering isotropic flow field. For the sake of comparison, the experimental data measured by Dyduch et al. (2016) are also shown [189]. The comparison shows a good agreement starting from 0.3 s.

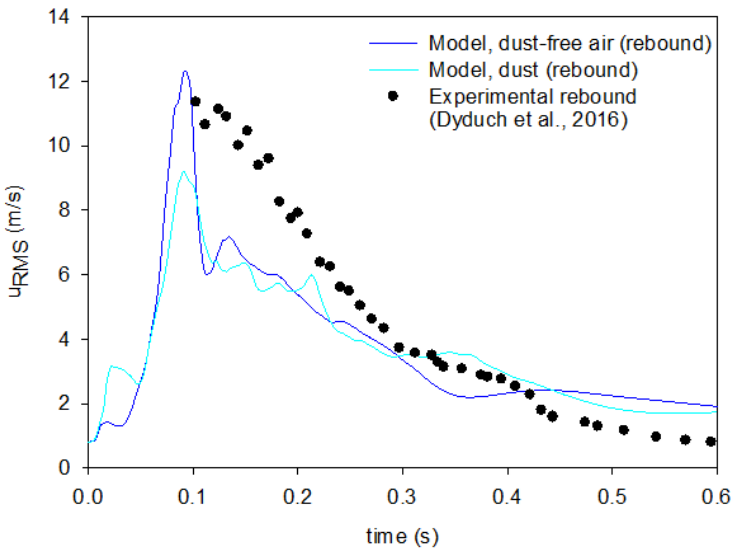

Figure IV.89 *RMS turbulence velocity (m/s) as a function of the time at the centre of the 1 m^3 vessel for dust free air (blue line) and dust-air mixture (cyan lines)* [188]. *Literature data are also shown for the sake of comparison (black scatter plot)* [189]

In **Figure IV.90** the time sequence of the turbulent kinetic energy maps is shown as computed over the frontal (x-z) plane in case of dust-free air (a) and dust at 100 g/m^3 (b). At 400 ms and 600 ms, the maps with dust present non-symmetric fields, differently from the results obtained in the case of dust-free air (a). The occurrence of an asymmetric flow is determined by the action of gravity on the dispersed phase. Kartushinsky et al. (2011) developed a three-dimensional model of particulate flow in a horizontal pipe using the *RANS* method, showing that in spite of the geometric symmetry, the presence of solid particles in the flow may produce asymmetric fields due to gravity and particle sedimentation. The flow asymmetry cannot be accounted for with two-dimensional models [182]. Moreover, in our previous papers, we showed that in both the 20 L spherical vessel and in the 1 m^3 vessel, a non-symmetric flow may establish in the presence of dust particles ([122], [185]). Although the level of turbulence is not completely uniform within the sphere at 600 ms, showing a decay moving from the centre to the walls, the variation range of turbulent kinetic energy is very narrow (from 4.5 m^2/s^2 to 0 m^2/s^2).

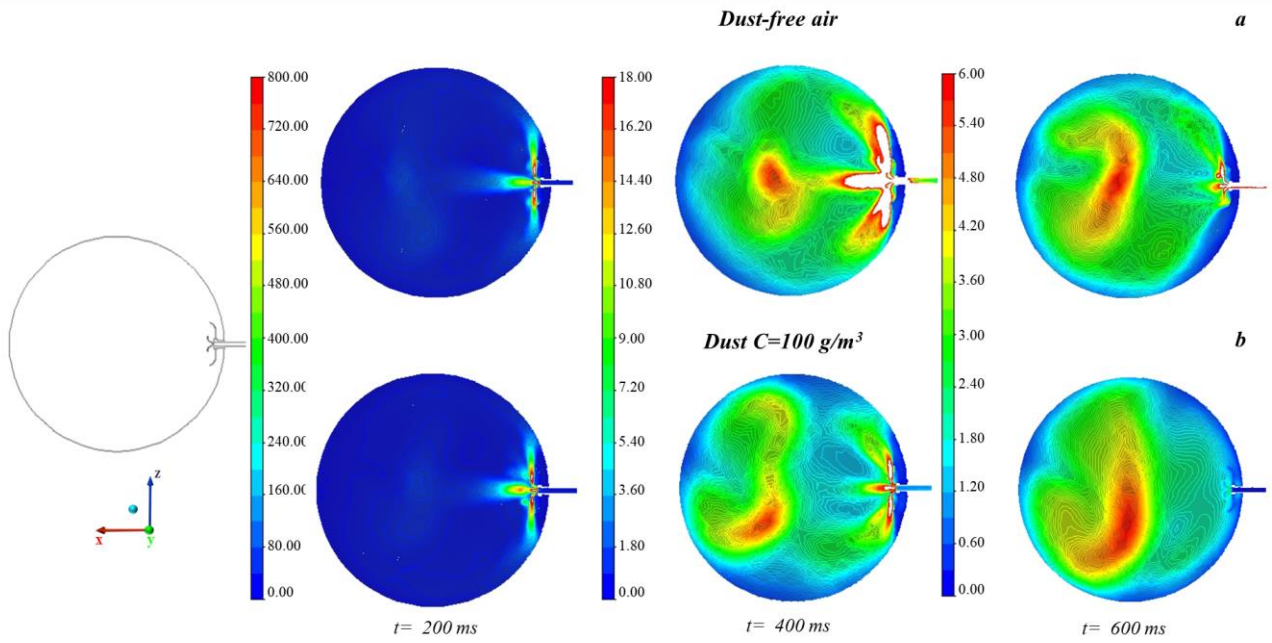

Figure IV.90 *Time sequence of computed maps of turbulent kinetic energy (m^2/s^2): dust-free air (a) and dust C=100 g/m^3 (b), (x-z) plane, rebound nozzle* [188]

Figure IV.91 shows the spatial-temporal distribution of the dust concentration inside the sphere represented through the ratio γ between the dust concentration and the nominal dust concentration (C=100 g/m^3) as obtained on the (x-z) plane (a) and in the whole sphere (b) oriented as in the empty image. The highest dust concentrations are attained on the vortex's edges. Dust is highly concentrated at the sphere walls and in the centre, reaching concentrations much higher than the nominal value (γ=2; C=200 g/m^3), while in the bulk of the sphere, the dust concentration is lower than the nominal value (γ<1; C<100 g/m^3). On increasing time, dust particles start to settle, increasing the amount of particles at the bottom walls. At 600 ms, the highest concentration of particles was obtained at the bottom of the sphere due to the gravity effect, acting in the negative z-direction. This result is in agreement with the findings by Kalejaiye et al. (2010) [121]. In their work, lower values of transmission (and then higher values of concentration) were found in correspondence to the probes close to the vessel walls with respect to those closer to the sphere centre [121].

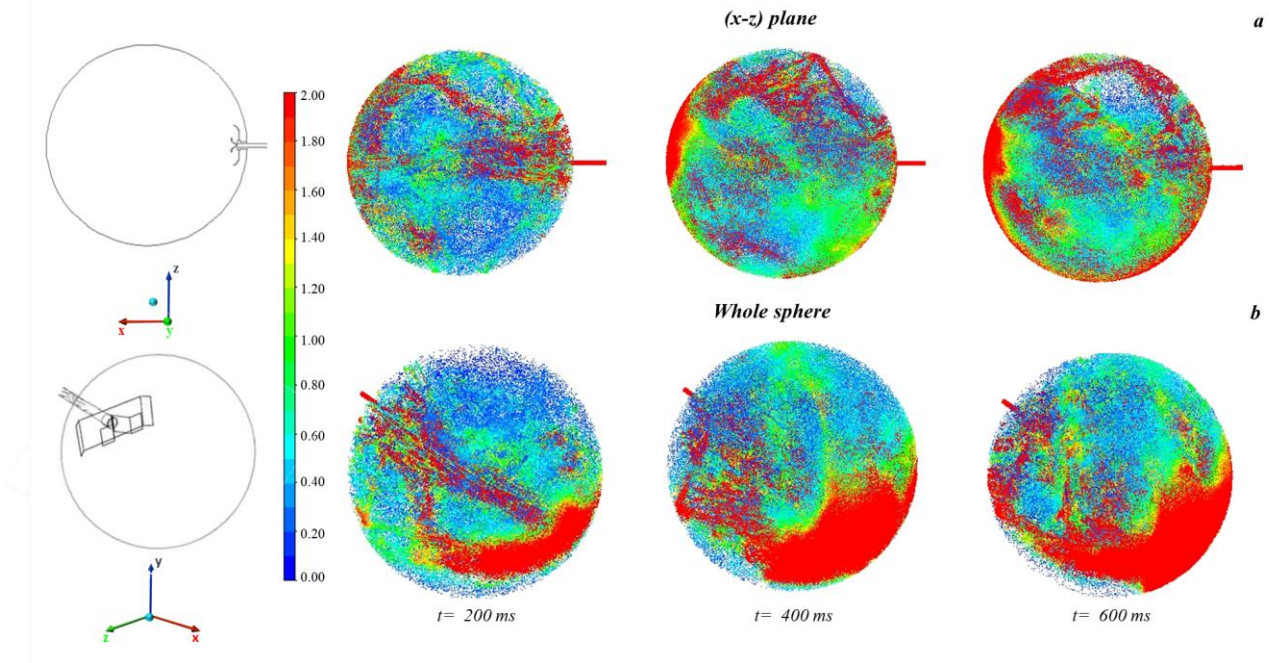

Figure IV.91 *Time sequence of particle tracks coloured by γ: (x-z) plane (a) and whole sphere (b), dust C=100 g/m^3, rebound nozzle* [188]

As stated before, in the standard procedures the annular and rebound nozzles are presented as interchangeable alternatives. For example, in the standard for the 1 m^3 dust explosion vessel, the rebound nozzle is deemed as a suitable alternative in the case of fibrous dusts testing ([9], [84]).

In **Figure IV.92** the time sequence of the turbulent kinetic energy maps is shown as computed over the (x-z) plane for the 1 m^3 vessel equipped with rebound nozzle (a) and perforated annular nozzle (b). At all times, the turbulent kinetic energy computed in the 1 m^3 vessel equipped with rebound nozzle is higher and less uniform than the one found with perforated annular nozzle. Indeed, at the ignition delay time (600 ms), the former has a maximum turbulent kinetic energy (in the centre) equal to 4.5 m^2/s^2, while the latter has a very narrow variation range of turbulent kinetic energy from the centre to the wall is (from 1.25 m^2/s^2 to 0 m^2/s^2) [185].

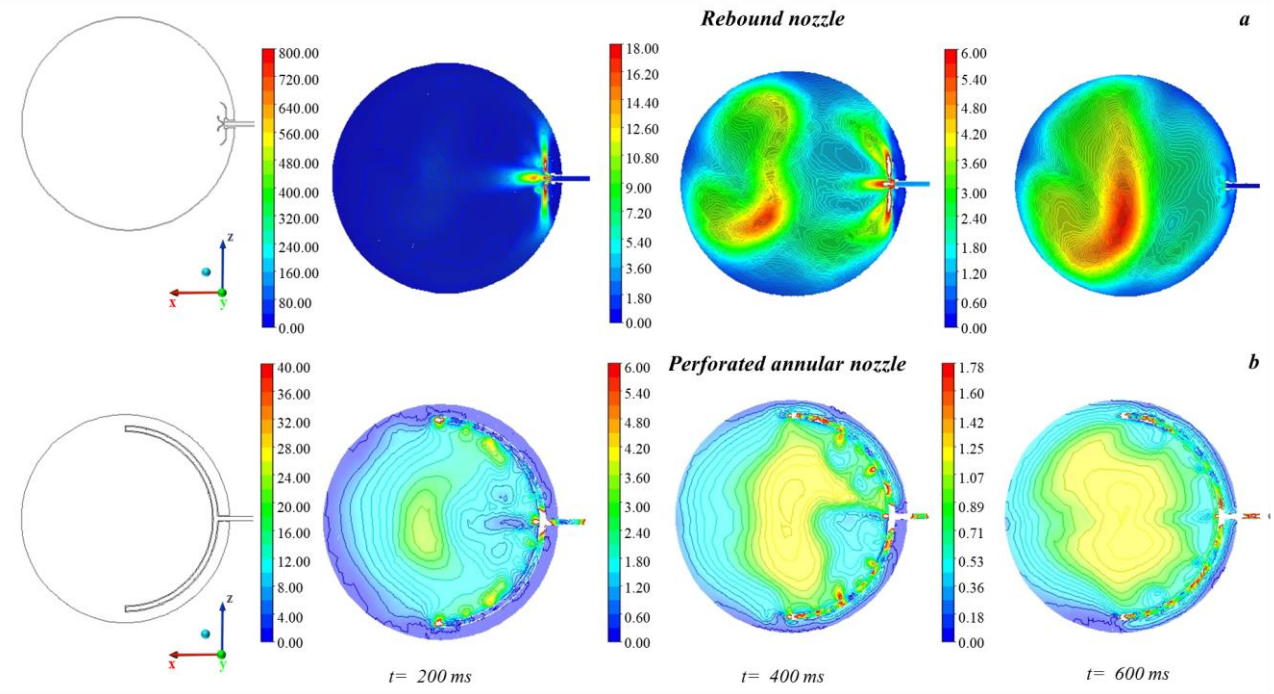

Figure IV.92 *Time sequence of turbulent kinetic energy maps (m^2/s^2): rebound nozzle (a) and perforated annular nozzle (b) ((x-z) plane), dust C=100 g/m^3* [188]

Figure IV.93 shows the temporal trend of the turbulent kinetic energy as computed in the centre of the vessels as a function of time. The experimental data measured by Dyduch et al. (2016) for the rebound nozzle and by Hauert and Vogl (1995) for the perforated annular nozzle ([119], [189]) are reported for the sake of comparison. At each time in the ignition point, the vessels show values of turbulent kinetic energy very different from each other. In particular, the turbulent kinetic energy is always higher in the case of the rebound nozzle than for the perforated annular one. The experimental data measured for both nozzles reach the same plateau value of 1.25 m^2/s^2 starting from 0.45 s, while the data deriving from the model with rebound nozzle (cyan line) are always higher. From these data, we conclude that to achieve a comparable turbulence level within the vessel, the ignition delay time may be increased in the case of rebound nozzle. According to standards, the recommended ignition delay time for the 1 m^3 vessel is equal to (600 ± 100) ms and in the case of rebound nozzle, the calibrated condition in the case of fibrous dust are 700 ms as ignition delay time [191]. Following the cyan line in **Figure IV.93** up to 700 ms, a reduction in terms of turbulent kinetic energy can be seen reaching a value of 1.3 m^2/s^2.

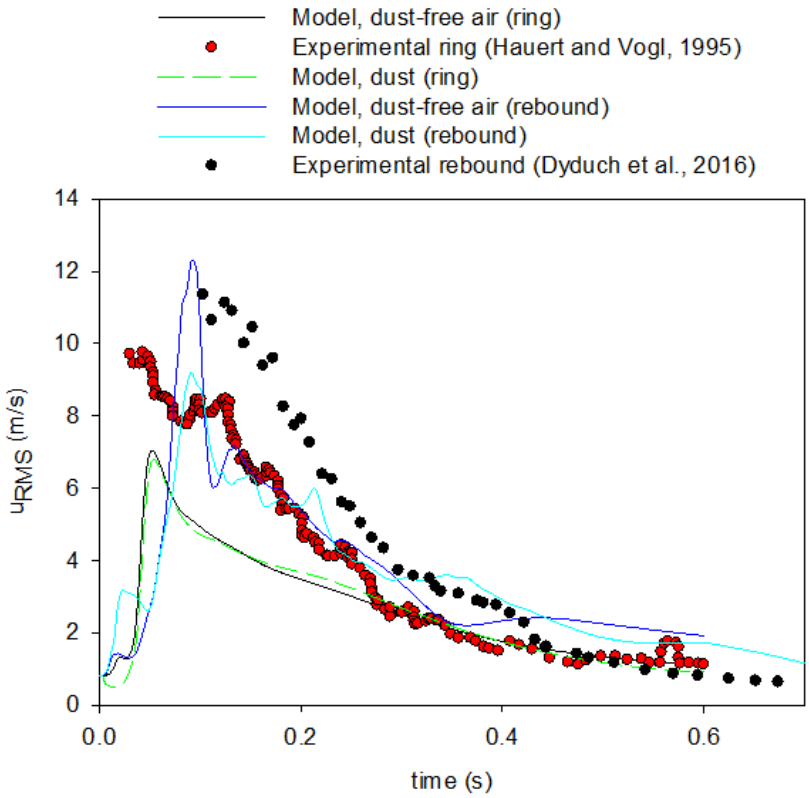

Figure IV.93 *RMS turbulence velocity (m/s) as a function of the time at the centre of the 1 m^3 vessel for dust free air (black and blue lines for ring and rebound nozzles, respectively) and dust-air mixture (green dash and cyan lines for ring and rebound nozzles, respectively)* [188]. *Literature data are also shown for comparison (black scatter plot* [189] *and red scatter plot* [119]*)*

Figure IV.94 shows the spatial-temporal distribution of dust concentration inside the sphere represented through the ratio γ for the 1 m^3 vessel equipped with rebound nozzle (a) and perforated annular nozzle (b). At ignition, the vessels show particle distributions very different from each other. Starting from 400 ms, in the case of perforated annular nozzle, the dust creates a three-dimensional cross inside the vessel. Conversely, in the case of rebound nozzle, no three-dimensional cross can be seen, and the dust distribution is characterized by an accumulation of dust in the centre and at the bottom of the sphere due to the gravity influence. In both cases, at the ignition time (t=600 ms), the cloud is not uniform, suggesting that the flame will start propagating in a stratified flammable mixture, eventually leading to K_{St} values very different.

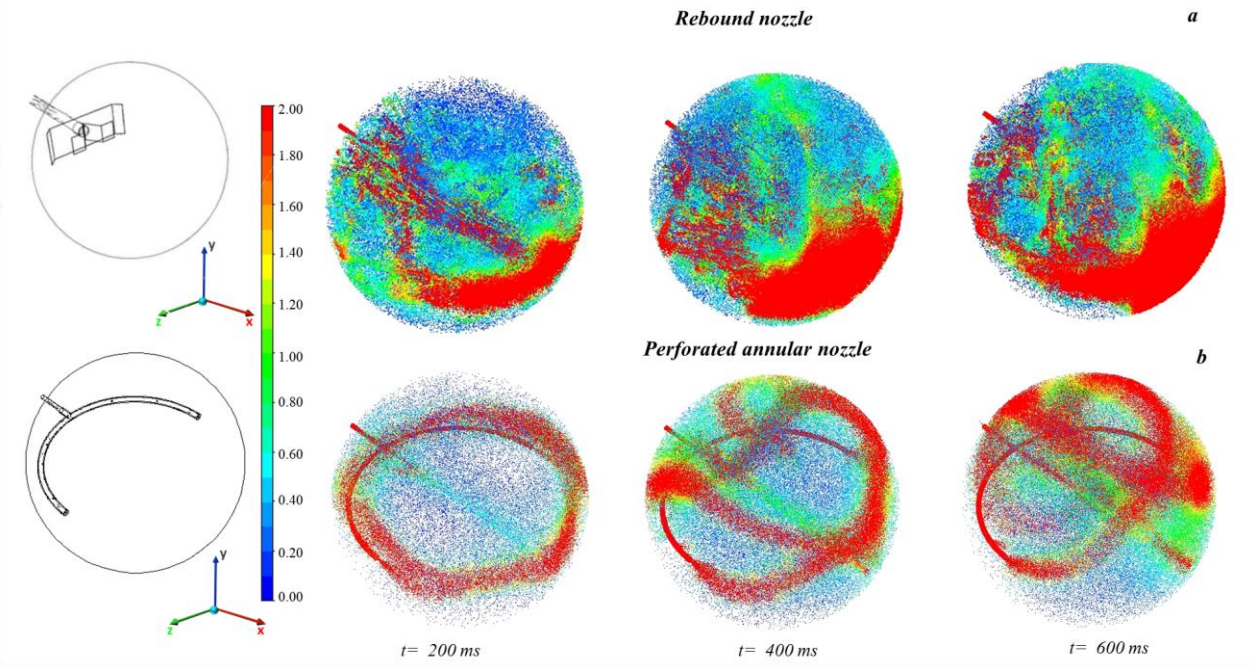

Figure IV.94 *Time sequence of particle tracks coloured by γ computed in the whole spheres: rebound nozzle (a) and perforated annular nozzle (b) ((x-z) plane), dust C=100 g/m*^{3} [188]

Figure IV.95 shows the temporal trend of the *DPM* concentration as computed in the centre of the vessels as a function time. The experimental data measured by Hauert and Vogl (1995) for the perforated annular nozzle are reported for the sake of comparison [119]. At the best of our knowledge, no experimental data about dust concentration in the centre of the 1 m^3 vessel equipped with rebound nozzle are available. As can be seen, the concentration of the dust in the case of rebound is always higher than in the case of perforated annular nozzle due to the vortices generation and the dust accumulation on their edges. Extending the ignition delay time up to 700 ms, the turbulence dissipation corresponds to a reduction in the concentration at the centre of the sphere, with a more uniform condition in the core of the sphere but a greater accumulation on the bottom due to gravity.

The huge difference between the dust concentration at the centre in the case of rebound and annular nozzles, suggest that the evaluation of explosion parameters may give significantly different results when using different nozzles.

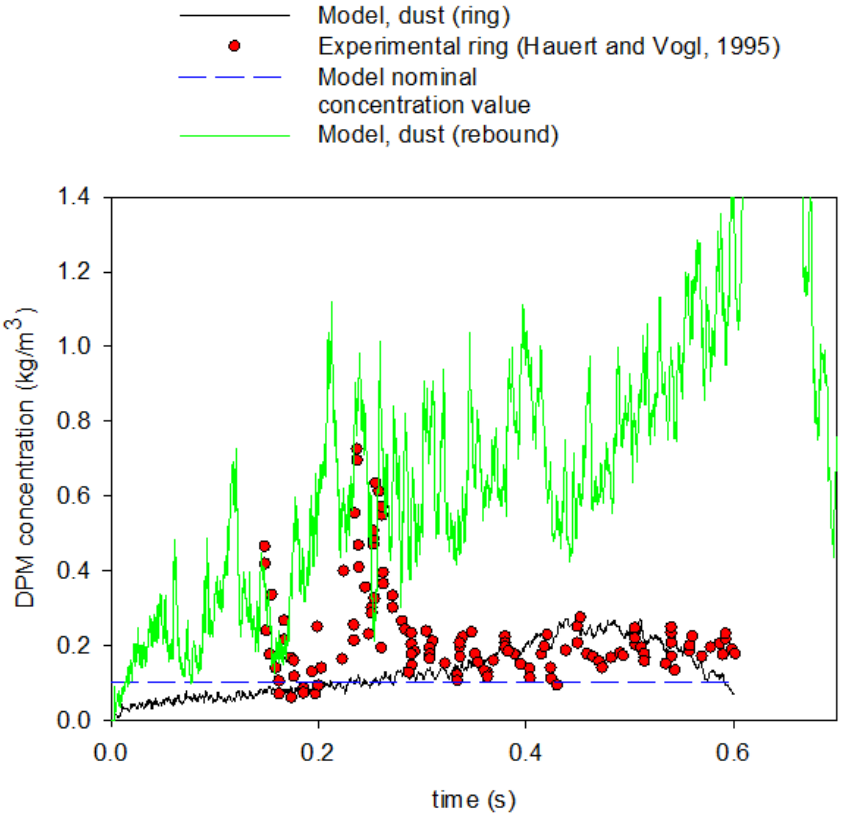

Figure IV.95 *DPM concentration as computed in the centre of the spheres for perforated annular (black line) and rebound (green line) nozzles as a function of time* [188]. *Nominal concentration value 100 g/m^3 (dotted blue line) and literature data are also shown for comparison (red scatter plot* [119]*)*

IV.5.3. Final remarks

CFD simulations allow the quantification of the temporal/spatial profiles of turbulent kinetic energy and dust concentration in the 1 m^3 vessel. Comparison of the computed turbulent kinetic energy and dust concentration with the (few) experimental data available show a good agreement only at times higher than 300 ms. The spatial distribution of the turbulent kinetic energy is quite uniform inside the whole vessel. Conversely, the dust is mainly concentrated at the outer zones of the vortices generated in the vessel and then dust concentration is not uniform. Simulations also show that a large part of dust is not fed, being trapped in the annular nozzle. Comparison with the turbulent kinetic energy in the 20 L vessel, shows that the turbulence level in the 20 L is much higher. As a result, the deflagration index estimated in the lab-scale 20 L vessel, considering the spatial distribution of the level of turbulence (calculated through CFD simulations), was found to be 2.4 times higher than the value obtained in the 1 m^3 vessel, providing a more conservative assessment. It is worth noting other effects must be taken into consideration in the K_{St} assessment such as overdriving, preheating, thermal radiation and turbulence level. CFD simulations of the

dust dispersion inside the 1 m^3 standard vessel were performed at different values of the dust diameter. The time sequences of turbulent kinetic energy maps show that turbulent kinetic energy is quite uniform inside the whole vessel and in the case of 400 μm, at 600 ms the flow field is more similar to that of dust-free air, due to the occurrence of particle sedimentation and incomplete feeding. The different particles-fluid interaction obtained varying the dust diameter is further confirmed by the time sequence of particle tracks. On increasing the dust diameter, the dust and the fluid flows are independent, and the sedimentation phenomenon becomes more severe as the turbulence dissipates leaving the velocity flow field similar to that of the dust-free air case. Moreover, a worse feeding is attained, with most of the dust trapped in the perforated annular nozzle on increasing dust diameter. However, from a comparison with the 20 L vessel in terms of theoretical deflagration index assessment, given the great uniformity of turbulence degree, the 1 m^3 vessel is less susceptible and influenced by the dust intrinsic properties that influence the kind of particles-fluid flow interaction. CFD simulations allow the quantification of the temporal/spatial profiles of turbulent kinetic energy and dust concentration in the 1 m^3 vessel equipped with rebound nozzle. The computed turbulent kinetic energy and dust concentration were validated against the experimental available data (at times higher than 300 ms). Although the level of turbulence is not completely uniform within the sphere at 600 ms, showing a decay moving from the centre to the walls, the variation range of turbulent kinetic energy is very narrow (from 4.5 m^2/s^2 to 0 m^2/s^2). Conversely, the dust is mainly concentrated at the outer zones of the vortices generated in the vessel and then dust concentration is not uniform. Comparison with the turbulent kinetic energy in the 1 m^3 vessel equipped with perforated annular nozzle, shows that the turbulence level in the case of the rebound is higher, as the amount of dust fed in the vessel.

IV.5.4. Published articles

Results discussed in this section have been published in peer-reviewed scientific journals ([185], [186], [188]):

- M. Portarapillo, M. Trofa, R. Sanchirico, and A. Di Benedetto, “CFD simulations of dust dispersion in the 1 m3 explosion vessel,” *J. Loss Prev. Process Ind.*, vol. 68, no. July, p. 104274, 2020.
- M. Portarapillo, M. Trofa, R. Sanchirico, and A. Di Benedetto, “CFD simulations of the effect of dust diameter on the dispersion in the 1 m3 explosion vessel,” *Chem. Eng. Trans.*, vol. 86, 2021.

- M. Portarapillo, M. Trofa, R. Sanchirico, and A. Di Benedetto, "CFD simulation of turbulent fluid flow and dust dispersion in the 1 m3 Explosion Vessel equipped with the rebound nozzle," *Under Rev. J. Loss Prev. Process Ind.*, 2021.

IV.6. Effect of turbulence spatial distribution on the deflagration index: Comparison between 20 L and 1 m^3 vessels

In this section, we aimed at quantifying the effect of spatial distribution and values of the turbulent kinetic energy on the explosion parameters (deflagration index and maximum pressure). Starting from the turbulent kinetic energy maps as computed in both 20 L and 1 m^3 vessels, we calculated the pressure-time history and from this the explosion parameters. To highlight the effect of the turbulence level homogeneity inside the vessels on the explosion parameters evaluation, the calculations will be carried out in three cases: variable turbulence, maximum turbulence (as computed in the centre of the vessels) and minimum turbulence (found close to the wall). The variability of the explosion parameters between the three cases for each vessel will be indicative of the turbulence level in the vessel and its uniformity. In particular, the smaller the explosion parameters variation between the three cases described, the more homogeneous the turbulence flow field and the less influenced by the properties of the dust. Consequently, in this case, the measurements will be more reliable and repeatable. The maximum explosion pressure P_{max} (bar) and the deflagration index K_{St} (bar m/s) were calculated starting from the pressure-time history.

IV.6.1. Methodologies

In the following the procedure for the calculation of the pressure time histories in the explosion vessel is described. The steps of the procedure are based on the calculation of:

1. turbulent kinetic energy k
2. turbulent burning velocity S_t
3. pressure-time history $P(t)$ to calculate P_{max} and K_{St}

To get the map of the turbulent kinetic energy, we performed CFD simulations of the temporal evolution of fluid dynamic conditions in both vessels (20 L and 1 m^3) by means of a previously developed and validated models ([122], [185]). Computations were performed for cornstarch with density and diameter equal to 1500 kg/m^3 and 14 μm, respectively. The choice of the dust was made since the availability of literature data. From the computed maps of the turbulent kinetic energy k, the maps of the velocity fluctuation u' have been calculated using the Equation (58).
In the following figures, computed maps of the turbulent kinetic energy (a) and of the velocity fluctuations (b) for the 20 L (**Figure IV.96**) and for the 1 m^3 vessel (**Figure IV.97**) are shown.

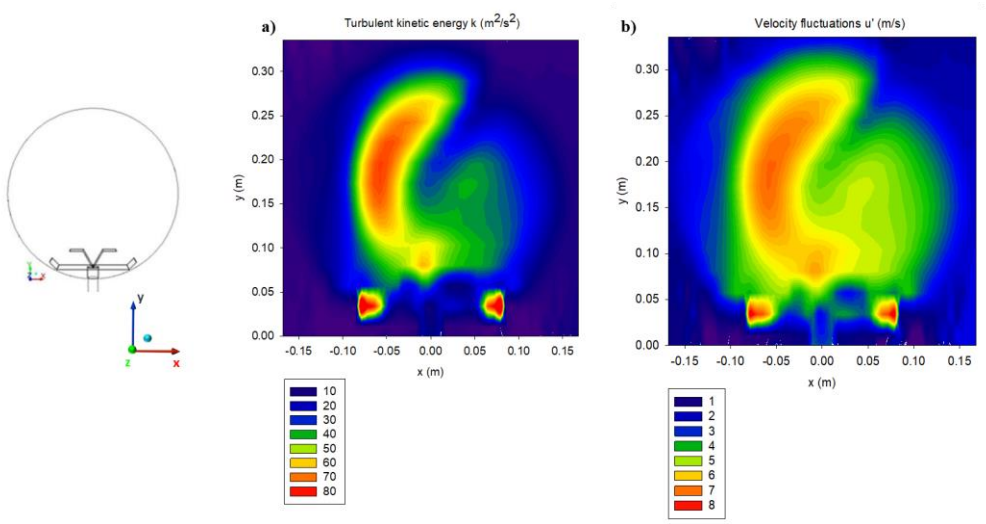

Figure IV.96 *Maps of the turbulent kinetic energy k (a) and of the velocity fluctuations, u' (b), C_{dust} = 200 g/m³, V=20 L, (x-y) plane* [187]

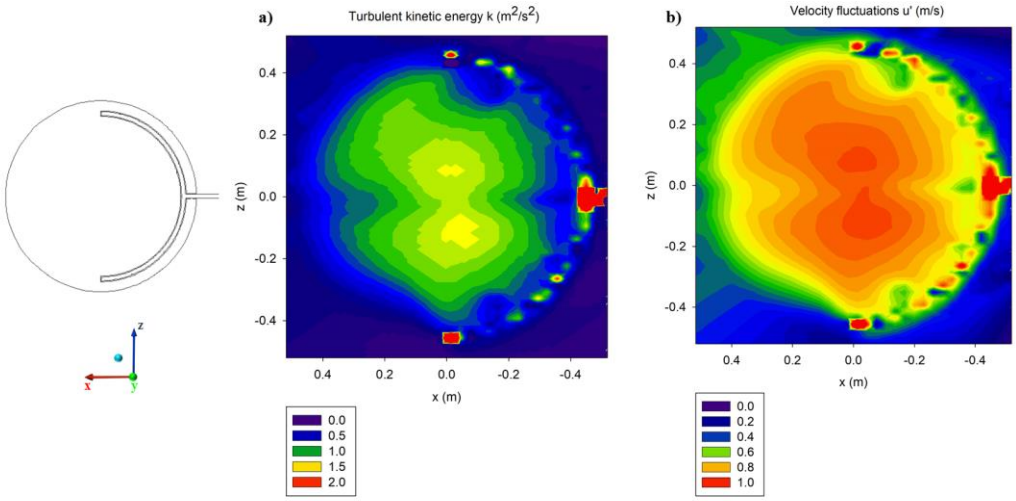

Figure IV.97 *Map of the turbulent kinetic energy, k (a) and of the velocity fluctuations, u' (b), C_{dust} = 200 g/m³, V=1 m³, (x-z) plane* [187]

The turbulent burning velocity S_t has to be calculated as function of the velocity fluctuation *u'*. Several formulas are available which correlate S_t to *u'*, for both gas and dust flame propagation. In a previous paper [192], we showed that the relation which better fits the effect of turbulence on S_t is that proposed by Pocheau (1994) (**Table II.3**) [57]. In this equation, S_t strictly depends on *u'* and S_l.

The value of the laminar burning velocity S_l was calculated by simulating the flame propagation

of the volatiles coming from the dust pyrolysis. To do that, we assumed that the pyrolysis time t_{pyro} is lower than the combustion time t_{comb}. Starting from each volatile composition, we performed the simulation of the flame propagation by means of the software CHEMKIN and evaluate the laminar burning velocity [193]. The amount and composition of the volatiles produced by the pyrolysis of cornstarch were obtained by the literature [68]. In particular, in this work, the thermal decomposition products of the cornstarch are reported at two temperatures 450 °C and 550 °C. In **Table IV.40**, the literature data are given at 450 °C and 550 °C. Starting from the composition given in **Table IV.40**, we computed the volatile amount and composition at varying the dust concentration in the vessel. Volatile matter was determined equal to 80%wt of the dried sample initial weight through the proximate analysis. In **Table IV.41** and **Table IV.42** the data are given for the 20 L and 1 m^3 vessel, respectively.

Table IV.40 *Volatiles produced by the pyrolysis of cornstarch* [68], [187]

Gaseous species	**450 °C**	**550 °C**
H_2 (%)	0.86	4.82
CO (%)	42.73	39.06
CH_4 (%)	18.27	25.05
CO_2 (%)	38.13	31.06

Table IV.41 *Volatiles produced by the pyrolysis of cornstarch, oxygen and nitrogen in the 20 L and 1 m^3 vessels, at varying the dust concentration at 450 °C [68]. The stoichiometric oxygen amount is also shown* [187]

C (g/m^3)	H_2 (%)	O_2 (%)	N_2 (%)	CO (%)	CH_4 (%)	CO_2 (%)	$O_{2,stoich}$ (%)
400	0.17	16.84	63.36	8.46	3.62	7.55	11.55
500	0.20	16.05	60.37	10.08	4.31	8.99	13.76
600	0.23	15.33	57.66	11.55	4.94	10.30	15.76
700	0.26	14.67	55.17	12.89	5.51	11.50	17.60
800	0.29	14.06	52.89	14.12	6.04	12.60	19.28
900	0.31	13.50	50.79	15.26	6.52	13.61	20.83

Table IV.42 *Volatiles produced by the pyrolysis of cornstarch, oxygen and nitrogen in the 20 L and 1 m^3 vessels, at varying the dust concentration at 550 °C [68]. The stoichiometric oxygen amount is also shown* [187]

C (g/m^3)	H_2 (%)	O_2 (%)	N_2 (%)	CO (%)	CH_4 (%)	CO_2 (%)	$O_{2,stoich}$ (%)
200	0.58	18.48	69.53	4.68	3.00	3.72	8.64
300	0.82	17.44	65.60	6.63	4.25	5.27	12.22
400	1.03	16.51	62.09	8.36	5.36	6.65	15.43
500	1.23	15.67	58.93	9.92	6.37	7.89	18.30
600	1.40	14.91	56.09	11.33	7.27	9.01	20.90
700	1.56	14.22	53.50	12.61	8.09	10.03	23.26

In **Figure IV.98**, the laminar burning velocity obtained by CHEMKIN simulations are shown starting from the volatile compositions at 450 °C and 550 °C. Literature data obtained with different experimental rigs, granulometries and concentration are also reported. From the data shown in **Figure IV.98**, it appears that an acceptable agreement is obtained with the data provided by Krause and Kasch (1994) [69]. It is worth noting that considering the contribution of all the step occurring in the flame propagation as reported in Section IV.1, the agreement with literature data was better.

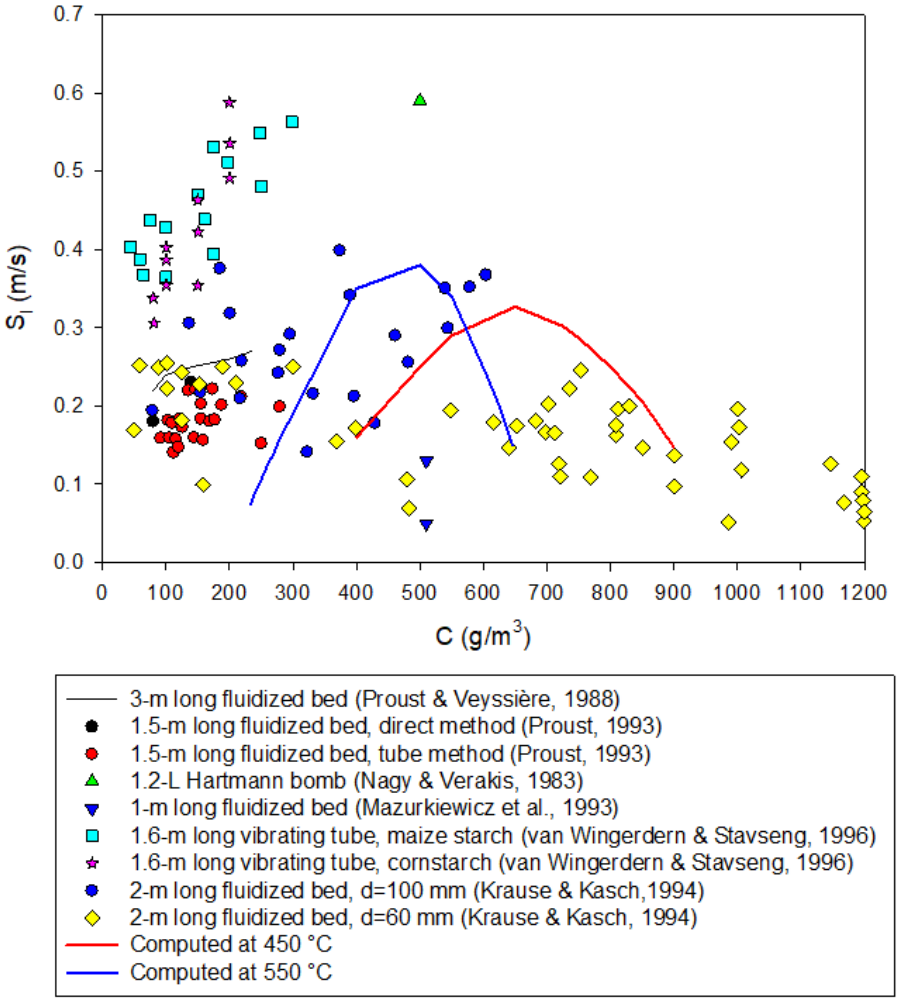

Figure IV.98 *Laminar burning velocity as function of the dust concentration as computed at pyrolysis temperature: 450 °C and 550 °C [68]. Literature data are also shown* ([51], [65]–[69])

To evaluate the pressure time history, the equation of Dahoe et al. (1996) [190] was used:

$$r_f = r_{vessel}\left[1-\left(\frac{P_0}{P}\right)^{\frac{1}{\kappa}}\frac{P_{MAX}-P}{P_{MAX}-P_0}\right]^{\frac{1}{3}} \tag{61}$$

where r_f (m) is the flame radius, κ (-) is the heat capacity ratio. In Equation (61), P_{max} is the maximum pressure which was calculated by means of GASEQ software [135].

At each radius value which corresponds to the flame position, the corresponding pressure has been calculated. To evaluate the flame position (r_f) as function of time, we used the turbulent burning velocity (S_t):

$$t = \frac{r}{S_t} \tag{62}$$

Once obtained the pressure-time history, the deflagration index can be calculated through the cubic law (Equation (2)).

IV.6.2. Results

Figure IV.99 shows the radial profile of the turbulent kinetic energy (*k*) as computed at 60 ms which is the ignition delay time according to the standard in the 20 L vessel [9]. The turbulent kinetic energy significantly varies along the radius, reaching a maximum at r = 0.04 m.

The evaluation of the pressure histories has been performed at three different conditions:

1) CASE 1: implementing the radial profile of turbulent kinetic energy
2) CASE 2: assuming the turbulent kinetic energy as constant and equal to the maximum value
3) CASE 3: assuming the turbulent kinetic energy as constant and equal to the minimum value.

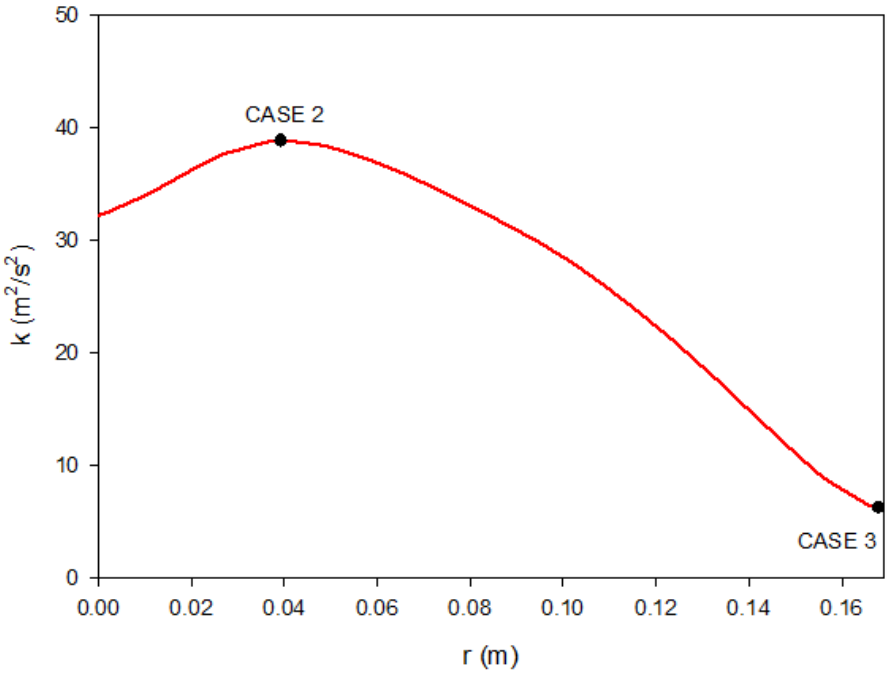

Figure IV.99 *Turbulent kinetic energy as function of the radial position in the 20 L vessel as computed at 60 ms* [187]

Figure IV.100 (a) shows the pressure histories as obtained varying the dust concentration in the 20 L vessel at two pyrolysis temperature values (450 °C, top; 550 °C, bottom). The pressure histories have calculated assuming the turbulent kinetic energy varies along the radius as obtained

by the CFD simulations (CASE 1). From the profiles of **Figure IV.100 (a)**, we calculated the maximum rate of pressure rise and then the deflagration index (Equation (2)). In **Figure IV.100** (b) the maximum pressure (top) and the deflagration index (bottom) are plotted as function of the nominal dust concentration, as obtained by using the pyrolysis data at 450 °C and 550 °C.

At the two pyrolysis temperatures, the maximum values of K_{St} are almost similar: 238 bar m/s at 550 °C and 223 bar/m s at 450 °C. In both cases, the dust is classified as *St-2* (200< K_{st} <300).

The maximum value of P_{max} is slightly higher when pyrolysis occurs at 550 °C (8 bar) than at 450 °C (7.6 bar). The dust concentration at which the $K_{St,max}$ and P_{max} are attained changes as function of temperature: C = 500 g/m^3 at 550 °C and at C = 725 g/m^3 at 450 °C.

Calculations of the deflagration index were also performed by assuming *u'* corresponding to the maximum value simulated inside the 20 L vessel (CASE 2).

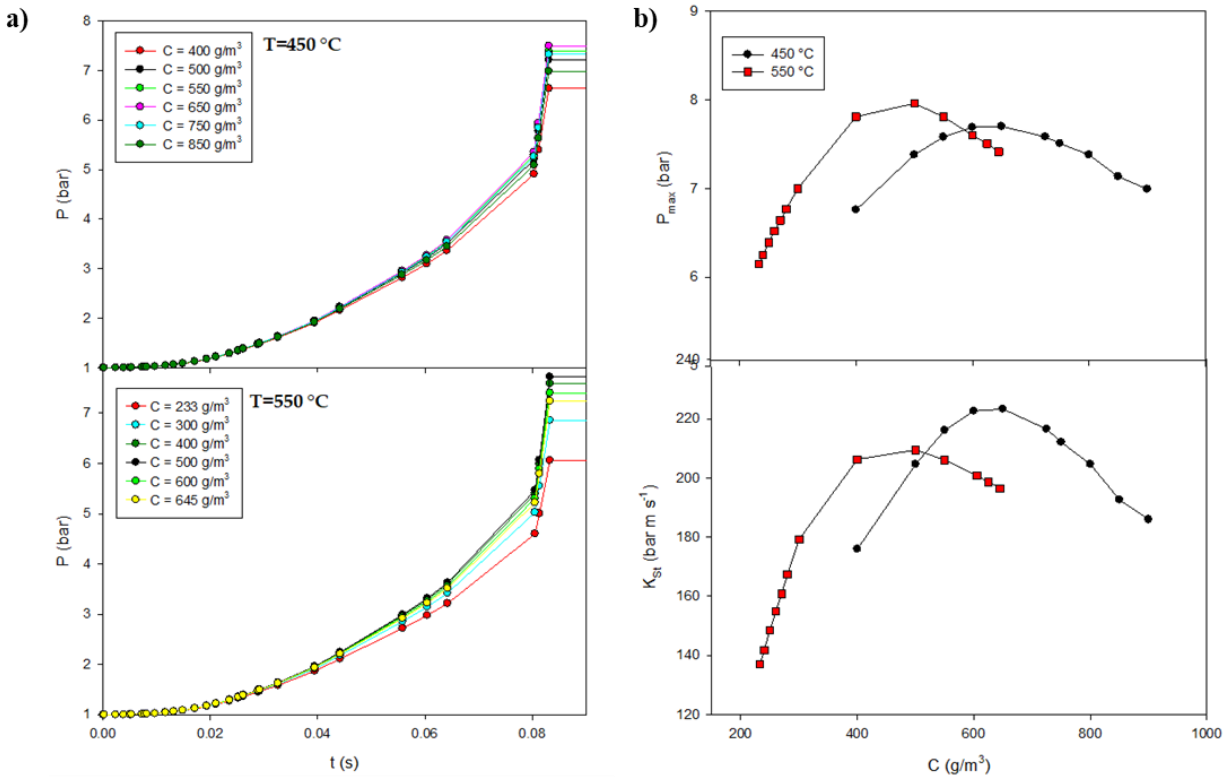

Figure IV.100 *Pressure time histories as function of time at different dust concentration and pyrolysis temperature (top: 450 °C; bottom: 550 °C) calculated in the 20 L vessel; CASE 1 (a) and maximum pressure (P_{max}, top) and deflagration index (K_{St}, bottom) as function of nominal dust concentration as calculated at two pyrolysis temperature values (450 °C and 550 °C), CASE 1 (b)* [187]

In **Figure IV.101 (a)** the pressure time histories plotted as function of time, as calculated at

different nominal dust concentration and pyrolysis temperature (450 °C and 550 °C). From the pressure temporal profiles, we calculated the deflagration index and the maximum pressure. In **Figure IV.101 (b)** the maximum pressure (top) and the deflagration index (bottom) are plotted as function of the nominal dust concentration, as obtained by using the pyrolysis data at 450 °C and 550 °C. In this case, the values are much higher, and the dust would be classified as *St-3*. At the two pyrolysis temperatures, the maximum values of K_{St} are almost similar: 540 bar m/s at 550 °C and 527 bar/m s at 450 °C. The maximum value of P_{max} is slightly higher when pyrolysis occurs at 550 °C (7.96 bar) than at 450 °C (7.7 bar). The dust concentration at which the $K_{St,max}$ and P_{max} are attained changes as function of temperature: C = 500 g/m^3 at 550 °C and at C = 650 g/m^3 at 450 °C.

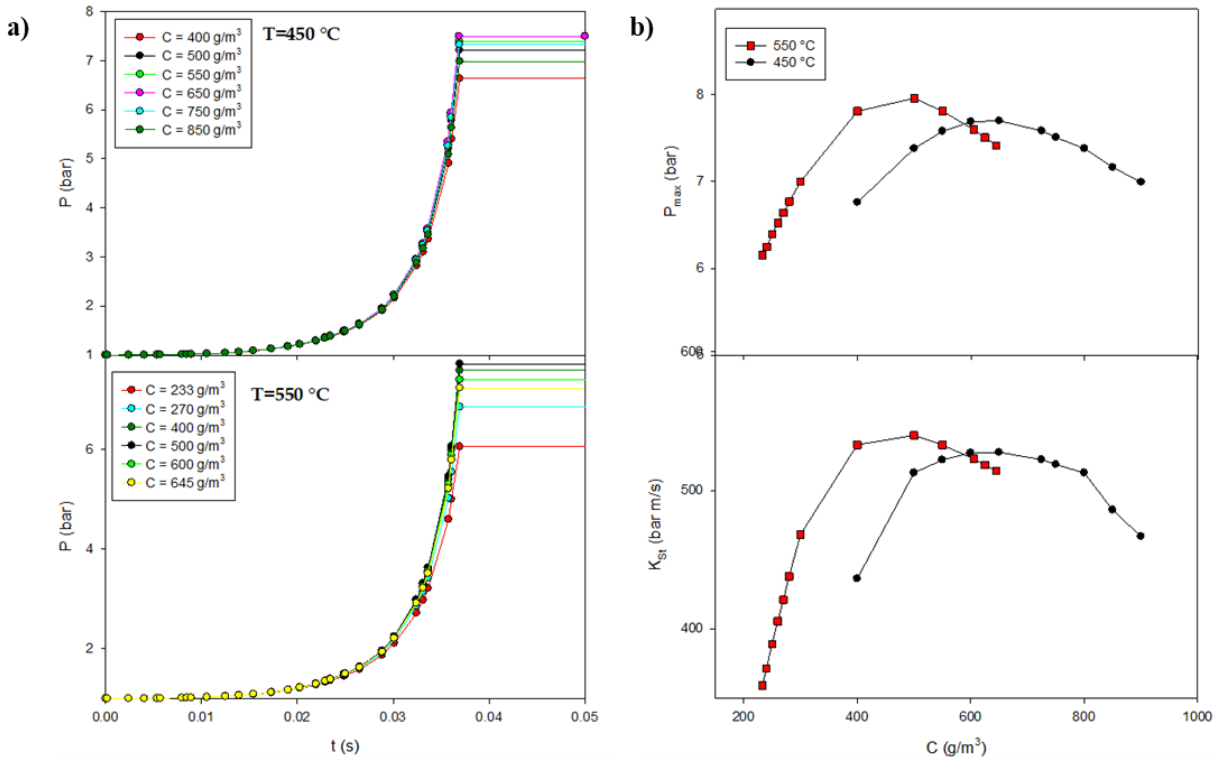

Figure IV.101 *Pressure time histories as function of time at different dust concentration and pyrolysis temperature (top: 450 °C; bottom: 550 °C) calculated in the 20 L vessel; CASE 2 (a) and maximum pressure (P_{max}, top) and deflagration index (K_{St}, bottom) as function of nominal dust concentration as calculated at two pyrolysis temperature values (450 °C and 550 °C), CASE 2 (b)* [187]

In **Figure IV.102 (a)** the pressure time histories are as calculated at different nominal dust concentration and pyrolysis temperature (450 °C, top and 550 °C, bottom) in the case of minimum turbulence (CASE 3). From the temporal profiles of figure, we calculated the deflagration index

and the maximum pressure. In **Figure IV.102 (b)** the maximum pressure (top) and the deflagration index (bottom) are plotted versus the nominal dust concentration at the two temperature values. In this case, the effect of the pyrolysis temperature is more significant. This result is related to the major role of the mixture reactivity with respect to the turbulence level. The maximum values of K_{St} are 50 bar m/s at 550 °C and 35 bar/m s at 450 °C. In both cases, the dust is classified as *St-1*. The maximum value of P_{max} is slightly higher when pyrolysis occurs at 550 °C (8 bar) than at 450 °C (7.6 bar). It is worth noting that the value of P_{max} does not depend on the fluid flow conditions. The dust concentration at which the $K_{St,max}$ and P_{max} are attained changes as function of temperature: C = 500 g/m^3 at 550 °C and at C = 650 g/m^3 at 450 °C.

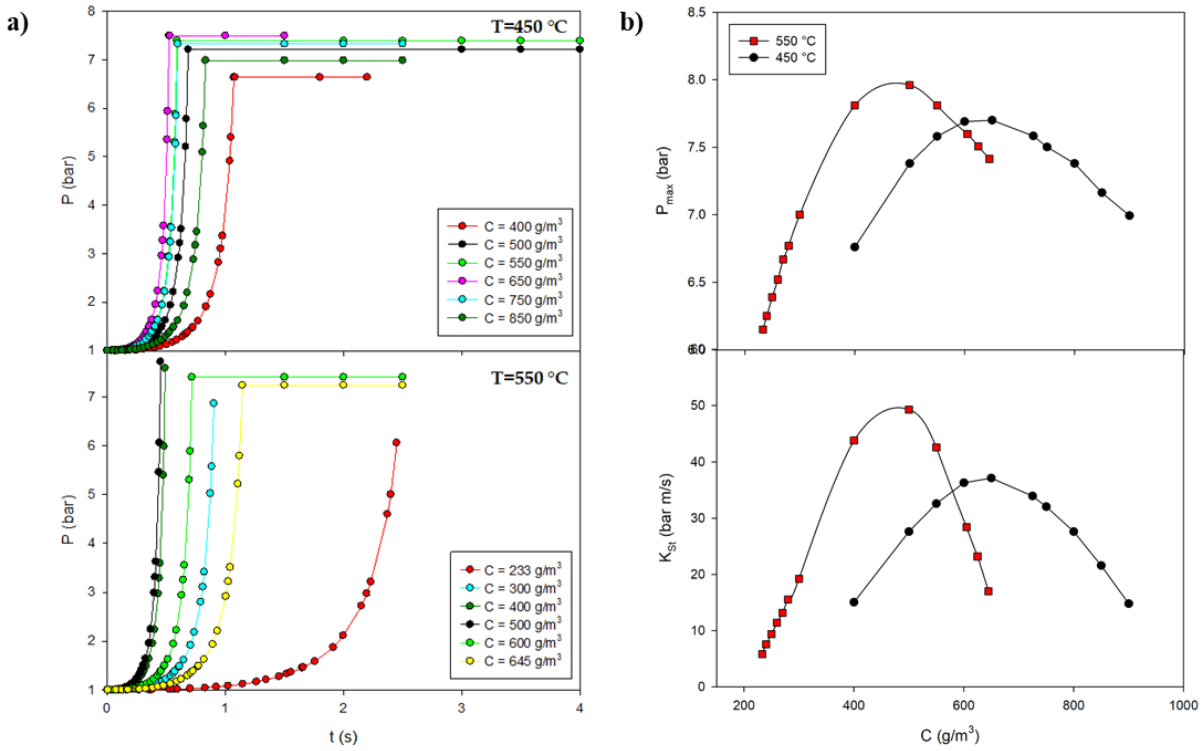

Figure IV.102 *Pressure time histories as function of time at different dust concentration and pyrolysis temperature (top: 450 °C; bottom: 550 °C) calculated in the 20 L vessel; CASE 3 (a) and maximum pressure (P_{max}, top) and deflagration index (K_{St}, bottom) as function of nominal dust concentration as calculated at two pyrolysis temperature values (450 °C and 550 °C), CASE 3 (b)* [187]

In **Figure IV.103**, the deflagration index as calculated at different fluid flow conditions (CASE 1, CASE 2 and CASE 3) and at two temperature values (450 °C, top and 550 °C, bottom), are shown together with the literature data. Eckhoff and Mathisen (1978) investigated the influence of moisture of 37 μm starch grains on the rate of pressure rise during explosions in a 1.2 L Hartmann

bomb at 500, 1000 and 2000 g/m^3 [194]. Nagy and Verakis (1983) investigated the influence of moisture of starch grains on the rate of pressure rise during explosions in a 1.2 L Hartmann bomb at 500 g/m^3 [67]. The Table E.1(a) of the NFPA 68, Guide for Venting of Deflagrations, 2002 Edition shows the deflagration index result in the 1 m^3 vessel for cornstarch with mean diameter and concentration equal to 7 μm and 230 g/m^3 respectively [8]. Proust (1993) determined the explosion parameters of cornstarch-air mixtures with mean diameter and concentration equal to 28 μm and 233 g/m^3 respectively in the 20 L vessel [66]. The best agreement is obtained at pyrolysis temperature equal to 450 °C and laminar (CASE 3) and/or variable turbulence conditions (CASE 1). It is worth noting that in our calculations the effect of variable concentration along the radius has not been taken into account. Calculations have been performed by assuming constant dust concentration (i.e., constant laminar burning velocity within the vessel) and equal to the nominal value.

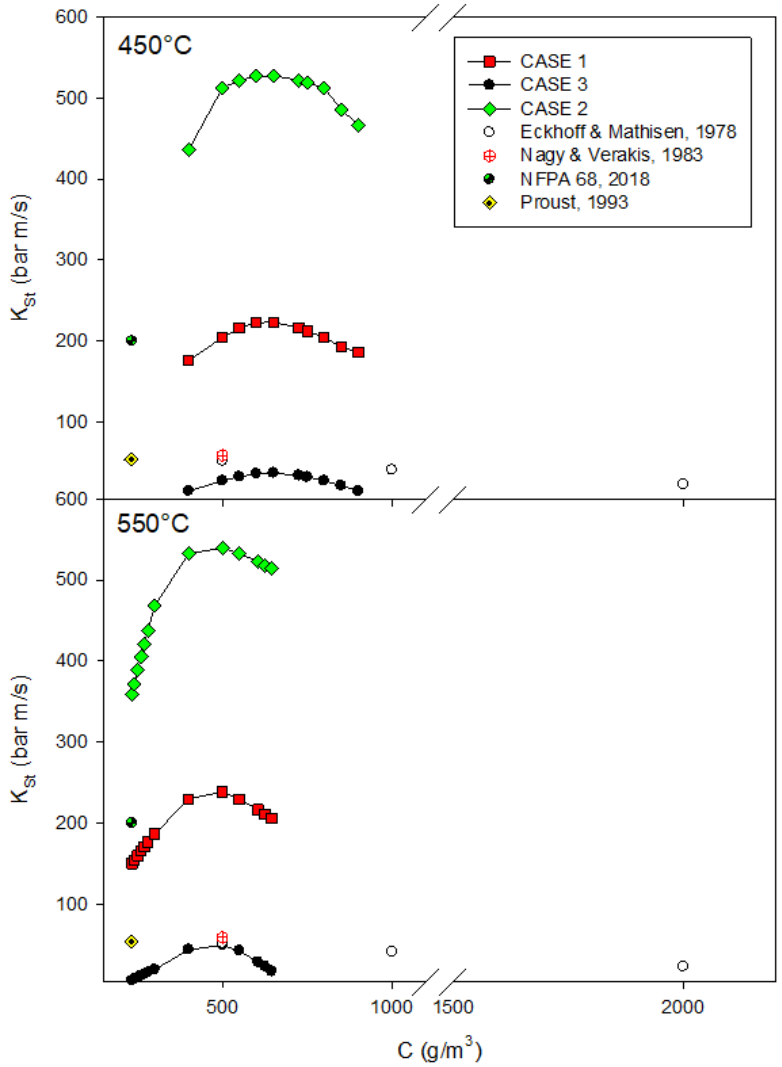

Figure IV.103 *Deflagration index as function of nominal dust concentration as calculated at different fluid dynamic conditions, at pyrolysis temperature equal to 450 °C (top) and 550°C (bottom)* [187]. *Literature data are also shown (*[51], [65]–[69]*)*

Pressure-time histories have been calculated as function of time, at different pyrolysis temperature values (450 °C, top and 550 °C, bottom) and different nominal dust concentrations in the 1 m^3 vessel. As in the case of the 20 L vessel, calculations were performed at different initial conditions: variable turbulence (CASE 1), maximum turbulence (CASE 2) and laminar (CASE 3). From the temporal trend of pressure, the maximum rate of pressure rise and the maximum pressure have been calculated. In **Figure IV.104 (a)** the pressure histories as obtained at varying the dust concentration in the 1 m^3 vessel at two temperature values (450 °C, top; 550 °C, bottom) are shown. The pressure histories have calculated assuming the turbulent kinetic energy variable along the radius as obtained by the CFD simulations (CASE 1). From the values of the rate of pressure

rise it has been possible to calculate the deflagration index as a function of the dust concentration. In **Figure IV.104 (b)** the maximum pressure (top) and the deflagration index (bottom) are plotted versus the nominal dust concentration at the two temperature values. The maximum value of K_{St} ($K_{St\ max}$) is attained at different dust concentration but the values are almost similar: 16.3 bar m/s at 550 °C and 14 bar m/s at 450 °C. In both cases, the dust is classified as *St-1*. The maximum values are attained at C = 500 g/m^3 at 550 °C and at C = 650 g/m^3 at 450 °C. The maximum pressure is attained at C = 500 g/m^3 at 550 °C and at C = 725 g/m^3 at 450 °C.

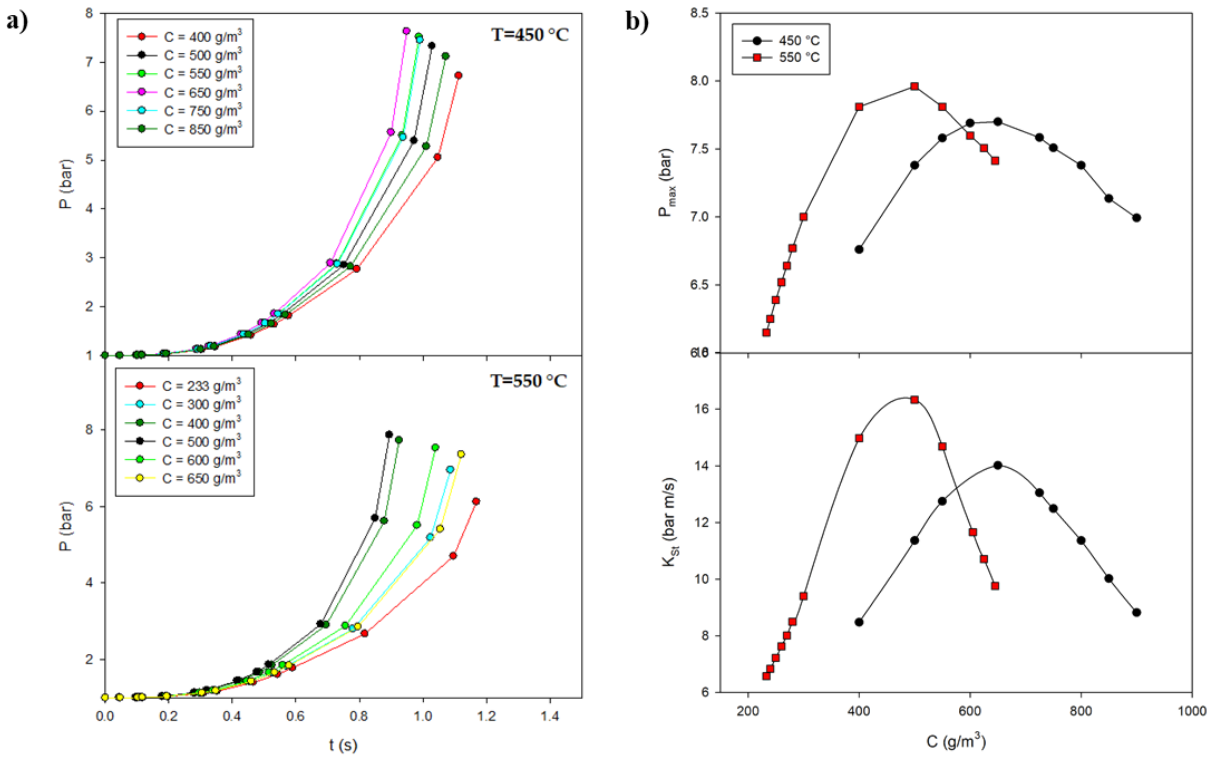

Figure IV.104 *Pressure time histories as function of time at different dust concentration and pyrolysis temperature (top: 450 °C; bottom: 550 °C) calculated in the 1 m^3 vessel, CASE 1 (a) and maximum pressure (P_{max}, top) and deflagration index (K_{St}, bottom) as function of nominal dust concentration as calculated at two pyrolysis temperature values (450 °C and 550 °C), 1 m^3 vessel, CASE 1 (b)* [187]

In **Figure IV.105 (a)** the computed temporal histories of pressure are shown, at different nominal dust concentration and at 450 °C (top) and 550 °C (bottom), assuming the turbulent kinetic energy uniform and equal to the maximum value attained in the vessel (CASE 2). From the values of the rate of pressure rise it has been possible to calculate the deflagration index as a function of the dust concentration. In **Figure IV.105 (b)** the maximum attained pressure (top) and the deflagration index (bottom) are plotted versus the nominal dust concentration, as obtained by using the

pyrolysis data at 450 °C and 550 °C. The maximum value of K_{St} ($K_{St\ max}$) is attained at different dust concentration but the values are almost similar: 43 bar m/s at 550 °C and 39 bar/m s at 450 °C. In both cases, the dust is classified as *St-1*. The maximum values are attained at C = 500 g/m^3 at 550 °C and at C = 725 g/m^3 at 450 °C.

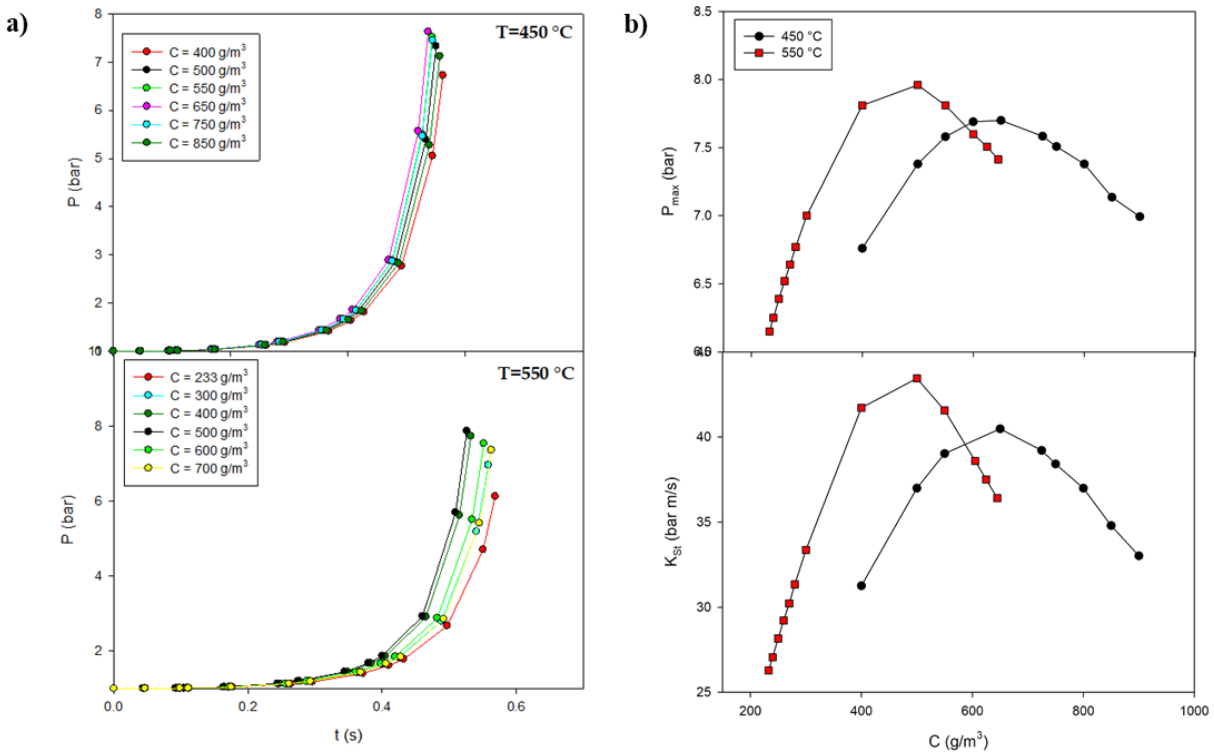

Figure IV.105 *Pressure time histories as function of time at different dust concentration and pyrolysis temperature (top: 450 °C; bottom: 550 °C) calculated in the 1 m^3 vessel; CASE 2 (a) and maximum pressure (P_{max}, top) and deflagration index (K_{St}, bottom) as function of nominal dust concentration as calculated at two pyrolysis temperature values (450 °C and 550 °C), 1 m^3 vessel. CASE 2 (b)* [187]

In order to quantify the effect of the spatial variation of turbulence on the explosion parameters, we performed the calculation also assuming a uniform value of the turbulence intensity. In the following figures, we report the results obtained by assuming that the turbulence level is negligible thus simulating a laminar flame propagation (CASE 3). In **Figure IV.106 (a)** the computed temporal histories of pressure are shown, at different nominal dust concentration and at 450 °C (top) and 550 °C (bottom). From the values of the rate of pressure rise it has been possible to calculate the deflagration index as a function of the dust concentration. In **Figure IV.106 (b)** the maximum attained pressure (top) and the deflagration index (bottom) are plotted versus the nominal dust concentration, as obtained by using the pyrolysis data at 450 °C and 550 °C. The

trend is almost similar to that relative to the CASE 1. The maximum value of K_{St} ($K_{St\,max}$) is attained at different dust concentration but the values are almost similar: 16.3 bar m/s at 550 °C and 14 bar m/s at 450 °C. In both cases, the dust is classified as *St-1*. The maximum values are attained at C = 500 g/m^3 at 550 °C and at C = 650 g/m^3 at 450 °C. The maximum pressure is attained at C = 500 g/m^3 at 550 °C and at C = 725 g/m^3 at 450 °C.

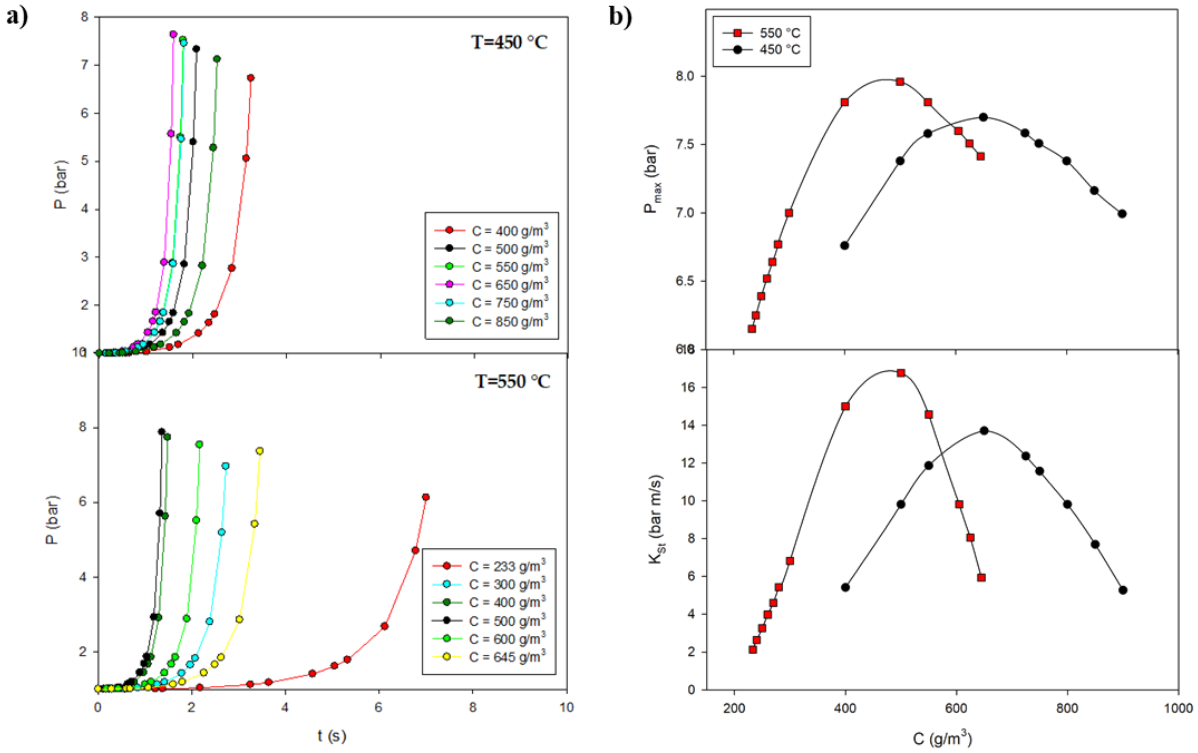

Figure IV.106 *Pressure time histories as function of time at different dust concentration and pyrolysis temperature (top: 450 °C; bottom: 550 °C) calculated in the 1 m^3 vessel; CASE 3 (a) and maximum pressure (P_{max}, top) and deflagration index (K_{St}, bottom) as function of nominal dust concentration as calculated at two pyrolysis temperature values (450 °C and 550 °C), 1 m^3 vessel, CASE 3 (b)* [187]

In the following **Figure IV.107**, the deflagration index as calculated in the 1 m^3 vessel at different fluid flow conditions (CASE 1, CASE 2 and CASE 3) and at two temperature values (450 °C, top and 550 °C, bottom), are shown together with the literature values. In the following figures, the deflagration index as calculated at laminar conditions, radially varying turbulence and turbulence value at the centre are shown. The best agreement is obtained in the case of turbulent conditions (CASE 2). It is worth noting that in our calculations the effect of variable concentration has not been considered. Calculations have been performed by assuming constant dust concentration and equal to the nominal value.

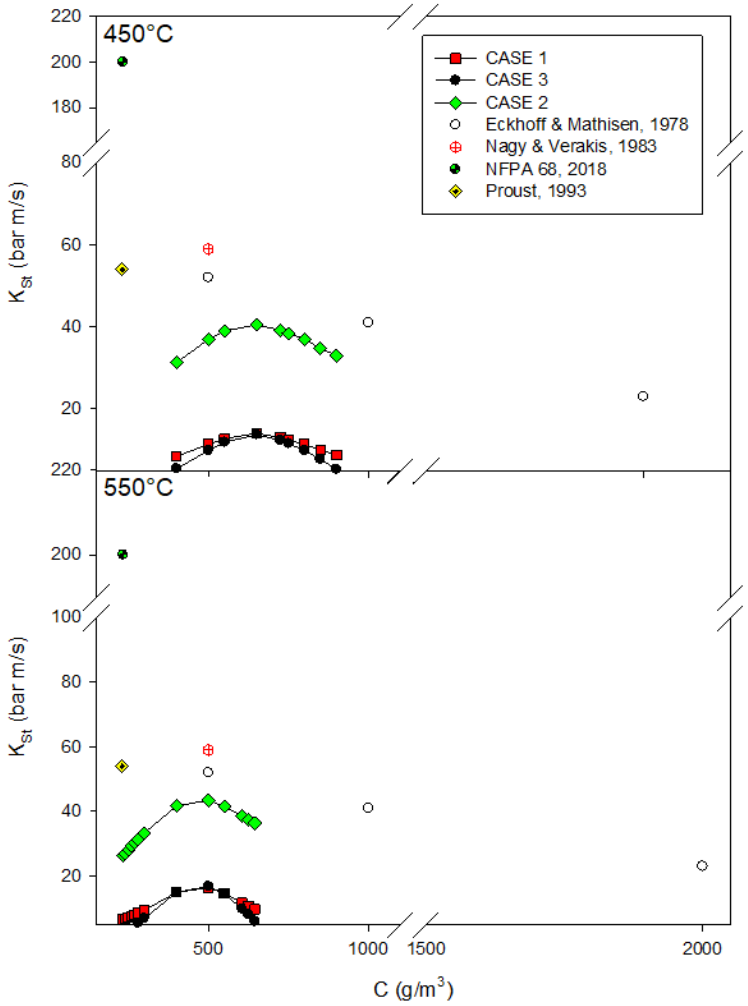

Figure IV.107 *Deflagration index as function of nominal dust concentration as calculated at different fluid dynamic conditions (CASE 1, 2 and 3), at pyrolysis temperature equal to 450 °C (top) and 550 °C (bottom), 1 m³ vessel* [187]. *Literature data are also shown* ([51], [65]–[69])

The results of our calculations are summarised in the following tables. The maximum values of K_{St} together with the corresponding dust concentration are given in **Table IV.43** and in **Table IV.44** for the 20 L and 1 m^3 vessels, respectively. It is found that the concentration corresponding to the maximum value of the deflagration index is the same in both vessels: C = 500 g/m^3 when the pyrolysis temperature is 450 °C and 650 g/m^3 when the pyrolysis temperature is 550 °C. The main difference lies in the values of the maximum deflagration index. In the case of the 20L vessel, the dust is classified *St-2* and *St-3* in the presence of turbulence (CASE 1 and CASE 2), while *St-1* in the case of laminar (CASE 3) conditions. Conversely, in the 1 m^3 vessel, the class is always *St-1*.

Table IV.43 *Maximum values of K_{St} as calculated at two pyrolysis temperatures (450 °C and 550 °C), 20 L vessel* [187]

T=550 °C				T=450 °C		
***C* (g/m³)**	***$K_{St,max}$* (bar m/s)**	**Class**		***C* (g/m³)**	***$K_{St,max}$* (bar m/s)**	**Class**
500	540	*St-3*	CASE 2	650	527	*St-3*
500	238	*St-2*	CASE 1	650	223	*St-2*
500	49	*St-1*	CASE 3	650	37	*St-1*

Table IV.44 *Maximum values of K_{St} as calculated at two pyrolysis temperatures (450 °C and 550 °C), 1 m^3 vessel* [187]

T=550 °C				T=450 °C		
***C* (g/m³)**	***$K_{St,max}$* (bar m/s)**	**Class**		***C* (g/m³)**	***$K_{St,max}$* (bar m/s)**	**Class**
500	43	*St-1*	CASE 2	650	40	*St-1*
500	16	*St-1*	CASE 1	650	14	*St-1*
500	17	*St-1*	CASE 3	650	14	*St-1*

The variability of turbulence in the 20 L vessel is much more significant than in the 1 m^3 and consequently the variability of the K_{St} is much higher. In **Figure IV.108** the K_{St} values are shown together with the deviation from the average value. It clearly appears that the variability of the turbulence level inside the vessels and then on the deflagration index is higher in the 20 L vessel than in the 1m^3 vessel. As a consequence, the repeatability of the measurements of K_{St} is much higher in the 1 m^3 vessel than in the 20 L vessel. Indeed, in the 1 m^3 vessel, the turbulence level is relatively low and almost uniform in space. Consequently, quasi laminar conditions stablish. At quasi-laminar conditions, the tests of combustible dusts are less susceptible to turbulence variations due to different dust properties like dust density, size and shape. Conversely, in the case of the 20 L vessel, the turbulence level is highly non-uniform in space, and its value is very high. The spatial turbulence level variation is much wider than that in the 1 m^3 vessel. Therefore, every parameter which may affect turbulence (like dust properties) may have a great impact on the test result. In this sense, the evaluations in the 1 m^3 sphere are more reliable and repeatable, less dependent on the properties of the dust in question.

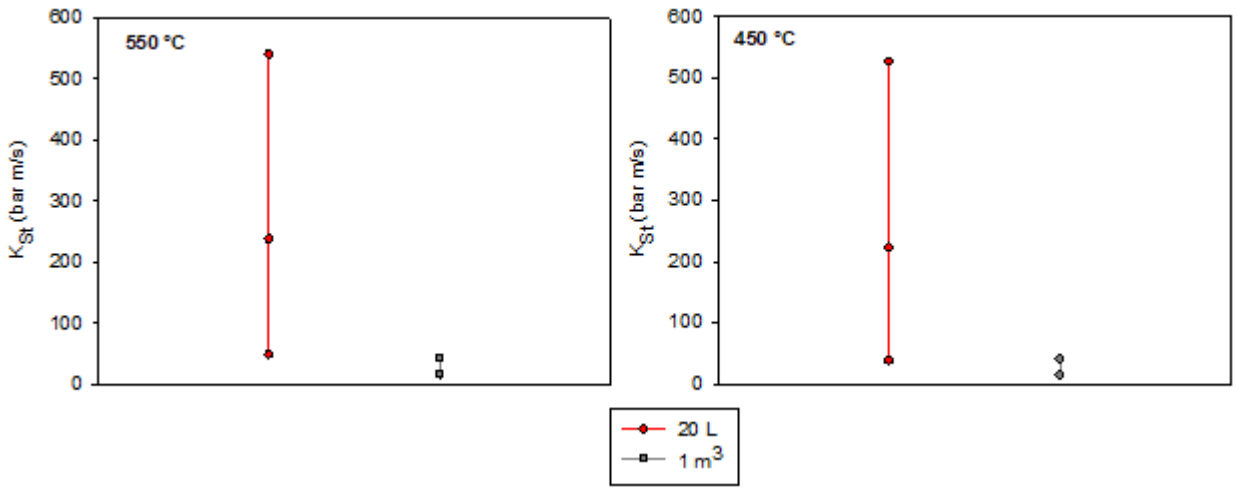

Figure IV.108 *K_{St} calculated in the 20 L and 1 m^3 vessels together with the deviation, at 450°C and 550°C* [187]

Immediately after the dust dispersion inside the test vessel, turbulence builds up and starts decreasing. Consequently, the turbulence level at moment of ignition significantly depends on the ignition delay time t_d. According to the standard procedure, measurements of the deflagration index in the two vessels may be considered as equivalent if the ignition delay times are properly chosen. The ignition delay time should be (60 ±5) ms in the 20 L vessel and (600 ± 100) ms in the 1 m^3 vessel. However, when comparing the results obtained at these values of the ignition delay time, the turbulence level and consequently the deflagration index in the 20 L vessel are much higher than those obtained in the 1 m^3. We then performed calculations at increasing the ignition delay time in the 20 L vessel, to find the conditions at which the spatial-temporal distribution of turbulence is equivalent. From the CFD simulations, we obtained the turbulent kinetic energy as function of time and space in the 20 L vessel. In **Figure IV.109** the turbulent kinetic energy as calculated at the centre of the vessel is plotted versus the ignition delay time. The black line represents the turbulent kinetic energy in the centre of the 1 m^3 vessel, at t_d=600ms. It appears that only at 260 ms, the turbulent kinetic energy in the 20 L vessel is equal to that attained in the 1 m^3 vessel. It is important to underline that in this section the aim is to isolate the effect of the turbulence level on the deflagration index from all the other phenomena. However, by extending the ignition delay time, the fraction of settled dust that does not take part in the explosive process will increase. To take this phenomenon into account, with reference to Section IV.4, it may be necessary to create an adjustment parameter to modify the measured deflagration index value considering the fraction of sedimented dust.

In **Figure IV.110**, the spatial profile of the turbulent kinetic energy (*k*) is plotted as function of the radius inside the 20 L vessel, at different values of the ignition delay time. It can be concluded that on increasing the ignition delay time, the turbulent kinetic energy profile becomes flattener and more homogeneous.

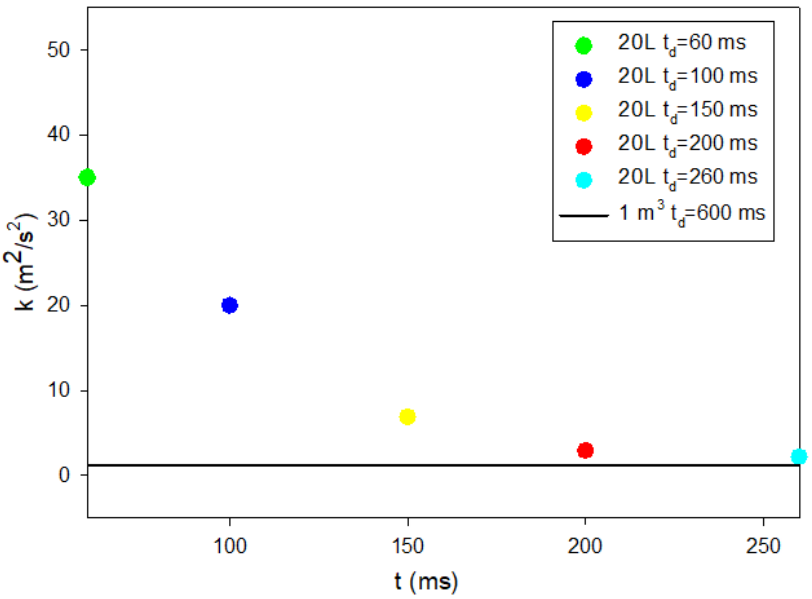

Figure IV.109 *Turbulent kinetic energy as function of the ignition delay time in the centre of the 20 L vessel. Black line is the value obtained in the 1 m^3 vessel* [187]

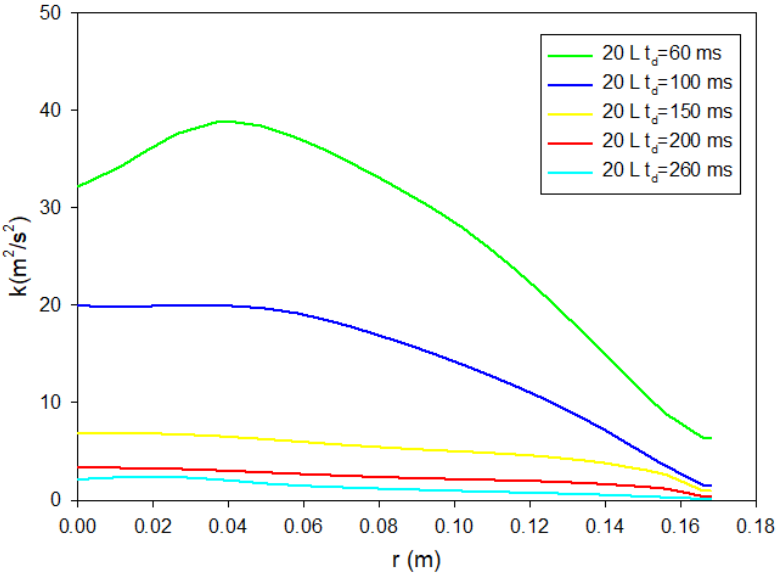

Figure IV.110 *Turbulent kinetic energy as function of the radius at different values of the ignition delay time, V=20 L* [187]

Starting from the pressure temporal profiles, we calculated the deflagration index at different

values of the ignition delay time. In **Figure IV.111** the values of the maximum deflagration index are plotted versus the ignition delay time. The error bars represent the values obtained by assuming the fluid flow uniform and equal to laminar conditions (CASE 3, minimum) and fully turbulent conditions (CASE 2) at the maximum value. The values of K_{St} computed in the 1 m^3 vessel in the CASE 2 and CASE 3 are also shown. It is worth noting that on increasing the ignition delay time, the deflagration index calculated in the 20 L vessel decreases, reaching the values obtained in the 1 m^3 vessel. It is also noting that the deviation from the average value decreases as a result of the more uniform turbulent kinetic energy profile.

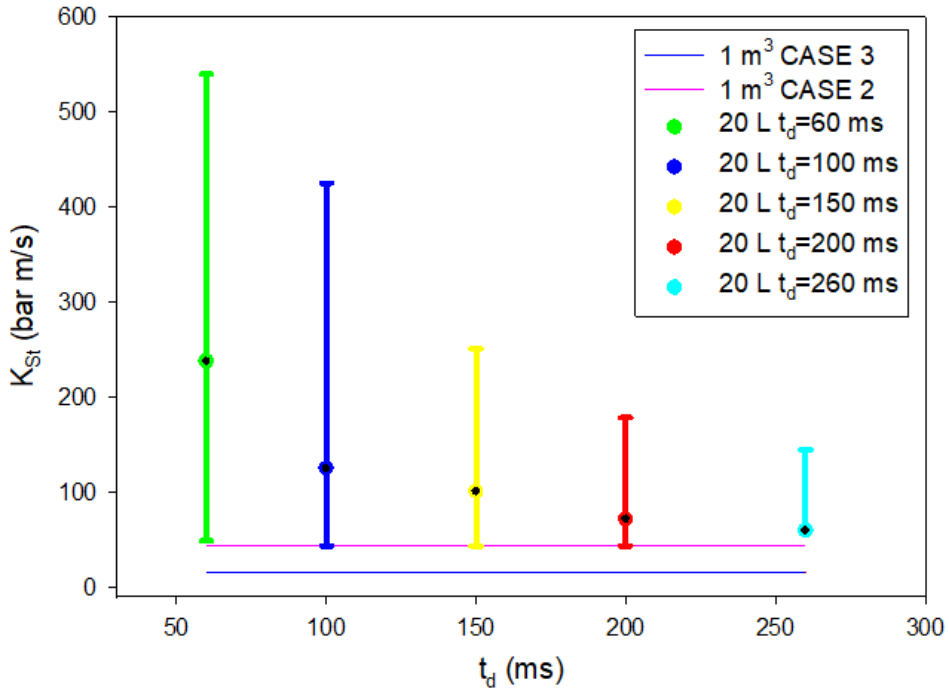

Figure IV.111 *Deflagration index and its deviation as function of the ignition delay time, V=20 L. Red and blue lines are the value obtained in the 1 m^3 vessel for the CASE 2 and CASE 3, respectively* [187]

The different values measured of the explosion parameters in the two standard vessels derive from the different turbulence level which significantly affect the flame propagation. Depending on the flame burning rate and the turbulence level, the interaction between the flame front and the eddies significantly changes, thus leading to turbulent combustion regimes: corrugated flamelet regime, distributed regimes, pocket regime [195]. Depending on the combustion regime, different flame propagation modes and then different flame propagation velocity establish. All these have a significant impact on the explosion severity and then on the deflagration index.

In **Table IV.45** the values of all the parameters and dimensionless numbers to assess the turbulent

combustion regime are given. Once set a reasonable value for the flame laminar burning velocity S_l (e.g., 0.4 m/s) and obtained the turbulent kinetic energy k and the dissipation rate ε from the CFD computations in the centre of the vessels, the velocity fluctuation u' and the flame thickness l_F were calculated. The former was calculated assuming isotropy of turbulence and using Equation (58) [95].

Once calculated the kinematic viscosity by definition and the Kolmogorov length scale from Equation (21), Equation (22) was used to calculate the flame thickness. In this relationship, the flame thickness strongly depends on the vessel geometry (l) and on the established turbulence level (η, u'). Moreover, the turbulent Reynolds Re (Equation (23)) and Karlovitz Ka (Equation (24)) numbers are given in **Table IV.45**.

The turbulence level in the 20 L sphere, is always higher than that in the 1 m^3 vessel, leading to the generation of a flame propagation in the thin reaction zone, whatever the nozzle used. In the thin reaction zones regime, the Kolmorogov scale becomes smaller than the flame thickness, which implies $Ka>1$. Turbulence then increases the transport within the preheating region. Moreover, mixing is enhanced at higher Ka numbers, which leads to higher volumetric heat release and shorter combustion times. Conversely, in the 1 m^3 vessel, the corrugated flamelets regime is established. In the corrugated flamelet regime, the laminar flame thickness is smaller than the Kolmogorov scale, and hence $Ka<1$. Turbulence will therefore wrinkle the flame but will not enters in the laminar flame structure (the flow is quasi laminar). The same turbulent flame regime is established when in the 20 L vessel the ignition delay time is equal to 260 ms. As a main conclusion, the difference between the explosion tests in the 20 L and 1 m^3 vessels, are qualitative other than quantitative being not only the turbulent kinetic energy different but also the turbulent combustion regime which significantly affects the flame propagation mode and eventually the explosion severity.

Moreover, results show that, although in the case of the rebound at 600 ms the initial turbulence level is higher than in the case with the ring, the larger dimensions of the vessel studied (compared to that of 20 L on a laboratory scale) entail a lower and uniform level of turbulence and corrugated type flame structure. By increasing the ignition delay time of the rebound case, the velocity field becomes more similar to that found in the case of the ring. It is worth noting that in the case of rebound at 600 ms the Kolmogorov length scale is more similar to the corresponding flame thickness compared to the other cases. Thus, the case of rebound at 600 ms is that closer to the transition line between corrugated flamelets and the thin reaction zone regimes in the Borghi diagram [91]. In conclusion, the greatest effect on the initial level of turbulence and turbulent combustion regime is exerted by the size of the vessel and not by the nozzle used.

Table IV.45 *Numbers of the Borghi diagram as calculated for all the configuration* ([187], [188])

	S_l [m/s] (max)	k [m^2/s^2] (centre)	ε [m^2/s^3] (centre)	u' [m/s] (centre)	η [m]	l_F [m]	u'/S_l	l/l_F	Ka	Re	Turbulent flame regime
20 L rebound (60 ms)	0.4	35	4000	4.8	3.03E-05	3.08E-05	12	$\approx 10^5$	1.03	$\approx 10^5$	thin reaction zone
20 L perforated (only air)	0.4	35	2190	4.8	3.52E-05	2.79E-05	12.0	$\approx 10^5$	0.9	$7.42 \cdot 10^4$	thin reaction zone - corrugated flamelets
20 L rebound (260 ms)	0.4	2.1	47	1.2	9.20E-05	2.64E-05	3.1	$\approx 10^5$	0.08	$2.00 \cdot 10^4$	corrugated flamelets
1 m^3 rebound (600 ms)	0.4	4.5	60	1.7	8.66E-5	2.16E-5	4.3	$\approx 10^5$	0.06	$\approx 10^5$	corrugated flamelets
1 m^3 rebound (700 ms)	0.4	1.3	40	0.9	9.58E-5	1.33E-5	2.3	$\approx 10^5$	0.01	$\approx 10^5$	corrugated flamelets
1 m^3 perforated (600 ms)	0.4	1.2	6	0.8	1.54E-4	2.40E-5	2.2	$\approx 10^5$	0.02	$\approx 10^4$	corrugated flamelets

IV.6.3. Final remarks

The role of turbulence on the explosion parameters (maximum pressure and deflagration index) in terms of level and spatial distribution was quantified in both 20 L and 1 m^3 vessels by means of CFD simulations . The computed maps show significant spatial variation of the turbulent kinetic energy in the 20 L vessel. Conversely, in the 1 m^3 vessel, the turbulence level is much more uniform. The value of the turbulent kinetic energy computed at the ignition delay time (60 ms in the 20 L and 600 ms in the 1 m3 vessel) is much higher in the smaller vessel. Accordingly, by taking into account only the turbulence effect, we found that the computed value of the deflagration index is much higher in the case of the 20 L vessel. Cornstarch which is classified as St- 1 in the 1 m^3 vessel, is classified St-1 or St-2 or St-3 in the 20 L sphere, depending on if uniform maximum or variable values of the turbulent kinetic are assumed. In order to get agreement between the data calculated in the two vessels, a more uniform turbulence level in the smaller vessel, less dependent on the size, shape, density and concentration of the dust, is mandatory. CFD simulations performed at varying the ignition delay time in the 20 L, suggest that the turbulent kinetic energy profile is much more uniform and similar to that of 1 m^3 vessel at ignition delay time equal to 260 ms. As a consequence, on increasing the ignition delay time, the deflagration index calculated in the 20 L vessel decreases reaching the values obtained in the 1 m^3 vessel. Therefore, an extension of the ignition delay time in the case of the 20 L vessel would lead to an improvement of the measurements in terms of reliability: once the dust is fixed (with its chemical nature), the

evaluations would no longer be strongly influenced by diameter, concentration, shape, and humidity as the range of variation of the turbulence level and then the variability of the explosion parameters, would be narrower. Moreover, in this way, the explosion tests would be qualitatively and quantitatively similar in terms of initial level of turbulence and turbulent combustion regime.

IV.6.4. Published articles

Results discussed in this section have been published in a peer-reviewed scientific journal ([187]):

- M. Portarapillo, R. Sanchirico, and A. Di Benedetto, "Effect of turbulence spatial distribution on the deflagration index: Comparison between 20 L and 1 m3 vessels," *J. Loss Prev. Process Ind.*, vol. 71, no. December 2020, 2021.

IV.7. Role of pyrotechnic ignitors in dust explosion testing: comparison between 20 L and 1 m^3 explosion vessels

In this work, we aimed at quantifying the effect of the ignition energy provided by pyrotechnic ignitors and of the heat propagation of the hot and dense dispersed particles cloud generated by them on the 20 L and 1 m^3 vessels measurements, to justify the contradictory results found. To determine the role of the ignition energy, we run explosions in the 20 L vessel, by using dust-free air, just measuring the pressure-time history due to the pyrotechnic ignitors action, at different values of the ignition energy. To assess the role of the heat propagation, we performed CFD simulations of the generated particles cloud from the vessel centre toward the walls, to evaluate the temperature distribution and then the ability to heat the dust particles.

IV.7.1. Methodologies

The quantification of the pyrotechnic ignitors role was performed using the 20 L sphere, according to the ASTM E1226-19 standard, varying the ignition energy and using dust-free air [9]. The ignition source is placed at the centre of the sphere through a couple of Teflon electrodes fixed to a flange located on the top of the combustion chamber. Pyrotechnic ignitors of 500 J (2×250 J), 1 000 J (2×500 J), 2 000 J (2×1 000 J), 5 000 J (2×2 500 J) and 10 000 J (2×5 000 J) were used. The chemical igniters are activated electrically by a low-voltage source and provide a dense cloud of hot dispersed particles with very little gas by-product. The ignition delay time t_d (60 ms) was set constant for all tests performed. The explosion chamber, which was initially filled with air at atmospheric pressure, was then evacuated to 0.4 bar. An automatic test sequence was initiated to pressurize the dust container to 20 barg, and then the fast-acting valve on the dust container outlet was opened to inject pressurized air into the explosion chamber through a rebound nozzle [9]. The pressure-time curve in the centre was recorded by using a pressure transducer and a charge amplifier. Once assessed the pressure-time history, the thin-flame model [190] has been used to quantify the flame radius (Equation (61)). It is worth noting that the thin-flame model is suitable for the investigated condition (explosion of ignitors only). Conversely, in the case of real dust explosions, the three-zone model is more adequate [190]. In Equation (61), P_{max} is the maximum pressure that was set equal to 8 bar. To assess the role of the hot and dense dispersed particles cloud generated by pyrotechnic ignitors in the 20 L and 1 m^3 vessels, we used a CFD model previously developed and validated, whose details are reported elsewhere ([122], [185]). In both cases, we assumed the generated particles cloud as a central hot core at a temperature equal to 2000 K and radius equal to 0.13 m (i.e., the flame radius at 10 000 J) and simulated the evolution

of the temperature maps. The initial conditions (i.e., pressure, turbulence, temperature etc.) are that computed at the ignition delay time (60 ms for 20 L and 600 ms for 1 m^3 vessel). To neglect the effect of the underdriving phenomenon in the 20 L sphere, we considered both the vessels as adiabatic systems (heat flux towards the external zone equal to zero).

IV.7.2. Results

Proust et al. (2007) performed explosions of 21 dusts in both 20 L and 1 m^3 vessels (**Figure II.23**) [105]. They found that 5 dusts give rise to flame propagation in the 20 L sphere but not in the 1 m^3 vessel (Class A). Moreover, 9 dusts showed values of deflagration index higher when exploding in the 20 L rather than in the 1 m^3 vessel (Class B). This behaviour may be addressed to the overdriving phenomenon due to the pyrotechnic ignitors explosion. In **Figure IV.112**, the pressure histories as measured in the 20 L vessel with pyrotechnic ignitors (no dust) are shown, at varying the ignition energy (IE). Two main phases can be identified: in the first phase, pressure increases up to 1 bar (0 barg) due to the air feed from the dust container; the second phase starts after 60 ms from the feeding activation and it is related to the increase of pressure due to the pyrotechnic ignitors explosion. It is worth noting that on increasing the ignition energy (IE) from 500 J up to 10 000 J (i.e., standard ignition energy), the pressure increase becomes much more severe in terms of both maximum pressure and maximum rate of pressure rise.

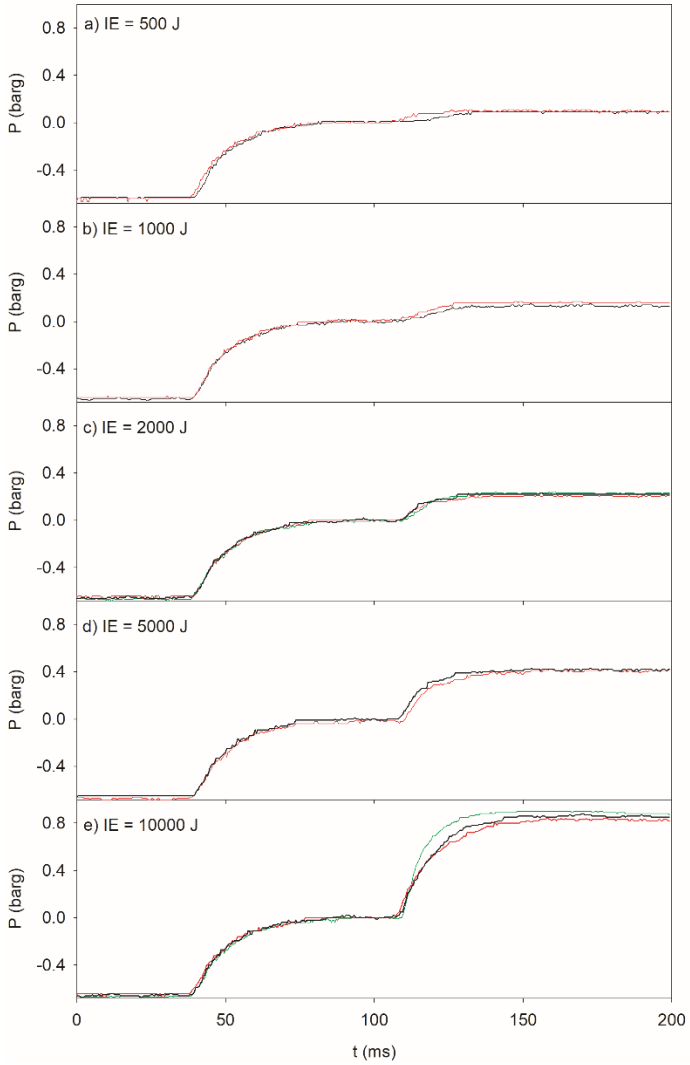

Figure IV.112 *Pressure P (barg) versus time (ms) as measured at different values of the ignition energy: 500 J (a), 1 000 J (b), 2 000 J (c), 5 000 J (d) and 10 000 J (e), pyrotechnic ignitors only (no dust). Red/blue/green traces are related to different test repetitions* [196]

In **Table IV.46** the maximum pressure P_{acc} due to pyrotechnic ignitors explosion is shown as a function of the ignition energy. On increasing the ignition energy, the maximum pressure increases. When going from 500 J up to 10 000 J, the maximum pressure generated by the igniters doubles from 0.8 bar up to 1.9 bar. This result suggests that the explosion of igniters may not be neglected when dealing with high values of ignition energy (IE > 2 000 J).

Table IV.46 *Maximum pressure P_{acc} (bar) in phase II as function of the ignition energy IE (J)* [196]

E (J)	P_{acc} (20 L)
500	1.14
1 000	1.18
2 000	1.24
5 000	1.45
10 000	1.90

By using Equation (61), we calculated the radius of the flame front propagation due to the ignitors explosion. In **Figure IV.113** the radius is plotted versus the ignition energy. The ratio between the flame radius and the vessel radius is also shown. It is worth noting that the flame radius significantly increases up to reaching values very close to the 20 L vessel radius (r_f/r_{vessel} = 0.92 at IE = 10 000 J). These results suggest that the igniters may significantly affect the explosion of dusts in the 20 L vessel because it may involve the whole vessel. These data may explain the behaviour of dusts of Class A and Class B (**Figure II.23**). The ignition/explosion of these dusts in the 20 L may be the results of the overdriving process generated by the ignitors explosion which sustains the course of the flame propagation, also involving the dust.

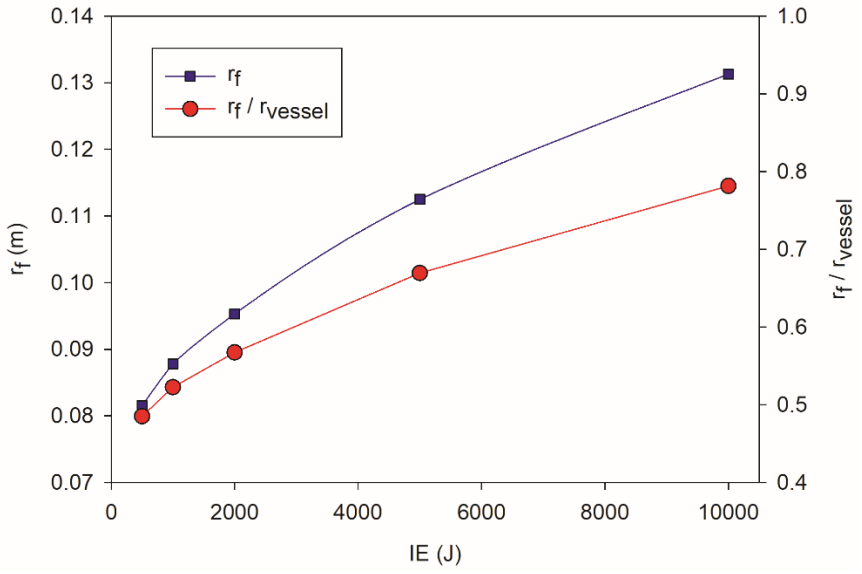

Figure IV.113 *Igniter flame radius r_f (m) and ratio between the igniter flame radius and the vessel radius r_{vessel} (m) as function of the ignition energy (20 L sphere)* [196]

Metal dusts (Class C dusts) exhibit an opposite behaviour than organic dusts (Class B dusts). More

precisely, the explosion parameters measured in the 1 m^3 chamber are higher than those measured in 20 L sphere ([102]–[104]). As a consequence, it seems that in this case overdriving is not playing a role. To understand this behaviour, we performed *CFD* simulation of the heat propagation of the hot and dense dispersed particles cloud generated by pyrotechnic ignitors inside the 20 L and 1 m^3 vessels. In both vessels, the initial conditions (i.e., pressure, turbulence, temperature, etc.) are that computed at the ignition delay time (60 ms and 600 ms for 20 L and 1 m^3 vessel, respectively). **Figure IV.114** shows the computed maps of turbulent kinetic energy at ignition delay time for 20 L sphere (a) ((x–y) plane) and 1 m^3 vessel (b), (x–z) plane. The turbulent kinetic energy computed in the 20 L vessel is higher than that found in the 1 m^3 vessel. Notably, the 20 L vessel shows a non-uniform degree of turbulence, resulting in not reliable and not repeatable measurements of the explosibility parameters ([122], [124], [125], [128], [181]). This issue appears to be solved in the 1 m^3 vessel since the variation range of turbulent kinetic energy from the centre to the wall at the ignition delay time is very narrow ([185]–[187]). In order to neglect the underdriving phenomenon in the 20 L sphere, we considered both vessels as adiabatic systems (heat flux equal to zero). Basically, in this way, we assessed the effect of turbulence level on the heat wave propagation.

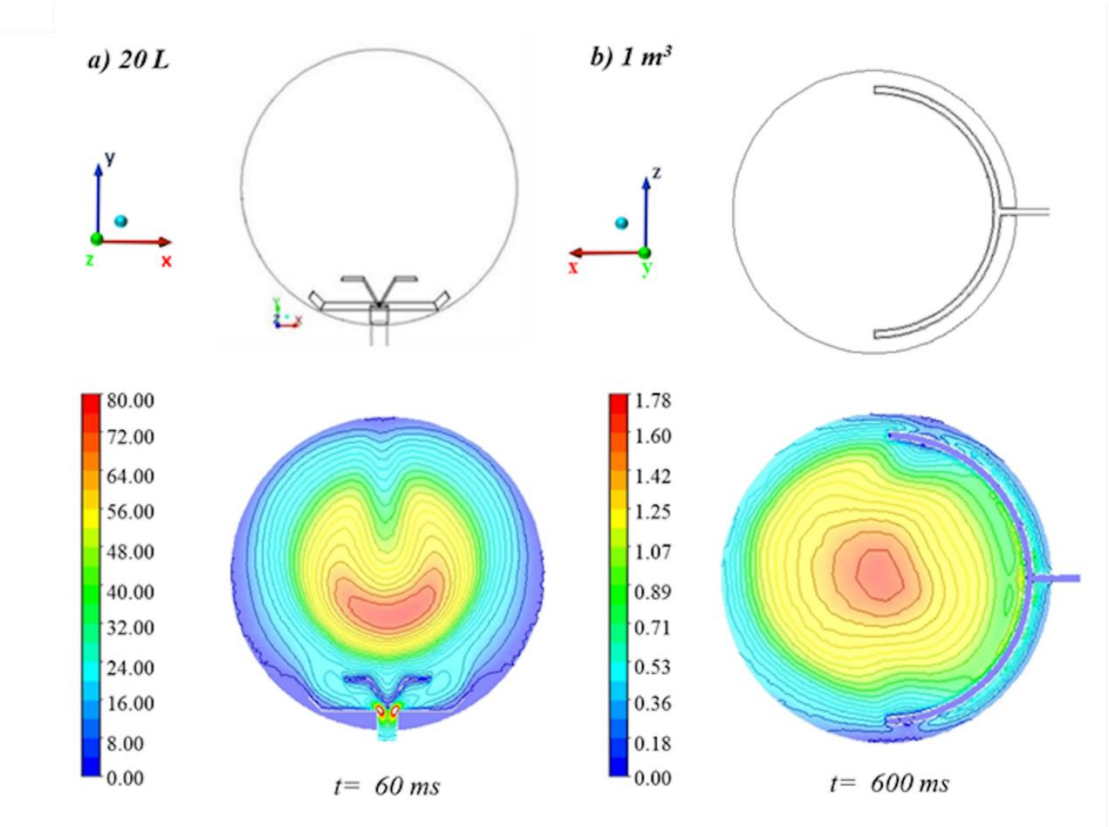

Figure IV.114 *Computed maps of turbulent kinetic energy k (m^2/s^2) at ignition delay time for 20 L sphere (a) ((x–y) plane) and 1 m^3 vessel (b), (x–z) plane* [196]

In **Figure IV.115** the temperature maps as computed in the 20 L (a) and 1 m^3 (b) vessels are shown at t_d, t_d + 10 ms, t_d + 20 ms, t_d + 30 ms. It is worth noting that the flame radius reaches values very close to the 20 L vessel radius at ignition delay time while, in the case of 1 m^3 vessel, only a central hot core is present. After 30 ms, the temperature is quite uniform in the whole 20 L vessel and the temperature value is equal to 500 K. Conversely, in the 1 m^3 vessel, the temperature does not uniformise and its value is higher in the centre of the sphere and equal to 770 K. These results are the consequence of the higher turbulence level attained in the 20 L vessel that affects the mixing of heat thus uniformising the temperature, as shown in **Figure IV.114** ([185], [187]). Therefore, the heat dissipation is higher in the 20 L not only due to the heat loss towards the outside, given the higher value of the surface-to-volume ratio, but also due to the high level of turbulence. Conversely, in the case of flame propagation controlled by heat diffusion as in the case of metal dusts, the heat dissipation occurring in the 20 L vessel may have a significant impact on the flame propagation speed and then on the severity of the explosion.

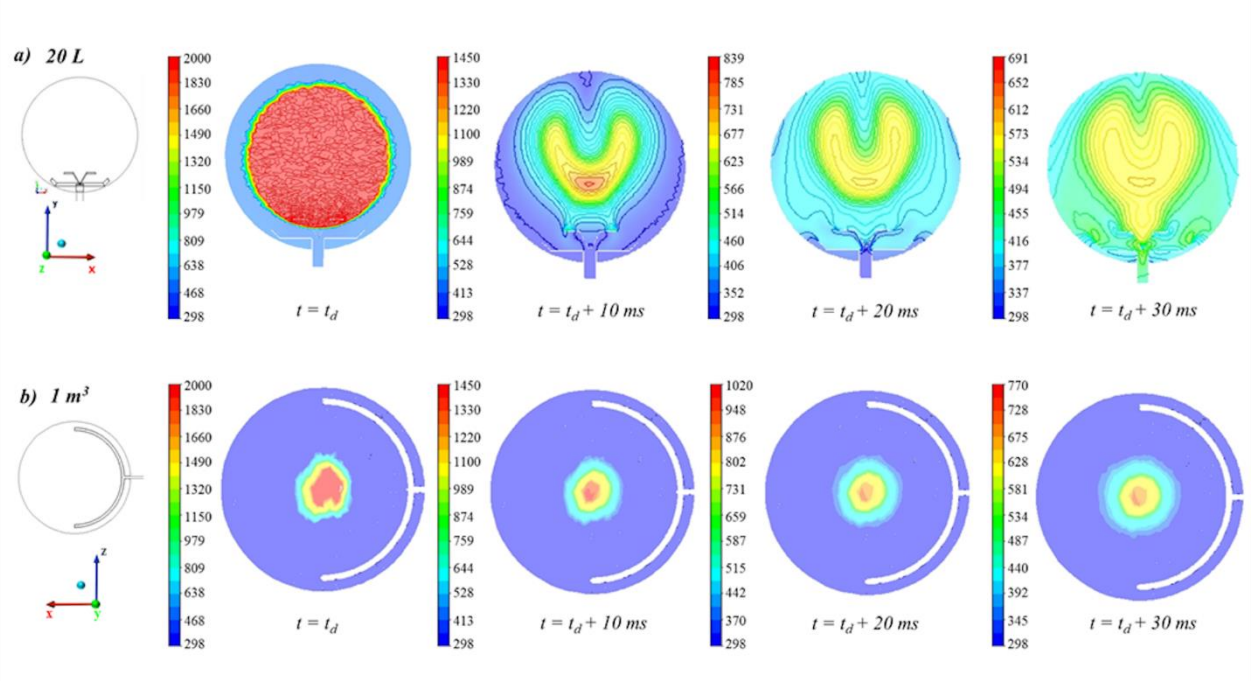

Figure IV.115 *Temperature maps (K) in the 20 L (a) and 1 m^3 (b) vessels, simulated at different times* [196]

In the heat dissipation phenomenon, the key parameter is represented by the integral turbulent time scale τ_t (s), defined as the ratio between the dimension of the hot core generated by igniters r_f (m) and the turbulent velocity fluctuations u'. τ_t represents the characteristic time for mixing at the

large eddy scale. Comparing the values of τ_t for the 20 L and 1 m^3 vessels, we obtained that the ratio between these times is:

$$\frac{\tau_{t,20\ L}}{\tau_{t,1\ m^3}} = 0.17 \ll 1 \quad (63)$$

Therefore, the high turbulence level in the 20 L vessel, promotes a rapid decrease of temperature close to the ignition point and makes the temperature inside the sphere uniform.

IV.7.3. Final remarks

From the obtained results, the pyrotechnic ignitors double role was explained and quantified: the triggering effect and the heating dissipation effect. For the triggering effect, it is meant that they start the flame propagation that may involve the dusts (even if slightly flammable) while the heating dissipation effect is associated with their generation of a hot core in the vessel centre at the ignition delay time.

In the 20 L vessel, the triggering effect is quite significant: at high values of the ignition energy (IE > 500 J), the pressure wave involves almost the entire vessel thus triggering, initiating and overdriving the dust flame propagation. Consequently, also combustible dusts which are not in the conditions to sustain the flame propagation (low concentration, high size, high humidity content etc.) may be involved in the ignitors explosion contributing to an increase of pressure and deflagration index. This phenomenon may justify the experimental findings of the explosions of many organic dusts for which the deflagration index values measured in the 20 L are much higher than those measured in the 1 m^3 vessel (Class A and B dusts).

When the ignition energy is released through the ignitor explosions, the central core of the vessel reaches very high temperatures. The spatial/temporal evolution of the temperature is significantly dependent on the initial turbulence level. In the 20 L, the heat rapidly dissipates not only due to the heat loss towards the outside (i.e., underdriving phenomena) but mainly due to the high level of turbulence that quickly uniformises the temperature within the vessel. Conversely, in the 1 m^3 vessel, the lower level of turbulence inhibits the heat diffusion and then the hot core is preserved.

When the dust flame propagation is controlled by particle heating (heterogeneous combustion), as in the case of metal dusts, the explosion parameters are higher in the 1 m^3 than in the 20 L vessel due to the presence of the thermal effect. For this kind of dusts (Class C dusts), the thermal effect in the 1 m^3 vessel seems to prevail on the pressure effect, relevant in the 20 L sphere.

IV.7.4. Published articles

Results discussed in this section have been published in a peer-reviewed scientific journal ([196]):

- M. Portarapillo, R. Sanchirico, and A. Di Benedetto, “On the pyrotechnic ignitors role in dust explosion testing : Comparison between 20 L and 1 m 3 explosion vessels,” *Process Saf. Prog.*, no. February, pp. 1–7, 2021.

IV.8. Which standard vessel should I use and which issues I have to consider?

As a main conclusion, **Table IV.47** summarises all the phenomena and issues that influence the measurement of K_{St} in the two standard vessels. As discussed in **Section IV.6**, the pre-ignition turbulence level is higher and not uniform in space at the ignition delay time in the 20 L sphere compared to the 1 m^3 vessel. Considering only this effect, the measured value of the deflagration index in the smaller vessel would be higher and more dependent on dust properties and consequently on relaxation time. Al low relaxation time, the turbulence level is maximum and comparable to that of dust-free air system while at high relaxation time values the sedimentation phenomenon has to be taken into account. Indeed, the pre-ignition turbulence level is high but the amount of suspended dust at the ignition delay time is low, very different from the nominal value. As discussed in **Section IV.7**, due to the higher surface-to-volume ratio, the 20 L sphere suffers from the underdriving phenomenon caused by heat loss towards the external environment. In the case of 1 m^3 vessel, this phenomenon is very low (quite negligible) and consequently, isolating only this effect, the K_{St} value will be high in this vessel for those dusts whose flame propagation occurs in heterogeneous phase and is controlled by particle heating. As discussed in **Section IV.7**, the pyrotechnic ignitors have a double effect: the flame propagation related to the ignitors explosion may trigger, sustain and overdrive the flame propagation of dusts whose flame propagation occurs in homogeneous phase while the hot core generated by their explosion and preserved in the 1 m^3 vessel due to the low pre-ignition turbulence level may sustain and overdrive the flame propagation when controlled by particle heating. It is worth noting that both in the 20 L sphere and in the 1 m^3 vessel the homogeneous dispersion requirement is not satisfied and worsens as the relaxation time of the dust increases due to sedimentation. This problem needs to be considered but can only be solved through the development and use of alternative dust dispersion systems.

Table IV.47 *Summary of all the phenomena and issues influencing the measurement of K_{St} in the two standard vessels* [196]

Phenomenon/Issue	Comments	Effect on K_{St}
Initial turbulence level and control	High turbulence level, not uniform in space in 20 L sphere. Low turbulence level, uniform in space in 1 m^3 sphere.	Higher in the 20 L sphere, dependent on the relaxation time
Sedimentation	Intense sedimentation as the relaxation time increases.	Different from that obtainable with nominal concentration
Heat loss towards the environment	High, high surface-to-volume ratio (underdriving phenomenon) in 20 L sphere. Low heat loss in 1 m^3 sphere.	Higher in the 1 m^3 sphere for dust with predominant heterogeneous combustion
Pyrotechnic ignitors (triggering effect)	As the energy increases, the heat wave occupies the whole sphere: overdriving phenomenon in 20 L sphere.	Higher in the 20 L sphere for dust with predominant homogeneous combustion
Pyrotechnic ignitors (heating dissipation effect)	High turbulence level uniformises temperature in 20 L sphere. Hot core is preserved in 1 m^3 sphere.	Depends on dust flame propagation mechanism: higher in the 1 m^3 sphere for dust with predominant heterogeneous combustion and higher in the 20 L sphere for dust with predominant homogeneous combustion
Not-uniform dust distribution	Non-uniform, the non-uniformity increases with the relaxation time.	Stratified combustion, false positive or negative

To understand all the phenomena and issues occurring during the testing of a specific combustible dust, a procedure can be suggested as reported in **Figure IV.116**. As deeply discussed in the first part of this thesis, to get insight into the flame propagation mechanism and, consequently, to understand which vessel leads to the most conservative evaluation of explosion parameter, a complete chemico-physical and thermal characterization is mandatory. **Figure IV.117** explicates all sections shown in **Figure IV.116.** Through the chemico-physical characterization, that consists in the determination of size, shape, density and molecular structure, the relaxation time can be calculated and the role of the oxygen diffusivity can be assessed. Though the thermal characterization, the decomposition and combustion phenomena can be investigated and the proximate analysis can be used to mainly evaluate the moisture and volatile content. Moreover, the gaseous species produced can be individuated by *FTIR* analysis. The thermal analysis is of crucial importance to understand which combustion path is predominant during the flame propagation and if marginal explosibility may occur. In the last section, the dimensionless number have to be evaluated to focus on the step controlling the overall explosion phenomena. In the case of dusts characterized by low value of relaxation time and high content of volatile, all flammable or mixed with inert, the evaluation of thermal dimensionless number is of key importance. For the dust whose flame propagation is controlled by heterogeneous combustion path, the evaluation of mass transfer dimensionless numbers is useful to understand the role and effectiveness of oxygen diffusion. After having studied the dust as per procedure and having identified the predominant flame propagation path and the controlling step, it is possible to determine the vessel to be used for the explosion tests in order to have the most conservative parameters and all the issues to take into account during the measurement. In the of dusts whose flame propagation occurs mainly in the homogeneous phase (with no or fast combustion in the heterogeneous phase), the use of the 20 L sphere is recommended. If the produced volatiles are a mixture of flammable and inert species, a phenomenon of marginal explosibility may occur. In the case of dusts whose flame propagation is controlled by phenomena in the heterogeneous phase, the use of the 1 m^3 vessel is recommended.

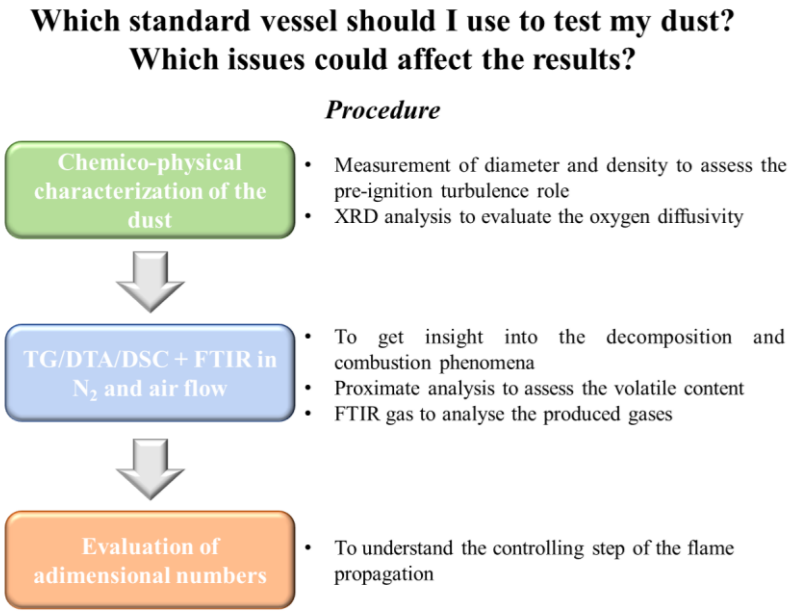

Figure IV.116 *Schematization of the suggested procedure to understand the predominant flame propagation mechanism*

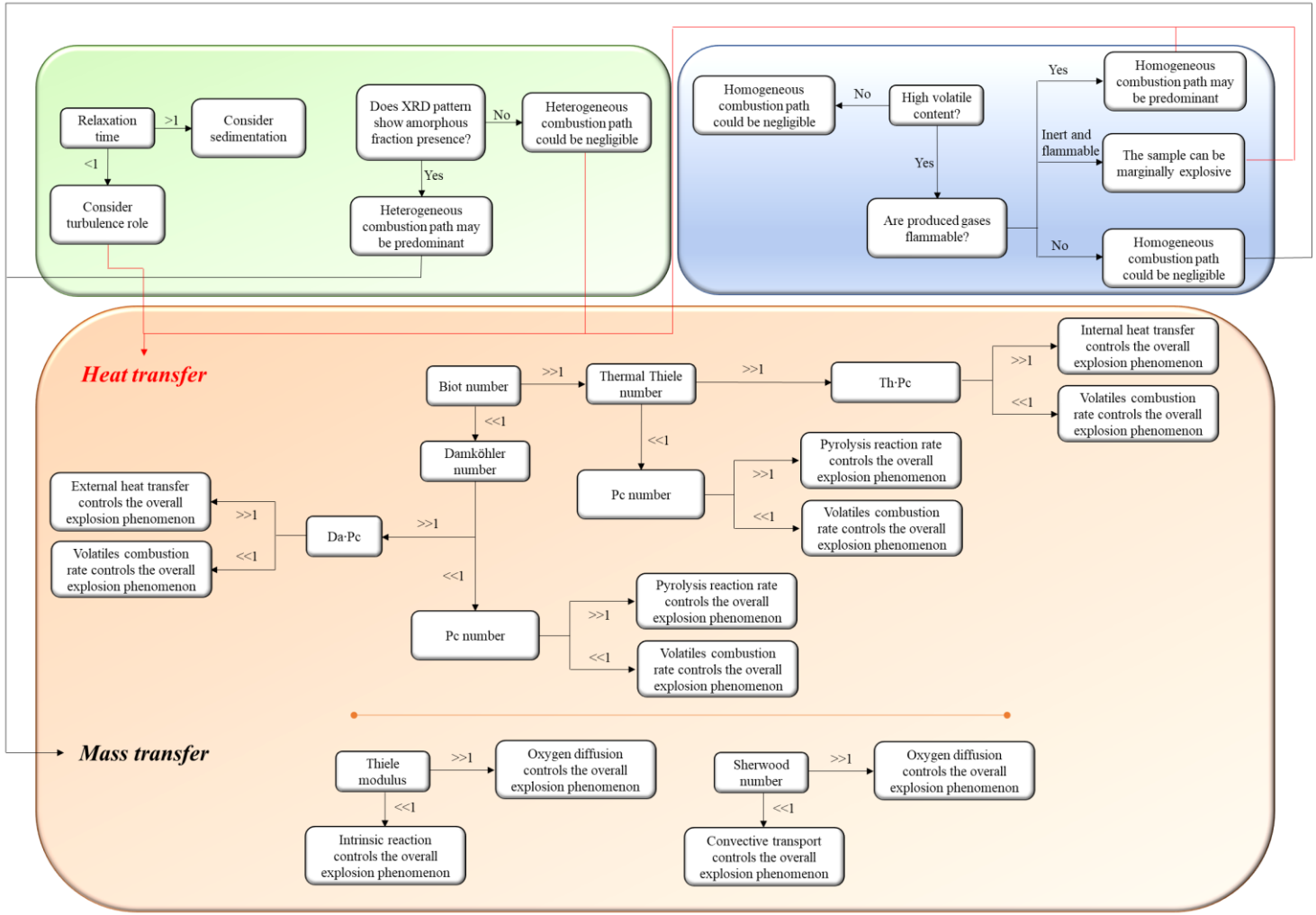

Figure IV.117 *Explanation of each section of the suggested procedure*

Example of a preliminary analysis on marginally explosive combustible dusts

This preliminary analysis was carried out in collaboration with Albert Addo, PhD student at Dalhousie University, and Prof. Paul Amyotte. Laboratory-scale testing of selected organic powders was conducted at the Dust Explosion Laboratory of Dalhousie University located in Halifax, NS. These materials were also tested using the 1 m^3 chamber at Fauske & Associates, LLC (Fauske) located in Burr Ridge, IL.

The aim of this activity was to get insight into the reasons why some samples showed marginal explosibility. Marginally explosible dusts are primarily characterized by low values of explosion severity parameters P_{max} and K_{St}. These dusts may be explosible using a standard 20 L sphere while their explosibility in larger test chambers are not certain. Some studies have been conducted by researchers to provide explanations for their distinctive behaviour on both testing scales.

Palmer et al. (1968) tested phenol formaldehyde resin and magnesium oxide dusts, and their mixtures, in a vertical explosion tube and concluded that marginally explosible dusts have a narrow range of flammable concentrations, generate only moderate explosion pressures and are unlikely to cause severe explosions. They also inferred that marginal dusts and their mixtures require a relatively high-energy ignition source in small-scale tests and will not propagate an explosion on a larger scale [197]. After Palmer et al. (1968) work, many researchers have dealt with the subject and most of these studies have agreed with the potential effects of "preconditioning" which may be more critical in the smaller chamber with a very strong ignition energy. Preconditioning occurs when the initial conditions of the system are altered significantly prior to flame propagation, with the more prominent effect being "overdriving". The phenomenon of overdriving is further attributed to differences in turbulence between the two chambers and pre-heating of the dust-air mixture by the ignitors in the 20 L vessel ([99], [101], [112], [113], [198], [199]). Another complication associated with marginally explosible dusts is the different behaviour of metallic marginally explosible dusts relative to non-metallic marginally explosible dusts. As found by Bucher et al. (2012), out of the 13 metallic dust samples tested, a significant majority of 12 dusts that tested to be explosible in the 20 L chamber with K_{St} values below 50 bar·m/s, were found to have greater values of both P_{max} and K_{St} in the 1 m^3 vessel [200].

The tested samples are four and the preliminary results are in agreement with the proposed procedure as reported in **Table IV.48**.

Table IV.48 *Summary of investigated dusts and relative flame propagation path*

Material	Flame propagation path		Comments	Most conservative K_{St}
	PATH A	PATH B		
1	Yes	Low	Low flammable volatile content and rapid heterogeneous combustion	20 L
2	High temperature	Yes	Mainly homogeneous combustion	20 L
3	No	Yes	Homogeneous combustion	20 L
4	Yes	No	Layer-by-layer heterogeneous combustion	1 m^3

IV.8.1. Final remarks

In this last section, we tried to formulate a procedure to fully understand the flame propagation mechanism of the investigated dust, which standard test vessel is better to use and which issues have to be considered during testing. It involves a summary of all the observations done in the previous sections and consists of the chemico-physical characterization, the thermal analysis and the evaluation of dimensionless numbers in order to get insight into the flame propagation mechanism and the steps controlling it.

V. CONCLUSIONS AND FUTURE WORK

V.1. Conclusions

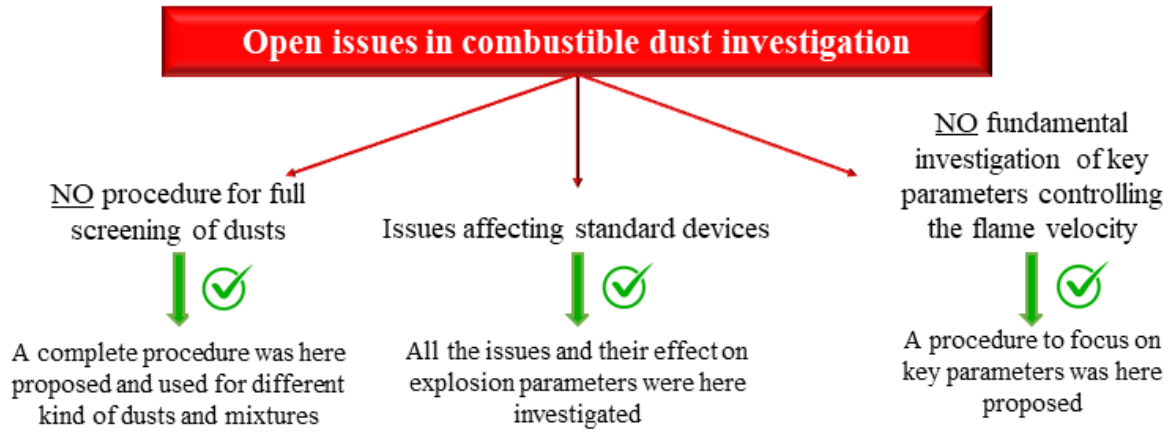

This thesis work aimed at giving an answer to all the open issues relative to the flammability and the explosibility of combustible dusts whose most critical mechanisms are still not completely understood.

1. **A procedure for fully characterising the dust explosion likelihood and severity has not yet been developed**

Starting from the preliminary results of a Mallard-Le Chatelier-inspired theoretical flame propagation model, the importance of a full chemico-physical and thermal screening of any combustible dust was evidenced in order to fully understand the explosive behavior both in terms of intrinsic (laminar) burning velocity but also in terms of flammability/explosibility parameters. Consequently, a complete screening consisting in flammability/explosibility testing, chemico-physical and thermal characterization was developed. Firstly, this approach was used to get insight into the reason why synergistic effects may occur in dust mixtures. Indeed, measurements of the flammable and explosion parameters of mixtures of flammable dusts show that these parameters are not always the combination of the pure values and then it is not possible to predict *a priori* the behaviour of the parameters of flammability and explosibility of the mixture. Particularly, significant physical–chemical interactions may arise among the powders, leading to unexpected and sometimes worse behaviours than those of pure compounds. From the thermal analysis results,

we may conclude that the physical interactions may be related to the formation of a eutectic point which reduces the temperature with respect to the pure dust at which melting and then boiling occur. Thermal analysis results combined with chemico-physical characterization also show the possibility of chemical reactions that lead to the formation of volatiles, which contribute to the explosion phenomenon. On this basis, we propose a classification of mixture of dusts in three mixtures safety classes (*MSC* 0; *MSC* 1; *MSC* 2). In the case of both *MSC* 1 and *MSC* 2.

Moreover, this complete characterization was used to understand the different behavior of nylon fibres and the effect of the content of lignocellulosic components and aging on a grape pomace. As regards the nylon fibres, the size of nylon 6.6 fibres, considered in terms of equivalent diameter, is the main feature to be considered in the flammability and explosibility risk. Smaller samples have a faster thermal degradation as observed both in inert and oxidative atmosphere. The higher reactivity exhibited in the thermal tests was confirmed in the flammability tests as shown by the measured values of the minimum ignition energy. Dimensionless analysis allowed the evaluation of the step controlling the fibre reaction paths. It was found that in the homogeneous path, the pyrolysis controls flame propagation path while the heterogeneous combustion path is controlled by the intrinsic kinetic and then mainly affected by the specific surface area.

As regards the grape pomace sample, the thermal analysis allowed the calculation of the contribution of the lignocellulosic components. The hemicellulose is the main component and the major contributor to volatiles. However, it generally gives mainly CO_2 and not really contributing to the propagation of the explosion/flammability process of the dust. Conversely, lignin generates CH_4 at high temperature and cellulose generates CO. As a result of the aging process, the sample is richer in cellulosic component at the expense of the lignin content, a typical component of fresh biomass, and without moisture. The degradation of lignin to cellulose makes the sample intrinsically more reactive while the lack of humidity makes the sample more dispersible. In addition, it is possible to notice a morphological difference between the pre and post-aging sample with a reduction of flakes. Consequently, the aged sample was susceptible to electric discharge compared to the pre-aging sample also thanks to a reduction in post-dispersion mean diameter in MIKE3 due to a greater fragility of the aged sample.

2. All the issues affecting the standard testing device have already been identified but are scarcely discussed in literature. Moreover, the effects of these critical phenomena on dusts characterized by different flame propagation path have not been investigated yet

In order to assess all the effect of phenomena such as pre-ignition turbulence, overdriving, underdriving etc. we carried out an intensive simulative campaign. A validated three-dimensional

CFD model was used to simulate the dust dispersion inside the 20 L sphere for niacin/anthraquinone mixtures at different compositions (i.e., pure dust ratios, while keeping the total dust concentration constant). In the case of dust mixtures, the dispersion inside the sphere is strongly non-uniform, with zones richer in niacin and poorer in anthraquinone and *vice versa*. Overall, the obtained results demonstrate that, to perform a correct and reliable evaluation of flammability and explosibility parameters for dusts and dust mixtures, a different dispersion method has to be developed. When testing dust mixtures, this is needed not only to guarantee a uniform dispersion of the solid particles, but to also ensure the nominal mixture composition in each point of the sphere. The search for a new dust dispersion system also appears necessary to solve the problem related to the sedimentation of the powder, which is increasingly severe as the relaxation time of the powder increases. Due to sedimentation, a lower dust aliquot than the nominal one is tested and the results in terms of explosivity parameters cannot be considered reliable.

Since no simulation is available for 1 m^3 vessel, CFD model was formulated to assess the temporal/spatial profiles of turbulent kinetic energy and dust concentration in the 1 m^3 vessel. Comparison of the computed turbulent kinetic energy and dust concentration with the (few) experimental data available show a good agreement only at times higher than 300 ms. The spatial distribution of the turbulent kinetic energy is quite uniform inside the whole vessel. Conversely, the dust is mainly concentrated at the outer zones of the vortices generated in the vessel and then dust concentration is not uniform. Simulations also show that a large part of dust is not fed, being trapped in the annular nozzle. Comparison with the turbulent kinetic energy in the 20 L vessel, shows that the turbulence level in the 20 L is much higher.

CFD simulations of the dust dispersion inside the 1 m^3 standard vessel were performed at different values of the dust diameter. The time sequences of turbulent kinetic energy maps show that turbulent kinetic energy is quite uniform inside the whole vessel and in the case of 400 μm, at 600 ms the flow field is more similar to that of dust-free air, due to the occurrence of particle sedimentation and incomplete feeding. The different particles-fluid interaction obtained varying the dust diameter is further confirmed by the time sequence of particle tracks. On increasing the dust diameter, the dust and the fluid flows are independent, and the sedimentation phenomenon becomes more severe as the turbulence dissipates leaving the velocity flow field similar to that of the dust-free air case. Moreover, a worse feeding is attained, with most of the dust trapped in the perforated annular nozzle on increasing dust diameter.

CFD simulations allow the quantification of the temporal/spatial profiles of turbulent kinetic energy and dust concentration in the 1 m^3 vessel equipped with rebound nozzle. The computed

turbulent kinetic energy and dust concentration were validated against the experimental available data (at times higher than 300 ms). Although the level of turbulence is not completely uniform within the sphere at 600 ms, showing a decay moving from the centre to the walls, the variation range of turbulent kinetic energy is very narrow (from 4.5 m^2/s^2 to 0 m^2/s^2). Conversely, the dust is mainly concentrated at the outer zones of the vortices generated in the vessel and then dust concentration is not uniform. Comparison with the turbulent kinetic energy in the 1 m^3 vessel equipped with perforated annular nozzle, shows that the turbulence level in the case of the rebound is higher, as the amount of dust fed in the vessel.

The role of turbulence on the explosion parameters (maximum pressure and deflagration index) in terms of level and spatial distribution was quantified in both 20 L and 1 m^3 vessels by means of CFD simulations . Accordingly, by taking into account only the turbulence effect, we found that the computed value of the deflagration index is much higher in the case of the 20 L vessel. Cornstarch which is classified as *St-1* in the 1 m^3 vessel, is classified *St-1* or *St-2* or *St-3* in the 20 L sphere, depending on if uniform maximum or variable values of the turbulent kinetic are assumed. In order to get agreement between the data calculated in the two vessels, a more uniform turbulence level in the smaller vessel, less dependent on the size, shape, density and concentration of the dust, is mandatory. *CFD* simulations performed at varying the ignition delay time in the 20 L, suggest that the turbulent kinetic energy profile is much more uniform and similar to that of 1 m^3 vessel at ignition delay time equal to 260 ms. As a consequence, on increasing the ignition delay time, the deflagration index calculated in the 20 L vessel decreases reaching the values obtained in the 1 m^3 vessel. Therefore, an extension of the ignition delay time in the case of the 20 L vessel would lead to an improvement of the measurements in terms of reliability: once the dust is fixed (with its chemical nature), the evaluations would no longer be strongly influenced by diameter, concentration, shape, and humidity as the range of variation of the turbulence level and then the variability of the explosion parameters, would be narrower. Moreover, in this way, the explosion tests would be qualitatively and quantitatively similar in terms of initial level of turbulence and turbulent combustion regime. Moreover, we focused on the role of the pyrotechnic ignitors on the pressure trend and the temperature distribution. We run explosion tests in the 20 L vessel to measure the pressure–time history generated by the explosion of pyrotechnic ignitors. Furthermore, we performed CFD simulations to simulate the spatial/temporal evolution of the temperature map from the hot core due to the igniter explosion toward the vessel walls. The explosion of the pyrotechnic ignitors shows a significant increase of pressure in the 20 L vessel, suggesting that flame propagation is occurring inside the vessel. Furthermore, the localized increase of temperature due to the ignitor explosions, diffuse, and then uniformize much more

rapidly in the 20 L vessel than in the 1 m^3 vessel. The flame propagation generated by the ignitors is very relevant in the 20 L sphere leading to the overdriving phenomenon. This result justifies the fact that for many organic dusts, the deflagration index values measured in the 20 L are much higher than those measured in the 1 m^3 vessel. CFD simulations show that the hot core generated by the ignitors dissipate much faster in the 20 L vessel than in the 1 m^3 vessel, due to the higher turbulence level of the smaller vessel. Therefore, dusts whose combustion is controlled by particle heating are more prone to sustain combustion in the 1 m^3 than in the 20 L vessel.

3. A fundamental investigation of flame propagation features and key parameters (physical, operating, chemical) controlling the flame velocity has never been proposed

By collecting all the obtained results, we tried to formulate a procedure to fully understand the flame propagation mechanism of the investigated dust, which standard test vessel is better to use and which issues have to be considered during testing. It involves a summary of all the observations done in the previous sections and consists of the chemico-physical characterization, the thermal analysis and the evaluation of dimensionless numbers in order to get insight into the flame propagation mechanism and the steps controlling it.

V.2. Future work

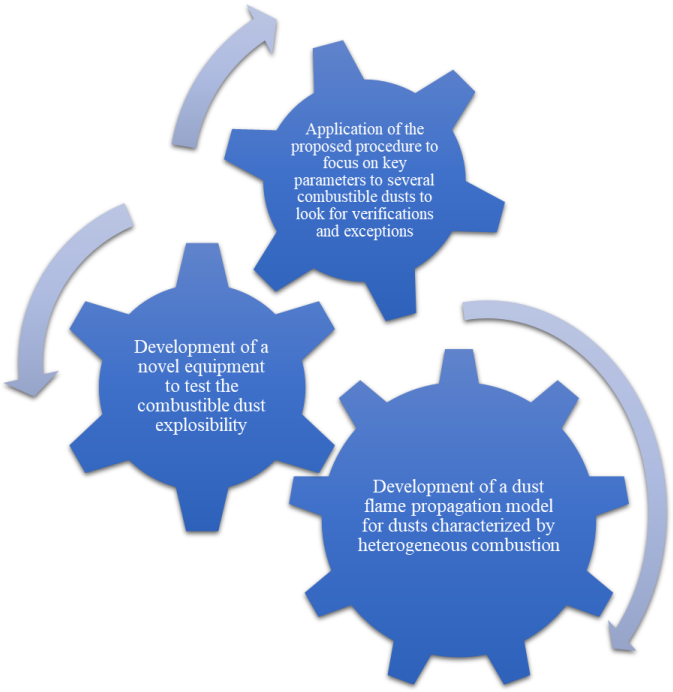

The work of this thesis has evidenced critical issues related to flammability/explosion tests in the standard vessels. The numerical and experimental results here obtained are the starting point for designing, developing and testing a novel equipment able to overcome all the issues and ensure the main requisites requested by all the standards (i.e., uniform dust concentration, controlled pre-ignition turbulence level, negligible effects of ignitors).

The development of the novel test device will be supported by detailed models of flame propagation of dust and hybrid mixtures by taking into account both homogeneous and heterogeneous path.

In addition, the procedure developed in this work will be tested and applied to a large number of combustible dusts to assess its reliability and to improve it eventually developing a “universal” complete and consistent procedure.

REFERENCES

[1] W. Bartknecht, *Dust explosions: Course, prevention, protection*. Springer Verlag, 1989.

[2] N. 654, "Prevention of Fire and Dust Explosions from Combustible Particulate Solids," 2017.

[3] G. Colonna, "Fire and Life Safety Inspection Manual," vol. 50, 2013.

[4] C. Cloney, "2020 Combustible Dust Incident Report - Version #1," *DustEx Research Ltd*, 2021. www.dustsafetyscience.com.

[5] U.S. Chemical Safety Board, "www.csb.gov/combustible-dust-hazard-investigation/," 2021. .

[6] M. P. Clouthier, L. Cormier, M. Hodapp, and D. Ogungbemide, "Dust explosions: Safety measures," vol. 3, pp. 193–228, 2019, doi: 10.1016/bs.mcps.2019.05.001.

[7] U. Bisignano, C. Esposito, G. Marena, A. Mazzei, N. Mazzei, and G. Mazzoli, "SOSTANZE IN POLVERE DURANTE LA MANIPOLAZIONE E LO STOCCAGGIO," pp. 61–68.

[8] National Fire Protection Association, "NFPA 68, Guide for Venting of Deflagrations, 2002 Edition," vol. 2002 Editi, p. 11, 2004.

[9] ASTM E1226-19, "Standard Test Method for Explosibility of Dust Clouds," *ASTM Int. West Conshohocken, PA*, pp. 1–15, 2019, doi: 10.1520/E1226-19.

[10] P. R. Amyotte and R. K. Eckhoff, "Dust explosion causation, prevention and mitigation: An overview," *J. Chem. Heal. Saf.*, vol. 17, no. 1, pp. 15–28, Jan. 2010, doi: 10.1016/j.jchas.2009.05.002.

[11] R. K. Eckhoff, *Dust Explosion in the Process Industries*. Boston: Gulf Professional Publishing, 2003.

[12] R. K. Eckhoff, *Dust explosions in the process industries-3rd Edition*. Gulf Professional Publishing, 2003.

[13] Z. Yuan, N. Khakzad, F. Khan, and P. R. Amyotte, "Dust explosions: A threat to the process industries," *Process Saf. Environ. Prot.*, vol. 98, pp. 57–71, Nov. 2015, doi: 10.1016/j.psep.2015.06.008.

[14] CEN - EN 1127-1, "Explosive Atmospheres - Explosion Prevention and Protection - Part 1: Basic concepts and Methodology.," 2019.

[15] L. G. Britton *et al.*, "The role of ASTM E27 methods in hazard assessment Part II: Flammability and Ignitability," *Process Saf. Prog.*, vol. 24, no. 1, pp. 12–28, 2005, doi: 10.1002/prs.10058.

[16] ASTM E2019-03, "Standard Test Method for Minimum Ignition Energy of a Dust Cloud in Air," *ASTM Int. West Conshohocken, PA*, pp. 1–9, 2013.

[17] ASTM E2021-15, "Standard Test Method for Hot-Surface Ignition Temperature of Dust Layers," *ASTM Int. West Conshohocken, PA*, pp. 1–10, 2015.

[18] ASTM E1491-06, "Standard Test Method for Minimum Autoignition Temperature of Dust Clouds," *ASTM Int. West Conshohocken, PA*, pp. 1–10, 2012.

[19] ASTM E2931-13, "Standard Test Method for Limiting Oxygen (Oxidant) Concentration of Combustible," *ASTM International, West Conshohocken, PA*. pp. 1–9, 2013, doi: 10.1520/ E2931-13.

[20] ASTM E1515-14, "Standard Test Method for Minimum Explosible Concentration of Combustible Dusts 1," *ASTM Int. West Conshohocken, PA*, no. Reapproved 2014, pp. 1–9, 1993, doi: 10.1520/E1515-14.

[21] ASTM E502-07, "Standard Test Method for Selection and Use of ASTM Standards for the Determination of Flash Point of Chemicals by Closed Cup Methods," *ASTM Int. West Conshohocken, PA*, no. Reapproved 2013, pp. 1–6, 1984, doi: 10.1520/E0502-07E01.priate.

[22] R. Sanchirico, V. Di Sarli, and A. Di Benedetto, "Volatile point of dust mixtures and hybrid mixtures," *J. Loss Prev. Process Ind.*, vol. 56, no. September, pp. 370–377, 2018, doi: 10.1016/j.jlp.2018.09.014.

[23] H. M. Cassel and United States. Bureau of Mines., "Some fundamental aspects of dust flames," 1964.

[24] W. Mitsui and T. Tanaka, "Simple Models of Dust Explosion. Predicting Ignition Temperature and Minimum Explosive Limit in Terms of Particle Size," *Ind. Eng. Chem. Process Des. Dev.*, vol. 12, pp. 384–389, 1973.

[25] M. Mittal and B. K. Guha, "Minimum ignition temperature of polyethylene dust: A theoretical model," *Fire Mater.*, vol. 21, no. 4, pp. 169–177, 1997, doi: 10.1002/(SICI)1099-1018(199707/08)21:4<169::AID-FAM604>3.0.CO;2-Y.

[26] N. Kalkert and H. Schecker, "Theoretische Überlegungen zum Einfluß der Teilchengröße auf die Mindestzündenergie von Stäuben," *Chemie Ing. Tech.*, vol. 51, no. 12, pp. 1248–1249, 1979, doi: 10.1002/cite.330511222.

[27] S. Copelli, M. S. Scotton, M. Barozzi, M. Derudi, and R. Rota, "A Practical Tool for Predicting the Minimum Ignition Energy of Organic Dusts," *Ind. Eng. Chem. Res.*, 2021, doi: 10.1021/acs.iecr.1c00309.

[28] A. Di Benedetto and P. Russo, "Thermo-kinetic modelling of dust explosions," *J. Loss Prev.*

Process Ind., vol. 20, no. 4–6, pp. 303–309, 2007, doi: 10.1016/j.jlp.2007.04.001.

[29] G. Jaeckel, "Die Staubexplosionen," *Zeitschrift fur Tech. Phys.*, pp. 67–67, 1924.

[30] J. Zehr, "Anleitung zu den Berechnungen iiber die Ziindgrenzwerte und die maximalen Explosionsdriicke," *VDI. Ber.*, vol. 19, pp. 63–68, 1957.

[31] I. Schonewald, "VereinfachteMethode zur Berechnung der unteren Ziindgrenze von StaubLuft- Gemischen," *Staub-Reinhalt*, vol. 31, pp. 376–378, 1971.

[32] W. Ishihama, "Studies on the Critical Explosion Density of Coal Dust Clouds," 1961.

[33] M. Hertzberg, K. L. Cashdollar, and C. P. Lazzara, "Limits of flammability of pulverized coals and other dusts," in *Eighteenth Symposium (Int.) on Combustion. The Combustion Institute, Pittsburgh*, 1981, pp. 717–719.

[34] W. Buksowicz and P. Wolanski, "No Title," *Progr. Astronaut. Aeronaut.*, vol. 87, pp. 414–425, 1983.

[35] D. Bradley, G. Dixon-Lewis, and S. El-Din Habik, "Lean flammability limits and laminar burning velocities of CH4-air-graphite mixtures and fine coal dusts," *Combust. Flame*, vol. 77, no. 1, pp. 41–50, 1989, doi: 10.1016/0010-2180(89)90103-X.

[36] Bartknecht, *Dust Explosions*. 1989.

[37] R. Siwek, "20-l-Laborapparatur fur die Bestimmung der Explosionskenngrossen brennbarer Staube. [20-liter laboratory apparatus for determination of explosion characteristics of combustible dusts]," Winterthur, Switzerland: Ciba-Geigy AG(Basel) and Winterthur Engineering College, 1977.

[38] R. Siwek, "Reliable determination of the safety characteristics in 20-l apparatus," in *Proceedings of the Flammable Dust Explosion Conference*, 1988, pp. 529–573.

[39] BS EN 14034-1, "Determination of explosion characteristics of dust clouds Part 1: Determination of maximum pressure Pmax of dust clouds," vol. 3, 2004.

[40] W. Gao, T. Mogi, J. Yu, X. Yan, J. Sun, and R. Dobashi, "Flame propagation mechanisms in dust explosions," *J. Loss Prev. Process Ind.*, vol. 36, pp. 186–194, 2015, doi: 10.1016/j.jlp.2014.12.021.

[41] A. Di Benedetto, P. Russo, P. Amyotte, and N. Marchand, "Modelling the effect of particle size on dust explosions," *Chem. Eng. Sci.*, vol. 65, no. 2, pp. 772–779, 2010, doi: 10.1016/j.ces.2009.09.029.

[42] D. Menon, D. Dollimore, and K. S. Alexander, "A TG – DTA study of the sublimation of nicotinic acid," *Thermochim. Acta*, vol. 392–393, pp. 237–241, 2002.

[43] C. Proust, "Experimental determination of the maximum flame temperatures and of the

laminar burning velocities for some combustible dust-air mixtures," 2014.

[44] A. Di Benedetto *et al.*, "Flame Propagation of Dust and Gas-Air Mixtures in a Tube," *Chia Laguna, Cagliari, Sardinia*, vol. 1, no. September, pp. 11–13, 2011.

[45] S. Hosseinzadeh, M. Vanierschot, F. Norman, F. Verplaetsen, and J. Berghmans, "Flame propagation and fl ow fi eld measurements in a Hartmann dust explosion tube," *Powder Technol.*, vol. 323, pp. 346–356, 2018, doi: 10.1016/j.powtec.2017.10.001.

[46] C. Proust, "A few fundamental aspects about ignition and flame propagation in dust clouds," *J. Loss Prev. Process Ind.*, vol. 19, no. 2–3, pp. 104–120, Mar. 2006, doi: 10.1016/J.JLP.2005.06.035.

[47] U. Krause and T. Kasch, "The influence of flow and turbulence on flame propagation through dust-air mixtures," *J. Loss Prev. Process Ind.*, vol. 13, no. 3–5, pp. 291–298, May 2000, doi: 10.1016/S0950-4230(99)00062-5.

[48] S. Wang, Y. Pu, F. Jia, and A. Gutkowski, "Effect of turbulence on flame propagation in cornstarch dust-air mixtures," *J. Therm. Sci.*, vol. 15, no. 2, pp. 186–192, 2006, doi: 10.1007/s11630-006-0186-4.

[49] H. Schneider and C. Proust, "Determination of turbulent burning velocities of dust air mixtures with the open tube method," *J. Loss Prev. Process Ind.*, vol. 20, no. 4–6, pp. 470–476, 2007, doi: 10.1016/j.jlp.2007.04.035.

[50] C. Proust, "Flame propagation and combustion in some dust-air mixtures," *J. Loss Prev. Process Ind.*, vol. 19, no. 1, pp. 89–100, Jan. 2006, doi: 10.1016/J.JLP.2005.06.026.

[51] K. Van Wingerden and L. Stavseng, "Measurements of the laminar burning velocities in dust-air mixtures," *VDI Berichte*, no. 1272, pp. 553–564, 1996.

[52] J.-L. Chen, R. Dobashi, and T. Hirano, "Mechanisms of flame propagation through combustible particle clouds," *J. Loss Prev. Process Ind.*, vol. 9, no. 3, pp. 225–229, May 1996, doi: 10.1016/0950-4230(96)00001-0.

[53] W.-J. Ju, R. Dobashi, and T. Hirano, "Reaction zone structures and propagation mechanisms of flames in stearic acid particle clouds," *J. Loss Prev. Process Ind.*, vol. 11, no. 6, pp. 423–430, Nov. 1998, doi: 10.1016/S0950-4230(98)00027-8.

[54] S. Wang, Y. Pu, F. U. Jia, A. Gutkowski, and J. Jarosinski, "An experimental study on flame propagation in cornstarch dust clouds," *Combust. Sci. Technol.*, vol. 178, no. 10–11, pp. 1957–1975, 2006, doi: 10.1080/00102200600790979.

[55] Center for Chemical Process Safety (CCPS), "CCPS Process Safety Glossary," *AIChE*, 2021. .

[56] M. A. Liberman, "Introduction to Physics and Chemistry of Combustion," *Introd. to Phys. Chem. Combust.*, no. January 2008, pp. 4–7, 2008, doi: 10.1007/978-3-540-78759-4.

[57] A. Pocheau, "Scale invariance in turbulent front propagation," *Phys. Rev. E*, vol. 49, no. 2, pp. 1109–1122, 1994, doi: 10.1103/PhysRevE.49.1109.

[58] H. N. Phylaktou, C. L. Gardner, G. E. Andrews, D. Barry, and A. Slattery, "Investigation into `rate of rise' detection systems for dust explosion suppression," *Inst. Chem. Eng. Symp. Ser.*, no. 147, pp. 629–644, 2000.

[59] P. Clavin and F. A. Williams, "Theory of premixed-flame propagation in large-scale turbulence," *J. Fluid Mech.*, vol. 90, no. 3, pp. 589–604, Feb. 1979, doi: 10.1017/S002211207900241X.

[60] C. W. Kauffman, S. R. Srinath, F. I. Tezok, J. A. Nicholls, and M. Sichel, "Turbulent and accelerating dust flames," *Symp. Combust.*, vol. 20, no. 1, pp. 1701–1708, Jan. 1985, doi: 10.1016/S0082-0784(85)80666-4.

[61] M. Gieras, W. Glinka, R. Klemens, and P. Wolanski, "Investigation of flame structure during laminar and turbulent burning in dust--air mixtures," in *Conf. Dust Expl. Prot. People Equip. Env*, 1995, vol. 168.

[62] G. Zhen and W. Leuckel, "Determination of Dust-Dispersion-lnduced Turbulence and its Influence on Dust Explosions," *Combust. Sci. Technol.*, vol. 113, no. 1, pp. 629–639, 1996, doi: 10.1080/00102209608935518.

[63] K. van Wingerden, B. Arntzen, and P. Kosinski, "Modelling of dust explosions," *VDI Berichte*, pp. 411-421+755, 2001.

[64] A. E. Dahoe, R. S. Cant, and B. Scarlett, "On the decay of turbulence in the 20-liter explosion sphere," *Flow, Turbul. Combust.*, vol. 67, no. 3, pp. 159–184, 2002, doi: 10.1023/A:1015099110942.

[65] C. Proust and B. Veyssiere, "Fundamental Properties of Flames Propagating in Starch Dust-Air Mixtures," *Combust. Sci. Technol.*, vol. 62, no. 4–6, pp. 149–172, 1988, doi: 10.1080/00102208808924007.

[66] C. Proust, "Experimental determination of the maximum flame temperatures and of the laminar burning velocities for some combustible dust-air mixtures," 1993.

[67] J. Nagy and H. C. Verakis, *Development and Control of Dust Explosions*. 1983.

[68] J. Mazurkiewicz, J. Jarosinski, and P. Wolanski, "Investigations of burning properties of cornstarch dust-air flame," *Arch. Combust.*, vol. 13, no. 3–4, 1993.

[69] U. Krause and T. Kasch, "Investigations on burning velocities of dust/air mixtures in

laminar flows," 1994.

[70] Y. Shag and F. You, "The effect of particle size on the minimum ignition temperature of flour powder," *1st CCPS Asia-Pacific Conf. Process Saf. 2013, APCPS 2013*, no. September 2013, pp. 586–593, 2013.

[71] N. Piccinini, "Dust explosion in a wool factory: Origin, dynamics and consequences," *Fire Saf. J.*, vol. 43, no. 3, pp. 189–204, 2008, doi: 10.1016/j.firesaf.2007.06.008.

[72] P. Salatino, A. Di Benedetto, R. Chirone, E. Salzano, and R. Sanchirico, "Analysis of an explosion in a wool-processing plant," *Ind. Eng. Chem. Res.*, vol. 51, no. 22, pp. 7713–7718, 2012, doi: 10.1021/ie2023614.

[73] S. M. Worsfold, P. R. Amyotte, F. I. Khan, A. G. Dastidar, and R. K. Eckhoff, "Review of the explosibility of nontraditional dusts," *Ind. Eng. Chem. Res.*, vol. 51, no. 22, pp. 7651–7655, 2012, doi: 10.1021/ie201614b.

[74] A. Di Benedetto, R. Sanchirico, and V. Di Sarli, *Dust explosions: Emerging/unique scenarios*, 1st ed., vol. 3. Elsevier Inc., 2019.

[75] L. Marmo and D. Cavallero, "Minimum ignition energy of nylon fibres," *J. Loss Prev. Process Ind.*, vol. 21, no. 5, pp. 512–517, 2008, doi: 10.1016/j.jlp.2008.04.003.

[76] L. Marmo, R. Sanchirico, A. Di Benedetto, V. Di Sarli, D. Riccio, and E. Danzi, "Study of the explosible properties of textile dusts," *J. Loss Prev. Process Ind.*, vol. 54, no. March, pp. 110–122, 2018, doi: 10.1016/j.jlp.2018.03.003.

[77] A. Klippel, M. Scheid, and U. Krause, "Investigations into the influence of dustiness on dust explosions," *J. Loss Prev. Process Ind.*, vol. 26, no. 6, pp. 1616–1626, 2013, doi: 10.1016/j.jlp.2013.07.016.

[78] HSE, "Risk of carbon monoxide release during the storage of wood pellets," 2021. http://www.hse.gov.uk/safetybulletins/co-wood-pellets.htm.

[79] T. Ennis, "Fire and explosion hazards in the biomass industries," *Inst. Chem. Eng. Symp. Ser.*, vol. 2016-Janua, no. 161, pp. 1–9, 2016.

[80] Canadian Biomass, "Explosion protection needs and awareness in the biomass industry," 2017. www.canadianbiomassmagazine.ca.

[81] P. Amyotte *et al.*, "Explosibility of nontraditional dusts: Experimental and modeling challenges," *Inst. Chem. Eng. Symp. Ser.*, no. 158, pp. 83–90, 2012.

[82] I. Iarossi, P. R. Amyotte, F. I. Khan, L. Marmo, A. G. Dastidar, and R. K. Eckhoff, "Explosibility of polyamide and polyester fibers," *J. Loss Prev. Process Ind.*, vol. 26, no. 6, pp. 1627–1633, 2013, doi: 10.1016/j.jlp.2013.07.015.

[83] R. Pilão, E. Ramalho, and C. Pinho, "Overall characterization of cork dust explosion," *J. Hazard. Mater.*, vol. 133, no. 1–3, pp. 183–195, 2006, doi: 10.1016/j.jhazmat.2005.10.015.

[84] UNI EN 14034-(1-4), "Determinazione delle caratteristiche di esplosione di nubi di polvere." 2011.

[85] L. Marmo, "Case study of a nylon fibre explosion: An example of explosion risk in a textile plant," *J. Loss Prev. Process Ind.*, vol. 23, no. 1, pp. 106–111, 2010, doi: 10.1016/j.jlp.2009.06.006.

[86] V. Di Sarli, E. Danzi, L. Marmo, R. Sanchirico, and A. Di Benedetto, "CFD simulation of turbulent flow field, feeding and dispersion of non-spherical dust particles in the standard 20 L sphere," *J. Loss Prev. Process Ind.*, vol. 62, no. July, p. 103983, 2019, doi: 10.1016/j.jlp.2019.103983.

[87] M. Traoré, O. Dufaud, L. Perrin, S. Chazelet, and D. Thomas, "Dust explosions: How should the influence of humidity be taken into account?," *Process Saf. Environ. Prot.*, vol. 87, no. 1, pp. 14–20, 2009, doi: 10.1016/j.psep.2008.08.001.

[88] D. H. Cho, D. R. Armstrong, and R. P. Anderson, "Combined vapor and chemical explosions of metals and water," *Nucl. Eng. Des.*, vol. 155, no. 1–2, pp. 405–412, 1995, doi: 10.1016/0029-5493(94)00885-3.

[89] Q. S. M. Kwok, R. C. Fouchard, A. M. Turcotte, P. D. Lightfoot, R. Bowes, and D. E. G. Jones, "Characterization of Aluminum Nanopowder Compositions," *Propellants, Explos. Pyrotech.*, vol. 27, pp. 229–240, 2002, doi: 10.1002/prep.200390018.

[90] P. R. Amyotte, S. Chippett, and M. J. Pegg, "Effects of turbulence on dust explosions," *Prog. Energy Combust. Sci.*, vol. 14, pp. 293–310, 1989, doi: 10.1016/S0950-4230(97)00021-1.

[91] R. Borghi, "On the Structure and Morphology of Turbulent Premixed Flames," in *Recent Advances in the Aerospace Sciences*, 1985, pp. 117–138.

[92] N. Peters, "Laminar flamelet concepts in turbulent combustion," in *21th symposium international on combustion*, 1986, pp. 1231–1250.

[93] R. G. Abdel-Gayed and D. Bradley, "Combustion Regimes and the Straining of Turbulent Premixed Flames," *Combust. Flame*, vol. 76, pp. 213–218, 1989, doi: 10.1163/187529293X00358.

[94] T. J. Poinsot, "Direct simulation of turbulent combustion," 1990.

[95] N. Peters, *Turbulent Combustion*. Cambridge: Cambridge University Press, 2000.

[96] A. Kolmogorov, "The Local Structure of Turbulence in Incompressible Viscous Fluid for

Very Large Reynolds' Numbers," *Dokl. Akad. Nauk SSSR*, vol. 30, pp. 301–305, 1941.

[97] I. Glassman and R. A. Yetter, *Combustion-Fourth edition*. Elsevier, 2008.

[98] K. L. Cashdollar and K. Chatrathi, "Minimum explosible dust concentrations measured in 20-L and 1-M3 chambers," *Combust. Sci. Technol.*, vol. 87, no. 1–6, pp. 157–171, 1992, doi: 10.1080/00102209208947213.

[99] J. E. Going, K. Chatrathi, and K. L. Cashdollar, "Flammability limit measurements for dusts in 20-L and 1-m3 vessels," *J. Loss Prev. Process Ind.*, vol. 13, no. 3–5, pp. 209–219, 2000, doi: 10.1016/S0950-4230(99)00043-1.

[100] A. Di Benedetto, A. Garcia-Agreda, P. Russo, and R. Sanchirico, "Combined effect of ignition energy and initial turbulence on the explosion behavior of lean gas/dust-air mixtures," *Ind. Eng. Chem. Res.*, vol. 51, no. 22, pp. 7663–7670, 2012, doi: 10.1021/ie201664a.

[101] S. A. Rodgers and E. A. Ural, "Practical Issues with Marginally Explosible Dusts—Evaluating the Real Hazard," *Process Saf. Prog.*, vol. 30, no. 3, pp. 266–279, 2011, doi: 10.1002/prs.

[102] M. P. Clouthier *et al.*, "Iron and aluminum powder explosibility in 20-L and 1-m3 chambers," *J. Loss Prev. Process Ind.*, vol. 62, p. 103927, Nov. 2019, doi: 10.1016/J.JLP.2019.103927.

[103] J. R. Taveau, S. M. Lemkowitz, S. Hochgreb, and D. Roekaerts, "Scaling up metal dusts deflagrations severity," 2018.

[104] J. R. Taveau, S. M. Lemkowitz, S. Hochgreb, and D. J. E. M. Roekaerts, "Metal dusts explosion hazards and protection," *Chem. Eng. Trans.*, vol. 77, pp. 7–12, 2019, doi: 10.3303/CET1977002.

[105] C. Proust, A. Accorsi, and L. Dupont, "Measuring the violence of dust explosions with the '20 l sphere' and with the standard 'ISO 1 m3 vessel'. Systematic comparison and analysis of the discrepancies," *J. Loss Prev. Process Ind.*, vol. 20, no. 4–6, pp. 599–606, 2007, doi: 10.1016/j.jlp.2007.04.032.

[106] ISO 6184-1:1985, "Explosion Protection Systems, Part 1, Determination of Explosion Indices of Combustible Dusts in Air," 1985.

[107] N. 68 NFPA, "Explosion protection by deflagration venting," 2018.

[108] M. P. Clouthier, D. Ogungbemide, C. Cloney, R. G. Zalosh, R. C. Ripley, and P. R. Amyotte, "Numerical Investigation of Overdriving in the 20-L Siwek Chamber," in *13 th International Symposium on Hazards, Prevention and Mitigation of Industrial Explosions*

ISHPMIE2020 Physikalisch-Technische Bundesanstalt, 2020, pp. 663–676, doi: 10.7795/810.20200724.

[109] J. R. Taveau, J. E. Going, S. Hochgreb, S. M. Lemkowitz, and D. J. E. M. Roekaerts, "Igniter-induced hybrids in the 20-l sphere," *J. Loss Prev. Process Ind.*, vol. 49, pp. 348–356, 2017, doi: 10.1016/j.jlp.2017.07.014.

[110] K. J. Mintz, "Problems in experimental measurements of dust explosions," *J. Hazard. Mater.*, vol. 42, no. 2, pp. 177–186, 1995, doi: 10.1016/0304-3894(95)00011-I.

[111] K. L. Cashdollar, "Overview of dust explosibility characteristics," *J. Loss Prev. Process Ind.*, vol. 13, no. 3–5, pp. 183–199, 2000, doi: 10.1016/S0950-4230(99)00039-X.

[112] C. T. Cloney, R. C. Ripley, P. R. Amyotte, and F. I. Khan, "Quantifying the effect of strong ignition sources on particle preconditioning and distribution in the 20-L chamber," *J. Loss Prev. Process Ind.*, vol. 26, no. 6, pp. 1574–1582, 2013, doi: 10.1016/j.jlp.2013.08.010.

[113] W. Gao, S. Zhong, N. Miao, and H. Liu, "Effect of ignition on the explosion behavior of 1-Octadecanol/air mixtures," *Powder Technol.*, vol. 241, pp. 105–114, 2013, doi: 10.1016/j.powtec.2013.03.015.

[114] The Fauske Team, "Combustible Dust Basics, Part 3: What is Overdriving?," 2014. https://www.fauske.com/blog/combustible-dust-basics-part-3-what-is-overdriving.

[115] K. L. Cashdollar, "Coal dust explosibility," *J. Loss Prev. Process Ind.*, vol. 9, no. 1, pp. 65–76, Jan. 1996, doi: 10.1016/0950-4230(95)00050-X.

[116] Y. K. Pu, J. Jarosinski, V. G. Johnson, and C. W. Kauffman, "Turbulence effects on dust explosions in the 20-liter spherical vessel," *Symp. Combust.*, vol. 23, no. 1, pp. 843–849, 1990, doi: 10.1016/S0082-0784(06)80338-3.

[117] P. G. J. van der Wel, J. P. W. van Veen, S. M. Lemkowitz, B. Scarlett, and C. J. M. van Wingerden, "An interpretation of dust explosion phenomena on the basis of time scales," *Powder Technol.*, vol. 71, no. 2, pp. 207–215, Aug. 1992, doi: 10.1016/0032-5910(92)80010-T.

[118] D. B. Mercer *et al.*, "The influence of injector design on the decay of pre-ignition turbulence in a spherical explosion chamber," *J. Loss Prev. Process Ind.*, vol. 14, no. 4, pp. 269–282, 2001, doi: 10.1016/S0950-4230(00)00051-6.

[119] F. Hauert and A. Vogl, "Measurement of Dust Cloud Characteristics in Industrial Plants (Number: PL 910695)," 1995. [Online]. Available: www.fsa.de › exschutz_projektliste%0A.

[120] O. Kalejaiye, "An investigation of the effectiveness of dust dispersion in the Siwek 20-l

chamber," Dalhousie University, Halifax, Nova Scotia, 2001.

[121] O. Kalejaiye, P. R. Amyotte, M. J. Pegg, and K. L. Cashdollar, "Effectiveness of dust dispersion in the 20-L Siwek chamber," *J. Loss Prev. Process Ind.*, vol. 23, no. 1, pp. 46–59, 2010, doi: 10.1016/j.jlp.2009.05.008.

[122] A. Di Benedetto, P. Russo, R. Sanchirico, and V. Di Sarli, "CFD Simulations of Turbulent Fluid Flow and Dust Dispersion in the 20 Liter Explosion Vessel," *AIChE*, vol. 59, no. 7, pp. 2485–2496, 2013, doi: 10.1002/aic.

[123] P. Russo, P. R. Amyotte, F. I. Khan, and A. Di Benedetto, "Modelling of the effect of size on flocculent dust explosions," *J. Loss Prev. Process Ind.*, vol. 26, no. 6, pp. 1634–1638, 2013, doi: 10.1016/j.jlp.2013.07.012.

[124] V. Di Sarli, P. Russo, R. Sanchirico, and A. Di Benedetto, "CFD simulations of the effect of dust diameter on the dispersion in the 20L bomb," *Chem. Eng. Trans.*, vol. 31, pp. 727–732, 2013.

[125] V. Di Sarli, P. Russo, R. Sanchirico, and A. Di Benedetto, "CFD simulations of dust dispersion in the 20 L vessel: Effect of nominal dust concentration," *J. Loss Prev. Process Ind.*, vol. 27, no. 1, pp. 8–12, 2014, doi: 10.1016/j.jlp.2013.10.015.

[126] P. Russo and A. Di Benedetto, "Review of a dust explosion modeling," *Chem. Eng. Trans.*, vol. 31, pp. 955–960, 2013, doi: 10.3303/CET1331160.

[127] A. Di Benedetto, P. Russo, R. Sanchirico, and V. Di Sarli, "A Fan-Equipped Reactor for Dust Explosion Tests," *AIChE*, vol. 61, no. 5, pp. 1572–1580, 2015, doi: 10.1002/aic.

[128] V. Di Sarli, R. Sanchirico, P. Russo, and A. Di Benedetto, "CFD modeling and simulation of turbulent fluid flow and dust dispersion in the 20-L explosion vessel equipped with the perforated annular nozzle," *J. Loss Prev. Process Ind.*, vol. 38, pp. 204–213, Nov. 2015, doi: 10.1016/j.jlp.2015.09.015.

[129] ASTM D7582 - 15, "Standard Test Methods for Proximate Analysis of Coal and Coke by Macro Thermogravimetric Analysis," *ASTM Int. West Conshohocken, PA*, 2015.

[130] B. E. Launder and D. B. Spalding, *Lectures in mathematical models of turbulence*. London; New York: Academic Press, 1972.

[131] Fluent Inc, "Chapter 15 Discrete Phase Modelling, Section 4 Laws for Heat and Mass Exchange," *ANSYS FLUENT User's Guid.*, pp. 1–170, 2016, [Online]. Available: http://www.afs.enea.it/fluent/Public/Fluent-Doc/PDF/chp19.pdf.

[132] S. A. Morsi and A. J. Alexander, "An investigation of particle trajectories in two-phase flow systems," *J. Fluid Mech.*, vol. 55, no. 2, pp. 193–208, 1972, doi:

10.1017/S0022112072001806.

[133] S. Elghobashi, "On predicting particle-laden turbulent flows," *Appl. Sci. Res.*, vol. 52, no. 4, pp. 309–329, 1994, doi: 10.1007/BF00936835.

[134] Ansys, "Chemkin Theory Manual 17.0," *Chemkin® Software*. 2016.

[135] C. Morley, "GASEQ, a chemical equilibrium program for windows." 2005.

[136] S. Pérez and E. Bertoft, "The molecular structures of starch components and their contribution to the architecture of starch granules: A comprehensive review," *Starch/Staerke*, vol. 62, no. 8, pp. 389–420, 2010, doi: 10.1002/star.201000013.

[137] O.-S. Han, M. Yashima, T. Matsuda, H. Matsui, A. Miyake, and T. Ogawa, "A study of flame propagation mechanisms in lycopodium dust clouds based on dust particles' behavior," *J. Loss Prev. Process Ind.*, vol. 14, no. 3, pp. 153–160, Jan. 2001, doi: 10.1016/S0950-4230(00)00049-8.

[138] L. Centrella, M. Portarapillo, G. Luciani, R. Sanchirico, and A. Di Benedetto, "Synergistic behavior of flammable dust mixtures: A novel classification," *J. Hazard. Mater.*, vol. 397, no. January, p. 122784, 2020, doi: 10.1016/j.jhazmat.2020.122784.

[139] E. S. Domalski and E. D. Hearing, "Heat Capacities and Entropies of Organic Compounds in the Condensed Phase. Volume III," *J. Phys. Chem. Ref. Data*, vol. 25, no. 1, pp. 1–525, Jan. 1996, doi: 10.1063/1.555985.

[140] M. Portarapillo, G. Luciani, R. Sanchirico, and A. Di Benedetto, "Ignition mechanism of flammable dust and dust mixtures: an insight through TG/DSC analysis," *Under Rev. AIChE J.*, 2019.

[141] "NIST Standard Reference Database 69: NIST Chemistry WebBook." 2018.

[142] S. Jingyan, L. Yuwen, W. Zhiyong, and W. Cunxin, "Investigation of thermal decomposition of ascorbic acid by TG-FTIR and thermal kinetics analysis," *J. Pharm. Biomed. Anal.*, vol. 77, pp. 116–119, Apr. 2013, doi: 10.1016/j.jpba.2013.01.018.

[143] Royal Society of Chemistry, "ChemSpider - Search and Share Chemistry," 2020.

[144] N. Bartsch *et al.*, "Thermal Stability of Polymer Additives: Comparison of Decomposition Models Including Oxidative Pyrolysis," *J. Vinyl Addit. Technol.*, vol. 25, pp. E12–E27, 2018, doi: 10.1002/vnl.21654.

[145] M. Portarapillo, G. Luciani, R. Sanchirico, and A. Di Benedetto, "Ignition mechanism of flammable dust and dust mixtures: An insight through thermogravimetric/differential scanning calorimetry analysis," *AIChE J.*, vol. 66, no. 8, 2020, doi: 10.1002/aic.16256.

[146] X. Fan, "Formation of Furan from Carbohydrates and Ascorbic Acid Following Exposure

to Ionizing Radiation and Thermal Processing," *J. Agric. Food Chem.*, vol. 53, pp. 7826–7831, 2005, doi: 10.1021/jf051135x.

[147] A. Limacher, J. Kerler, B. Conde-Petit, and I. Blank, "Formation of furan and methylfuran from ascorbic acid in model systems and food," *Food Addit. Contam.*, vol. 24, no. sup1, pp. 122–135, 2007, doi: 10.1080/02652030701393112.

[148] E. Wiercigroch *et al.*, "Raman and infrared spectroscopy of carbohydrates: A review," *Spectrochim. Acta - Part A Mol. Biomol. Spectrosc.*, vol. 185, pp. 317–335, 2017, doi: 10.1016/j.saa.2017.05.045.

[149] J. Saunier, J. M. Herry, N. Yagoubi, and C. Marlière, "Exploring complex transitions between polymorphs on a small scale by coupling AFM, FTIR and DSC: the case of Irganox 1076® antioxidant," *RSC Adv.*, vol. 7, no. 7, pp. 3804–3818, 2017, doi: 10.1039/c6ra25632e.

[150] Agilent Technologies Inc., "Screening and qualitative identification of antioxidant polymer additives by HPLC with UV/Vis and ApCI-MS Detection," 2003.

[151] M. Akkbik, Z. Bin Assim, and F. B. Ahmad, "Optimization and Validation of RP-HPLC-UV/Vis Method for Determination Phenolic Compounds in Several Personal Care Products," *Int. J. Anal. Chem.*, vol. 2011, pp. 1–9, 2011, doi: 10.1155/2011/858153.

[152] ASTM International, "Standard Test Method for Minimum Ignition Energy of a Dust Cloud in Air," 2003, pp. 1–11.

[153] M. Pietraccini, E. Danzi, L. Marmo, A. Addo, and P. Amyotte, "Effect of particle size distribution, drying and milling technique on explosibility behavior of olive pomace waste," *J. Loss Prev. Process Ind.*, vol. 71, no. January, p. 104423, 2021, doi: 10.1016/j.jlp.2021.104423.

[154] M. Portarapillo, E. Danzi, R. Sanchirico, L. Marmo, and A. Di Benedetto, "Energy recovery from vinery waste: dust explosion issues," *Submitt. to Appl. Sci.*, vol. SI:Dust Ex, 2021.

[155] E. Danzi, A. Di Benedetto, R. Sanchirico, M. Portarapillo, and L. Marmo, "Biomass from Winery Waste : Evaluation of Dust Explosion Hazards," *Chem. Eng. Trans.*, vol. 86, 2021.

[156] G. Bekiaris, G. Koutrotsios, P. A. Tarantilis, C. S. Pappas, and G. I. Zervakis, "FTIR assessment of compositional changes in lignocellulosic wastes during cultivation of Cyclocybe cylindracea mushrooms and use of chemometric models to predict production performance," *J. Mater. Cycles Waste Manag.*, vol. 22, no. 4, pp. 1027–1035, 2020, doi: 10.1007/s10163-020-00995-7.

[157] A. M. Raspolli Galletti *et al.*, "Midinfrared FT-IR as a tool for monitoring herbaceous

biomass composition and its conversion to furfural," *J. Spectrosc.*, vol. 2015, 2015, doi: 10.1155/2015/719042.

[158] ASTM D3176 − 15, "Standard Practice for Ultimate Analysis of Coal and Coke," *ASTM Int. West Conshohocken, PA*, 2015, doi: 10.1520/D3176-15.2.

[159] M. Hu *et al.*, "Thermogravimetric kinetics of lignocellulosic biomass slow pyrolysis using distributed activation energy model, Fraser-Suzuki deconvolution, and iso-conversional method," *Energy Convers. Manag.*, vol. 118, pp. 1–11, 2016, doi: 10.1016/j.enconman.2016.03.058.

[160] N. Zeniya, E. Obataya, K. Endo-Ujiie, and M. Matsuo-Ueda, "Application of time–temperature–humidity superposition to the mass loss of wood through hygrothermally accelerated ageing at 95–140 °C and different relative humidity levels," *SN Appl. Sci.*, vol. 1, no. 1, pp. 1–8, 2019, doi: 10.1007/s42452-018-0009-8.

[161] K. Endo, E. Obataya, N. Zeniya, and M. Matsuo, "Effects of heating humidity on the physical properties of hydrothermally treated spruce wood," *Wood Sci. Technol.*, vol. 50, no. 6, pp. 1161–1179, 2016, doi: 10.1007/s00226-016-0822-4.

[162] D. Sandberg, P. Haller, and P. Navi, "Thermo-hydro and thermo-hydro-mechanical wood processing: An opportunity for future environmentally friendly wood products," *Wood Mater. Sci. Eng.*, vol. 8, no. 1, pp. 64–88, 2013, doi: 10.1080/17480272.2012.751935.

[163] C. Ganne-Chédeville, A. S. Jääskeläinen, J. Froidevaux, M. Hughes, and P. Navi, "Natural and artificial ageing of spruce wood as observed by FTIR-ATR and UVRR spectroscopy," *Holzforschung*, vol. 66, no. 2, pp. 163–170, 2012, doi: 10.1515/HF.2011.148.

[164] M. Portarapillo *et al.*, "Chemico-physical and thermal characterization of flammable nylon 6,6 dusts," *Submitt. to Fuel*, 2021.

[165] C. A. Schneider, W. S. Rasband, and K. W. Eliceiri, "NIH Image to ImageJ: 25 years of image analysis.," *Nat. Methods*, vol. 9, no. 7, pp. 671–675, 2012, doi: 10.1038/nmeth.2089.

[166] L. A. Diaz-Alejo, E. C. Menchaca-Campos, J. U. Chavarin, R. Sosa-Fonseca, and M. A. Garcia-Sanchez, "Effects of the addition of ortho- and para-N[H.sub.2] substituted tetraphenylporphyrins on the structure of Nylon 66," *Int. J. Polym. Sci.*, Jul. 2013, [Online]. Available: https://link.gale.com/apps/doc/A375698681/AONE?u=anon~3de483cc&sid=googleScholar&xid=6063c5dd.

[167] P. Debye and P. Scherrer, "Interference of irregularly oriented partcles in x-rays," *Phys.*, vol. 17, pp. 277–283, 1916.

[168] W. H. Bragg and W. L. Bragg, “The Reflexion of X-rays by Crystals,” *Proc. R. Soc. Lond. A.*, vol. 88, no. 605, pp. 428–38, 1913, doi: 10.1098/rspa.1913.0040.

[169] T. Nabatame, T. Yasuda, M. Nishizawa, M. Ikeda, T. Horikawa, and A. Toriumi, “Comparative Studies on Oxygen Diffusion Coefficients for Amorphous and γ-al2o3 Films using 18O Isotope,” *Japanese J. Appl. Physics, Part 1 Regul. Pap. Short Notes Rev. Pap.*, vol. 42, no. 12, pp. 7205–7208, 2003, doi: 10.1143/jjap.42.7205.

[170] P. R. Hornsby, J. Wang, R. Rothon, G. Jackson, G. Wilkinson, and K. Cossick, “Thermal decomposition behaviour of polyamide fire-retardant compositions containing magnesium hydroxide filler,” *Polym. Degrad. Stab.*, vol. 51, no. 3, pp. 235–249, 1996, doi: 10.1016/0141-3910(95)00181-6.

[171] H. Xia, J. Peng, and L. Zhang, “Preparation of high surface area activated carbon from Eupatorium adenophorum using K2CO3 activation by microwave heating,” *Green Process. Synth.*, vol. 4, no. 4, pp. 299–305, 2015, doi: 10.1515/gps-2015-0025.

[172] W. E. Ranz and W. R. Marshall Jr., “Evaporation from drops,” *Chem. Eng. Prog.*, vol. 48, p. (part i) 141–146 and (part ii) 173–180, 1952.

[173] P. N. Rowe, K. T. Claxton, and J. B. Lewis, “Heat and mass transfer from a single sphere in an extensive flowing fluid,” *Trans. Inst. Chem. Eng.*, vol. 43, pp. T14–T31, 1965.

[174] J. H. Flynn and L. A. Wall, “A Quick, Direct Method for the Determination of Activation Energy from Thermogravimetric Data,” *Polym. Lett.*, vol. 4, pp. 323–328, 1966.

[175] L. J. Zhao and Q. Sun, “Calculations of effectiveness factors and the criteria of mass transfer effect for hightemperature methanation (HTM) catalyst,” *Int. J. Low-Carbon Technol.*, vol. 10, no. 3, pp. 288–293, 2013, doi: 10.1093/ijlct/ctu005.

[176] A. S. Michaels and H. J. Bixler, “Flow of gases through polyethylene,” *J. Polym. Sci.*, vol. 50, no. 154, pp. 413–439, 1961, doi: 10.1002/pol.1961.1205015412.

[177] H. W. Starkweather, P. Zoller, and G. A. Jones, “Heat of Fusion of 66 Nylon.,” *J. Polym. Sci. Part A-2, Polym. Phys.*, vol. 22, no. 9, pp. 1615–1621, 1984, doi: 10.1002/pol.1984.180220905.

[178] Professional Plastics, “Thermal Properties of Plastic Materials.” https://www.professionalplastics.com/professionalplastics/ThermalPropertiesofPlasticMaterials.pdf.

[179] C. Sheng and J. L. T. Azevedo, “Estimating the higher heating value of biomass fuels from basic analysis data,” *Biomass and Bioenergy*, vol. 28, no. 5, pp. 499–507, 2005, doi: 10.1016/j.biombioe.2004.11.008.

[180] A. Berrocal, J. Baeza, J. Rodríguez, M. Espinosa, and J. Freer, "Effect of tree age on variation of pinus radiata D. Don chemical composition," *J. Chil. Chem. Soc.*, vol. 49, no. 3, pp. 251–256, 2004, doi: 10.4067/s0717-97072004000300012.

[181] M. Portarapillo, V. Di Sarli, R. Sanchirico, and A. Di Benedetto, "CFD Simulation of the Dispersion of Binary Dust Mixtures in the 20 L Vessel," *J. Loss Prev. Process Ind.*, vol. 67, no. April, p. 104231, 2020, doi: 10.1016/j.jlp.2020.104231.

[182] A. I. Kartushinsky, E. E. Michaelides, Y. A. Rudi, S. V. Tisler, and I. N. Shcheglov, "Numerical simulation of three-dimensional gas-solid particle flow in a horizontal pipe," *AIChE J.*, vol. 57, no. 11, pp. 2977–2988, 2011, doi: 10.1002/aic.12528.

[183] G. G. Stokes, "On the Effect of the Internal Friction of Fluids on the Motion of Pendulums," *Trans. Cambridge Philos. Soc.*, vol. 9, pp. 1–86, 1851, doi: 10.1017/cbo9780511702266.002.

[184] D. Vigolo, S. Radl, and H. A. Stone, "Unexpected trapping of particles at a T junction-Supporting Information," *Proc. Natl. Acad. Sci. U. S. A.*, vol. 111, no. 13, pp. 1–15, 2014.

[185] M. Portarapillo, M. Trofa, R. Sanchirico, and A. Di Benedetto, "CFD simulations of dust dispersion in the 1 m3 explosion vessel," *J. Loss Prev. Process Ind.*, vol. 68, no. July, p. 104274, 2020, doi: 10.1016/j.jlp.2020.104274.

[186] M. Portarapillo, M. Trofa, R. Sanchirico, and A. Di Benedetto, "CFD simulations of the effect of dust diameter on the dispersion in the 1 m3 explosion vessel," *Chem. Eng. Trans.*, vol. 86, 2021.

[187] M. Portarapillo, R. Sanchirico, and A. Di Benedetto, "Effect of turbulence spatial distribution on the deflagration index: Comparison between 20 L and 1 m3 vessels," *J. Loss Prev. Process Ind.*, vol. 71, no. December 2020, 2021, doi: 10.1016/j.jlp.2021.104484.

[188] M. Portarapillo, M. Trofa, R. Sanchirico, and A. Di Benedetto, "CFD simulation of turbulent fluid flow and dust dispersion in the 1 m3 Explosion Vessel equipped with the rebound nozzle," *Under Rev. J. Loss Prev. Process Ind.*, 2021.

[189] Z. Dyduch, A. Toman, and W. Adamus, "Measurements of turbulence intensity in the standard 1 m3 vessel," *J. Loss Prev. Process Ind.*, vol. 40, pp. 180–187, 2016, doi: 10.1016/j.jlp.2015.12.019.

[190] A. E. Dahoe, J. F. Zevenbergen, S. M. Lemkowitz, and B. Scarlett, "Dust explosions in spherical vessels: The role of flame thickness in the validity of the 'cube-root law,'" *J. Loss Prev. Process Ind.*, vol. 9, no. 1 SPEC. ISS., pp. 33–44, 1996, doi: 10.1016/0950-4230(95)00054-2.

[191] H. Sattar, C. Huescar-Medina, D. Slatter, G. E. Andrews, H. N. Phylaktou, and B. M. Gibbs, "Calibration of new dust dispersion systems in the 1m 3 standard dust explosion vessel for fibrous biomass testing," 2016.

[192] A. Garcia Agreda, A. Di Benedetto, P. Russo, E. Salzano, and R. Sanchirico, "The Role of Ignition Delay Time on the Deflagration Index in a 20l Bomb," *Comput. Methods Appl. Mech. Eng.*, vol. 57, no. 1, pp. 683–694, 2011, [Online]. Available: http://rpsonline.com.sg/proceedings/9789810877248/html/978-981-08-7724-8_10-04.xml.

[193] Reaction Design: San Diego, "CHEMKIN-PRO Release 2019." 2019.

[194] R. K. Eckhoff and K. P. Mathisen, "A critical examination of the effect of dust moisture on the rate of pressure rise in Hartmann bomb tests," *Fire Saf. J.*, vol. 1, no. 4–5, pp. 273–280, 1978, doi: 10.1016/0379-7112(78)90016-4.

[195] T. Poinsot and D. Veynante, *Theoretical and numerical combustion - Second edition*. Edwards, 2005.

[196] M. Portarapillo, R. Sanchirico, and A. Di Benedetto, "On the pyrotechnic ignitors role in dust explosion testing : Comparison between 20 L and 1 m 3 explosion vessels," *Process Saf. Prog.*, no. February, pp. 1–7, 2021, doi: 10.1002/prs.12249.

[197] K. N. Palmer, M. A. Tonkin, and P. S. Tonkin, "The explosibility of Dusts in Small-Scale Tests and Large- Scale Industrial Plant," *I.Chem.E. Symp. Ser.*, vol. 25, pp. 66–75, 1968.

[198] N. Kuai *et al.*, "Experiment-based investigations on the effect of ignition energy on dust explosion behaviors," *J. Loss Prev. Process Ind.*, vol. 26, no. 4, pp. 869–877, 2013, doi: 10.1016/j.jlp.2013.03.005.

[199] J. K. Thomas, D. C. Kirby, and J. E. Going, "Explosibility of a Urea Dust Sample," *Process Saf. Prog.*, vol. 32, no. 2, pp. 189–192, 2013, doi: 10.1002/prs.

[200] J. Bucher, A. Ibarreta, K. Marr, and T. Myers, "Testing of Marginally Explosible Dusts: Evaluation of Overdriving and Realistic Ignition Sources in Process Facilities," 2012.